SCUOLA DI DOTTORATO
UNIVERSITÀ DEGLI STUDI DI MILANO-BICOCCA

Department of **Physics "G. Occhialini"**

PhD program in **Physics and Astronomy**, **XXXVIII** cycle
Curriculum: **Subnuclear Physics**

Gate-Based Enhancement of Superconducting Qubit Sensitivity to Ultralight Bosonic Dark Matter

Roberto Moretti
Registration number: 825617

Tutor: **Prof. Andrea Giachero**
Supervisor: **Prof. Angelo Nucciotti**

Coordinator: **Prof. Stefano Ragazzi**

Academic Year **2024/2025**

UNIVERSITY OF MILANO-BICOCCA

Department of Physics "G. Occhialini"

Gate-Based Enhancement of Superconducting Qubit Sensitivity to Ultralight Bosonic Dark Matter

Roberto MORETTI

Abstract

The nature of dark matter remains one of the most pressing mysteries in fundamental physics. Among the particles proposed as dark matter constituents, ultralight photon-coupled bosons stand out as promising candidates, including axions, axion-like particles (ALPs), and dark photons. In the hypothesis that these particles make up the galactic dark matter halo, they can generate coherent electromagnetic fields oscillating at frequencies determined by their masses. In the microwave regime, these fields can be detected through resonant interactions with highly sensitive superconducting quantum devices.
This thesis examines practical approaches for axions, ALPs, and dark photons searches using superconducting transmon qubits as detectors. The detection exploits direct resonant excitation: when a transmon qubit is resonant with the monochromatic dark matter signal, energy exchange between the two drives a coherent population transfer from the ground to the excited state, analogous to driven Rabi oscillations. The qubit's excitation probability after a fixed interaction time (constrained by qubit coherence, typically $\sim$ 100 µs) encodes information about the signal strength. Sweeping the qubit's frequency enables the search for resonances with dark matter at a specific dark particle mass, covering wide frequency ranges.

The main contribution of this thesis addresses a critical challenge in superconducting dark matter search experiments: weak dark-sector couplings yield excitation probabilities that are difficult to distinguish from noise and thermal background. We introduce a quantum signal amplification protocol that post-processes the state of the sensing qubit after it interacts with dark matter via a programmable, gate-based enhancement circuit. The circuit we developed dramatically improves the detector's response to small dark matter signals. This protocol leverages an ancilla qubit coupled to the sensor, implementing a small-sized quantum circuit followed by ancilla measurement and post-selection of the outcome. Successful post-selection greatly improves sensitivity to weak signals, while unsuccessful post-selection destroys the sensing qubit interaction history. Our approach requires optimizing the trade-off between achieving a high post-selection success rate and, at the same time, a large sensitivity enhancement in the success case.
A significant practical advantage over other quantum enhancement schemes in existing literature, based on preparing fully-entangled multi-qubit states and letting them evolve under dark matter, is that our enhancement circuit is applied only *after* the sensing qubit is exposed to dark matter interaction, avoiding the stringent requirements of maintaining multi-qubit entanglement throughout long sensing time intervals. Moreover, the protocol requires only one two-qubit gate, ensuring natural compatibility with modern noisy superconducting quantum computing platforms.

Comprehensive performance characterization of our experiment was conducted, incorporating realistic noise sources, i.e. finite coherence times (T_1, T_2), state preparation errors, readout infidelity on both qubits, and thermal population effects. The analysis focuses on dark photon detection, as axion and ALP searches would require applying a few-tesla magnetic field directly to the chip, severely degrading qubit coherence. Our results demonstrate that readout fidelity and accuracy in state preparation heavily affect the overall performance of the experiment. Under optimal (yet achievable) error conditions (0.5% readout error, 0.1% preparation error), a two-qubit enhanced detector achieves an integration time speedup factor of $\mathcal{G} \sim 1.05$ - 2.75 relative to the baseline Rabi-sampling approach without enhancement, depending on the frequency of interest in the range 2.5 - 6.0 GHz. Scaling to multi-sensor architectures with shared ancilla for sequential enhancement increases the speedup to $\mathcal{G} \sim$ 2.10 - 5.50. Sensitivity projections for a reference deployment of 120 physical qubits operating for three years of active data-taking yield an exclusion limit on the dark photon kinetic mixing of $\epsilon \approx 1 \times 10^{-14}$ at the 95% confidence level, uniformly across the frequency range 2.5 GHz - 6.0 GHz, corresponding to the mass range 10 eV - 25 eV. Such exclusion limits are much lower than those set by cosmological bounds ($\gtrsim 10^{-11}$) and experimental limits currently achieved by other experiments, for a large portion of the mass interval under study.

The experimental component of this thesis involves the design, fabrication, and characterization of transmon-based architectures towards a prototype dark photon sensor compatible with the enhancement protocol developed in this thesis. Design and simulation methodologies, addressing Hamiltonian engineering (targeting resonant frequencies, Kerr non-linearities, mode coupling strengths) and decoherence mitigation (charge noise suppression, Purcell filtering, dielectric losses mitigation) were developed and validated experimentally. Three test devices with increasing architectural complexity, ranging from uncoupled fixed-frequency qubits to qubits coupled through bus resonators, were fabricated at the US National Institute of Standards and Technology (NIST) and characterized at both NIST and the University of Milan–Bicocca. Measured parameters confirm design predictions, though Purcell-limited relaxation emerged as the primary coherence bottleneck due to lower-than-expected readout resonator quality factors.

This work demonstrates that programmable superconducting quantum processors represent a viable platform for quantum-enhanced dark matter detection, establishing a bridge between quantum computing and fundamental physics. The combination of hardware-efficient enhancement protocols, realistic noise modeling, and experimental device development provides a concrete step towards competitive dark-sector searches using quantum technologies available today.

Contents

Chapter 1

Introduction

Quantum technologies have made remarkable progress in the past few decades, enhancing our capabilities to detect and manipulate individual quanta and control the temporal evolution of increasingly complex quantum states.
These advancements have enabled practical –and disruptive– applications across multiple domains, including quantum computing [1], precision metrology [2], quantum simulation [3–6], quantum sensing [7], secure communications [8, 9], and artificial intelligence [10–12]. The implementation of quantum devices spans multiple experimental platforms such as superconducting circuit technology [11], trapped ions [13], cold atoms [14], photonic systems [15], semiconductor quantum dots [16], and diamond vacancies [17], each one offering distinct advantages and challenges.
Among these platforms, the superconducting one stands out due to its scalability, microwave-controlled fast operations, and the flexibility to engineer customized electrical circuits tailored to facilitate specific types of quantum interactions required for targeted applications. Moreover, quantum sensors based on superconductivity have demonstrated the ability to detect extremely weak electromagnetic [18] and acoustic [19] signals. This feature can be leveraged in particle physics to carry out the search for electromagnetically coupled dark matter candidates [20–23] –primarily axions and dark photons– and gravitational waves [24–26]. Such experiments, which exploit the principles of quantum mechanics and the properties of coherent quantum states, are expected to offer advantages over conventional methods in terms of speed, signal-to-background ratio, and access to previously unexplored energy-mass intervals.

This thesis examines the latest developments in qubit-based, superconducting quantum sensors for dark matter detection, focusing on two primary approaches: non-destructive photon measurements through quantum non-demolition (QND) techniques [27], and direct energy exchange between qubits and dark fields, referred to as direct detection (DD) [21]. The primary contribution of this thesis is proposing a new speedup technique able to enhance existing DD methods by achieving an effective signal amplification from the interaction between coupled qubit systems and dark fields. This approach, positioned at the intersection of quantum sensing and quantum computing, demonstrates resilience to noise and is compatible with the current limitations of quantum hardware engineering, particularly those inherent to Noisy Intermediate-Scale Quantum (NISQ) devices [28], i.e. quantum systems that operate with a limited number of qubits and without full error correction, thus experiencing significant noise.

The introductory chapter of this thesis provides the necessary theoretical foundation on dark matter, focusing on axion and dark photon candidates, as well as the qubit formalism and the quantum computing fundamentals. Chapter 2 presents an overview of the superconducting qubit and the elementary components of a qubit-based device. Chapter 3 examines state-of-the-art dark matter detection techniques with quantum sensors, with particular focus on direct detection, while Chapter 4

presents the enhanced detection scheme developed in this work, quantifying the achievable speedup and demonstrating the method's efficiency through comprehensive simulations and numerical analysis. Chapter 5 focuses on the design and simulation of quantum devices of increasing complexity, up to a detection device prototype compatible with the enhanced dark matter direct search discussed in Chapter 4. Experimental characterizations in cryogenic environments of the preliminary superconducting qubit devices are also presented in Chapter 5. In Chapter 6, we draw our conclusions and outline future research directions, leveraging the enhanced Direct Detection technique here developed.

1.1 Dark Matter search

Astrophysical and cosmological investigations have provided multiple independent evidence indicating that approximately 85% of the mass of the Universe does not emit, absorb, or reflect electromagnetic radiation, is collisionless, and interacts predominantly through gravity [29, 30]. The fundamental nature of this large mass fraction, referred to as dark matter (DM), is unknown, and detection at the particle level remains a challenging open problem in physics. The current consensus supported by observational data and theoretical models points toward a non-baryonic composition and beyond standard model (BSM) [31] particles.

1.1.1 Evidence for Dark Matter

The evidence supporting DM's existence is exclusively gravitational and spans a wide range of astronomical scales, from a few kiloparsecs (the size of small galaxies) to the scale of the entire observable Universe. Below is a list of the main findings supporting the existence of DM.

- **Anomalous rotation curves of spiral galaxies:** High-resolution spectroscopic observations, based on Doppler shifts in atomic and molecular lines, demonstrated how the orbital velocities of stars and gas in spiral galaxies remain nearly constant at large distances from the galactic center, far beyond the regions densely populated by visible matter [32, 33]. This behavior deviates from the predictions of Newtonian gravity, for which at a sufficiently large radius, the orbital velocity should decrease as $\propto 1/\sqrt{r}$, where r is the distance from the galaxy's center.
  However, the observed flat rotation curves can be reconciled by postulating the presence of an invisible matter distribution with density $\rho \sim 1/r^2$, at least within the peripheral regions of the galaxies.

- **Gravitational lensing observations:** The deflection of light by mass as predicted by General Relativity serves as a probe of the total mass distribution in the Universe. When light from distant galaxies travels near massive objects, such as galaxy clusters, it is bent and distorted, producing observable phenomena such as arcs, multiple images, and Einstein rings [34].
  The analyses of gravitational lensing effects reveal that the gravitational potential responsible for the observed distortions cannot be attributable to baryonic matter alone [35, 36]. A notable example is the case of the Bullet Cluster, a system composed of two colliding galaxy clusters: lensing mass reconstructions exhibited a clear spatial offset between the peaks of the baryonic mass (traced by X-ray emitting gas) and the overall mass distribution inferred from lensing [37].

This study suggested that while the baryonic matter interacted significantly during the collision, the dark matter remained largely unaffected, providing strong evidence that dark matter is both non-luminous and collisionless.

- **Cosmic Microwave Background (CMB) anisotropies:** During the early Universe, as it began to expand and cool down, it eventually reached a temperature where electrons and protons could combine into neutral hydrogen, which allowed photons to decouple and travel freely. During this stage, slight overdensities in the matter distribution created gravitational potential wells. The competition between gravitational pull and radiation pressure in the baryon and photon fluid induced acoustic oscillations, which left distinct peaks in the CMB power spectrum. The shape of the CMB peaks indicates that these potential wells were deeper than what baryonic matter alone could produce, implying the existence of a substantial amount of non-baryonic, cold, and collisionless dark matter that enhanced the depth of the wells.
  Observations from Planck [38], WMAP [39], and the South Pole Telescope-3G [40], interpreted within the Lambda cold dark matter (ΛCDM) framework, robustly support this scenario and provide stringent constraints on the dark matter density in the Universe.

- **Large scale structure formation:** During the formation of large-scale structures in the Universe, dark matter, not being subject to photon-induced radiation pressure, began aggregating earlier than baryonic matter, forming the potential wells related to CMB acoustic peaks and serving as the scaffolding for the later aggregation of baryonic gas, ultimately leading to the formation of galaxies and clusters.
  N-body simulations [41], combined with observations of the cosmic microwave background and galaxy clustering [42], robustly support the ΛCDM paradigm, highlighting that introducing dark matter in the framework is essential for reproducing the observed structure of the Universe.

- **Big Bang Nucleosynthesis (BBN) Constraints:** Predictions of primordial abundances of light elements (such as ^{2}H, ^{4}He, and Li) based on the standard BBN framework are very sensitive to the baryon-to-photon ratio [43].
  Observations consistently yield a baryon density that agrees with the one inferred from CMB studies, and it is only a fraction of the total matter density inferred from dynamical and CMB studies. The BBN-predicted baryon-to-photon ratio is an important consistency test of the ΛCDM model, as BBN probes an earlier, much hotter stage of the Universe than CMB analyses do.

1.1.2 Dark Matter candidates

Theoretical studies have proposed several DM particle candidates, exploring their possible production mechanisms in the early Universe and identifying the signals they might produce in experiments. In this section, we briefly (and non-exhaustively) discuss some of the principal DM candidates, with a particular emphasis on ultralight, electromagnetically coupled candidates (axions and dark photons), being the central topic of investigation for this thesis.

Weakly Interacting Massive Particles (WIMPs)

WIMPs [44] interact via the weak nuclear force, gravity, and other hypothetical forces weaker than the weak nuclear one. They naturally arise in many extensions of the

Standard Model, for example as the lightest supersymmetric particles (neutralinos) or Kaluza-Klein excitations in extra-dimensional models.
Experimental searches for WIMPs involve multiple approaches. Indirect detection experiments search for byproducts of WIMP annihilations (e.g., gamma rays, neutrinos, and cosmic rays) in regions of high dark matter density. Direct detection experiments aim to measure the elastic scattering of WIMPs off atomic nuclei in highly sensitive projection chambers [45, 46], while collider experiments, such as those conducted at the Large Hadron Collider (LHC), aim at direct WIMP production [47]. However, results from direct detection experiments and the lack of evidence for supersymmetry at the LHC since the early 2010s have increasingly challenged the viability of the simplest WIMP models.

Sterile neutrinos

Sterile neutrinos [48] are proposed to interact only via gravity and through a small mixing with the Standard Model neutrinos, making them hard to detect with conventional detectors. Their production mechanisms, such as oscillations from active neutrinos or decay of heavier particles during the early cosmic epochs, could yield a relic population with properties characteristic of warm dark matter. The warm dark matter (WDM) model [49] differs from the ΛCDM in that the dark matter particles have non-negligible thermal velocities in the early universe.
Although sterile neutrinos have not yet been observed, they remain an intriguing possibility that continues to motivate both theoretical studies and observational searches, for example, through sterile neutrino-atomic nuclei scattering experiments [50] or neutrino flavor oscillation experiments such as DUNE [51].

Primordial black holes

Primordial black holes (PBHs) [52] are hypothesized to have formed in the early Universe, shortly after the Big Bang, due to the collapse of high-density fluctuations. Unlike black holes resulting from stellar evolution, PBHs could span a wide range of masses, from as small as 10^{-5} grams to several thousand solar masses. Recent interest in PBHs has increased after the gravitational wave detections from LIGO and Virgo [53], which have observed mergers of black holes with masses on the order of tens of solar masses. However, astrophysical constraints from cosmic microwave background observations and microlensing surveys restrict the mass ranges in which PBHs can account for the entirety of dark matter. Current research continues to refine these constraints and investigate the possible roles of PBHs in cosmic structure formation.

Axions and axion-like particles (ALPs)

Axions are widely considered one of the most promising candidates for ultralight bosonic dark matter, originally proposed as a solution to the strong CP problem in quantum chromodynamics (QCD) [54]. The CP operation combines the actions of charge conjugation (C) (transforming particles into their own anti-particles) and the parity transformation (P) (inverting spatial coordinates signs). Although the Standard Model exhibits CP-symmetry violation in weak interactions, no such violation is observed in QCD despite the most general Lagrangian formulations containing the term

$$\mathcal{L}_\theta = \theta \frac{g_s^2}{32\pi^2} G^a_{\mu\nu} \tilde{G}^{a\mu\nu}, \tag{1.1}$$

where θ is a dimensionless parameter quantifying the CP violation strength, g_s the QCD coupling constant, $G^a_{\mu\nu}$ the gluon field tensor and its dual $\tilde{G}^{a\mu\nu} = \frac{1}{2}\epsilon^{\mu\nu\rho\sigma}G^a_{\rho\sigma}$. The term $\epsilon^{\mu\nu\rho\sigma}$ is the rank-4 Levi-Civita pseudotensor. It is possible to demonstrate that $G^a_{\mu\nu}\tilde{G}^{a\mu\nu}$ is C-symmetric and P-antisymmetric, therefore not invariant under P and CP. A non-zero value for θ would imply a non-zero electric dipole for the neutron, although experimental constraints impose a stringent upper bound of $|d_n| < 1.8 \times 10^{-16}\, e$ cm (90% C.L.) [55], translating to $\theta \lesssim 10^{-10}$.
A possible explanation for the lack of CP violation in QCD is given by introducing a global $U(1)$ symmetry, named Peccei-Quinn (PQ) symmetry [56], that is anomalous with respect to the QCD color group $SU(3)_C$. When this symmetry spontaneously breaks at an energy scale f_a, it gives rise to a light pseudoscalar field a, i.e. the so-called QCD axion. In this framework, the CP-violating parameter θ is replaced by the dynamical variable a/f_a. QCD confinement [57] consequently generates a potential for the axion which is minimized at $\theta = 0$, canceling CP-violating effects in QCD.
The symmetry-breaking energy scale f_a is expected to be much higher than the Higgs vacuum expectation value $v = 246$ GeV. The large value of f_a implies an ultralight axion mass and extremely small coupling terms to Standard Model particles since the coupling terms scale as inverse powers of f_a.
The axion-photon interaction term can be written as

$$\mathcal{L}_{a\gamma\gamma} = -\frac{1}{4} g_{a\gamma\gamma} a F_{\mu\nu}\tilde{F}^{\mu\nu}, \tag{1.2}$$

where $g_{a\gamma\gamma}$ is the coupling strength between axion and photon, $F_{\mu\nu}$ the electromagnetic field tensor and $\tilde{F}^{\mu\nu} = \frac{1}{2}\epsilon^{\mu\nu\rho\sigma}F_{\rho\sigma}$ the dual of $F_{\mu\nu}$. This type of coupling is common not only to axions but to a variety of axion-like particles (ALPs) not directly introduced to solve the strong CP problem, hence not bound by the same QCD constraint.

The search experiments leveraging the coupling term in eq. 1.2 span a large mass interval and can be grouped into the following categories:

- **Haloscope:** Haloscopes are superconducting resonant cavities with high quality factors designed to store an intense magnetic field. The power produced by axions converting to photons when in resonance with the cavity is [58]

$$P_a = g^2_{a\gamma\gamma} V B^2 \frac{\rho_a}{m_a} C \min\left(Q_A, Q_L\right), \tag{1.3}$$

  which is converted to an electrical signal to be detected. Here, V is the cavity volume and B is the magnetic field intensity. The term ρ_a corresponds to the local axion density and m_a its mass. C is the form factor of the particular cavity mode considered, while Q_A is the axion quality factor, i.e. the axion energy divided by its spread, and Q_L is the loaded haloscope quality factor.
  Haloscope-based experiments such as ADMX [59], HAYSTAC [60], CAPP [61], ORGAN [62], and QUAX [63] probe mass ranges between $\sim$ 1-100 µeV.

- **Helioscope:** These experiments search for axions originating from the sun through the Primakoff effect and consist of large magnets to induce conversion from axions into detectable X-ray photons. The CERN Axion Solar Telescope (CAST) experiment [64] was able to set 95% Confidence Level (C.L.) exclusion limits on $g_{a\gamma\gamma}$ below 10^{-10} GeV^{-1} for axion masses up to 0.02 eV.

- **Light Shining Through a Wall:** In such experiments, a high-power laser is directed towards an opaque barrier into a strong magnetic field where photons convert into axions (via the Primakoff effect). On the other side of the barrier,

another strong magnetic field converts the axions, which can pass through the barrier, back into photons, which are then detected with a single-photon detector. For instance, the ALPS experiment [65] set a 95% C.L. exclusion limit for $g_{a\gamma\gamma}$ of $\sim 3 \times 10^{-8}$ GeV^{-1} for m_a below ~ 10 μeV.

Other detection strategies that do not rely on the axion–photon coupling include approaches based on nuclear magnetic resonance (NMR) techniques, such as those employed in the CASPEr [66] experiment, which target the coupling between axions and nuclear spins, and searches for exotic decays or direct production of axion-like particles at colliders [67]. Collider experiments typically explore mass ranges from a few MeV up to about 1 TeV, which are generally more relevant for ALPs than QCD axions.

Fig. 1.1 illustrates the current constraints in the axion parameter space (axion-photon coupling strength versus mass), focusing on mass ranges probed by haloscopes. The yellow-shaded band represents the range of predicted properties for the QCD axion. This region, identified by theoretical and observations bounds, based on the relationship between m_a, $g_{a\gamma\gamma}$ and f_a, indicate where axions can represent the solution to the strong CP problem, and act as a candidate for cold dark matter. The two solid lines within the constrained region relates to the two main axion theoretical models, the Kim–Shifman–Vainshtein–Zakharov (KSVZ) [68] and Dine–Fischler–Srednicki–Zhitnitsky (DFSZ) [69] models, further characterizing the QCD axions properties. The KSVZ model introduces a new heavy quark carrying the Peccei–Quinn (PQ) charge. The standard quarks and leptons are expected to be PQ-neutral and, therefore, unable to couple with the axion at the tree level, but only through loops. The DFSZ model, on the other hand, extends the Standard Model by adding a second Higgs doublet and assigning PQ charges to the standard quarks and leptons, allowing axion and SM particles to couple also at the tree level.

Dark photons

Dark photons are gauge bosons associated with a new hypothetical $U(1)$ gauge symmetry, which can acquire mass through the Higgs or the Stueckelberg mechanism [71]. One of the most appealing features of dark photons is that they can interact with ordinary matter through a mechanism known as kinetic mixing, acting as mediators between SM particles and potential DM sectors, or constituting DM themselves in the form of ultralight bosons. The Lagrangian term involving kinetic mixing is

$$\mathcal{L}_{\text{mix}} = -\frac{\epsilon}{2} F_{\mu\nu} F'^{\mu\nu}, \tag{1.4}$$

where $F_{\mu\nu}$ and $F'^{\mu\nu}$ are the electromagnetic and dark field strength tensors, and ϵ is a dimensionless parameter denoted as mixing strength. If the dark photon is massless, the kinetic mixing can be removed with a field redefinition, making the dark photon effectively decoupled from SM particles. However, if the dark photon acquires a mass, this mixing leads to a small but measurable coupling between the dark photon and electrically charged particles.
Experimental searches can be divided into the following categories:

- **Haloscope and Resonant Cavity Searches:** Similarly to the case of axions, haloscope experiments like ADMX [72] aim to detect a coherently oscillating dark photon field, as they produce the same type of signal as axions. Since the presence of a magnetic field is not required for dark photon searches, even simpler resonant cavities or antennas can be employed to pick up the small electromagnetic signals induced by dark photon dark matter.

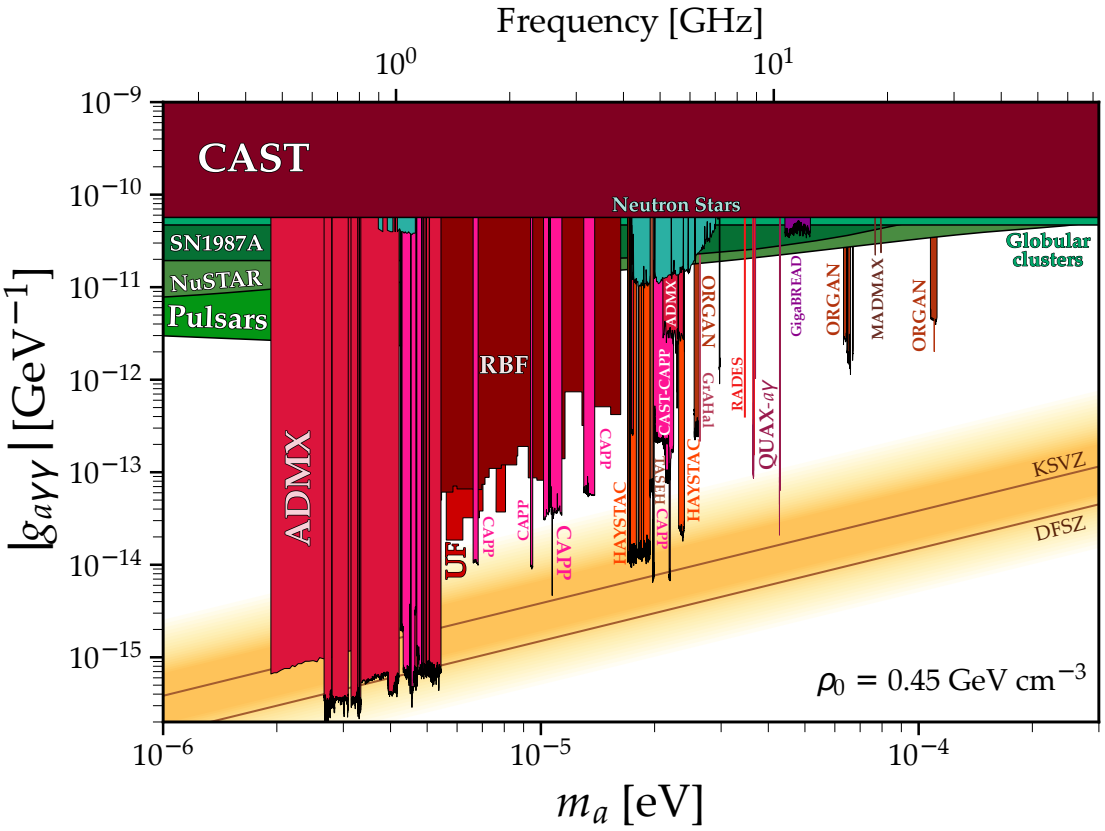

FIGURE 1.1: Axion exclusion limits to $|g_{a\gamma\gamma}|$ at 95% C.L. set by several experiments in the typical mass-frequency range spanned by haloscope experiments. Image credits to [70].

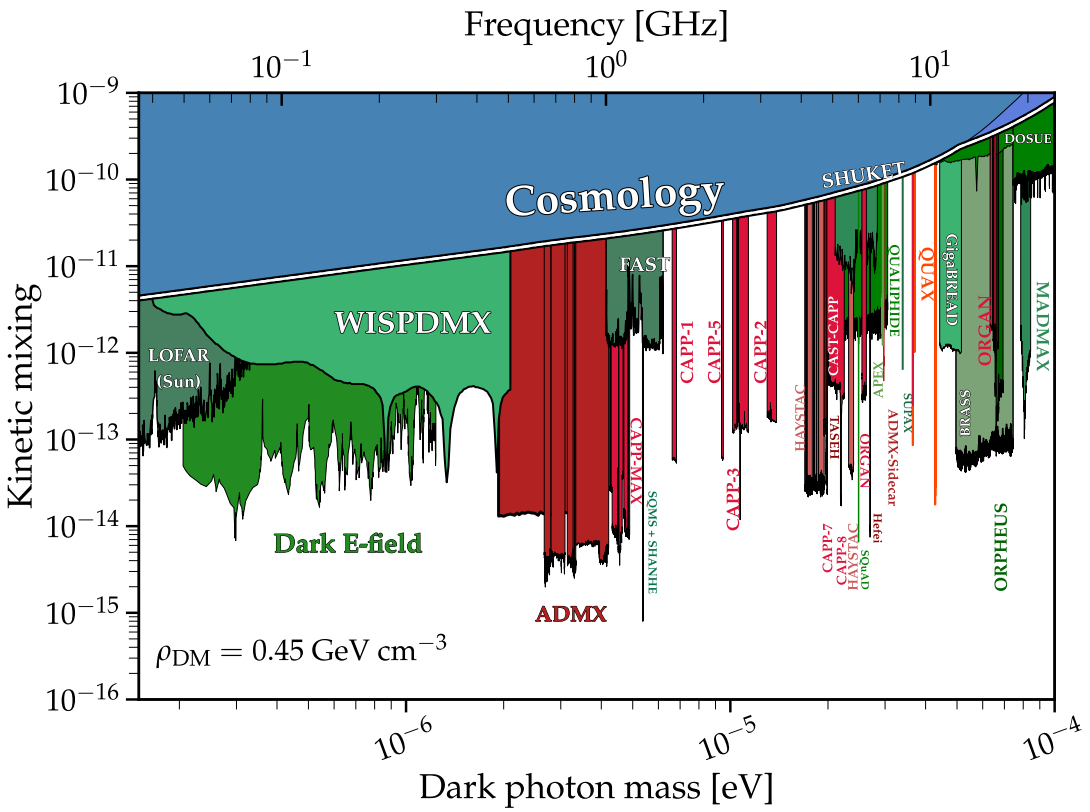

FIGURE 1.2: Dark photon exclusion limits to the mixing strength parameter ϵ at 95% C.L. set by several experiments in the typical mass-frequency range spanned by haloscope experiments. Image credits to [70].

- **Collider experiments:** Hadron and lepton collider experiments [73, 74] look for dark photons produced in particle collisions, appearing as resonances in invariant mass distributions (e.g. in e^+e^- or $\mu^+\mu^-$ pairs) or contributing to events with missing energy. The BaBar experiment set a 90% C.L. exclusion limit of ϵ at the level of 10^{-3} - 10^{-4} for dark photon masses between 0.02 and 10.2 GeV [75].

- **Fixed target and beam dump experiments:** These experiments leverage a high-intensity electron or proton beam directed onto a fixed target. Dark photons can be produced via kinetic mixing in the collisions and then decay into detectable Standard Model particles, or they can travel a significant distance before decaying. Experiments such as APEX [76], HPS [77], and NA64 [78] fall into this category.

- **Precision low-energy experiments:** Precision measurements in atomic physics [79], fixed-target neutrino experiments [80], or dedicated fifth force searches [81] can provide indirect evidence for dark photons by detecting small deviations from expected electromagnetic interactions.

Fig. 1.2 shows the constraint on the dark photon parameter space (kinetic mixing strength versus mass), with a close-up view of the mass intervals probed by haloscopes and cavity experiments.

The coupling of axion, ALPs, and dark photon to electromagnetism, and the ongoing experimental effort to probe their coupling strength in the $\sim$ 1 - 100 µeV mass range, corresponding to an interval of $\sim$ 0.25 - 25 GHz in the microwave frequencies,

has motivated the development of new detectors based on superconducting quantum devices, which typically operate in the same range. Superconducting qubits, for instance, are extremely sensitive to external electromagnetic fields. This high susceptibility can be exploited both to enhance the signal-to-background ratio in haloscope and cavity experiments and to create entirely new detection schemes based on single or multi-qubit interactions.

Superconducting qubits are discussed in Chapter 2, while the following section in this Chapter introduces a platform-independent mathematical framework for describing qubits, the operations between them, and their interactions with the environment as open systems.

1.2 Qubits and superconducting circuits

Qubits are considered the fundamental unit of quantum information and are a key component in many applications such as quantum computing, quantum sensing, and quantum cryptography. A qubit (or quantum bit) is a two-level quantum mechanical system which, in contrast to a classical bit, can exist in a generic superposition of two eigenstates, commonly named *computational states* and represented in the Dirac notation as $|0\rangle$ and $|1\rangle$:

$$|\psi\rangle = \alpha\,|0\rangle + \beta\,|1\rangle\,. \tag{1.5}$$

In Eq. 1.5, the coefficients α and β are complex amplitudes that satisfy the normalization condition $|\alpha|^2 + |\beta|^2 = 1$. By leveraging the invariance of observables to global phase transformations, any single-qubit state can be expressed using only two real parameters:

$$|\psi\rangle = \cos\left(\frac{\theta}{2}\right)|0\rangle + \sin\left(\frac{\theta}{2}\right)e^{i\varphi}\,|1\rangle\,. \tag{1.6}$$

Here, the angles $\theta \in [-\pi, \pi]$ and $\varphi \in [0, 2\pi]$ serve as spherical coordinates that map a qubit state onto the surface of the unit-radius Bloch sphere, as illustrated in Fig. 1.3. In this representation, the basis states $|0\rangle$ and $|1\rangle$ occupy the north and south poles, respectively, corresponding to the positive and negative directions of the $\hat{z}$ axis. Additionally, states aligned along the $\hat{x}$ and $\hat{y}$ axes (commonly denoted as $|+\rangle$ and $|-\rangle$ for the $\hat{x}$ direction, and $|+i\rangle$ and $|-i\rangle$ for the $\hat{y}$ direction) represent equiprobable superpositions of $|0\rangle$ and $|1\rangle$, i.e. with a $1/2$ probability of measuring either $|0\rangle$ or $|1\rangle$:

$$\begin{aligned} |+\rangle &= \frac{1}{\sqrt{2}}\left(|0\rangle + |1\rangle\right), \quad |-\rangle = \frac{1}{\sqrt{2}}\left(|0\rangle - |1\rangle\right) \\ |+i\rangle &= \frac{1}{\sqrt{2}}\left(|0\rangle + i\,|1\rangle\right), \quad |-i\rangle = \frac{1}{\sqrt{2}}\left(|0\rangle - i\,|1\rangle\right). \end{aligned} \tag{1.7}$$

1.2.1 Quantum gates

Single-qubit gates

A common way of controlling the quantum states of single and multi-qubit systems is through quantum gates, which can be interpreted as an extension of classical logic gates. Single-qubit Hilbert spaces are isomorphic to $\mathbf{C}^2$ and have dimension 2. By representing the physical states of a qubit as $|0\rangle = (1,0)^T$ and $|1\rangle = (0,1)^T$, single-qubit quantum gates act as elements of $U(2)$, represented by 2×2 complex, unitary matrices. Ignoring global phases, the most general single-qubit state transformation

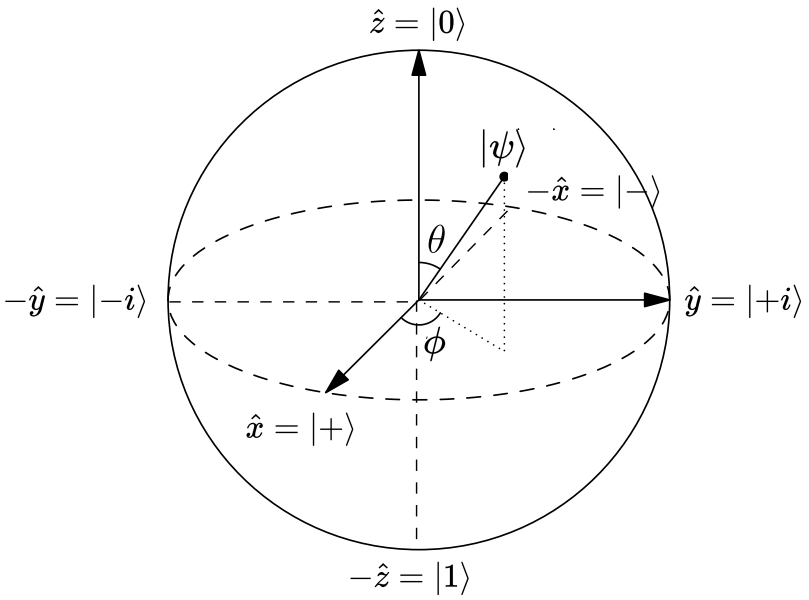

FIGURE 1.3: Bloch sphere representing a qubit state $|\psi\rangle$ as a vector connecting the sphere's center to a surface point, characterized by angles θ and ϕ.

can be written in terms of Euler angles (θ, ϕ, λ) as follows [82]:

$$U(\theta, \phi, \lambda) = \begin{pmatrix} e^{i\frac{\phi+\lambda}{2}} \cos(\theta/2) & e^{-i\frac{\phi-\lambda}{2}} \sin(\theta/2) \\ -e^{-i\frac{\phi-\lambda}{2}} \sin(\theta/2) & e^{-i\frac{\phi+\lambda}{2}} \cos(\theta/2) \end{pmatrix}, \tag{1.8}$$

or, decomposed into simpler rotations:

$$U(\theta, \phi, \lambda) = R_z(\phi) R_y(\theta) R_z(\lambda), \tag{1.9}$$

where

$$R_\alpha(\theta) = e^{-i\frac{\theta}{2}\sigma_\alpha}, \qquad \alpha = x, y, z \tag{1.10}$$

represents rotations along the Bloch sphere's α-axis, with σ_α being the α-indexed Pauli matrix, often also indicated as RX, RY, RZ.
Common examples of single-qubit quantum gates are:

- **X (NOT):**

$$\mathrm{X} = \begin{pmatrix} 0 & 1 \\ 1 & 0 \end{pmatrix} \tag{1.11}$$

  acting as a qubit flip, $\mathrm{X}|0\rangle = |1\rangle$, $\mathrm{X}|1\rangle = |0\rangle$.

- **SX ($\sqrt{\mathrm{X}}$):**

$$\mathrm{SX} = \begin{pmatrix} 1+i & 1-i \\ 1-i & 1+i \end{pmatrix} \tag{1.12}$$

  corresponding to $e^{i\frac{\pi}{4}} R_x(\frac{\pi}{2})$, i.e. a rotation of $\pi/2$ about the $\hat{x}$-axis on the Bloch sphere followed by a $\pi/4$ rotation on the $\hat{z}$-axis.

- **Hadamard:**

$$\mathrm{H} = \frac{1}{\sqrt{2}} \begin{pmatrix} 1 & 1 \\ 1 & -1 \end{pmatrix} \tag{1.13}$$

creating equiprobable superposition states from base states, $\mathrm{H}|0\rangle = |+\rangle$, and $\mathrm{H}|1\rangle = |-\rangle$.

Multi-qubit gates

A quantum state of n qubits is represented by a unit vector in a Hilbert space that is the tensor product of n single-qubit Hilbert spaces. Since each qubit space is $\mathbb{C}^2$, the composite state space is given by

$$\mathcal{H}^{\otimes n} = \left(\mathbb{C}^2\right)^{\otimes n}, \tag{1.14}$$

which has dimension 2^n. Consequently, a generic quantum gate acting on n qubits is described by a $2^n \times 2^n$ complex matrix. This exponential growth in the state space dimension hints at the potential of quantum information, as a quantum processor with a relatively small number of qubits ($\gtrsim 60$) can encode and elaborate an amount of data inaccessible to any classical hardware.
Restricting to the case where $n = 2$, common two-qubit quantum gates are:

- **Contolled-NOT (CX):**

$$\mathrm{CX} = \begin{pmatrix} 1 & 0 & 0 & 0 \\ 0 & 1 & 0 & 0 \\ 0 & 0 & 0 & 1 \\ 0 & 0 & 1 & 0 \end{pmatrix} \tag{1.15}$$

  which implements a logical XOR operation on the computational basis. i.e. flipping the state of a target qubit only if the state of a control qubit is $|1\rangle$. For example, in the equation:

$$\mathrm{CX}\left(\frac{|01\rangle + |10\rangle}{\sqrt{2}}\right) = \frac{|01\rangle + |11\rangle}{\sqrt{2}}, \tag{1.16}$$

  where the first qubit is the control and the second one the target, the $|01\rangle$ term remains unchanged while $|10\rangle$ transforms into $|11\rangle$.

- **iSWAP:**

$$\mathrm{iSWAP} = \begin{pmatrix} 1 & 0 & 0 & 0 \\ 0 & 0 & i & 0 \\ 0 & i & 0 & 0 \\ 0 & 0 & 0 & 1 \end{pmatrix} \tag{1.17}$$

  swapping the states of two qubits while introducing a phase factor of i. On the computational basis, states $|00\rangle$ and $|11\rangle$ remain unchanged while $|10\rangle$ transforms into $i\,|01\rangle$ and $|01\rangle$ into $i\,|10\rangle$.

- **Controlled-Z (CZ):**

$$\mathrm{CZ} = \begin{pmatrix} 1 & 0 & 0 & 0 \\ 0 & 1 & 0 & 0 \\ 0 & 0 & 1 & 0 \\ 0 & 0 & 0 & -1 \end{pmatrix} \tag{1.18}$$

  applying a phase shift only when both qubits are in the $|11\rangle$ state, without affecting the other states.

- **Echoed Cross-Resonance (ECR):**

$$\mathrm{ECR} = \frac{1}{2}\begin{pmatrix} 0 & 1 & 0 & i \\ 1 & 0 & -i & 0 \\ 0 & i & 0 & 1 \\ -i & 0 & 1 & 0 \end{pmatrix} \tag{1.19}$$

  which is equivalent to CNOT up to single-qubit rotations. It can be written as:

$$\frac{1}{\sqrt{2}}\left(I \otimes \sigma_x - \sigma_x \otimes \sigma_y\right), \tag{1.20}$$

  where I is the 2×2 identity matrix.

The universality of a quantum processor with n qubits, i.e. the ability to implement any unitary operation $U(2^n)$ with arbitrary precision, is a fundamental requirement of quantum information [83]. In this regard, two-qubit gates are an essential building block in quantum information as they enable interaction between qubits and entanglement. Without entanglement, any multi-qubit state would be separable into the tensor product of single-qubit states.

$$|\psi\rangle = |\psi_0\rangle \otimes |\psi_1\rangle \otimes \ldots \otimes |\psi_{n-1}\rangle . \tag{1.21}$$

In this scenario, the overall state would be completely determined by the individual states of each qubit, which would require specifying only $2n$ complex numbers (ignoring normalization and global phase constraints). Furthermore, the only possible operations would be described by single-qubit gates, i.e. 2×2 complex matrices, which are easy to handle classically. In other words, the exponentially large Hilbert space would not be exploited.
More generally, the universality of single-qubit and two-qubit gates was demonstrated in [84], establishing that any unitary transformation on an n-qubit system can be decomposed into a finite sequence of these simpler operations. This result ensures that a quantum device able to implement a small set of *basis gates*, consisting of some single-qubit rotations and an entangling two-qubit gate, is universal. For example, two basis gate sets are $\{\mathrm{CZ}, \mathrm{I}, \mathrm{RZ}, \mathrm{SX}, \mathrm{X}\}$ and $\{\mathrm{ECR}, \mathrm{I}, \mathrm{RZ}, \mathrm{SX}, \mathrm{X}\}$. A useful quantitative statement is provided by the Solovay–Kitaev theorem [85]: if a finite gate set generates a dense subgroup of $\mathrm{SU}(2)$, then any single-qubit unitary can be approximated to accuracy ϵ by a sequence of length $\mathcal{O}(\log^c(1/\epsilon))$ (for some constant c), and a multi-gate sequence of m constant-size gates can be approximated by $\mathcal{O}(m \log^c(m/\epsilon))$ elementary gates from the finite set.

1.2.2 Quantum circuits

Quantum circuits provide a widely adopted and intuitive framework for representing sequences of quantum gate operations. In quantum circuits, each qubit corresponds to a register where quantum gates, identified by unique symbols, are positioned from left to right following the order in which they are applied. Typically, quantum circuits end with a measurement operation, extracting information from the system by saving the measured outcome on classical bits, which are also represented in the circuit by registers. Due to the inherently projective nature of quantum state measurements, extracting meaningful information from a quantum circuit often requires reinitializing the qubit state and repeating the circuit execution multiple times, sampling the outcome probability distribution.

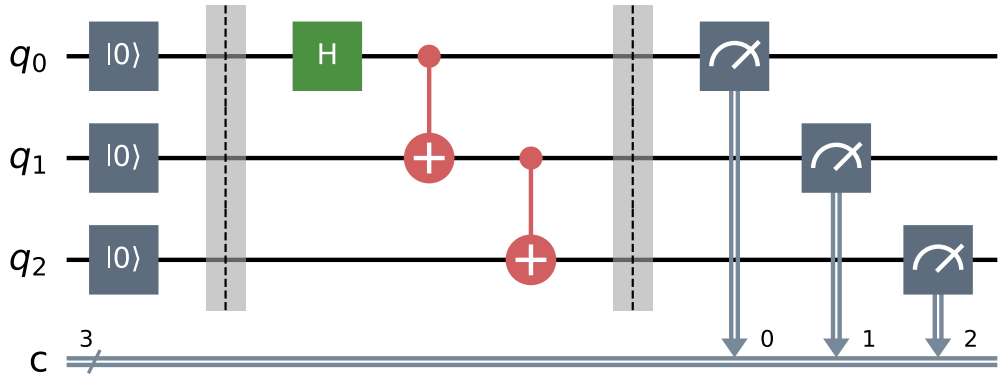

FIGURE 1.4: Quantum circuit for preparing and measuring a three-qubit GHZ state. The qubit registers are labeled as q_0, q_1, q_2. The green box represents a Hadamard gate, while the CX gate is depicted with a dot on the control qubit connected to a plus symbol on the target qubit. Measurements on each qubit yield outcomes stored in three-bit registers, which are visually combined into a single one for simplicity.

As an example, Fig. 1.4 shows a quantum circuit example using three qubits, implementing a Greenberger–Horne–Zeilinger (GHZ) state [86]. The state is initialized in $|000\rangle$, evolving under the action of a Hadamard gate on q_0:

$$\mathrm{H}_0 |000\rangle = \frac{1}{\sqrt{2}} \left(|000\rangle + |100\rangle\right). \tag{1.22}$$

Concatenating two CX gates as in Fig. 1.4 yields to:

$$\begin{aligned} \mathrm{CX}_{12}\mathrm{CX}_{01} \frac{1}{\sqrt{2}} \left(|000\rangle + |100\rangle\right) &= \mathrm{CX}_{12} \frac{1}{\sqrt{2}} \left(|000\rangle + |110\rangle\right) \\ &= \frac{1}{\sqrt{2}} \left(|000\rangle + |111\rangle\right), \end{aligned} \tag{1.23}$$

where bottom-indices specify which qubits are involved in the transformations. When double indices are present, the first one indicates the control qubit, and the second one the target qubit.
The state in Eq. 1.23 is entangled in such a way that measuring one qubit in the system will uniquely determine the state of all other qubits, collapsing all in state $|0\rangle$ or $|1\rangle$. Under ideal conditions, in the absence of noise, sampling from a GHZ state will lead to only two possible outcomes out of the 2^n computational states. GHZ states are widely used in quantum information as a benchmarking tool for quantum processors [87] and possess remarkable properties for quantum sensing, as discussed in Chapter 3.
Quantum circuits composed of variational gates (such as parametrized rotations $R_x(\theta)$, $R_y(\theta)$, $R_z(\theta)$, or controlled-rotations) are named Variational Quantum Circuits (VQCs) and they have a central role in the development of quantum algorithms for solving optimization problems. A VQC implements a unitary operation $U(\boldsymbol{\theta})$ parametrized by an array $\boldsymbol{\theta}$ of degrees of freedom. For instance, in the Variational Quantum Eigensolver (VQE), the circuit is designed to prepare a trial state that approximates the ground state of a molecular Hamiltonian, with the parameters optimized to minimize the expected energy. Similarly, the Quantum Approximate Optimization Algorithm (QAOA) employs a layered ansatz where alternating applications of cost and mixing Hamiltonians, with corresponding parametrized gates, guide the system toward high-quality solutions of combinatorial problems. In the

realm of quantum machine learning, VQCs implement quantum classifiers and generative models by encoding classical data into quantum states and iteratively adjusting parameters to improve model accuracy [88]. In general, VQCs might effectively combine machine learning and quantum sensing by learning data-informed transformations to achieve an advantage in the experiment.

1.2.3 Open system dynamics

Qubits, regardless of their physical implementation, are subject to noise and nontrivial interaction with the environment, causing decoherence and leading to errors in the preparation, control, and readout of their state. To describe the dynamics of a qubit as an open system, it is convenient to express qubit states in a more generic form than the one in Eq. 1.5, which only represents pure states, by referring to the density operator ρ defined as:

$$\rho = \sum_{i=1}^{m} p_i \left|\psi_i\right\rangle \left\langle\psi_i\right|, \tag{1.24}$$

where p_i are probabilities associated to m pure states $|\psi_i\rangle$. The operator ρ, also known as *density matrix*, generally describes mixed states as a weighted ensemble of pure states, is characterized by $\mathrm{Tr}(\rho) = 1$, and evolves under unitary transformations as:

$$\rho(t) = U(t)\rho U^{\dagger}(t), \tag{1.25}$$

where $U(t)$ is the unitary operator.
For a Markovian process, where the time derivative of the density matrix $d\rho(t)/dt$ depends only on ρ at time t and not on its history, the evolution of an open quantum system is governed by the Lindblad master equation [89], also known as the Lindbladian form:

$$\frac{d\rho}{dt} = -\frac{i}{\hbar}[\mathcal{H}, \rho] + \sum_i \left(2L_i \rho L_i^{\dagger} - \frac{1}{2}\{L_i^{\dagger} L_i, \rho\}\right), \tag{1.26}$$

where $\mathcal{H}$ is the Hamiltonian of the system, and L_i are called Lindblad operators, representing specific noise channels due to coupling with the environment. In qubits, decoherence manifests itself as two phenomena. The first is energy relaxation, in which the qubit emits energy to the environment, transitioning from the higher-energy state ($|1\rangle$) to the lower-energy state ($|0\rangle$), (with spontaneous excitation usually being negligible). The second process is dephasing, during which the phase coherence between the computational basis states is lost. For a single qubit, the Lindblad operators are

$$L_1 = \sqrt{\Gamma_1}\left|0\right\rangle \left\langle 1\right| = \sqrt{\Gamma_1}\sigma_- \tag{1.27}$$

for energy relaxation and

$$L_2 = \sqrt{\frac{\Gamma_\phi}{2}}\sigma_z \tag{1.28}$$

for dephasing, where Γ_1 and Γ_ϕ are the rates that characterize the time scales after which the amplitude and phase information are lost. Qubit relaxation $T_1 = 1/\Gamma_1$ and dephasing $T_\phi = 1/\Gamma_\phi$ are important parameters for a qubit, as the qubit remains

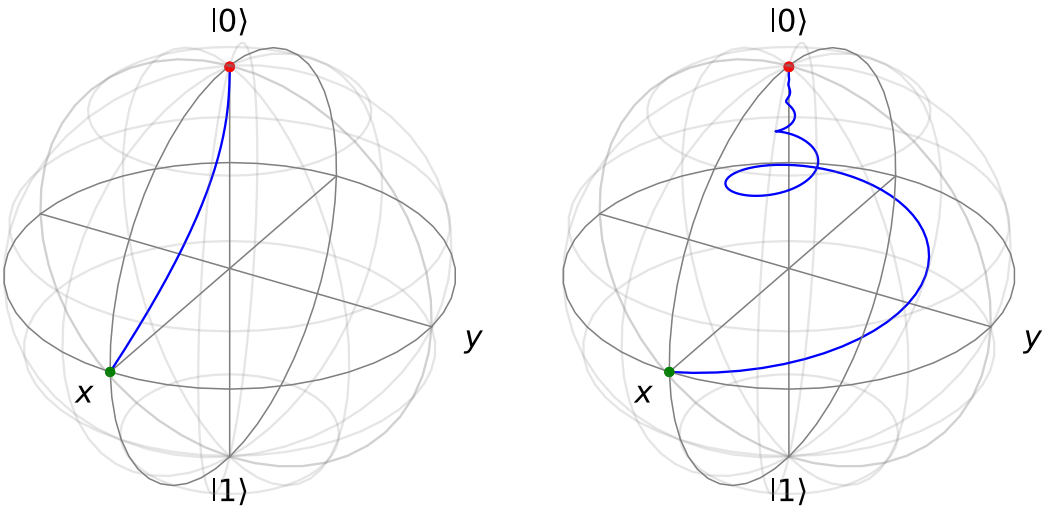

(A) Relaxation and dephasing. (B) Relaxation and dephasing while rotating.

FIGURE 1.5: Bloch vector evolution of a qubit starting from $\rho_i = |+\rangle\langle+|$ (green dot) under relaxation and dephasing, until stopping in $\rho_f = |0\rangle\langle 0|$ (red dot). (A) Static case, the Bloch vector is confined to the xz plane. (B) In the presence of a continuous rotation around $\hat{z}$.

usable for timescales of approximately $\min(T_1, T_\phi)$. Conventionally, the overall coherence time of a qubit is labeled as T_2 and is defined as:

$$T_2 = \left(\frac{\Gamma_1}{2} + \Gamma_\phi\right)^{-1} = \left(\frac{1}{2T_1} + \frac{1}{T_\phi}\right)^{-1}. \tag{1.29}$$

It is worth noting that a qubit state initialized as pure, when progressively undergoing relaxation and dephasing, becomes mixed, and its vector moves from the Bloch sphere's surface to its inside. In this case, the coordinates of the Bloch vector r_i derive from ρ as follows:

$$r_i = \mathrm{Tr}(\rho\sigma_i), \quad i \in \{x, y, z\}. \tag{1.30}$$

An example of a qubit state dynamics under relaxation and dephasing is depicted in Fig. 1.5.

When considering the evolution over a finite time interval Δt, the solution to the Lindblad master equation yields a completely positive trace-preserving (CPTP) map. This map encapsulates the overall effect of the environment on the quantum state and can be expressed in the Kraus representation as

$$\rho(t + \Delta t) = \sum_i K_i \rho(t) K_i^\dagger, \tag{1.31}$$

where the set of Kraus operators K_i comprises the noise channels and satisfies the completeness relation $\Sigma_i K_i^\dagger K_i = I$. This representation is particularly useful for modeling the effect of noise at the gate level and to simulate the outcome of noisy circuit sampling experiments. For a single qubit, Kraus operators can be written as:

$$K_0^r = \begin{pmatrix} 1 & 0 \\ 0 & \sqrt{1-\gamma} \end{pmatrix}, \qquad K_1^r = \begin{pmatrix} 0 & \sqrt{\gamma} \\ 0 & 0 \end{pmatrix} \tag{1.32}$$

for relaxation, and

$$K_0^d = \begin{pmatrix} 1 & 0 \\ 0 & \sqrt{1-\lambda} \end{pmatrix}, \qquad K_1^d = \begin{pmatrix} 0 & 0 \\ 0 & \sqrt{\lambda} \end{pmatrix} \tag{1.33}$$

for dephasing, where γ and λ are probabilities of amplitude and phase damping, respectively. Other noise channels may be utilized for modeling depolarization, phase flip, bit flip, and bit-phase flip. Upon extending the formalism to multi-qubit scenarios, quantum gates can be equipped with these noise channels, allowing the numerical propagation of errors into noisy quantum circuits, achieving an approximate simulation of real hardware effects.
Multiple noise channels can be applied when evolving a density matrix ρ. For instance, we can let ρ evolve under relaxation and dephasing by considering discrete small time steps and alternating the transformations

$$\mathcal{A} : \rho' \to \mathcal{A}(\rho') = K_0^r \rho' (K_0^r)^\dagger + K_1^r \rho' (K_1^r)^\dagger, \tag{1.34}$$

$$\mathcal{D} : \rho' \to \mathcal{D}(\rho') = K_0^d \rho' (K_0^d)^\dagger + K_1^d \rho' (K_1^d)^\dagger. \tag{1.35}$$

This approach would approximate the time evolution of ρ governed by the Lindblad master equation as in Fig. 1.5.

Chapter 2

Superconducting qubits and transmon regime

Implementing a qubit physically, the ability to control it accurately, and performing measurement operations pose significant technological challenges, starting with the choice of platform. For example, trapped-ion qubits offer high reproducibility, long coherence times [90], and precise control. However, the control speed is low and suffers from scalability challenges (i.e. engineering multi-qubit devices) [91]. Photonic qubits maintain coherence over long distances and operate at room temperature, but executing multi-qubit operations is challenging due to the absence of photon-photon interactions [15, 92]. Neutral atom qubits [14] benefit from inherent uniformity (since all atoms are identical, similarly to the trapped ions case), scalability, and long coherence times. However, their control tends to be slow and requires highly precise optical manipulation. Superconducting qubits, on the other hand, allow for fast operations and benefit from mature lithographic and microfabrication techniques that facilitate scalability and engineering of the individual qubit properties. Their main drawback is that they typically exhibit shorter coherence times with respect to the platforms mentioned above, and must operate in a cryogenic environment, at temperatures of a few-millikelvin.
In the current state of technology, the optimal platform choice ultimately depends on the target application. For the physics goal of this thesis, leveraging superconducting qubits is motivated by their well-known coupling to photons and the possibility of customizing each qubit's properties, making it the ideal candidate to probe photon-coupled dark matter candidates discussed in Chapter 3.
In this chapter, we present an overview of the superconducting platform, focusing on the fundamental mechanisms that enable superconducting qubits and the theoretical framework used to describe and predict their key parameters. We also introduce the coupling mechanism between qubits and readout systems, as well as the generation of entanglement between qubits.

2.1 LC oscillators and transmon qubits

Superconductivity is a condition in which a material exhibits zero electrical resistance and expels magnetic fields. This behavior can emerge in certain materials when their temperature drops below a material-dependent threshold, namely the critical temperature (T_C).
In 1957, the Bardeen–Cooper–Schrieffer (BCS) theory [93] modeled the microscopic origin of superconductivity. This theory explains that superconductivity emerges when electrons create specific bound states, the so-called *Cooper pairs*, overcoming the Coulomb repulsion. The bosonic nature of Cooper pairs allows them to condense into

a coherent quantum state described by a single wave function

$$\Psi(\mathbf{r}) = \sqrt{n_c} e^{i\theta(\mathbf{r})}, \tag{2.1}$$

where n_c is the Cooper pair density, and θ is the wave function phase common to all pairs. The vector $\mathbf{r}$ is a spatial coordinate variable.
In the absence of electrical resistance, a current flowing into a loop will circulate for an infinite amount of time. Under a magnetic vector potential $\mathbf{A}$, the current density of Cooper pairs can be written as

$$\mathbf{J} = \frac{e^* n_c}{2m^*} \left(\hbar \nabla \theta - \frac{e^*}{c} \mathbf{A} \right), \tag{2.2}$$

where $e^* \approx 2e$ and $m^* \approx 2m_e$ are the effective charge and mass of the Cooper pair, m_e being the electron mass. By imposing that $\mathbf{J}$ is null inside the bulk of a superconductor, we derive $\nabla\theta = e^*\mathbf{A}/(c\hbar)$. This condition leads to the quantization of the magnetic flux concatenated within the loop area, which is calculated by integrating $\mathbf{A}$ over the infinitesimal tangent vector $d\mathbf{l}$ as

$$\Phi = \oint \mathbf{A} d\mathbf{l} = \frac{\hbar c}{e^*} \oint \nabla\theta d\mathbf{l} = n \frac{hc}{e^*} \approx n \frac{hc}{2e}, \tag{2.3}$$

where n is an integer. The concatenated flux in a loop is therefore quantized in units of $\Phi_0 \approx 2.067 \times 10^{-15}$ Wb, *called magnetic flux quantum* [94].

2.1.1 Superconducting LC oscillators

One of the building blocks of superconducting quantum architectures is the quantized LC oscillator, consisting of a linear inductance (L) and a capacitance (C) in parallel. The quantum system can be understood starting from the Hamiltonian of a classical LC circuit:

$$\mathcal{H} = \frac{Q^2}{2C} + \frac{\Phi^2}{2L} \tag{2.4}$$

where Q and Φ are generalized coordinates corresponding to the charge on the capacitor and the time integral of the voltage across the inductor (or conductor), respectively, satisfying the Poisson bracket $\{\Phi, Q\} = 1$. Promoting Q and Φ to quantum operators leads to

$$\hat{\mathcal{H}} = \frac{\hat{Q}^2}{2C} + \frac{\hat{\Phi}^2}{2L}, \tag{2.5}$$

where $[\Phi, Q] = i\hbar$. Eq. 2.5 can be recast in terms of the Cooper pair excess number across the capacitor $n = Q/2e$ and the reduced flux variable $\phi = 2\pi\Phi/\Phi_0$:

$$\hat{\mathcal{H}} = 4E_C \hat{n}^2 + \frac{1}{2} E_L \phi^2. \tag{2.6}$$

Here, $E_C = e^2/(2C)$ is the charging energy, i.e. the energy needed to bring an electron in a Cooper pair to the other island of the capacitor, and $E_L = (\Phi_0/2\pi)^2/L$ is the inductive energy term.
Solving for the Hamiltonian eigenvalue problem in Eq. 2.6 gives an infinite set of eigenstates equally spaced in energy $E_{k+1} - E_k = \hbar\omega_r$, where $\omega_r = \sqrt{8E_C E_L}/\hbar = 1/\sqrt{LC}$ is the resonance frequency of the circuit. In terms of creation and annihilation

operators, defined as

$$\hat{a} = \frac{1}{\sqrt{\hbar\omega_r}}\left(\frac{\hat{\Phi}}{\sqrt{2L}} - i\frac{\hat{Q}}{\sqrt{2C}}\right); \quad \hat{a}^\dagger = \frac{1}{\sqrt{\hbar\omega_r}}\left(\frac{\hat{\Phi}}{\sqrt{2L}} + i\frac{\hat{Q}}{\sqrt{2C}}\right), \tag{2.7}$$

it is possible to rewrite the Hamiltonian of the quantum LC oscillator as [95]

$$\hat{\mathcal{H}} = \hbar\omega_r\left(\hat{a}^\dagger\hat{a} + \frac{1}{2}\right). \tag{2.8}$$

This description applies to various superconducting resonator geometries, such as three-dimensional (3D) cavities or coplanar waveguide resonators (2D). The latter are particularly relevant for this thesis as they are an essential building block for the quantum architectures discussed in Chapter 5.

The Coplanar Waveguide (CPW) Resonator

Coplanar waveguides (CPWs) are transmission lines consisting of a central signal conductor and two ground conductors printed on the same side of a dielectric substrate [96]. Terminating a signal line with open or short ends determines the boundary conditions of the oscillator and, together with other properties such as dielectric permittivity and geometry, determine the resonance frequency of each mode, spaced by $\omega_r/2\pi$ [97].
For a transmission line with negligible resistance and conductance, a traveling signal with voltage $V = V(x,t)$ and current $I = I(x,t)$ satisfies the telegrapher's equations [98]:

$$\frac{\partial V}{\partial x} = -L_l\frac{\partial I}{\partial t}, \tag{2.9}$$

$$\frac{\partial I}{\partial x} = -C_l\frac{\partial V}{\partial t}, \tag{2.10}$$

where L_l and C_l are the inductance and capacitance of the transmission line per unit length.
By differentiating with respect to x both terms in Eq. 2.9 and combining with Eq. 2.10, we retrieve a wave equation for V:

$$\frac{\partial^2 V}{\partial x^2} - L_l C_l\frac{\partial^2 V}{\partial t^2} = 0. \tag{2.11}$$

Similarly, differentiating Eq. 2.10 and combining with Eq. 2.9 we retrieve:

$$\frac{\partial^2 I}{\partial x^2} - L_l C_l\frac{\partial^2 I}{\partial t^2} = 0. \tag{2.12}$$

General solutions for one-dimensional waves signal moving in the forward (+) and backward (−) directions are:

$$V(x,t) = V^+e^{i(kx-\omega t)} + V^-e^{i(-kx-\omega t)}, \tag{2.13}$$

$$I(x,t) = \frac{1}{Z}\left[V^+e^{i(kx-\omega t)} - V^-e^{i(-kx-\omega t)}\right]. \tag{2.14}$$

The "−" sign in Eq. 2.14 accounts for the fact that the currents associated with the forward and reverse voltage waves are in opposite directions. The characteristic line impedance is defined as $Z = \sqrt{L_l/C_l}$, often designed to equal 50 Ω. This can be

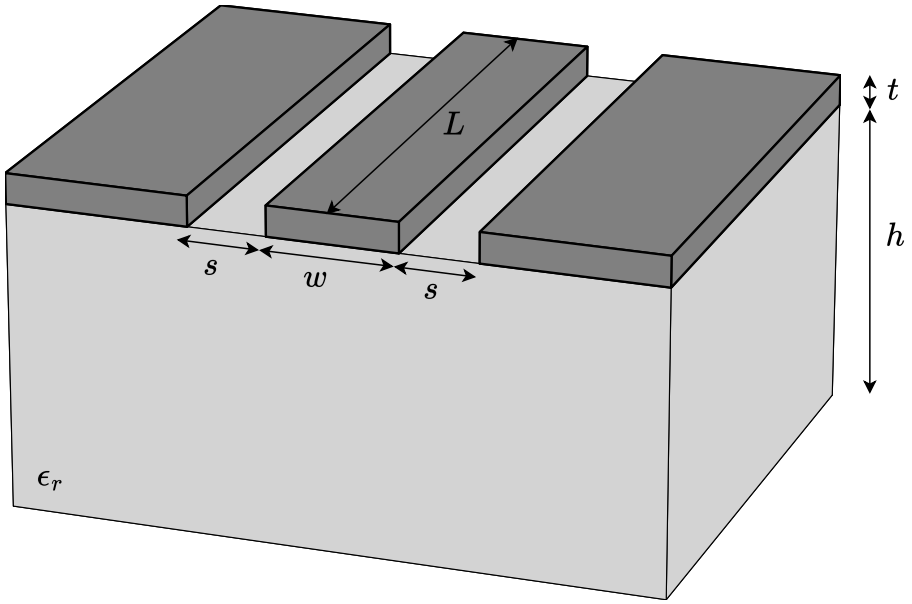

FIGURE 2.1: Coplanar waveguide structure (not to scale) of length L, consisting of a metallic (dark gray) central conductor with width w and two ground planes on both sides at a distance s (also denoted as gap) deposited on the surface of a dielectric substrate (light gray) with dielectric constant ϵ_r. The metal layer is a thin film of thickness $t \sim 100$ nm [99, 100], while the substrate thickness h can be hundreds of µm.

achieved by tuning the CPW geometrical parameters, such as the central conductor with w and gap s depicted in Fig. 2.1. In particular, C_l and L_l depend on w and s as follows:

$$C_l = 4\epsilon_0\epsilon_r \frac{K\left(\frac{w}{w+2s}\right)}{K\left(\sqrt{1-\frac{w^2}{(w+2s)^2}}\right)}, \tag{2.15}$$

$$L_l = \frac{\mu_0}{4} \frac{K\left(\sqrt{1-\frac{w^2}{(w+2s)^2}}\right)}{K\left(\frac{w}{w+2s}\right)} \tag{2.16}$$

where K indicates the complete elliptic integral of the first kind.
CPWs can acquire resonant modes by engineering boundary conditions at both ends. Two cases are particularly relevant for coplanar architectures:

- **Two floating ends:** At any time t (assuming standing waves) the current in Eq. 2.14 must satisfy $I(x = 0, t) = I(x = L, t) = 0$. Substituting the $x = 0$ condition leads to $V^+ = V^- = V_0$, meaning that the voltage of the forward and backward signals must be the same. The zero current at $x = L$ leads to:

$$e^{ikL} - e^{-ikL} = 2i\sin(kL) = 0, \tag{2.17}$$

which is true for:

$$kL = n\pi; \quad n = 0, 1, 2, 3, ... \tag{2.18}$$

Expressing the angular wavenumber k in terms of the mode wavelength λ ($k = 2\pi/\lambda$), we obtain

$$L = \frac{n\lambda}{2} \tag{2.19}$$

with frequencies

$$f_n = \frac{n\nu}{2L} = \frac{n}{2L\sqrt{L_l C_l}} \tag{2.20}$$

where $\nu = 1/\sqrt{L_l C_l}$ is the wave phase velocity. The factor of 2 in the denominator indicates that the length of a CPW with two floating ends corresponds to half the wavelength of its fundamental resonant mode. CPW resonators exhibiting these boundary conditions are commonly referred to as $\lambda/2$ resonators. Another consequence of $V^+ = V^-$ is that the potential in Eq. 2.13 can be expressed as

$$V(x,t) = 2V_0 \cos(kx) e^{-i\omega t}, \tag{2.21}$$

meaning that the voltage has a $\pi/2$ phase shift with respect to the current: to a current node corresponds a voltage maximum (or minimum), and to a voltage node corresponds the maximum of the current flow (in either direction).

- **One floating end and one grounded end:** Assuming the grounded end at $x = 0$ and the floating one at $x = L$, the boundary condition are, for any time t, $V(x = 0, t) = 0$ and $I(x = L, t) = 0$. Applying the first condition to Eq. 2.13 we obtain $V^+ = -V^- = V_0$, while applying the second one to Eq. 2.14 leads to

$$e^{ikL} + e^{-ikL} = 2\cos(kL) = 0 \tag{2.22}$$

thus, the condition is satisfied for

$$kL = \left(n + \frac{1}{2}\right)\pi; \quad n = 0,\, 1,\, 2,\, 3\,... \tag{2.23}$$

yielding

$$L = \frac{(2n+1)\lambda}{4}, \tag{2.24}$$

with mode frequencies

$$f_n = \frac{(2n+1)\nu}{4L} = \frac{(2n+1)}{4L\sqrt{L_l C_l}}. \tag{2.25}$$

In contrast with the two floating ends case, the factor of 4 in the denominator in Eq. 2.24 indicates that the length of a CPW with one floating end and one grounded end corresponds to a quarter of the fundamental mode wavelength at $n = 0$. CPW resonators with these boundary conditions are commonly addressed as $\lambda/4$ resonators. The voltage equation can now be written as

$$V(x,t) = 2iV_0 \sin(kx) e^{-i\omega t}, \tag{2.26}$$

meaning that voltage and current through the CPW still have a $\pi/2$ phase difference, as in the case mentioned above.

Fig. 2.2 represents the field intensity distributions along the CPW resonators for the nontrivial mode with the lowest frequency in the $\lambda/2$ and $\lambda/4$ cases. To match the same resonant modes, a $\lambda/2$ CPW resonator needs to be twice as long as its $\lambda/4$ counterpart, without considering other effects such as load capacitances that are discussed in Section 5.2.2.

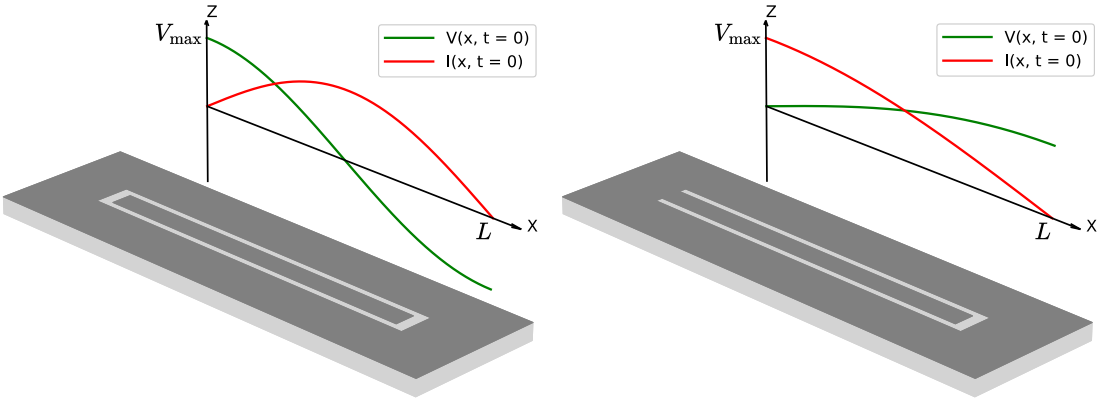

(A) CPW with floating ends. (B) CPW with grounded and floating ends.

FIGURE 2.2: Schematic illustration of first-harmonic voltage and current profiles in coplanar waveguide (CPW) resonators with different boundary conditions. The voltage $V(x,t)$ oscillates with amplitude V_{max}. (A) For the $\lambda/2$ resonator, the central conductor disconnects from the ground plane at both ends. (B) For the $\lambda/4$ resonator, one end of the central conductor is connected to ground while the other remains detached.

2.1.2 Josephson effect

The capacitive and inductive terms in Eq. 2.5 are linear, i.e. they remain constant with respect to the generalized coordinates Q and Φ. Instead, it is possible to introduce nonlinear inductive elements to break the resonator's harmonicity, in such a way that multiple eigenmodes with distinct resonant frequencies are still present, but no longer evenly spaced in energy. In this case, transitions between levels become uniquely identified, making it possible to operationally isolate the first two eigenstates and treat them as the computational base for a qubit. In other words, a superconducting qubit is a quantum anharmonic oscillator in which the capacitances and inductances are tailored to adjust the frequency separation between the $|0\rangle$ and $|1\rangle$ states.
A natural source of nonlinear inductance in superconductors is due to the inertia of Cooper pairs, generating a *kinetic inductance* [101]. The energy stored by the moving Cooper pairs increases non-proportionally with the current, resulting in nonlinearity. This phenomenon underpins several applications, including microwave kinetic inductance detectors (MKIDs) [102] and certain types of traveling-wave parametric amplifiers (TWPAs) [103]. However, this inductive contribution is not strong enough to provide significant anharmonicity to superconducting qubits with typical material choices. For instance, kinetic inductance is present in CPW transmission lines (discussed in Subsec. 2.1.1), but is negligible compared to the linear geometric inductance of the structure.
Another source of nonlinear inductance is provided by the Josephson effect [104] arising in Josephson junctions. This kind of nonlinear inductance is widely used in superconducting qubit implementations, as it can be engineered to create enough nonlinear inductance to dominate kinetic and geometric inductance terms in the system.

Josephson junction

Josephson junctions are fundamental components in superconducting quantum architectures, as they typically constitute the dominant –and nonlinear– inductive term for qubits. The Josephson junction consists of two superconductors connected by a weak link, which can be an insulator (S-I-S junction) [105], a normal, non-superconducting

metal (S-N-S junction) [106], or other physical obstacles at the point of contact, such as semiconductors [107], ferromagnetic materials [108], or superconducting constrictions (microbridges) [109]. The most common type of Josephson junction in qubit architectures is a S-I-S consisting of two aluminum conductors separated by a thin aluminum oxide layer. Cooper pairs can travel between conductors through quantum tunneling [110], hence the time evolution of the quantum states defined for the two superconductors

$$\Psi_1(\mathbf{r},t) = \sqrt{n_{c1}(\mathbf{r},t)}e^{i\theta_1(\mathbf{r},\mathbf{t})}, \tag{2.27}$$

$$\Psi_2(\mathbf{r},t) = \sqrt{n_{c2}(\mathbf{r},t)}e^{i\theta_2(\mathbf{r},\mathbf{t})}, \tag{2.28}$$

collectively evolve as $\Psi = (\Psi_1, \Psi_2)^T$ under the Hamiltonian:

$$\hat{\mathcal{H}} = \begin{pmatrix} E_1 & K \\ K & E_2 \end{pmatrix} \tag{2.29}$$

where E_1 and E_2 are the potential energies of the Cooper pairs in the two conductors, such that for a voltage V across the junction, $E_2 - E_1 = 2eV$. The term K is a characteristic constant of the junction that quantifies the tunnel effect.
From the Schrödinger equation, we derive:

$$-\hbar\frac{d\theta_1}{dt} + i\frac{\hbar}{2n_{c1}}\frac{dn_{c1}}{dt} = E_1 + K\sqrt{\frac{n_{c2}}{n_{c1}}}e^{i(\theta_2-\theta_1)}, \tag{2.30}$$

$$-\hbar\frac{d\theta_2}{dt} + i\frac{\hbar}{2n_{c2}}\frac{dn_{c2}}{dt} = E_2 + K\sqrt{\frac{n_{c1}}{n_{c2}}}e^{i(\theta_1-\theta_2)}. \tag{2.31}$$

The Cooper pair density variation over time on the two superconductor must be related such that $dn_{c1}/dt = -dn_{c2}/dt$. Considering the equalities of the imaginary parts in Eqs. 2.30 and 2.31 we obtain

$$\frac{dn_{c1}}{dt} = -\frac{dn_{c2}}{dt} = \frac{2}{\hbar}K\sqrt{n_{c1}n_{c2}}\sin(\theta_2 - \theta_1), \tag{2.32}$$

and since the current I flowing through the junction is proportional to dn_{c1}/dt:

$$I(t) = I_c \sin(\phi(t)). \tag{2.33}$$

In Eq. 2.33, I_c is called *critical current* of the junction and $\phi(t) = \theta_2(t) - \theta_1(t)$ is the phase difference between the Cooper pair states within the superconductors.
Considering the real parts in Eqs. 2.30 and 2.31

$$-\hbar\frac{d\theta_1}{dt} = E_1 + K\sqrt{\frac{\rho_2}{\rho_1}}\cos(\theta_2 - \theta_1), \tag{2.34}$$

$$-\hbar\frac{d\theta_2}{dt} = E_2 + K\sqrt{\frac{\rho_1}{\rho_2}}\cos(\theta_2 - \theta_1), \tag{2.35}$$

and subtracting them, we obtain:

$$\frac{d\phi}{dt} = \frac{2e}{\hbar}V(t) - \frac{K}{\hbar}\left(\sqrt{\frac{\rho_2}{\rho_1}} - \sqrt{\frac{\rho_1}{\rho_2}}\right)\cos(\phi). \tag{2.36}$$

The terms ρ_1 and ρ_2 are the Cooper pair density. Assuming them to be very similar, $\rho_1 \approx \rho_2$, the terms in the round parentheses cancel out, leaving:

$$\frac{d\phi}{dt} = \frac{2e}{\hbar}V(t) = \frac{2\pi}{\Phi_0}V(t). \tag{2.37}$$

Eqs. 2.33 and 2.37, known as *Josephson equations*, describe the current-phase relationship across the Josephson junction. A notable consequence of these equations is that for a voltage fixed in time $V(t) = V_0$, the phase difference ϕ evolves linearly with time, resulting in an alternating current. For $V_0 = 0$, ϕ and I remain constant, and generally nonzero over time. This means that a current can flow between two conductors at the same potential without energy dissipation, manifesting the properties of a superconductor. This dissipationless behavior holds for steady currents I below the critical current I_c. When $I > I_c$, a voltage develops across the junction, making it a dissipative element.
A remarkable consequence of the Josephson equations is that in the superconducting regime, the inductance is nonlinear in ϕ:

$$L_J(\phi) = \frac{V}{\frac{dI}{dt}} = \frac{\Phi_0}{2\pi I_c \cos(\phi)}, \tag{2.38}$$

making Josephson junctions suitable elements to introduce nonlinearity in superconducting oscillators.
The critical current can be measured at room temperature by leveraging the Ambegaokar-Baratoff formula [111]

$$I_c = \frac{\pi\Delta(T)}{2eR_n}\tanh\left(\frac{\Delta(T)}{2k_BT}\right), \tag{2.39}$$

where Δ is the temperature (T)-dependent superconducting gap of the material, k_B is the Boltzmann constant, and R_n is the junction *normal resistance*, which can be calculated as the ratio between a voltage difference applied to the junction and the resulting current at room temperature, thus determining I_c.

Josephson junctions can be integrated into coplanar architectures, and engineering the desired critical current $I_C \sim$ 10 - 30 nA requires sub-micron electron-beam lithography [112] to define junction areas on the order of 10^{-1} - 10^{-2} µm^2. The two most common approaches are the Dolan-bridge technique and the Manhattan-style method [113].
In the Dolan-bridge technique, a suspended resist *bridge* enables two-angle Al/AlOx/Al shadow evaporation. This process includes an in-situ oxidation step to form the tunnel barrier. In contrast, the Manhattan-style method uses overlapping electrode fingers patterned in a bilayer resist. This approach forms the junction without requiring a suspended bridge. Precise control of resist undercut, evaporation angles, and oxidation parameters is essential for junction uniformity and hence qubit coherence. Although we acknowledge the high impact of fabrication on the qubit performance, more detailed discussions of junction fabrication protocols lie beyond the scope of this thesis.

2.1.3 Superconducting qubits

In Subsec. 2.1.2 we introduced the Josephson junction as a nonlinear inductive element to implement superconducting qubits as anharmonic oscillators. By replacing

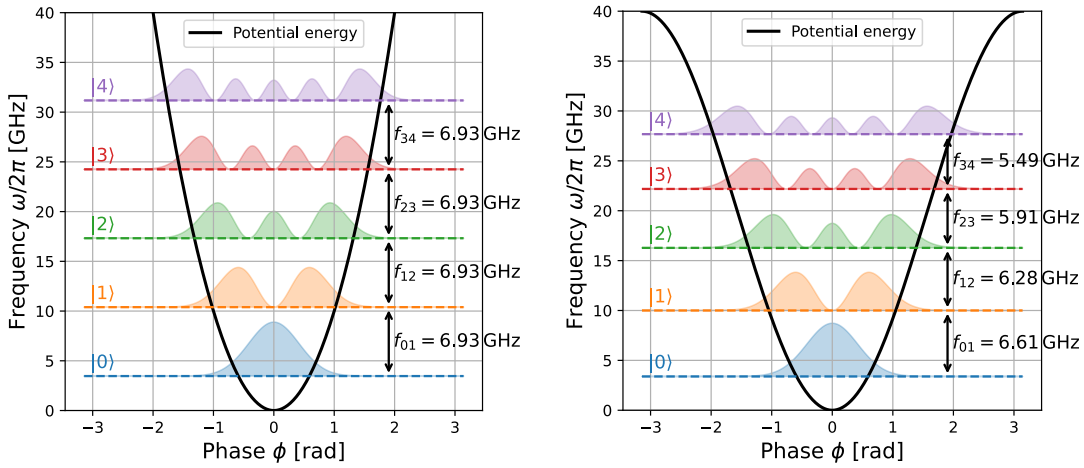

(A) Harmonic oscillator.

(B) Transmon.

FIGURE 2.3: Illustration of the transition frequencies up to the fourth excited state for a harmonic oscillator and a transmon. (A) Harmonic quantum oscillator with $E_C/h = 0.3$ GHz and $E_L/h = 20$ GHz, exhibiting equally spaced transitions at $\omega_r/(2\pi) = f_r = 6.93$ GHz. (B) Transmon with $E_C/h = 0.3$ GHz and $E_J/h = 20$ GHz with $\omega_{01}/(2\pi) = f_{01} = 6.61$ GHz, and $\alpha/(2\pi) = 0.33$ GHz $\sim E_C/h$. The colored regions represent the ϕ-dependent wavefunction square module for each eigenstate.

the inducting term in Eq. 2.6 with a Josephson energy $E_J = (\Phi_0/2\pi)^2/L_J$, we obtain:

$$\hat{\mathcal{H}} = 4E_C\hat{n}^2 - E_J\cos(\hat{\phi}). \tag{2.40}$$

Here, the capacitive energy is $E_C = e^2/(2C_\Sigma)$, with $C_\Sigma = C_s + C_J$, where C_s is the capacitive shunt to ground and C_J is the stray capacitance of the junction. The cosine potential in Eq. 2.40 differs from the parabolic one, shifting the Hamiltonian eigenvalues as shown in Fig. 2.3. Expanding the potential term up to the fourth power in ϕ near zero leads to

$$\hat{\mathcal{H}} \approx 4E_C\hat{n}^2 + \frac{1}{2}E_J\hat{\phi}^2 - \frac{1}{24}E_J\hat{\phi}^4. \tag{2.41}$$

The negative sign in front of the quartic term indicates that the displacement between the energy levels of $|0\rangle \leftrightarrow |1\rangle$ and $|1\rangle \leftrightarrow |2\rangle$, respectively indicated as ω_{01} and ω_{12}, is such that

$$\omega_{12} - \omega_{01} = \alpha < 0, \tag{2.42}$$

where α is defined as the qubit's anharmonicity. In terms of creation and annihilation operators, recalling Eq. 2.7, we can recast the Hamiltonian into

$$\hat{\mathcal{H}} \approx \sqrt{8E_JE_C}\hat{a}^\dagger\hat{a} - \frac{E_C}{12}\left(\hat{a} + \hat{a}^\dagger\right), \tag{2.43}$$

and, applying the rotating wave approximation (RWA) [114, 115], i.e. neglecting fast oscillating terms in the Hamiltonian in the interaction picture, we are left with

$$\hat{\mathcal{H}} \approx \sqrt{8E_JE_C}\hat{a}^\dagger\hat{a} - \frac{E_C}{2}\hat{a}^\dagger\hat{a}^\dagger\hat{a}\hat{a}. \tag{2.44}$$

Consequently, the qubit's anharmonicity α is approximately equal to the charging energy E_C, and $\omega_{01} \approx (\sqrt{8E_JE_C} - E_C)/\hbar$. The shunt capacitance C_s plays a fundamental role in trading off the anharmonicity and the susceptibility of the qubit to charge noise.

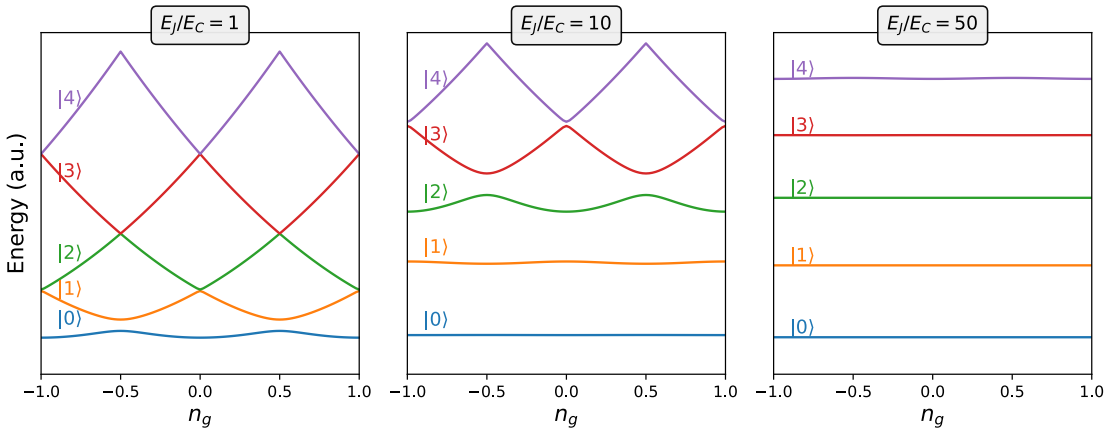

FIGURE 2.4: Transmon energy levels as a function of the offset charge n_g for different E_J/E_C ratios. Larger E_J/E_C suppresses the energy dispersions, making the qubit resilient to charge noise.

On a physical device, the kinetic term in Eq. 2.40 can be rewritten to elucidate an offset charge term in units of Cooper pair charge n_g

$$\hat{\mathcal{H}} = 4E_C(\hat{n} - n_g)^2 - E_J \cos(\hat{\phi}). \tag{2.45}$$

Increasing the shunt capacitance C_s decreases the charging energy E_C. This reduction leads to an exponential suppression of charge dispersion, making the energy levels less sensitive to fluctuations in n_g. However, as C_s increases, the anharmonicity decreases approximately in inverse proportion to C_s. The regime of interest for this thesis is the one in which the ratio of the Josephson energy is chosen to be $E_J/E_C \sim 40$ - 120, keeping an anharmonicity in the range $\alpha/(2\pi) \sim 100$ - 400 MHz for qubits with frequencies $\omega_{01}/(2\pi) \sim 1$ - 10 GHz. This operating regime is known as the *transmon regime*, and qubits designed under these conditions are referred to as *transmon qubits* [116]. Fig. 2.4 illustrates the effect of capacitive shunting on energy levels.

An important extension of the standard transmon qubit discussed so far involves making the qubit tunable in frequency. This is achievable by replacing the Josephson junction with a DC superconducting quantum interference device (DC-SQUID), consisting of two parallel Josephson junctions [95]. A consequence of the flux quantization discussed earlier in this Sect is that in a SQUID loop the sum of the flux contributions must satisfy, in units of Φ_0,

$$\theta_1 - \theta_2 + 2\phi_{\text{ext}} = 2\pi n, \tag{2.46}$$

where θ_1 and θ_2 are the junction contributions and ϕ_{ext} is an additional term arising from a concatenated flux in the SQUID loop originating from external sources. This relation removes one degree of freedom and allows us to model the SQUID as a single effective junction, with an inductance depending on ϕ_{ext}.
The Hamiltonian of a transmon qubit becomes

$$\hat{\mathcal{H}} = 4E_C\hat{n}^2 - E_{J\Sigma}\sqrt{\cos^2(\pi\phi_{\text{ext}}) + d^2\sin^2(\pi\phi_{\text{ext}})}\cos(\hat{\phi}). \tag{2.47}$$

By biasing the SQUID with a DC current, it is possible to tune the inductive energy of the transmon, modifying its transition frequencies. In Eq. 2.47, $E_{J\Sigma} = E_{J1} + E_{J2}$, where E_{J1} and E_{J2} are the maximum inductive energy of the individual junctions. The

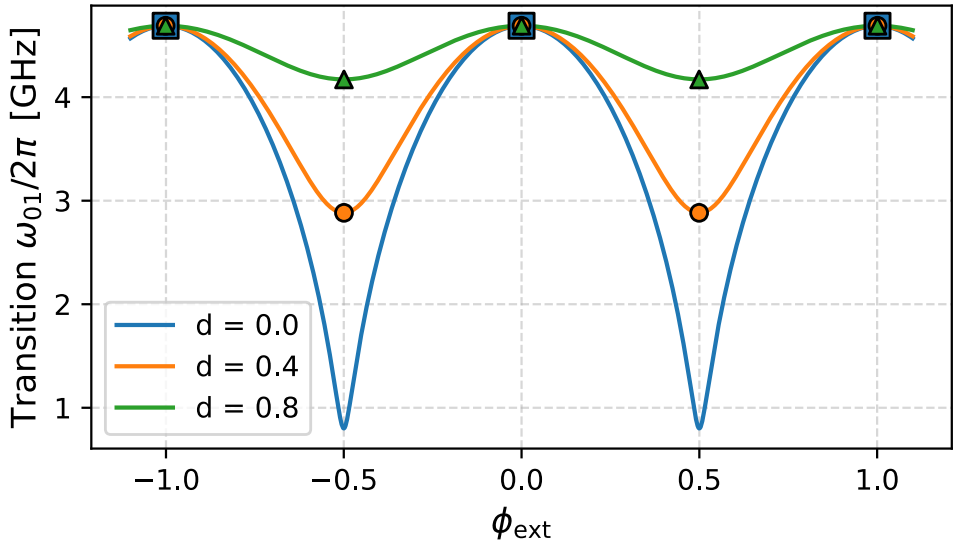

FIGURE 2.5: Flux-tunable transmon transition frequencies ω_{01} as a function of the concatenated flux ϕ_{ext} in the SQUID loop, with $E_C/h = 0.2$ GHz and $E_{J\Sigma}/h = 15$ GHz. Scatter points indicate operational sweet spots for different values of d.

d parameter is related to the junction asymmetry $\gamma = E_{J2}/E_{J1}$ defined as

$$d = \frac{\gamma - 1}{\gamma + 1}. \tag{2.48}$$

The presence of an asymmetry in the SQUID junctions is fundamental in transmon qubits, as it modifies how the energy levels vary with ϕ_{ext}, making it more or less robust to flux noise, trading off the qubit's frequency span [117] as exemplified in Fig. 2.5. For $d > 0$ (i.e. $\gamma \neq 1$), the transition frequency slope $\partial\omega_{01}/\partial\phi_{\text{ext}}$ has two minima in $\phi_{\text{ext}} = 0$ and $\phi_{\text{ext}} = (-)0.5$ that are suitable working points to implement two-qubit gates, idling, or general optimized operations, known as *sweet spots*.

While the transmon qubit is a popular choice in many research and industrial applications, other operating regimes and alternative superconducting qubit platforms are also available. For instance, lowering E_J/E_C leads to the conventional Cooper pair box regime [118], featuring high anharmonicity, but remaining more susceptible to charge fluctuations, leading to significantly lower coherence times. Another distinct approach is provided by *flux qubits* [119, 120], which harness the persistent current states in superconducting loops, offering a different balance between anharmonicity and noise sensitivity. More recently, the *fluxonium* architecture [121] incorporates a superinductance to achieve a rich, highly tunable energy spectrum reaching a few tens of MHz, with higher anharmonicity than the transmon at the cost of more complex manufacturing.

2.2 Control and readout

The precise control and accurate readout of transmon qubits are fundamental to the advancement of superconducting quantum technologies. Transmon control involves manipulating its state using microwave pulses, which is necessary for implementing quantum gates and algorithms. Furthermore, measuring the qubit state is crucial for extracting meaningful information from the system. This section introduces standard

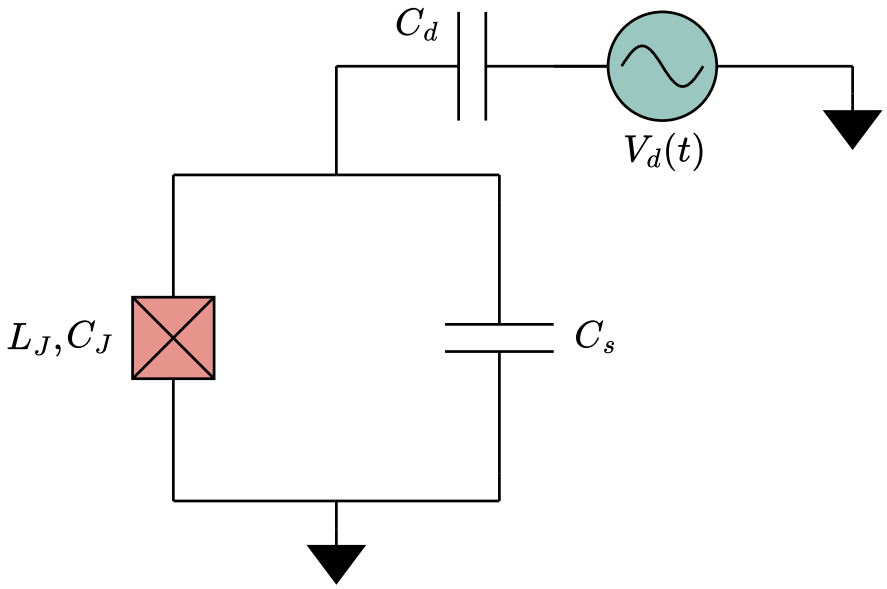

FIGURE 2.6: Circuit diagram of a transmon qubit capacitively coupled to a drive source $V_d(t)$.

techniques for implementing high-fidelity control and readout in transmons, which are as essential for quantum computing as for transmon-based detectors.

2.2.1 Implementing single-qubit gates

Quantum gates are implementable on transmon qubits through microwave pulses, steering the qubit's dynamics to reach a desired state. Considering a transmon qubit capacitively coupled to a drive channel, a new term in the system's Hamiltonian appears [95]:

$$\hat{\mathcal{H}}_d = \frac{C_d}{C_\Sigma + C_d} V_d(t) \hat{Q}, \tag{2.49}$$

following from Kirchhoff's laws applied to the circuit depicted in Fig. 2.6, under the assumption $C_d \ll C_\Sigma$. The term C_d is the effective capacitance between the drive channel and the qubit.

Recalling Eqs. 2.7, the charge operator can be written as $\hat{Q} = -iQ_{\text{zpf}}(\hat{a} - \hat{a}^\dagger)$, where $Q_{\text{zpf}} = \sqrt{\hbar/(2Z)}$ is the zero-point charge fluctuation, with Z the impedance of the circuit to ground. By making a two-level approximation, we can truncate $\hat{a}$ and $\hat{a}^\dagger$ into 2×2 matrices

$$\hat{a} \to \sigma^- = \begin{pmatrix} 0 & 1 \\ 0 & 0 \end{pmatrix}, \qquad \hat{a}^\dagger \to \sigma^+ = \begin{pmatrix} 0 & 0 \\ 1 & 0 \end{pmatrix}, \tag{2.50}$$

so that the driven transmon Hamiltonian is approximated with

$$\hat{\mathcal{H}} = -\frac{1}{2}\hbar\omega_{01}\sigma_z + \hbar\Omega v_d(t)\sigma_y, \tag{2.51}$$

where

$$\Omega = V_0 \frac{C_d Q_{\text{zpf}}}{(C_\Sigma + C_d)}, \tag{2.52}$$

and $V_d(t) = V_0 v_d(t)$. In the frame rotating at the qubit's frequency, the Hamiltonian becomes

$$\hat{\tilde{\mathcal{H}}}_d = \hbar\Omega v_d(t)\left(\cos(\omega_d t)\sigma_y + \sin(\omega_d t)\sigma_x\right). \tag{2.53}$$

Separating $v_d(t)$ into the in-phase (I) and quadrature (Q) components,

$$\begin{aligned} v_d(t) &= s(t)\left(\cos(\varphi)\sin(\omega_{01}t) + \sin(\varphi)\cos(\omega_{01}t)\right) \\ &= s(t)\left(I\sin(\omega_{01}t) + Q\cos(\omega_{01}t)\right), \end{aligned} \tag{2.54}$$

where $s(t)$ is the pulse envelope, substituting in Eq. 2.53 and applying RWA, we obtain the following formula for the drive Hamiltonian

$$\hat{\tilde{\mathcal{H}}}_d \approx -\hbar\frac{\Omega}{2}s(t)\begin{pmatrix} 0 & e^{i(\delta\omega t+\varphi)} \\ e^{-i(\delta t+\varphi)} & 0, \end{pmatrix}, \tag{2.55}$$

with $\delta = \omega_{01} - \omega_d$. For a drive pulse that is resonant with the transition frequency ($\delta\omega = 0$), we are left with

$$\hat{\tilde{\mathcal{H}}}_d \approx -\hbar\frac{\Omega}{2}s(t)\left(I\sigma_x + Q\sigma_y\right). \tag{2.56}$$

Eq. 2.56 means that resonant pulses induce rotations about the x and y axes of the Bloch sphere, depending on the phase term φ: in-phase pulses will implement R_x, and quadrature ones R_y, as defined in Eq. 1.10. The rotation angle depends on the duration of the pulse, its envelope, and its strength Ω, making it possible to implement the desired gates, such as the X gate (NOT), which is obtainable through a π-pulse, i.e. a pulse resulting in a rotation angle of π. Rotations around the z axis can be achieved using Euler's decomposition $R_z(\theta) = R_x(\pi/2)R_y(\theta)R_x(-\pi/2)$. Alternatively, R_z can be applied virtually, i.e. shifting the phase of the I and Q components, effectively adjusting the qubit's phase reference.
In terms of variation of excited state population $P_e(t)$, under a continuous drive in the two-level framework, the transmon experiences Rabi oscillations described by the following equation [122]:

$$P_e(t) = \frac{\Omega^2}{\Omega^2 + \delta^2}\sin^2\left(\frac{\sqrt{\Omega^2 + \delta^2}}{2}t\right). \tag{2.57}$$

By fixing $t = \pi/\Omega$ and varying δ, we observe a symmetric diffraction pattern with a peak centered at $\delta = 0$, as shown in Fig. 2.7. The envelope of gate pulses is a fundamental component that needs to be tuned to increase fidelity in transmons. In particular, due to the typically low anharmonicity ($\alpha/\omega_{01} \lesssim 0.1$), square or Gaussian pulses in the frequency domain may partially overlap with the ω_{12} frequency, causing leakage errors (i.e. the transmon state is taken out of the qubit's subspace). Dephasing also occurs, caused by the repulsion between the $|1\rangle$ and $|2\rangle$ energy levels, which in turn changes ω_{01}. These effects can be mitigated by modifying $s(t)$ through procedures such as the Derivative Reduction by Adiabatic Gate (DRAG) [123] or optimal control techniques [124].
The performance of a single-qubit gate implementation is often assessed in terms of error rate through the randomized benchmarking protocol [125]. At the time of writing, transmon-based quantum devices have reached errors per single-qubit gate around 10^{-4} on average [126–128] with pulse lengths ~ 10 ns.

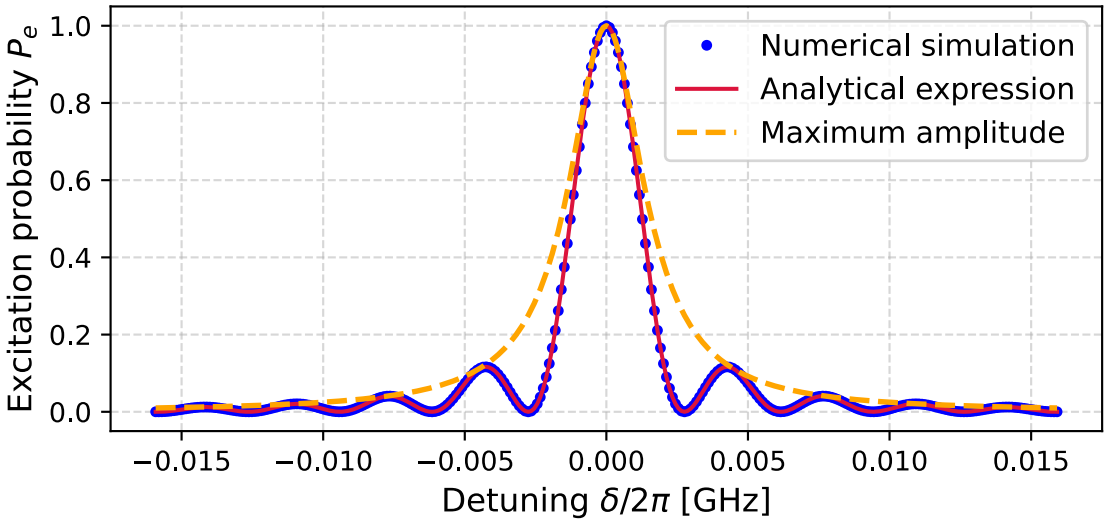

FIGURE 2.7: Excited state population of a qubit for a continuous and constant-amplitude drive at time $t = \pi/\Omega$, for different qubit-drive detunings and $\Omega/(2\pi) =$ 10 MHz.

2.2.2 Transmon state dispersive readout

Transmon qubit measurements are usually performed using the *dispersive readout* [129] technique, which involves coupling the qubit to a linear resonator mode, creating qubit state-dependent frequency displacements in the coupled modes. The system Hamiltonian can be written as

$$\hat{\mathcal{H}} = \hat{\mathcal{H}}_q + \hat{\mathcal{H}}_r + \hat{\mathcal{H}}_{\text{int}}, \tag{2.58}$$

where $\hat{\mathcal{H}}_q$ and $\hat{\mathcal{H}}_r$ are the uncoupled qubit and resonator terms, and $\hat{\mathcal{H}}_{\text{int}}$ is the interaction term. Assuming a purely capacitive coupling term, the circuit diagram is represented in Fig. 2.8.

The energy stored in the coupling capacitance is $C_g(V_1 - V_2)^2/2$. Expanding the quadratic term yields the coupling Hamiltonian term:

$$\hat{\mathcal{H}}_{\text{int}} = C_g \hat{V}_1 \hat{V}_2. \tag{2.59}$$

In the limit $C_g \ll C_\Sigma$, C_r and using Eqs. 2.7, the interaction term becomes

$$\hat{\mathcal{H}}_{\text{int}} = -\hbar g(\hat{a}_r - \hat{a}_r^\dagger)(\hat{a}_q - \hat{a}_q^\dagger), \tag{2.60}$$

with the coupling strength g defined for a $\lambda/4$ readout resonator as

$$g = \frac{E_C}{\hbar e}\left(\frac{E_J}{2E_C}\right)^{\frac{1}{4}} \frac{C_g}{C_r}\sqrt{2\hbar\omega_r C_r}. \tag{2.61}$$

Approximating the transmon to a two-level system and using RWA, we can write the full system Hamiltonian as follows:

$$\hat{\mathcal{H}} = \frac{1}{2}\hbar\omega_q\sigma_z + \hbar\omega_r\hat{a}_r^\dagger\hat{a}_r + \hbar g\left(\sigma_+\hat{a}_r + \sigma_-\hat{a}_r^\dagger\right). \tag{2.62}$$

Eq. 2.62 is known as the Jaynes-Cummings Hamiltonian [130], where σ_+ and σ_- represent the qubit excitation and relaxation processes. In the regime where

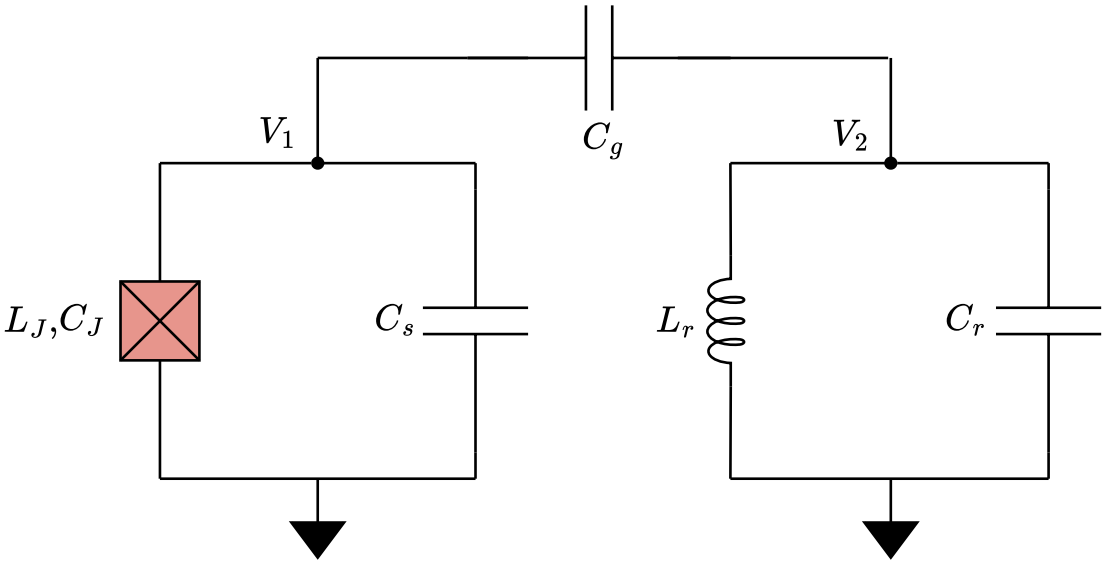

FIGURE 2.8: Circuit diagram of a transmon qubit capacitively coupled to a linear resonator.

$\Delta = |\omega_r - \omega_q| \ll g$, the qubit and the resonators are strongly coupled, allowing excitations to transfer between the two periodically. In the opposite regime, called the *dispersive* limit ($\Delta = |\omega_r - \omega_q| \gg g$), the direct excitation transfer does not occur, preventing the presence of the resonator from spoiling the qubit's dynamics.
Using second-order perturbation theory in g/Δ, the Jaynes-Cummings Hamiltonian can be written in diagonal form

$$\hat{\mathcal{H}} \approx \hbar\left(\omega_r + \chi\sigma_z\right)\left(\hat{a}_r^\dagger \hat{a}_r + \frac{1}{2}\right) + \frac{1}{2}\hbar\tilde{\omega}_q\sigma_z, \tag{2.63}$$

where

$$\chi = \frac{g^2}{\Delta} \tag{2.64}$$

is named *dispersive shift*. Eq. 2.63 underlines how the effective resonator frequency becomes $\omega_r + \chi$ when the qubit is in $|0\rangle$ and $\omega_r - \chi$ when the qubit is in $|1\rangle$. The qubit's frequency is now dressed, acquiring a *Lamb shift* term $\tilde{\omega}_q = \omega_q + g^2/\Delta$.
By coupling the resonator to a transmission line (feedline), it is possible to probe the resonator frequency in terms of amplitude and phase displacement between input and output signals traveling on the line. Sending a pulse at ω_r determines two distinct distributions in the IQ plane (in-phase and quadrature components) depending on whether the readout resonator has frequency $\omega_r + \chi$ or $\omega_r - \chi$, thus inferring the qubit state, as depicted in Fig. 2.9. Since the interaction term $\chi\sigma_z\hat{a}_r^\dagger\hat{a}_r$ in Eq. 2.64 commutes with σ_z, the qubit state collapses, preserving the computational basis, i.e. without prior state alterations due to the readout procedure. This makes the dispersive readout technique a quantum non-demolition (QND) [131] measurement.

The uncertainty in assigning the correct qubit states after the measurement is represented by the overlap between the blue and red distributions in Fig. 2.9b. The spread of these regions obtained experimentally is given by a combination of multiple factors, including intrinsic quantum fluctuations (Heisenberg limit), qubit relaxation [132], added noise in the output amplification stages [103], the readout pulse length and shape [133], and device miscalibrations, undermining the overall readout fidelity. Also higher-order excitation levels of the transmon are expected to lower the

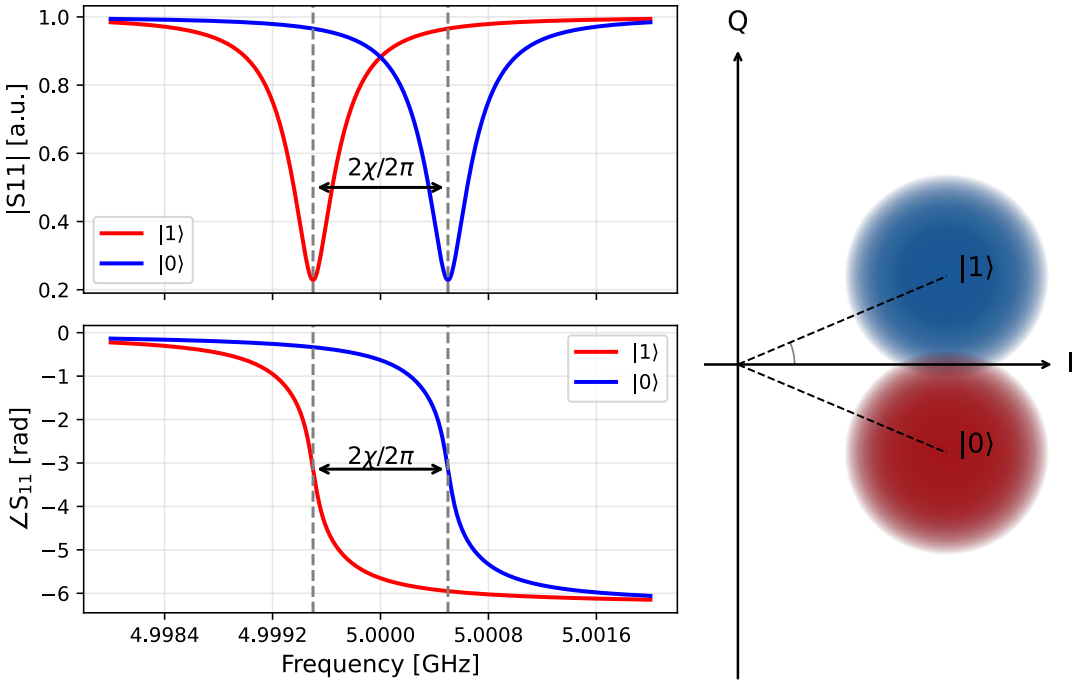

(A) Readout resonator spectroscopy. (B) IQ plane representation.

FIGURE 2.9: Dispersive qubit readout principle. (A) Reflected scattering parameter S_{11} in amplitude and phase, with $\omega_r/(2\pi) = 5$ GHz and $\chi/2\pi = 500$ KHz. (B) Schematic view of the IQ response distribution for a probe signal with frequency $\omega_r/(2\pi)$. In this case, the reflected magnitude is equal for the $|0\rangle$ and $|1\rangle$ cases, but the phase separation is maximal.

readout performance [134].
An important correction should be applied to Eq. 2.64, by taking into account the presence of the second excited state:

$$\chi = \frac{g^2}{\Delta\,(1+\Delta/\alpha)}. \tag{2.65}$$

Since Δ/α is typically on the order of ~ 10, the dispersive shift is significantly reduced with respect to the two-level approximation. State-of-the-art readout error rates for transmons amount to 10^{-2} - 10^{-3} [132, 135, 136] with pulse lengths of 0.1 - 1 µs.

2.2.3 Implementing two-qubit gates

As pointed out in Sec. 1.2, two-qubit gates are essential in multi-qubit devices to implement arbitrary transformations of the overall qubit state in the full Hilbert space. Two-qubit gates are often associated with the most critical operation in superconducting quantum processors because qubit interactions enrich the system's dynamics, introducing multiple spurious effects that lower the gate fidelity.

iSWAP gate

Assuming a direct capacitive coupling between qubits (labeled q_1 and q_2), the interaction Hamiltonian takes the same form as Eq. 2.60:

$$\hat{\mathcal{H}}_{\text{int}} = -\hbar g(\hat{a}_1 - \hat{a}_1^\dagger)(\hat{a}_2 - \hat{a}_2^\dagger). \tag{2.66}$$

Approximating both qubits as two-level systems, we obtain

$$\hat{\mathcal{H}}_{\text{int}} \approx \hbar g \sigma_{y,1}\sigma_{y,2} = -\hbar g\left(\sigma_1^+ - \sigma_1^-\right) \otimes \left(\sigma_2^+ - \sigma_2^-\right). \tag{2.67}$$

Moving to the interaction picture of the non-interacting Hamiltonian and using RWA, we are left with

$$\hat{\mathcal{H}}_{\text{int}} \approx \hbar g\left(e^{i(\omega_1-\omega_2)t}\sigma_1^+\sigma_2^- + e^{-i(\omega_1-\omega_2)t}\sigma_1^-\sigma_2^+\right). \tag{2.68}$$

When the qubits are resonant, i.e. $\omega_1 = \omega_2$, the unitary evolution of the two-qubit state is [137]

$$U(t) = e^{-ig\left(\sigma_1^+\sigma_2^- + \sigma_1^-\sigma_2^+\right)t} = \begin{pmatrix} 1 & 0 & 0 & 0 \\ 0 & \cos gt & -i\sin gt & 0 \\ 0 & -i\sin gt & \cos gt & 0 \\ 0 & 0 & 0 & 1 \end{pmatrix}, \tag{2.69}$$

meaning that a periodical exchange in the $|10\rangle$ and $|01\rangle$ amplitudes occur. By utilizing flux-tunable transmons, one can engineer iSWAP interactions by dynamically tuning the qubits into resonance for a controlled duration τ, then detuning them to stop the interaction. For $\tau = \pi/(2g)$, Eq. 2.69 corresponds to the iSWAP unitary in Eq. 1.17.

CZ gate

The CZ gate implementation leverages the presence of higher excitation levels in the transmon. In a three-level approximation, we identify a ZZ interaction strength term as

$$\zeta_{ZZ} = \omega_{11} - (\omega_{10} + \omega_{01}), \tag{2.70}$$

where the first index indicates q_1 and the second one q_2. The term ζ_{ZZ} is generally non-zero due to the presence of level $|20\rangle$ or $|02\rangle$ that, being close to the energy of $|11\rangle$, introduce an Hamiltonian component proportional to $\sigma_{z,1} \otimes \sigma_{z,2}$, also denoted as ZZ, due to avoided level crossing [138]. By preparing the transmons in state $|11\rangle$ and varying the frequency of the first one towards the avoided crossing between $|11\rangle$ and $|20\rangle$, the time evolution of the system in the computational basis will be a diagonal operator of the form

$$U = \begin{pmatrix} 1 & 0 & 0 & 0 \\ 0 & e^{i\theta_{01}(l)} & 0 & 0 \\ 0 & 0 & e^{i\theta_{10}(l)} & 0 \\ 0 & 0 & 0 & e^{i\theta_{11}(l)} \end{pmatrix}, \tag{2.71}$$

where the phase terms θ_{01}, θ_{10} and θ_{11} depends on the bias flux trajectory $l(t)$, resulting in controlled-phase (CPHASE) dynamic. For an interaction time τ:

$$\theta_{ij}(l_\pi) = \int_0^\tau \omega_{ij}(l_\pi) dt, \quad i, j = 0, 1. \tag{2.72}$$

If we choose a trajectory l_π such that

$$\int_0^\tau \zeta(t) dt = \pi = \theta_{11}(l_\pi) - [\theta_{01}(l_\pi) + \theta_{10}(l_\pi)], \tag{2.73}$$

Eq. 2.71 becomes

$$U = \begin{pmatrix} 1 & 0 & 0 & 0 \\ 0 & e^{i\theta_{01}(l_\pi)} & 0 & 0 \\ 0 & 0 & e^{i\theta_{10}(l_\pi)} & 0 \\ 0 & 0 & 0 & e^{i(\pi+\theta_{01}(l_\pi)+\theta_{10}(l_\pi))} \end{pmatrix}. \tag{2.74}$$

Upon device characterization, the terms θ_{01} and θ_{10} can be reduced to zero by applying single-qubit Z gates, leading to the same unitary expression as the CZ gate in Eq. 1.18. Due to the Landau-Zener-Stückelberg-Majorana effect [139], the flux variation driving a CZ gate must sweep the qubit frequency slowly enough to ensure adiabaticity, i.e. to prevent exchange between the $|11\rangle$ state and $|20\rangle$ or $|02\rangle$. As exemplified in Fig. 2.10, in qubits with negative anharmonicity (such as transmons), the avoided crossing between levels $|11\rangle$ and $|20\rangle$ occurs before the $|10\rangle$ - $|01\rangle$ iSWAP, so that the dynamics of the two process remain well separated.

ECR gate

The echoed cross-resonance differs from iSWAP and CNOT by not requiring tunability in the qubit frequencies, being an all-microwave operation (i.e. driven by RF pulses without DC currents generating external flux). A coupled two-qubit system with frequencies ω_{q_1} and ω_{q_2}, where q_1 is driven at ω_{q_2}, is described by the Hamiltonian [140]

$$\hat{\mathcal{H}} = \frac{1}{2}\hbar\omega_{q_1}\mathrm{ZI} + \frac{1}{2}\hbar\omega_{q_2}\mathrm{IZ} + \hbar g\,(\mathrm{XX} + \mathrm{YY}) + \hbar\Omega(t)\cos\big(\omega_{q_2}t + \varphi\big)\mathrm{XI}, \tag{2.75}$$

where g is the coupling strength and the notation ZI indicates $I_1 \otimes \sigma_{z,2}$, IZ indicates $\sigma_{z,1} \otimes I_2$, and so on. Moving to the frame rotating at ω_{q_2} and handling non-computational levels through the Schrieffer–Wolff transformation, the effective

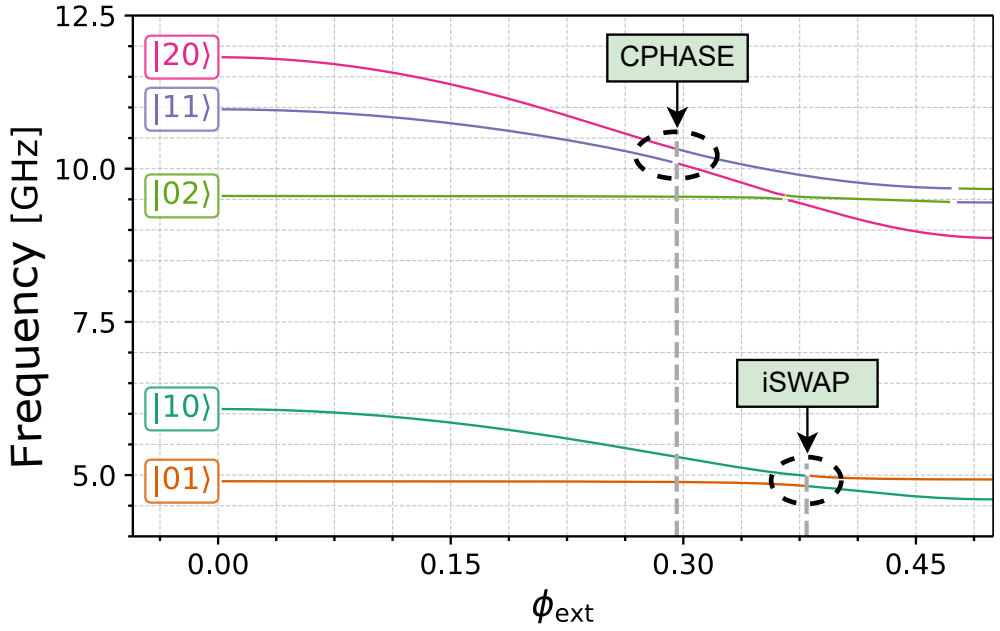

FIGURE 2.10: Resonant modes of two transmon qubits coupled capacitively with $g/(2\pi) = 35$ MHz, as a function of the flux bias applied to one qubit in units of Φ_0. The circled avoided crossings are leveraged in implementing CPHASE and iSWAP. The first (tunable) has $E_C/h = 0.3$ GHz and zero-bias $E_J/h = 17$ GHz. The second (fixed-frequency) qubit has $E_C/h = 0.22$ GHz and $E_J/h = 15$ GHz.

Hamiltonian becomes

$$\hat{\mathcal{H}}_{\text{eff}} = \frac{1}{2}\hbar\left(\omega_{\text{ZI}}\text{ZI} + \omega_{\text{IZ}}\text{IZ} + \omega_{\text{ZX}}\text{ZX} + \omega_{\text{IX}}\text{IX} + \omega_{\text{IY}}\text{IY} + \omega_{\text{ZZ}}\text{ZZ}\right). \tag{2.76}$$

Each term in Eq. 2.76 contributes with components that are either static, drive-induced, or both. Their magnitude can be evaluated through perturbative analysis. The relevant term for the cross-resonance interaction is ZX, which, in the absence of non-computational levels, the presence of a constant drive amplitude Ω, and using first order approximation in $\Omega/|\omega_{q_1} - \omega_{q_2}|$, is:

$$\omega_{\text{ZX}} = -\frac{g\Omega}{|\omega_{q_1} - \omega_{q_2}|}. \tag{2.77}$$

The consequence of a nonzero ZX term is that q_2 experiences Rabi oscillations with a frequency that depends on the q_1 state, manifesting entanglement. In this sense, q_1 is considered as the control qubit and q_2 the target. Terms other than ZX in Eq. 2.76 are considered spurious and negatively affect ZX fidelity. The ZZ interaction includes the static contribution described in Eq. 2.70 and an additional driven (i.e. Ω-dependent) component, which can be minimized either by leveraging specific design choices or carefully engineering the qubit frequencies, anharmonicities, and coupling strengths. More accurate estimations of the cross-resonance Hamiltonian component for a realistic device are reported in Sec. 5.3.
The remaining terms in the effective Hamiltonian generate single-qubit rotations that need to be canceled out. This can be achieved through an echoed protocol [141] by applying, in order:

1. A drive pulse of duration τ, amplitude Ω and phase φ on q_1.

2. A π-rotation on q_1.

3. A second drive pulse of duration τ, amplitude Ω and phase $\varphi + \pi$ on q_1.

The net effect of the echoed protocol is to cancel out the IX, IY, and ZI terms. The remaining IZ can be suppressed by applying Z-rotations to q_2 as a final correction, or adding operations to q_2 directly during the echo sequence [142]. Further improvements may be achieved through active cancellation tones on q_2 [143], compensating for single-qubit rotations not fully addressed in the standard echoed cross-resonance protocol.
Regardless of the strengths and weaknesses of iSWAP, CZ, and ECR implementations, in terms of gate fidelity [144], they are all proven to reach values close to, or above 99.9% [145–148].

2.3 Loss mechanisms

Superconducting qubits are subject to a variety of dissipation channels, each one contributing to the energy relaxation time T_1 (and hence quality factor $Q = \omega_q T_1$). In general, one can write the total relaxation rate

$$\Gamma_1 = \frac{1}{T_1} = \sum_i \Gamma_i, \tag{2.78}$$

with each loss channel i contributing a partial quality factor Q_i such that

$$\frac{1}{Q} = \sum_i \frac{1}{Q_i}. \tag{2.79}$$

The dominant channels include dielectric loss, spontaneous emission into the readout system and the environment (Purcell loss), quasiparticle tunneling, flux noise, and direct radiative (antenna) loss. Other mechanisms, such as the motion of trapped vortices and stray infrared (pair-breaking) radiation, can also impact qubits' relaxation. The second decay time characterizing the qubit's coherence is the dephasing time T_ϕ, capturing the loss of phase information between states $|0\rangle$ and $|1\rangle$, which is determined by charge and flux noise, photon shot noise, and Two-Level System (TLS) defects in the oxide surfaces present on the device.
Transmon qubits have reached state-of-the-art coherence times on the order of a few hundred microseconds [149–151], corresponding to $Q \sim 10^7$. However, device reproducibility is still challenging to achieve. Refinement of fabrication protocols, improvement of design, and noise mitigation strategies remain open research lines.

2.3.1 Dielectric loss

Dielectric loss refers to the dissipation of electromagnetic energy in any insulating material, typically characterized by the complex permittivity $\epsilon(\omega) = \epsilon' - i\epsilon''$, with the loss tangent

$$\tan(\delta) = \frac{\epsilon''}{\epsilon'}, \tag{2.80}$$

which encompasses all types of dissipative processes occurring in the dielectric substrate or the oxide layers in a coplanar architecture, such as dipolar reorientation, phonon coupling, impurity absorption, and surface-state relaxation [152].
A peculiar kind of dielectric loss is represented by two-level systems (TLS), i.e. defects

(atomic tunneling centers, surface dangling bonds, trapped charges) in the material that couple to the qubit. TLSs contribute substantially to dielectric losses in transmons [153], as they can interact dispersively with the qubit, causing dephasing, or introduce spurious energy exchange when resonant, creating T_1 dips. A characteristic of TLS noise is its temperature-dependent behavior, as higher temperatures may saturate some TLS, reducing the overall impact on the qubit.

The dielectric contribution to the overall quality factor of a qubit Q_{dielec} accounts for the electric field intensity and distribution over different lossy materials. Given a total stored energy W, the energy participation ratio (EPR) of the i-th dielectric with volume V_i is [154]

$$p_i = \frac{\text{Re}(\epsilon_i)}{2W} \int_{V_i} |E(\mathbf{r})|^2 dV. \tag{2.81}$$

The resulting inverse quality factor terms for each dielectric are $1/Q_{\text{dielec},i} = p_i \tan\delta_i$, thus

$$Q_{\text{dielec}} = \left(\sum_i p_i \tan\delta_i \right)^{-1}. \tag{2.82}$$

For a typical 2D transmon, most of the capacitive energy resides in the vacuum/air above the metal layer and the substrate. However, since the electric field diverges at the metal edges, surface oxides have a non-negligible impact on Q_{dielec}, especially due to the large loss tangent values of oxides. The typical values for the loss tangents and the thicknesses of the surface oxides are reported in Table 2.1.

Loss tangents are heavily dependent on fabrication techniques, with their corresponding impurity levels and defectivity, as well as the operational frequency and temperature. Furthermore, separating the MA, MS, and SA contributions is challenging, often leading to large error bounds in the measurements. For these reasons, the values reported in Table 2.1 should be intended as orders of magnitude rather than precise benchmarks, and non-exhaustive (values for other metal choices, such as NbTiN [159], TiN [160], and Ta [161], are not shown).

TABLE 2.1: Approximate surface-oxide thicknesses and microwave loss tangents at $T \ll 100$ mK for Al, Nb metals and high-resistivity Si, sapphire substrates [155–158].

Region	**Material-Interface**	**Thickness** (nm)	**tan δ**
Metal-Air (MA)	Al	5	1×10^{-3}
	Nb	5	1×10^{-2}
Metal-Substrate (MS)	Al-Si	0.3	1×10^{-3}
	Nb-Si	0.3	1×10^{-3}
Substrate-Air (SA)	Si	2	5×10^{-3}
	Sapphire	2	1×10^{-3}
Bulk substrate	Si	—	$1 - 10 \times 10^{-7}$
	Sapphire	—	$1 - 10 \times 10^{-8}$

2.3.2 Purcell decay

A transmon qubit dispersively coupled to a readout resonator, which in turn is coupled to a transmission line, experiences the Purcell effect, i.e. enhanced photon emission (decay) mediated by the readout cavity [162]. In the dispersive regime

(qubit–resonator detuning $\Delta = \omega_q - \omega_r \gg g$, where g is the coupling strength), the Purcell decay rate [163] is well approximated by

$$\Gamma_{\text{Purcell, res}} \approx \frac{g}{\Delta^2} k, \tag{2.83}$$

where $k/(2\pi)$ is the readout resonator linewidth.
The Purcell decay can potentially become the limiting factor in a qubit's T_1, overcoming dielectric losses. For this reason, trading off parameters g, k, and Δ is usually required. Lowering g and k would enhance the Purcell limit $T_{1,\text{Purcell}}$ at the expense of slowing down the readout, affecting the dispersive shift χ and narrowing the resonator linewidth.
In practice, Purcell filters [164] (which incorporate additional resonant structures or impedance engineering strategies) are used to suppress Γ_{Purcell} while still allowing for rapid measurement [165]. Purcell filters are designed to maximize the coupling between the qubit and the environment (represented, for instance, by a feedline) at frequencies close to $\omega_r/(2\pi)$, suppressing the coupling at $\omega_q/(2\pi)$.
The presence of drivelines and fluxlines also affects the Purcell limit. A direct capacitive coupling C_c to a transmission line with characteristic impedance Z_0 induces the decay rate [166]

$$\Gamma_{\text{Purcell, cap}} \approx \frac{\omega_q^2 C_c^2 Z_0}{C_\Sigma}. \tag{2.84}$$

For an inductive coupling with mutual inductance M, assuming that the inductance of the qubit is dominated by the Josephson component L_J:

$$\Gamma_{\text{Purcell, ind}} \approx \frac{\omega_q^2 M^2}{L_J Z_0}. \tag{2.85}$$

More generally, the Purcell relaxation rate through a linear environment is quantified by

$$\Gamma_{\text{Purcell}} = \frac{\omega_q^2}{\hbar} |\langle e| \hat{n} |g\rangle|^2 \,\text{Re}[Y(\omega_q)], \tag{2.86}$$

where $Y(\omega_q)$ is the admittance seen by the qubit at frequency $\omega_q/(2\pi)$. Approximating the qubit to a harmonic oscillator, Eq. 2.86 simplifies to

$$\Gamma_{\text{Purcell}} \approx \frac{\text{Re}[Y(\omega_q)]}{C_\Sigma}. \tag{2.87}$$

2.3.3 Quasiparticle losses

Quasiparticles (broken Cooper pairs) in the superconducting film can tunnel across the Josephson junction, causing energy relaxation. In thermal or non-equilibrium regimes, the quasiparticle density (n_{qp}) normalized by the Cooper pair density is [167]

$$x_{\text{qp}} = \frac{n_{\text{qp}}}{2N_0\Delta}, \tag{2.88}$$

where Δ is the metallic superconducting gap and N_0 is the normal-state density of states at the Fermi level. The dominant relaxation rate refers to the $|0\rangle \rightarrow |1\rangle$ transition, which, for a perfectly symmetric flux-tunable transmon, is

$$\Gamma_{\text{qp}} = \frac{8E_J}{\pi\hbar} x_{\text{qp}} \sqrt{\frac{2\Delta}{\hbar\omega_q}} \frac{[1+\cos(\varphi_{\text{ext}})]}{2}. \tag{2.89}$$

Eq. 2.89 underlines how the impact of quasiparticle loss depends on flux. However, residual terms arise from the SQUID asymmetry. In the fixed-frequency case, $\cos(\varphi_{\text{ext}}) \approx 1$.
Additional decoherence mechanisms include quasiparticle recombination, diffusion out of the junction region, or phonon-mediated energy exchanges. Dephasing also occurs in quasiparticle tunneling when it does not induce transitions. Quasiparticle formations have been demonstrated to limit qubit coherence times [168, 169], although they are generally less impactful than dielectric losses.

2.3.4 Other loss channels

In addition to dielectric, Purcell, and quasiparticle channels, transmon qubits suffer small but ultimately limiting losses from purely electromagnetic and radiation-driven mechanisms, discussed below.

Radiative antenna losses

Radiative losses arise because the qubit's capacitor pads and wiring form an effective microwave antenna, coupling energy from the circuit into free space or package modes. The 2D transmon radiative behavior can be approximated by a dipole [116], which in free space would emit with a rate

$$\Gamma_{\text{rad}} = \frac{d^2\omega_q^3}{12\pi\epsilon_0\hbar c^3}. \tag{2.90}$$

The chip packaging (sample holder) is designed to suppress spontaneous emission by enclosing the qubit in a metallic cavity with modes (often referred to as box-modes) at frequencies far above ω_q. Sub-optimal sample holders may spoil the qubit's performance in the presence of box-modes below $\lesssim 10$ GHz.

Magnetic vortex motion

Trapped Abrikosov vortices [170] in the superconducting film move under microwave currents, dissipating energy via flux-flow resistance. Recent measurements in niobium devices at millikelvin temperatures show that vortex motion limits the T_1 to hundreds of microseconds for 1 mG of trapped field, becoming negligible with respect to dielectric losses in the presence of a magnetic field shield [171].

Stray pair-breaking radiation

Photons in the infrared or blackbody radiation above $\sim$ 100 GHz are absorbed resonantly by qubit antenna modes, breaking Cooper pairs and generating nonequilibrium quasiparticles. Resonant absorption of 4 K blackbody radiation through these

modes produces quasiparticle poisoning rates sufficient to limit T_1 to $\sim$ 1 ms in unshielded devices [172], but this limit can be overcome by using infrared-absorbing filters.

Chapter 3

Dark matter searches with superconducting qubits

As discussed in Chapter 1, superconducting qubits are sensitive to the electromagnetic fields and can be seen as powerful detectors for dark matter candidates that admit couplings with few-MHz to few-GHz photons. These candidates coincide with the ones searched in haloscope and RF cavity experiments, namely dark photon, axion, and axion-like particles. This chapter presents notable experiments and detection schemes that use transmon qubits to outperform conventional microwave experiments.
Traditional detectors typically rely on continuous linear amplification of the field emitted by microwave cavities, a process fundamentally constrained by the standard quantum limit (SQL) [173]. By contrast, transmon-based techniques offer improvements in terms of signal-to-noise ratio and speed of the experiment. The two branches of interest in this Chapter are based on QND, which was briefly introduced in Subsec. 2.2.2, and direct energy exchange between the qubit and the dark field.

3.1 Quantum non-demolition detection

The dispersive interaction between a transmon qubit and a linear resonant cavity is described by the Jaynes-Cummings Hamiltonian in Eqs. 2.62 and 2.63. Upon factoring out the operator σ_z in Eq. 2.63 and discarding the constant vacuum-energy offset $\hbar\chi\omega_r/2$, we obtain

$$\hat{\mathcal{H}} = \hbar\omega_r\hat{a}^\dagger\hat{a} + \frac{\hbar}{2}\left(\tilde{\omega}_q + 2\chi\hat{a}^\dagger\hat{a}\right)\sigma_z, \tag{3.1}$$

meaning that the qubit frequency acquires a shift that is proportional to the number of photons $\hat{a}^\dagger\hat{a}$ stored inside the cavity. This is equivalent to the qubit acquiring a precession term at rate $\hat{a}^\dagger\hat{a}\chi$ around the $\hat{z}$ axis on the Bloch sphere. Crucially, the interaction term in Eq. 3.1 commutes with the bare (uncoupled) Hamiltonians of the qubit and the cavity. Therefore, when the qubit state collapses upon measurement, the resonator collapses to a Fock state, i.e. an eigenstate of $\hat{a}^\dagger\hat{a}$ associated with a well-defined number of stored photons. Repeated measurements of the qubit will not affect the collapsed cavity state, which keeps preserving the photon-cavity interaction history until the photons escape from the cavity and are lost in the environment. This non-demolition mechanism enables suppression of error sources such as readout infidelity and thermal noise through redundantly repeating the experiment within the photon trapping timescale, improving the sensitivity to single photon detection.

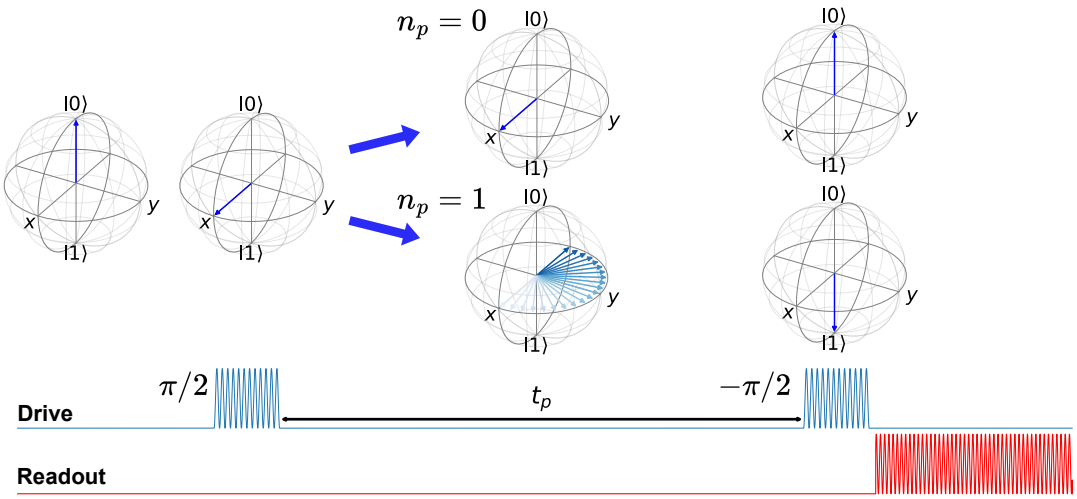

FIGURE 3.1: Ramsey parity measurement for QND photon detection in the zero and one photon cases. From left to right, the qubit is initially prepared in $|0\rangle$, then a $\pi/2$-pulse is applied (blue signal). During the free-evolution time $t_p = \pi/|2\chi_s|$, the qubit state vector either remains in the same position ($n_p = 0$) or makes half a turn around $\hat{z}$ ($n_p = 1$). Applying a $-\pi/2$-pulse results in state $|0\rangle$ or $|1\rangle$ depending on the value of n_p. The state is then read out via dispersive measurement on the readout cavity (red signal).

3.1.1 Single-qubit QND dark photon detection

A remarkable demonstration of QND detection follows from [20], where a transmon qubit was coupled to one cavity for dispersive readout and one for collecting photons, namely the storage cavity. This setup allows detection of photons originating from the dark-to-ordinary photon conversion mechanism, for dark photon masses m_X that are resonant with the storage cavity mode of interest, at frequency $\omega_s/2\pi$. The qubit state, prepared in a superposition of $|0\rangle$ and $|1\rangle$, rotates around the $\hat{z}$ axis of the Bloch sphere with frequency $\hat{a}_s^\dagger \hat{a}_s \chi_s/2\pi$, where χ_s is the storage cavity dispersive shift and $n_p = \hat{a}_s^\dagger \hat{a}_s$ the photon population:

$$|\psi(t)\rangle = \frac{1}{\sqrt{2}}\left(|0\rangle + e^{-i2n_p|\chi_s|t}\,|1\rangle\right). \tag{3.2}$$

The Ramsey measurement of the qubit state was structured as follows:

1. Prepare the qubit in $|0\rangle$.
2. Apply a $\pi/2$-pulse to bring the qubit to $(|0\rangle + |1\rangle)/\sqrt{2}$.
3. After waiting a time $t_p = \pi/|2\chi_s|$ apply a $-\pi/2$-pulse (differing from $\pi/2$ by a phase flip).
4. Measure the qubit state through the readout cavity.

If $n_p = 1$, after a time t_p the qubit state rotates around $\hat{z}$ by an angle π, so that applying a $-\pi/2$ pulse send it to $|1\rangle$ instead of returning to $|0\rangle$, as graphically depicted in Fig. 3.1. More generally, this procedure maps the qubit in state $|0\rangle$ when the number of photons in the storage cavity is even (making $n_p/2$ full turns around $\hat{z}$), and in state $|1\rangle$ when odd (making $n_p/2$ full turnes plus a half turn around $\hat{z}$).

Being a non-demolition measurement, repeating steps 1 to 4 does not affect the stor-

age cavity state, as long as the photon(s) remain trapped in the cavity, meaning that the qubit should also collapse to the same state. Different qubit measurement outcomes will be given by dark counts and noise, rather than a change in the photon population number in the storage cavity. Thus, repeating the procedure m times, each with a false positive rate p_{FP}, the probability of registering false positives will be exponentially suppressed, scaling as p_{FP}^m.
In [20], using a three-dimensional storage cavity with a quality factor of $Q_s \approx 2 \times 10^7$, with a corresponding decay time above 500 µs, the parity measurement was repeated more than 30 times, reducing the noise to 15.7 dB below SQL. This measurement resulted in an exclusion limit for the dark photon kinetic mixing of $\epsilon \leq 1.68 \times 10^{-15}$ at 90% C.L. in an integration time of $\approx$ 8 s, by far surpassing any of the experiments mentioned in Chapter. 1 for a narrow frequency band around 6.011 GHz. This photon number resolving detector was also leveraged to initialize a cavity in the Fock state $|n_p = 4\rangle$ [174]. With respect to the thermal state, when a cavity is in a Fock state, it experiences enhanced spontaneous photon emission and absorption mechanisms induced by dark matter, resulting in increased sensitivity to ϵ, proportionally to n_p.

Possible future directions leveraging the powerful mechanism of QND photon detection involve the use of multiple, entangled qubits coupled to the same storage cavity. For instance, assuming identical qubits and coupling strengths to the cavity, a GHZ state (introduced in Subsec. 1.2.2) composed of N qubits acquires a phase term enhanced proportionally to N [7]:

$$|\psi(t)\rangle = \frac{1}{\sqrt{2}} \left(|00 \ldots 0\rangle + e^{-i2n_p|\chi_s|Nt} |11 \ldots 1\rangle \right). \tag{3.3}$$

Consequently, since the SQL noise contribution remains unchanged, the detector now requires a delay between the $\pi/2$ and $-\pi/2$ pulses that is reduced by a factor N.
On the other hand, multi-qubit entangled states are generally harder to preserve over time, and typically decay much faster than single-qubit states [175]. This is important to consider, ensuring a GHZ lifetime significantly larger than t_p/N. Other quantum states may be more resilient to noise, providing further advantage, such as squeezed states [173, 176].

3.1.2 Adaptation to axion and ALP detection

A critical challenge in extending the use of superconducting quantum devices for axion and ALP searches is their incompatibility with the strong magnetic fields required for axion-photon conversion. Unlike dark photon detection, which can be carried out without external fields, axion-photon conversion typically requires fields on the order of a few tesla. These fields are detrimental to most superconducting qubit circuits, as even microtesla-level magnetic fields can detune the qubit and undermine its coherence [177]. Therefore, it is necessary to isolate the qubit from the magnetic field while still enabling it to interact with the microwave signals generated by axion conversion.
The standard practice in superconducting circuit design involves multiple layers of magnetic shielding, typically alternating high-permeability materials (such as mu-metal or Cryoperm) and superconducting enclosures (like aluminum or niobium cans) to reduce spurious magnetic fields [178]. However, these layered shields are insufficient against the intense magnetic fields produced by multi-tesla solenoids. Research is ongoing into flux-resistant qubit designs and new superconducting materials that could tolerate higher magnetic fields [177, 179]. An architectural solution

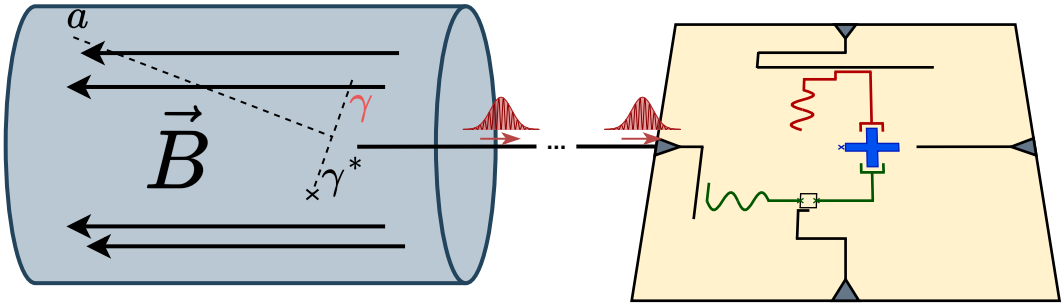

FIGURE 3.2: Representation of a QND axion detection scheme. The axion field a, interacting with the magnetic field **B** inside the haloscope, produces a photon (γ) and a virtual photon (γ^*). The photon is absorbed by a tunable storage cavity (green), inducing a phase precession in the qubit (blue) state. Repeated photon detection is achieved by performing parity measurements via the readout resonator (red).

consists of using an aperture-coupled dual-cavity design, where electromagnetic mode engineering allows the qubit sensor to reside in a magnetically shielded area, yet remain coupled to the relevant cavity mode [180]
One other promising strategy is to spatially separate the qubit from the axion-photon conversion site. Instead of detecting stored photons, it is possible to capture axion-conversion photons as traveling or *itinerant* signals [181]. These can then be detected by a qubit-cavity system located away from the magnetic field. This technique, demonstrated in [182], enables one or multiple QND photon detectors to operate outside the high-field region. When an itinerant photon reaches a cavity containing a photon, it is reflected with a phase difference that depends on the qubit state. This interaction is equivalent to a CZ operation between the photon and qubit phases, which can be inferred without destroying the photon.
In a different experimental approach described in [22], the axion conversion cavity was placed inside a 2 T magnetic field, while the transmon photon detector was located beyond the fringe field and connected via a low-loss coaxial cable. This setup allowed for efficient single-photon detection without the use of QND. Instead, it utilized a four-wave mixing (4WM) process to convert the signal frequency to a tone resonant with the qubit, thereby driving a transition from the ground to the excited state.

To improve scalability for multi-qubit axion detectors, similarly to the ones used in QND dark photon searches, the device described in Subsec. 3.1.1 could be redesigned in a coplanar architecture [183], as depicted in Fig. 3.1. In this scheme, a photon emitted from the haloscope would enter a resonant storage CPW cavity, enabling repeated Ramsey parity measurements. However, this approach introduces challenges, such as a reduced quality factor in the storage resonator, which limits photon trapping time.

3.2 Direct dark field detection

A second class of light dark matter detection techniques is based on the direct interaction between the corresponding EM-coupled dark field and a qubit, driving transitions between levels without intermediate passages such as photon conversion in cavities [21, 184]. This concept belongs to a broader context of DM-induced transitions of different kinds spanning different energy scales. Examples include transitions across the band gap in semiconducting or dielectric crystals, between molecular orbitals, and materials with spin-orbit coupling [185].

In the context of transmon qubits, resonant dark photon and axion fields induces a Rabi oscillation between energy levels. For simplicity, the transition rates derived in this Section will only consider the computational states $|0\rangle$ and $|1\rangle$. However, the results may straightforwardly extend to the higher-order levels of superconducting qubits.

3.2.1 Dark matter-induced Rabi oscillations

Due to the different coupling mechanisms, the DM-induced qubit dynamics follow separate derivations based on whether the field has a dark photon or axion-ALP nature. Both derivations are presented below, closely following [21] for dark photons and [186] for axions-ALPs.

Dark photon direct detection

The interaction term in the QED Lagrangian for electrons is

$$\mathcal{L}_{\text{int}} = e\bar{\psi}_e\gamma^\mu \left(A_\mu + \epsilon X_\mu\right)\psi_e, \tag{3.4}$$

where ψ_e, A_μ, and X_μ are the electron, photon, and dark photon fields, respectively. The natural unit convention is adopted, so that $c = \hbar = 1$, and the dark field contribution is weighted through the kinetic mixing strength ϵ.
Assuming a unique wavelike mass term m_X (i.e. the dark photon mass), the dark vector potential field is

$$\mathbf{X} = \bar{X}\mathbf{n}_X \cos(m_X t). \tag{3.5}$$

Here, $\mathbf{n}_X$ is a unit vector carrying directional information and $\bar{X}$ the oscillation amplitude, linked to the local DM density ρ_{DM}:

$$\rho_{\text{DM}} = \frac{1}{2}m_X^2\bar{X}^2. \tag{3.6}$$

Following the Maxwell-Faraday equation, the dark component of the electric field on the qubit is

$$\mathbf{E}_X = -\epsilon\frac{\partial \mathbf{X}}{\partial t} = \epsilon m_X \mathbf{n}_X \bar{X}\sin(m_X t), \tag{3.7}$$

therefore:

$$\mathbf{E}_X = \epsilon\sqrt{2\rho_{\text{DM}}}\mathbf{n}_X \sin(m_X t) = \bar{E}_X\mathbf{n}_X \sin(m_X t). \tag{3.8}$$

Another component of the electric field should be taken into account, due to the package's reactive field. The qubit is enclosed either within the readout cavity itself (if the architecture is three-dimensional) or a metallic sample holder containing the whole quantum device (if the architecture is two-dimensional), acting as a cavity [187]. In both cases, the DM-induced field causes electron motions on the walls of the cavity, creating a field $\mathbf{E}_{\text{EM}}$ such that the total electric field on the walls vanishes. Due to $m_X > 0$, $\mathbf{E}_X$ and $\mathbf{E}_{\text{EM}}$ propagate with a different dispersion relation, meaning that a perfect net field cancellation occurs only at the cavity walls and not inside its volume. The total effective field acting on a qubit is therefore

$$\mathbf{E}_{\text{eff}} = \mathbf{E}_X + \mathbf{E}_{\text{EM}}, \tag{3.9}$$

with a *package term k*

$$k \equiv \frac{\bar{E}_{\text{eff}}}{\bar{E}_X}, \tag{3.10}$$

typically close to one for cavities with resonant modes far from m_X. The effective electric field can be written as

$$\mathbf{E}_{\text{eff}} = \bar{E}_{\text{eff}}\mathbf{n}_{\text{eff}}\sin(m_X t) = k\epsilon\sqrt{2\rho_{\text{DM}}}\mathbf{n}_{\text{eff}}\sin(m_X t). \tag{3.11}$$

Rewriting the free transmon Hamiltonian in terms of the voltage difference across the junction element $\hat{V}$ leads to

$$\hat{\mathcal{H}} = \frac{1}{2}C_\Sigma\hat{V}^2 - E_J\cos(\hat{\phi}). \tag{3.12}$$

By adding the voltage difference induced by DM, $V_{\text{int}} = l\bar{E}_{\text{eff}}\cos(\Theta)\sin(m_X t)$, the interacting part of the transmon Hamiltonian becomes (up to the first order in ϵ):

$$\hat{\mathcal{H}}_{\text{int}} = C_\Sigma\hat{V}d\bar{E}_{\text{eff}}\cos(\Theta)\sin(m_X t). \tag{3.13}$$

The term l corresponds to the effective distance between the qubit's capacitor plates, and Θ is the angle between $\mathbf{n}_{\text{eff}}$ and the qubit's electric dipole moment vector. Recalling the expression for the annihilation and creation operators in Eq. 2.7, and substituting the relation $\hat{V} = \hat{Q}/C_\Sigma$, we obtain

$$\hat{V} = i\sqrt{\frac{\omega_q}{2C_\Sigma}}\left(\hat{a} - \hat{a}^\dagger\right), \tag{3.14}$$

and Eq. 3.13 becomes

$$\begin{aligned}\hat{\mathcal{H}}_{\text{int}} &= i\sqrt{\frac{\omega_q C_\Sigma}{2}}l\bar{E}_{\text{eff}}\cos(\Theta)\sin(m_X t)\left(\hat{a} - \hat{a}^\dagger\right)\\ &= i2\eta\sin(m_X t)\left(\hat{a} - \hat{a}^\dagger\right),\end{aligned} \tag{3.15}$$

with

$$\eta \equiv \frac{1}{2}\sqrt{\frac{\omega_q C_\Sigma}{2}}l\bar{E}_{\text{eff}}\cos(\Theta) = \frac{\sqrt{\omega_q C_\Sigma\rho_{\text{DM}}}}{2}lk\epsilon\cos(\Theta). \tag{3.16}$$

In the two-level approximation, a and $a^\dagger$ truncate to $\sigma^- = |0\rangle\langle 1|$ and $\sigma^+ = |1\rangle\langle 0|$, respectively. Since $(\sigma^- - \sigma^+) = -i\sigma_y$, the total Hamiltonian can be written as

$$\hat{\mathcal{H}} = \frac{1}{2}\omega_q\sigma_z + 2\eta\sin(m_X t)\sigma_y, \tag{3.17}$$

which has the same form as the driven qubit Hamiltonian in Eq. 2.51, meaning that the dark photon interaction is equivalent to a drive microwave tone with frequency m_X for the qubit. More explicitly, the time evolution of the qubit state $|\psi(t)\rangle$ can be obtained by solving the Schrödinger equation

$$i\frac{d}{dt}|\psi(t)\rangle = \hat{\mathcal{H}}|\psi(t)\rangle, \tag{3.18}$$

where we can write $|\psi(t)\rangle$ separating the time-dependent ground and excited states amplitudes $\psi_g(t)$ and $\psi_e(t)$:

$$|\psi(t)\rangle = \psi_g(t)|0\rangle + \psi_e(t)|1\rangle = \begin{pmatrix}\psi_g(t)\\ \psi_e(t)\end{pmatrix}. \tag{3.19}$$

The right side of Eq. 3.18 becomes

$$\hat{\mathcal{H}}\,|\psi(t)\rangle = \begin{pmatrix} \frac{1}{2}\omega_q & -i2\eta\sin(m_X t) \\ i2\eta\sin(m_X t) & -\frac{1}{2}\omega_q \end{pmatrix} \begin{pmatrix} \psi_g(t) \\ \psi_e(t) \end{pmatrix}. \tag{3.20}$$

We can remove the diagonal terms in the Hamiltonian by moving to the frame rotating at $\omega_q/2$, applying the unitary

$$U(t) = \begin{pmatrix} e^{-i\frac{\omega_q}{2}} & 0 \\ 0 & e^{i\frac{\omega_q}{2}} \end{pmatrix}, \tag{3.21}$$

so that

$$i\frac{d}{dt}\begin{pmatrix} \psi'_g(t) \\ \psi'_e(t) \end{pmatrix} = \begin{pmatrix} 0 & -i2\eta\sin(m_X t)e^{i\omega_q t} \\ i2\eta\sin(m_X t)e^{-i\omega_q t} & 0 \end{pmatrix} \begin{pmatrix} \psi'_g(t) \\ \psi'_e(t) \end{pmatrix}, \tag{3.22}$$

with $\psi'_g(t) = e^{i\frac{\omega_q}{2}t}\psi_g(t)$ and $\psi'_e(t) = e^{-i\frac{\omega_q}{2}t}\psi_e(t)$.
Assuming the dark photon mass to be resonant with the qubit ($m_X = \omega_q$) and applying the RWA (dropping terms oscillating at $2\omega_q$), Eq. 3.22 simplifies to

$$i\frac{d}{dt}\begin{pmatrix} \psi'_g(t) \\ \psi'_e(t) \end{pmatrix} \approx \begin{pmatrix} 0 & -i\eta \\ i\eta & 0 \end{pmatrix} \begin{pmatrix} \psi'_g(t) \\ \psi'_e(t) \end{pmatrix}. \tag{3.23}$$

Considering a qubit initially prepared in $|0\rangle$, hence $\psi'_g(0) = 1$ and $\psi'_e(0) = 0$, the solutions to Eq. 3.23 are:

$$\psi'_g(t) = \cos(\eta t); \qquad \psi'_e(t) = \sin(\eta t). \tag{3.24}$$

The probability of the qubit to collapse in $|1\rangle$ after a measurement is

$$P_e(t) = |\psi'_e(t)|^2 = \sin\left(\frac{\sqrt{\omega_q C_\Sigma \rho_{\rm DM}}}{2} lk\epsilon\cos(\Theta)t\right)^2. \tag{3.25}$$

We assume that ϵ is sufficiently small such that the resulting Rabi oscillations occur on a timescale much longer than the system's coherence time. Therefore, we consider the regime $\eta t \ll 1$, where the excitation probability exhibits a simple quadratic time dependence instead of an oscillatory behavior, implying that the qubit undergoes less than a quarter of a Rabi cycle during the experiment duration. The excitation probability becomes:

$$P_e(t) \approx \frac{1}{12}\omega_q C_\Sigma \rho_{\rm DM} l^2 k^2 \epsilon^2 t^2. \tag{3.26}$$

In Eq. 3.26, we also assumed the isotropy of the DM-induced field, taking the average

$$\frac{1}{4\pi}\int_0^{2\pi} d\varphi \int_0^{\pi} \cos(\Theta)^2 \sin(\Theta) d\Theta = \frac{1}{3}, \tag{3.27}$$

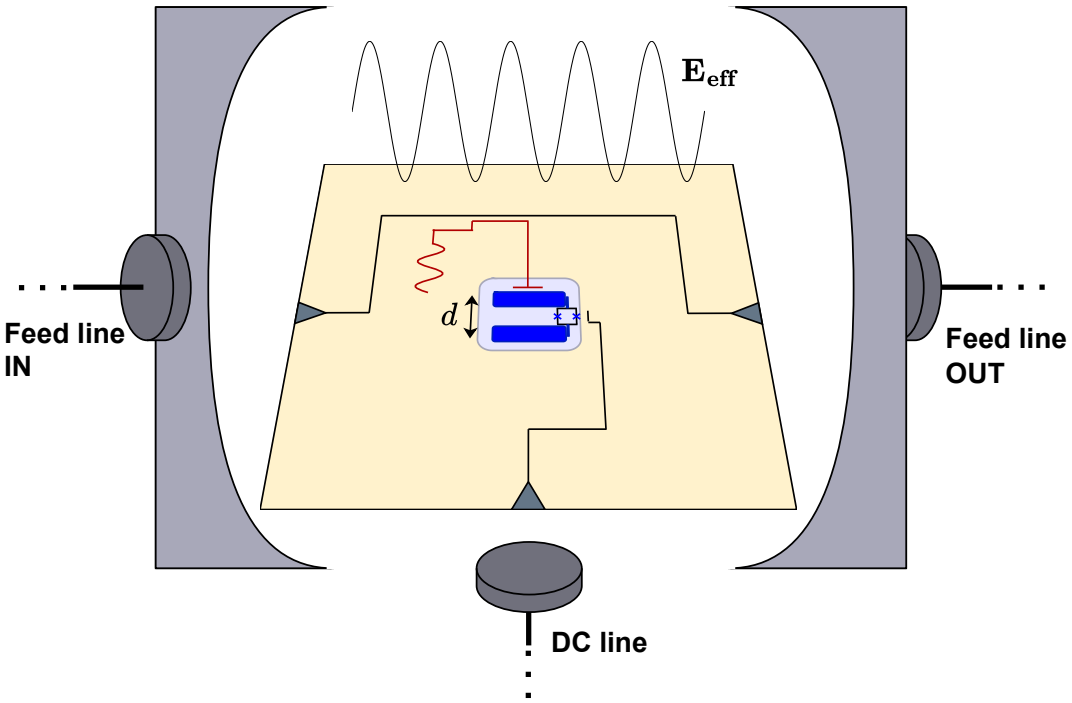

FIGURE 3.3: Representation of a 2D direct detection experiment suitable for dark photon searches. The effective electric field in the cavity $\mathbf{E}_{\text{eff}}$ present inside the metallic sample holder (acting as a far-detuned cavity) drives the qubit (blue) time evolution. The qubit is read dispersively through a CPW resonator (red) coupled to a feed line. A DC line biases the transmon SQUID to probe different frequency ranges. The dipole length is indicated as d.

with φ the azimuthal angle.
Numerically, and in terms of practical units for an experiment, the excitation probability can be written as

$$P_e(t) \approx 0.04k^2 \left(\frac{f_q}{1\,\text{GHz}}\right)\left(\frac{C_\Sigma}{0.1\,\text{pF}}\right)\left(\frac{\rho_{\text{DM}}}{0.45\,\text{GeV/cm}^3}\right) \times \left(\frac{l}{100\,\mu\text{m}}\right)^2\left(\frac{\epsilon}{10^{-11}}\right)^2\left(\frac{t}{100\,\mu\text{s}}\right)^2. \tag{3.28}$$

Because the dark-matter drive carries an unknown initial phase α relative to the qubit's own phase reference, the resulting Rabi oscillation of population between $|0\rangle$ and $|1\rangle$ acquires an arbitrary phase offset. Equivalently, on the Bloch sphere, the state is rotating about an axis in the $\hat{x}\hat{y}$-plane at an angle α from $\hat{x}$. This is irrelevant to the evaluation of $P_e(t)$ in this experiment, but it becomes an important element to consider when adding gate sequences that act before or after the DM drive (see Sec. 4.1).

Axion and ALPs direct detection

The presence of an axion-like field modifies the dynamics of the electromagnetic vector potential A_μ so that it can be described with the Lagrangian:

$$\mathcal{L} = \frac{1}{2}\partial_\mu \mathbf{A}\partial^\mu \mathbf{A} + g_{a\gamma\gamma}\partial_t a\mathbf{A}\cdot\mathbf{B}_0, \tag{3.29}$$

with $\mu = 0, 1, 2, 3$, where $\mu = 0$ refers to the time dimension and $\mu = 1, 2, 3$ to the spatial components, and the derivative notation is equivalent to:

$$\partial_\mu = \left(\frac{\partial}{\partial_t}, \quad \frac{\partial}{\partial_1}, \quad \frac{\partial}{\partial_2}, \quad \frac{\partial}{\partial_3}\right)^T. \tag{3.30}$$

In Eq. 3.29, the following gauge conditions are applied:

$$\nabla \cdot \mathbf{A} = 0; \qquad A_0 = 0. \tag{3.31}$$

The vector $\mathbf{A}$ contains the three spatial components ($\mu = 1, 2, 3$) of the gauge field. The axion potential a affects the system's dynamics when a magnetic field $B_0 \neq 0$ exists, which we assume to be spatially homogeneous and constant over time. An alternative view of the effect of the axion field is given by considering the contribution of the axion to the electromagnetic current density [188], which acts as a wave source. In the absence of background electric fields, this contribution is:

$$\mathbf{J}_a = -g_{a\gamma\gamma}\mathbf{B}_0\partial_t a. \tag{3.32}$$

Similarly to the dark photon case, we parametrize the axion field as a coherent oscillation with amplitude a_0 and mass term m_a:

$$a(t) = a_0 \cos(m_a t) \tag{3.33}$$

Solving Maxwell's equations inside a cavity with modes m, considering that the electric field $\mathbf{E}$ and $\mathbf{A}$ are conjugate variables and that $\mathbf{E} = -\partial_t \mathbf{A}$, gives

$$\hat{\mathbf{A}}(t, \mathbf{x}) = -\sum_m \frac{1}{\sqrt{2\omega_m}} \left(\hat{a} + \hat{a}^\dagger\right) \mathbf{E}_m(\mathbf{x}), \tag{3.34}$$

$$\hat{\mathbf{E}}(t, \mathbf{x}) = -\sum_m \sqrt{\frac{\omega_m}{2}} \left(\hat{a} - \hat{a}^\dagger\right) \mathbf{E}_m(\mathbf{x}), \tag{3.35}$$

where $\omega_m/2\pi$ is the mode frequency and $\mathbf{E}_m$ is the electric field spatial profile normalized such that

$$\int \mathbf{E_n}(\mathbf{x}) \cdot \mathbf{E_m}(\mathbf{x}) d^3\mathbf{x} = \delta_{nm}. \tag{3.36}$$

By solving for the time evolution of $\hat{a}$ and $\hat{a}^\dagger$ in the Heisenberg picture and substituting into Eq. 3.35, one obtains

$$\hat{\mathbf{E}}(t, \mathbf{x}) = \cos(m_a t) \sum_m \left(\frac{m_a^2}{m_a^2 - m_m^2} g_{a\gamma\gamma} a_0 \mathbf{E}_m(\mathbf{x}) \int \mathbf{E}_m(\mathbf{x}') \mathbf{B}_0 d^3\mathbf{x} \right), \tag{3.37}$$

which, by choosing the electric field orientation to be along the $\hat{z}$-axis, can be reparameterized as

$$\hat{\mathbf{E}}(t, \mathbf{x}) = \cos(m_a t) a_0 g_{a\gamma\gamma} |\mathbf{B}_0| k\hat{z}. \tag{3.38}$$

The term k is a package coefficient which, as in the dark photon case, can be assumed to be of order unity. With Eq. 3.38 being in the same form as for the dark photon case (Eq. 3.11), the derivation of the qubit dynamics remains unchanged, resulting in an

excitation probability over time of

$$P_e(t) \approx 0.11k^2 \left(\frac{m_a}{1\,\mu\text{eV}}\right)^{-1} \left(\frac{C_\Sigma}{0.1\,\text{pF}}\right) \left(\frac{\rho_{\text{DM}}}{0.45\,\text{GeV/cm}^3}\right) \times \left(\frac{l}{100\,\mu\text{m}}\right)^2 \left(\frac{B_0}{1\,\text{T}}\right)^2 \left(\frac{g_{a\gamma\gamma}}{10^{-10}\,\text{GeV}^{-1}}\right)^2 \left(\frac{t}{100\,\mu\text{s}}\right)^2 . \tag{3.39}$$

A fundamental challenge for the axion case with respect to the dark photon, as for the QND detection scheme, is the presence of a magnetic field. However, for direct detection experiments, the field must necessarily be present on the qubit region. Using thin-film Al/AlOx/Al junctions, transmon qubits are reported to have coherence times that stay above 1 µs up to fields approaching 1 T, when the field is parallel to the qubit plane (with a perpendicular stray component of a few mT) [177]. Other studies involve hybrid nanowire superconductor-semiconductor-superconductor junctions, creating transmon qubits with a decay and dephasing time of a few-hundreds ns in a 1 T magnetic field aligned with the wire [189]. Transmon qubits with graphene-based junctions exist [190], but addressing their limited coherence remains a challenge.

3.2.2 Experimental considerations for direct detection

The direct detection technique benefits from a considerably reduced technological overhead with respect to other qubit-based detectors, especially for the dark photon, as the required setup is essentially the same as in quantum computing applications. A schematic representation of a possible 2D architecture compatible with the experiment is depicted in Fig. 3.3. Moreover, a frequency-tunable transmon enables fast and easier broadband (at least a few hundred MHz) probing compared to experiments using tunable high-Q cavities. The latter typically result in competitive exclusion limits in terms of ϵ or $g_{a\gamma\gamma}$, but only for narrow frequency bands ($\ll 1$ MHz), meaning that the experiment must be repeated several times, probing several small frequency intervals to carry out a broadband search. Another notable advantage of direct detection is that the excitation probabilities over time, $P_e(t)$, do not depend on the cavity volume. In particular, the DM-induced power in a cavity grows with its volume (for instance, see Eq. 1.3). However, the volume of the cavity reduces at higher frequencies, decreasing the signal-to-noise ratio in cavity-haloscope experiments as the cavity shrinks. Fig. 3.4 illustrates the principles of a direct detection search experiment, based on the presence of a continuous, low-power Rabi drive induced by dark matter, summarized in the following steps:

1. Prepare the qubit in $|0\rangle$.
2. Let the qubit evolve for a time τ.
3. Measure the qubit, which collapses either in $|0\rangle$ or $|1\rangle$.
4. Register the outcome.

Steps 1 - 4 are repeated multiple times to estimate the qubit excitation probability for a fixed frequency. The experiment is then repeated at different flux biases, varying the qubit frequency to search for the resonant qubit-DM condition. The experimental signature consists of an excess of $|1\rangle$ state outcomes for a particular frequency. Upon ruling out spurious effects introduced by the experimental setup and on-chip impurities, such a resonant behavior may be explained by the presence of a beyond-SM oscillating electric field.

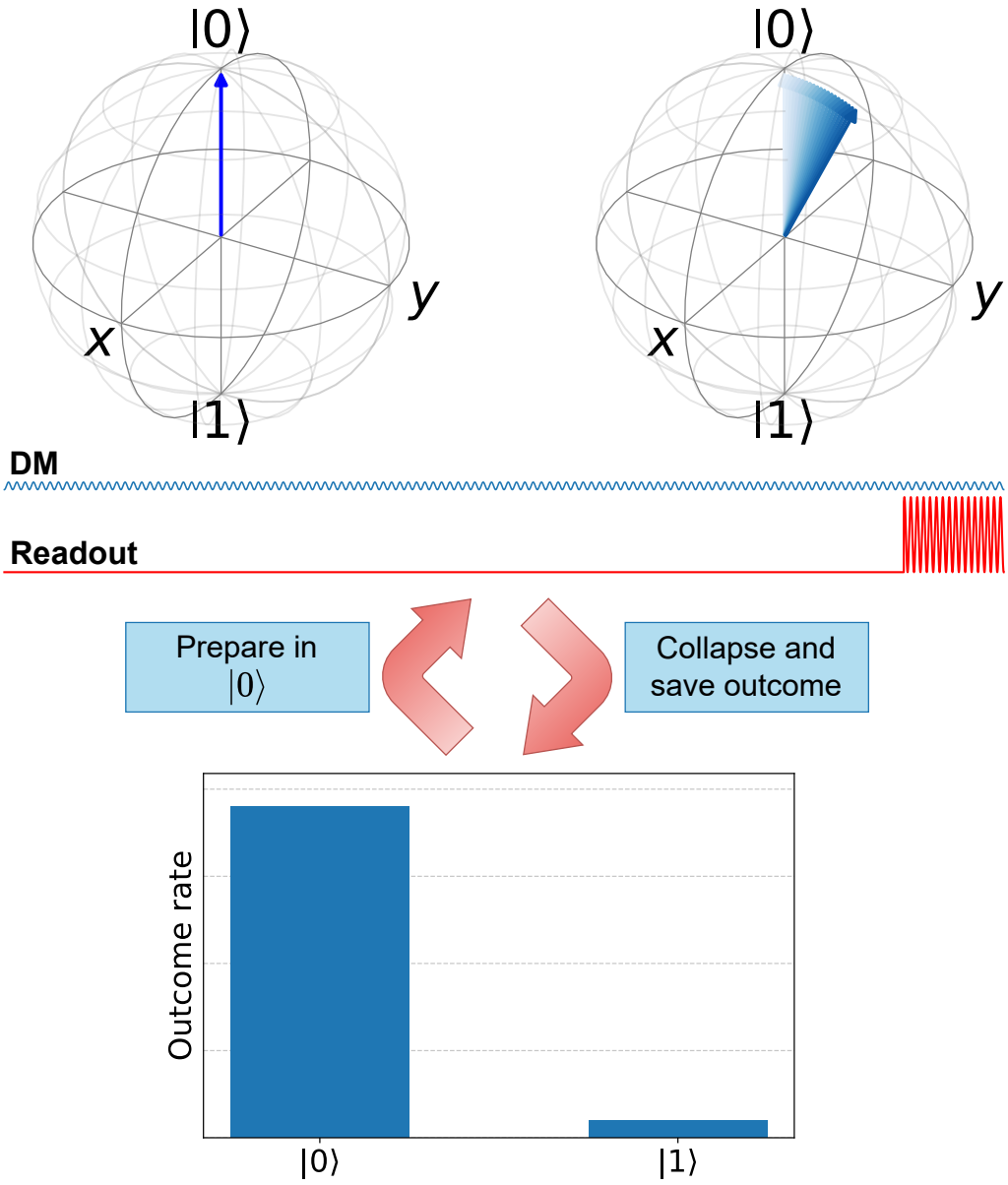

FIGURE 3.4: Rabi oscillation sampling from a qubit continuously interacting with a resonant electromagnetic wave induced by dark matter (dark photon, axion, or ALPs). From left to right (top), the qubit is prepared in $|0\rangle$ and undergoes a slow Rabi evolution. After waiting for a certain time, the qubit is measured, and the outcome populates the histogram (bottom). The qubit is then reinitialized in $|0\rangle$ and the cycle repeats several times, estimating the observed excitation probability. The blue and red signals represent the continuous action of the field to detect and the readout pulse, respectively.

Noise and dark counts

An important consideration is that Eqs. 3.28 and 3.39 do not account for the qubit's decoherence, which would damp the Rabi oscillation, resulting in a weaker signal to observe. Also, the wave-like dark matter coherence time τ_{DM} is not considered, which depends on the virial velocity dispersion v_{DM} and the mass of the considered particle m:

$$\tau_{\mathrm{DM}} \sim \frac{1}{m v_{\mathrm{DM}}^2}, \tag{3.40}$$

where $v_{\mathrm{DM}} \sim 10^{-3}$ in units of c [191]. For $m \sim 20$ μeV, roughly corresponding to $\omega/2\pi \sim 5$ GHz, we obtain $\tau \sim 100$ μs, which is similar to time-averaged state-of-the-art transmon coherence times in 2D architectures. Other detrimental effects to the experimental sensitivity are thermal excitations, readout error, and initial state preparation error.

- **Thermal excitations:** Cooper pairs obey the Bose-Einstein statistics, meaning that for a finite temperature T, the probability of occupying the state $|n\rangle$ of a transmon is

$$P_n^{\mathrm{th}} = \frac{e^{E_n/k_B T}}{Z}, \tag{3.41}$$

where E_n is the mode energy, k_B the Boltzmann constant, and Z is the partition function defined as:

$$Z = \sum_{m=0}^{\infty} e^{-E_m/k_B T}. \tag{3.42}$$

At cryogenic temperatures, especially the ones reached by dilution refrigerators < 50 mK, the populations of $n > 1$ states can be safely ignored for typical transmon frequencies ($\hbar\omega_q \ll k_B T$), therefore:

$$P_e^{\mathrm{th}} \approx \frac{1}{e^{\hbar\omega_q/K_B T} + 1}. \tag{3.43}$$

Despite modern dilution refrigerators achieving mixing chamber temperatures below 10 mK, reported effective transmon qubit temperatures usually saturate around $\sim$ 30 - 80 mK [192, 193], while $\sim$ 20 mK have been reported for fluxoniums [194]. The effective qubit temperature could be further reduced by implementing techniques such as sideband cooling [195]. This saturation effect can be attributed to imperfect thermalization, cable-mediated heat transfer, and radiative couplings. For $\omega_q/2\pi = 5$ GHz an effective temperature of $T = 35$ mK translates to a thermal population of $P_e^{\mathrm{th}} \approx 1.1 \times 10^{-3}$. When a qubit is initialized in $|0\rangle$ (hence P_e^{th} resets to 0), it will reach the thermal equilibrium with a time constant equal to the relaxation rate T_1.

- **Readout error:** As mentioned in Subsec. 2.2.2, even state-of-the-art high-fidelity dispersive readout possesses an error rate between 10^{-2} and 10^{-3}, due to an effective IQ-plane overlap between $|0\rangle$ and $|1\rangle$ distribution, and non-computational state leakage. More precisely, false-positives (i.e. measuring $|1\rangle$ when the qubit collapsed in $|0\rangle$) would contribute dark counts, and false-negatives (i.e. measuring $|0\rangle$ when the qubit collapsed in $|1\rangle$) would cause us to miss true excitations. The combined action of the two effects on the observed excitation probability P_e^{obs} can be modeled as follows:

$$P_e^{\mathrm{obs}} = (1 - r_{\mathrm{FN}}) P_e^{\mathrm{true}} + r_{\mathrm{FP}}(1 - P_e^{\mathrm{true}}), \tag{3.44}$$

where P_e^{true} is the true qubit excitation probability and r_{FN} and r_{FP} are the false-negative and false-positive probabilities.

- **State preparation error:** A crucial aspect of the experiment is the ability to prepare the qubit in $|0\rangle$ with the highest possible fidelity. A qubit collapsing in $|1\rangle$ instead of $|0\rangle$ will undergo a phase-shifted Rabi oscillation that impacts the excitation probability sampling, thus adding background counts. Transmon state *reset* techniques have been proposed, leveraging measurement-conditioned operations [196], or other drive protocols [197, 198], reducing the residual excitation probability to 2×10^{-3}. Alternatively, flux modulation in a tunable transmon can be leveraged to transfer the qubit excitation to its readout resonator, achieving residual excitation probabilities below 1×10^{-3} [199]. It is important to note, however, that this strategy relies on sufficient flux tunability of the transmon to bring its transition frequency close to that of the readout resonator. Following the reset operation, a large qubit-resonator detuning must be restored to suppress Purcell decay effectively during the dark matter-driven Rabi oscillation. Therefore, a tunability range of a few GHz is required. This large tunability comes at the cost of reduced qubit dephasing times when operating away from flux sweet spots (see Subsec. 2.1.3), increasing the oscillation damping.

The modeling of the noise effects discussed above, along with frequency detuning between the dark field and the qubit, is explored in Chapter 4. Additional factors, such as fluctuations and potential long-term drift in the refrigerator temperature, as well as variations in readout and drive fidelities, also influence the experimental results. However, analyzing and mitigating these effects falls outside the scope of this thesis, as they depend strongly on the specifics of the experimental setup.
Fig. 3.5 presents a simulated Monte Carlo dark photon search experiment using realistic transmon design parameters. Although the simulation does not account for many of the noise effects discussed in this section, it clearly shows a peak in excitation counts when the resonance condition is met. The histogram was generated setting a kinetic mixing strength value as low as $\epsilon = 2 \times 10^{-12}$, providing a preliminary estimate of the sensitivity achievable by the direct detection technique. Nevertheless, the sensitivity reached in a direct detection experiment is not expected to necessarily exceed that of next-generation cavity or haloscope detectors and sub-SQL (such as QND detection) techniques.
The potentialities of direct detection remain to be fully addressed, as they heavily depend on delicate and generally hard-to-replicate parameters (such as the qubit decay and dephasing rates), together with the qubit design, which determines C_Σ and the effective dipole length l.

3.3 Multi-qubit direct detection

Similarly to the QND detection case, it is possible to leverage entangled qubit states to achieve a significant experimental advantage. Following the scheme proposed in [200], a multi-qubit entangled state is prepared, which evolves coherently under the coupling to the dark matter field for a duration τ. After this interaction period, a decoding sequence of quantum gates is applied to map the accumulated phase information from all the qubits onto a single qubit, which is then measured. The resulting excitation probability exhibits oscillations that are significantly faster than those of a single-qubit experiment. Consequently, in the regime where τ is much shorter than the Rabi period, the measured qubit's excitation probability is enhanced, amplifying

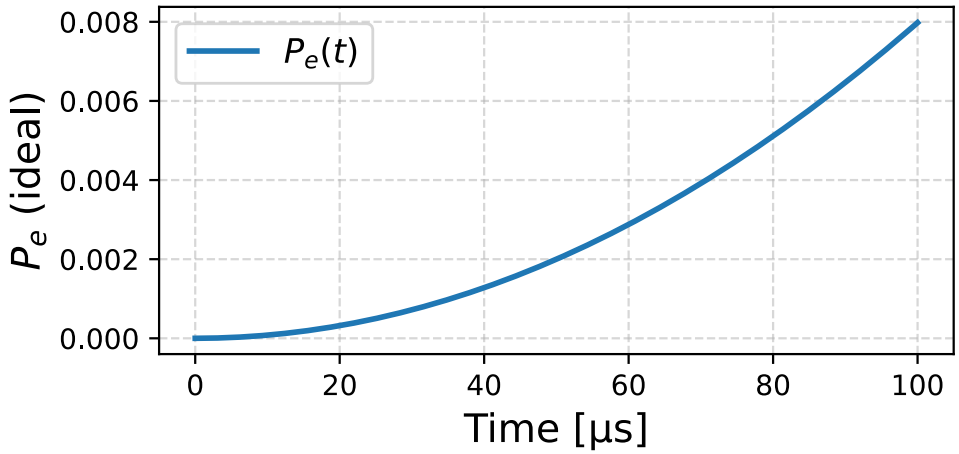

(A) Ideal excitation probability.

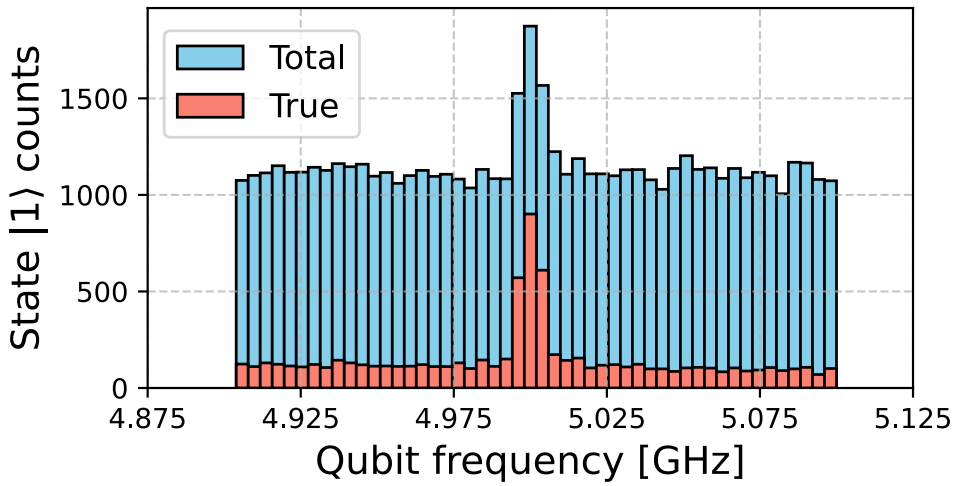

(B) Monte Carlo-generated experiment.

FIGURE 3.5: Simulated dark photon experiment, setting $\epsilon = 2 \times 10^{-12}$, $C_\Sigma = 100$ fF, $m_X = 5$ GHz, $\rho_{\mathrm{DM}} = 0.45$ GeV/cm^3, and $l = 100$ μm and assuming infinite qubit and DM coherence and perfect state preparation. (A) Ideal qubit excitation probability, without including thermal excitation and readout error rates. (B) The Monte Carlo-generated search experiment includes the thermal population at $T = 35$ mK and a readout error probability set to 0.01. The true excitations collected in the red histogram include the thermal background (the continuous distribution) and the dark photon signal (the overlapping peak).

the signal strength.
Considering a single qubit on resonance with DM, the unitary evolution of the quantum state under the RWA is

$$U_{\mathrm{DM}}(t) = \begin{pmatrix} \cos(\eta t) & ie^{-i\alpha}\sin(\eta t) \\ ie^{i\alpha}\sin(\eta t) & \cos(\eta t) \end{pmatrix}, \tag{3.45}$$

where η is defined in Eq. 3.16 for dark photon-induced oscillations. Without loss of generality, the following derivation can be extended also to axion-induced oscillations. The term α introduced in Subsec. 3.2.1 corresponds to the phase difference between the DM-induced drive and the qubit's phase convention. This phase is unknown, but for simplicity, we assume $\alpha = 0$ for a preliminary derivation of the multi-qubit enhancement scheme. In this case, the eigenstates of $U_{\mathrm{DM}}(t;\alpha=0)$ are

$$|\psi_\pm\rangle = \frac{1}{\sqrt{2}}\left(|0\rangle \pm |1\rangle\right), \tag{3.46}$$

with eigenvalues $e^{\pm i\eta t}$. Following the derivation described in [200], we consider n transmon qubits with the same transition frequency $\omega_q/2\pi$, each prepared in $|\psi_\pm\rangle$. The overall time evolution $U_{\mathrm{DM}}^{\otimes n}(t;\alpha=0)$ acts on $|\psi_\pm\rangle$ as:

$$U_{\mathrm{DM}}(t;\alpha=0)^{\otimes n}\,|\psi_\pm\rangle^{\otimes n} = e^{\pm in\eta t}\,|\psi_\pm\rangle^{\otimes n}. \tag{3.47}$$

By implementing the encoding gate sequence of the quantum circuit shown in Fig. 3.6, we end up in the state

$$|\Psi_1\rangle = \frac{1}{\sqrt{2}}\left(|\psi_+\rangle^{\otimes n} + |\psi_-\rangle^{\otimes n}\right), \tag{3.48}$$

which, after evolving under $U_{\mathrm{DM}}^{\otimes n}(t;\alpha=0)$, becomes:

$$|\Psi_2\rangle = U_{\mathrm{DM}}(t,\alpha=0)^{\otimes n}\,|\Psi_1\rangle = \frac{1}{\sqrt{2}}\left(e^{in\eta t}\,|\psi_+\rangle^{\otimes n} + e^{-in\eta t}\,|\psi_-\rangle^{\otimes n}\right). \tag{3.49}$$

The decoding gate sequence in Fig. 3.6 consists of applying a sequence of CX gates in reverse order with respect to the encoding sequence. By knowing that

$$\mathrm{CX}_{10}\left(|\psi_+\rangle \otimes |\psi_+\rangle\right) = \left(|\psi_+\rangle \otimes |\psi_+\rangle\right), \tag{3.50}$$

and

$$\mathrm{CX}_{10}\left(|\psi_-\rangle \otimes |\psi_-\rangle\right) = \left(|\psi_-\rangle \otimes |\psi_+\rangle\right), \tag{3.51}$$

the decoding sequence acts on $|\Psi_2\rangle$ by disentangling the multi-qubit state:

$$\begin{aligned} |\Psi_3\rangle &= \frac{1}{\sqrt{2}}\left(e^{in\eta t}\,|\psi_+\rangle + e^{-in\eta t}\,|\psi_-\rangle\right) \otimes |\psi_+\rangle^{\otimes(n-1)} \\ &= \left(\cos(\eta n t)\,|0\rangle + i\sin(\eta n t)\,|1\rangle\right) \otimes |\psi_+\rangle^{\otimes(n-1)}. \end{aligned} \tag{3.52}$$

In other words, all the qubits end up in the $|\psi_+\rangle$ state except the first one, which undergoes an effective Rabi oscillation that is accelerated by a factor n^2. In the limit $n\eta t \ll 1$, the excitation probability becomes:

$$P'_e(t,\alpha=0) \approx n^2\eta^2 t^2. \tag{3.53}$$

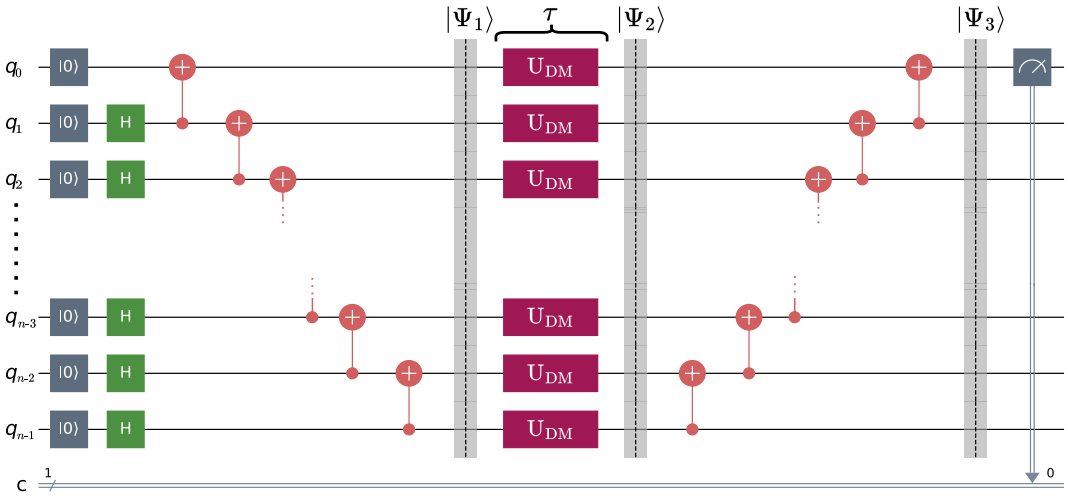

FIGURE 3.6: Entangled quantum circuit for enhanced DM detection. A system of n qubits is prepared in state $|\Psi_1\rangle$ through an encoding process. This state then evolves over a time interval τ under the influence of DM, represented by the unitary operator U_{DM}, resulting in state $|\Psi_2\rangle$. The evolved state is decoded (disentangled) to extract information about the DM interaction, mapping the relevant information to q_0 in state $|\Psi_3\rangle$.

Eq. 3.53 can be compared with a system of n isolated qubits undergoing Rabi oscillations with an excitation probability $P_e(t)$ given by Eq. 3.28. The probability of observing at least one excitation in the system is $nP_e(t)$, which means that the experiment with n coupled qubits would surpass the standard one by a factor n in terms of the number of signal events.
For a more general derivation, relaxing the $\alpha = 0$ condition, we start by expanding $U_{\text{DM}}(t,\alpha)$ to the first order in ηt, which is valid for $\eta\tau \ll 1$:

$$\begin{aligned} U_{\text{DM}}(t,\alpha) &= \mathrm{I} + \begin{pmatrix} 0 & ie^{-i\alpha}\eta t \\ ie^{i\alpha}\eta t & 0 \end{pmatrix} + \mathcal{O}(\eta^2 t^2) \\ &= \mathrm{I} + i\eta t\left(e^{-i\alpha}\,|0\rangle\langle 1| + e^{i\alpha}\,|1\rangle\langle 0|\right) + \mathcal{O}(\eta^2 t^2). \end{aligned} \tag{3.54}$$

In terms of Pauli matrices, and dropping the $\mathcal{O}(\eta^2 t^2)$ term:

$$\begin{aligned} U_{\text{DM}}(t,\alpha) &\approx \mathrm{I} + i\eta t\left[\cos(\alpha)\left(|0\rangle\langle 1| + |1\rangle\langle 0|\right) + i\sin(\alpha)\left(|1\rangle\langle 0| - |0\rangle\langle 1|\right)\right] \\ &= \mathrm{I} + i\eta t\left(\cos(\alpha)\sigma_x + \sin(\alpha)\sigma_y\right). \end{aligned} \tag{3.55}$$

The time evolution on state $|\Psi_1\rangle$ is

$$U_{\text{DM}}^{\otimes n}(t,\alpha) \approx \mathrm{I} + i\eta t\sum_{i=1}^{n}\left(\cos(\alpha)\sigma_x^i + \sin(\alpha)\sigma_y^i\right), \tag{3.56}$$

where σ_x^i and σ_y^i are the respective Pauli matrices acting on the i-th qubit. Using equations

$$\sigma_x\,|\psi_\pm\rangle = \pm\,|\psi_\pm\rangle, \tag{3.57}$$

$$\sigma_y\,|\psi_\pm\rangle = \mp i\,|\psi_\mp\rangle, \tag{3.58}$$

the state $|\Psi_2\rangle$ becomes:

$$
\begin{aligned}
|\Psi_2\rangle &= U_{\mathrm{DM}}^{\otimes n}(t,\alpha)\,|\Psi_1\rangle \\
&= \frac{1}{\sqrt{2}}\Big[|\psi_+\rangle^{\otimes n} + |\psi_-\rangle^{\otimes n} + i\eta nt\big(\cos(\alpha)\,|\psi_+\rangle^{\otimes n} - i\sin(\alpha)\,|\psi_-\rangle^{\otimes n}\big) \\
&+ i\eta nt\big(-\cos(\alpha)\,|\psi_+\rangle^{\otimes n} + i\sin(\alpha)\,|\psi_-\rangle^{\otimes n}\big)\Big] \\
&= \frac{1}{\sqrt{2}}\left(\mathrm{I} + i\eta nt\cos(\alpha)\right)|\psi_+\rangle^{\otimes n} + \frac{1}{\sqrt{2}}\left(\mathrm{I} - i\eta nt\cos(\alpha)\right)|\psi_-\rangle^{\otimes n}.
\end{aligned}
\tag{3.59}
$$

By applying the decoding sequence to Eq. 3.59, we obtain

$$
\begin{aligned}
|\Psi_3\rangle = &\frac{1}{\sqrt{2}}\left(\mathrm{I} + i\eta nt\cos(\alpha)\right)|\psi_+\rangle \otimes |\psi_+\rangle^{\otimes(n-1)} \\
&+ \frac{1}{\sqrt{2}}\left(\mathrm{I} + -i\eta nt\cos(\alpha)\right)|\psi_-\rangle \otimes |\psi_+\rangle^{\otimes(n-1)},
\end{aligned}
\tag{3.60}
$$

which corresponds to Eq. 3.49 when expanding $e^{in\eta t}$ and $e^{-in\eta t}$ up to the first order in $in\eta t$ and up to a $\cos(\alpha)$ factor. Hence the excitation probability on the measured qubit is:

$$
P'_e(t,\alpha) \approx \cos^2(\alpha) n^2\eta^2 t^2. \tag{3.61}
$$

By taking the average of $\cos^2(\alpha)$ for a uniformly distributed $\alpha \in [0, 2\pi]$, we finally obtain the excitation probability:

$$
\bar{P}'_e(t) \approx \frac{1}{2} n^2\eta^2 t^2. \tag{3.62}
$$

Eq. 3.62 still holds the dependence n^2, preserving a signal enhancement factor of $n/2$ with respect to n single-qubit experiments.

Despite the remarkable sensitivity of the multi-qubit state prepared in $|\Psi_1\rangle$ to direct dark matter signals, three major experimental challenges limit the effectiveness of this enhanced detection scheme:

- **Limited coherence time:** An n-qubit maximally entangled state is more fragile than single-qubit states, with a coherence time roughly scaling as $1/n$ [201]. As a result, if the duration of the experiment τ is limited by the coherence of the n-qubit state rather than by the dark matter coherence τ_{DM}, any sensitivity gain from entanglement is erased. On the other hand, if τ_{DM} limits τ, the use of entanglement becomes beneficial.

- **State preparation infidelity:** Preparing n qubits in the state $|\Psi_1\rangle$ requires high-fidelity in implementing the CX operation for all the consecutive pairs of a qubit chain, which is generally challenging [175, 202].

- **All qubits are resonant:** The requirement of n coupled qubits maintained at the same transition frequency introduces challenges from the detector design perspective. The quantum device must be designed to suppress spurious crosstalk and unwanted resonant interactions, which is a non-trivial task. In addition, each qubit frequency must be tuned and stabilized for the duration of the experiment with great precision to ensure resonance.

These drawbacks add to the experimental challenges of the single-qubit direct detection experiment and motivate the search for alternative methods to achieve sensitivity

advantages from entangled states. The method proposed in this thesis is detailed in Chapter 4 and is designed to be fully compatible with modern hardware limitations. The chapter focuses on describing the enhancement protocol and modeling the expected advantage factor with respect to the single-qubit search in the presence of noise.

Chapter 4

Enhanced and noise-resilient direct DM detection

This thesis is dedicated to developing enhanced direct dark matter detection strategies, benefiting from entangled qubit states, while addressing the typical limitations of quantum hardware in terms of gate fidelity, readout error, and scalability. Unlike the enhancement protocol described in Sec. 3.3, where all the qubits involved are exposed to the coherent drive induced by dark matter for as long as possible, this work introduces a novel architecture comprising qubits designed as *sensing* (the ones exposed to DM) and *ancilla* qubits. Ancilla qubits have the role of expanding the Hilbert space of the computational quantum system, enabling gate-based protocols that map the excitation probability accumulated in the sensing qubits into another observable that is easier to sample. This technique differs fundamentally from previous ones reported in the literature, and it effectively mitigates certain sources of dark counts, as elaborated in the following sections.

4.1 Gate-based detection enhancement

The general idea of the ancilla-assisted protocol revolves around finding a convenient set of gates that implement a transformation $\mathcal{T}_{\text{enh}}$:

$$|\Psi_3\rangle = \mathcal{T}_{\text{enh}}\left(|\Psi_2\rangle\right), \tag{4.1}$$

where, consistently with the notation adopted in Sec. 3.3, we define $|\Psi_1\rangle$ as the initial state before the DM interaction, $|\Psi_2\rangle$ as the state $U_{\text{DM}}^{\otimes n} \times \mathrm{I}^{\otimes m} |\Psi\rangle$ (with n and m the number of sensing and ancilla qubits, respectively), and $|\Psi_3\rangle$ the final state after applying the enhancement protocol.
Restricting, for simplicity, to the case with one sensing qubit and one ancilla ($n = 1$, $m = 1$), the transformation $\mathcal{T}_{\text{enh}}$ maps the excitation probability of the sensing qubit P_e into an excitation probability P'_e. Supposing that we have run an experiment that yielded an excitation probability P_e^{obs} for a single qubit frequency, we introduce the two hypotheses to be statistically discriminated:

- H_0: null hypothesis – DM interaction was not observed.
- H_1: signal hypothesis – DM interaction was observed with strength parameter ϵ (in the dark photon case), or $g_{a\gamma\gamma}$ (in the axion case) at the qubit frequency.

For simplicity, we focus on dark photon detection experiments, which do not require external magnetic fields acting on the qubit detector, referring only to the kinetic mixing strength ϵ as a signal strength parameter from now on. We expect $P_e^{\text{obs}}(\epsilon|H_1) \geq P_e^{\text{obs}}(H_0)$, where H_1 and H_0 coincide when $\epsilon = 0$, therefore, trivially, $P_e^{\text{obs}}(\epsilon = 0|H_1) =$

$P_e^{\text{obs}}(H_0)$. Also, since $P_e^{\text{obs}}(\epsilon|H_1)$ is expected to grow monotonically in ϵ because the true excitation probability is proportional to ϵ^2, we can write the observed excitation probability as a function of P_e given either H_0 or H_1, where the following equation holds:

$$P_e^{\text{obs}}(P_e > 0|H_1) > P_e^{\text{obs}}(H_0), \tag{4.2}$$

with

$$\lim_{\epsilon \to 0} P_e^{\text{obs}}(P_e|H_1) = P_e^{\text{obs}}(H_0). \tag{4.3}$$

To assess the sensitivity to the mixing strength ϵ, we need to perform a statistical test to discriminate whether the observed excitation probability is compatible with the null hypothesis. Generally, the larger the difference between the observed probabilities under H_0 and H_1, the smaller the number of measurements required to discriminate between the hypotheses. More specifically, the observed counts obey the binomial distribution, with standard deviation defined as:

$$\sigma_{P_e^{\text{obs}}} = \sqrt{\frac{P_e^{\text{obs}}\left(1 - P_e^{\text{obs}}\right)}{N}}. \tag{4.4}$$

Therefore, the experiment becomes sensitive in discriminating H_0 and H_1 when

$$P_e^{\text{obs}}(P_e|H_1) - P_e^{\text{obs}}(H_0) > \sigma_{P_e^{\text{obs}}}. \tag{4.5}$$

If we implement a transformation mapping the qubit's excitation probability to a different one, $f : P_e^{\text{obs}} \to \tilde{P}^{\text{obs}}$, such that

$$\tilde{P}^{\text{obs}}(P_e|H_1) - \tilde{P}^{\text{obs}}(H_0) > P_e^{\text{obs}}(P_e|H_1) - P_e^{\text{obs}}(H_0), \tag{4.6}$$

we obtain an experimental advantage, i.e. the same exclusion limit on ϵ can be achieved with a smaller number of measurements.

4.1.1 One sensing and one ancilla quantum circuit

A single qubit alone cannot satisfy the enhancement condition of Eq. 4.6 when using only gate-based operations. Geometrically, as depicted in Fig. 4.1, any single-qubit gate implements a fixed rotation on the Bloch sphere whose angles are set entirely by the gate's characteristics, rather than the initial state itself. The initial qubit state simply determines the initial point before rotation.

In order to implement the nontrivial, nonlinear transformations required by an enhancement protocol, we need to introduce at least one ancilla qubit. By entangling a sensing qubit with an ancilla and then performing a projective measurement on it, we partially collapse the joint Hilbert space. Depending on the outcome of this intermediate measurement, we can differentiate the following operations (post-selection). This measurement-induced nonlinearity belongs to techniques in quantum machine learning acting on quantum input data [11, 203]: unlike classical data, where information is always available and techniques such as *data reuploading* are possible [204], the input state is already encoded as a quantum state and inaccessible.

Considering a two-qubit system consisting of a sensing qubit coupled to an ancilla, we can implement a simple, yet powerful protocol described below, and shown in Fig. 4.2. The initial state is:

$$|\Psi_1\rangle = |0_{\text{A}} 0_{\text{S}}\rangle\,, \tag{4.7}$$

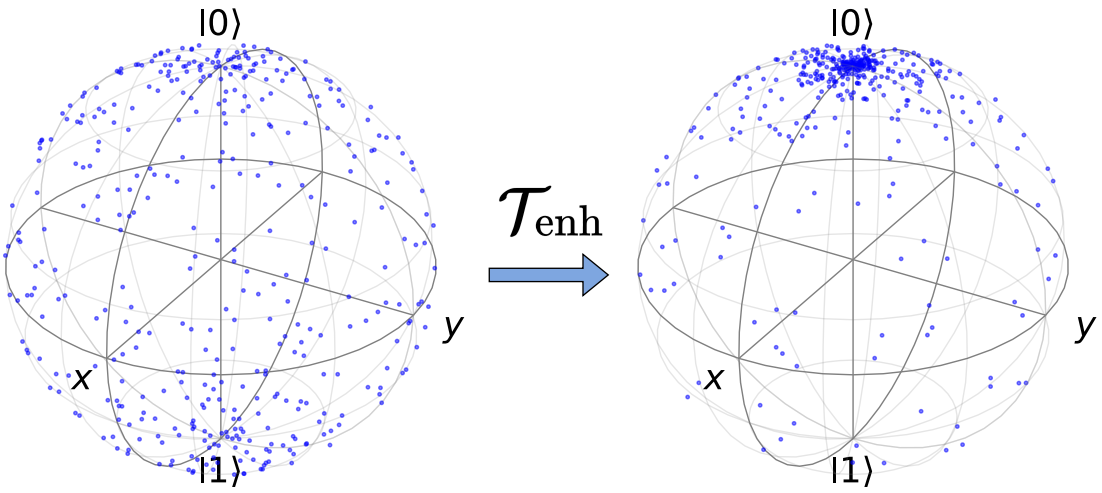

FIGURE 4.1: Non-trivial state vector transformation after applying the transformation $\mathcal{T}_{\text{enh}}$ with post-selection shown in Fig. 4.2, starting from a uniform surface distribution. The change in the state densities, higher around $|0\rangle$, indicates the non-linear nature of the transformation.

where we emphasize the position of the sensing (S) and ancilla (A) qubits in the overall state. After the action of DM for a time τ, the state becomes

$$|\Psi_2\rangle = U_{\text{DM}} |\Psi_1\rangle = \cos\left(\frac{\theta}{2}\right) |0_A 0_S\rangle + \sin\left(\frac{\theta}{2}\right) e^{i\alpha} |0_A 1_S\rangle . \tag{4.8}$$

We note that active state reset techniques can be leveraged to prepare the ancilla qubit in $|0_A\rangle$ right before the time interval τ ends (i.e. after the action of U_{DM}, see Fig. 4.2), to minimize state preparation errors. In $|\Psi_2\rangle$, θ and α follow the Bloch sphere representation, where θ is related to P_e and α is the DM-qubit phase difference.
By applying a CX gate targeting A and controlled on S,

$$\text{CX}_{\text{SA}} |\Psi_2\rangle = \cos\left(\frac{\theta}{2}\right) |0_A 0_S\rangle + \sin\left(\frac{\theta}{2}\right) e^{i\alpha} |1_A 1_S\rangle . \tag{4.9}$$

Then, flipping S by applying an X gate, we obtain

$$\text{X}_S\text{CX}_{\text{SA}} |\Psi_2\rangle = \cos\left(\frac{\theta}{2}\right) |0_A 1_S\rangle + \sin\left(\frac{\theta}{2}\right) e^{i\alpha} |1_A 0_S\rangle . \tag{4.10}$$

The next step is to apply a CRY gate with angle $\beta \in [0, \pi/2]$, with S as control and A as target, obtaining state $|\Psi_3\rangle$:

$$\begin{aligned} |\Psi_3\rangle &= \text{CRY}_{\text{SA}}\text{X}_S\text{CX}_{\text{SA}} |\Psi_2\rangle \\ &= \cos\left(\frac{\beta}{2}\right)\cos\left(\frac{\theta}{2}\right) |0_A 1_S\rangle + \sin\left(\frac{\beta}{2}\right)\cos\left(\frac{\theta}{2}\right) |1_A 1_S\rangle \\ &+ \sin\left(\frac{\theta}{2}\right) e^{i\alpha} |1_A 0_S\rangle . \end{aligned} \tag{4.11}$$

Finally, by post-selecting state $|1_A\rangle$ for the ancilla (i.e. the success condition), we de-

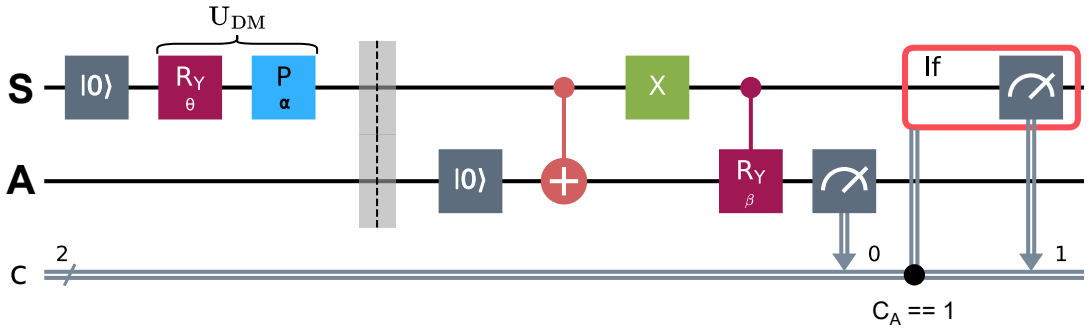

FIGURE 4.2: Quantum circuit describing an enhanced direct detection protocol using one sensing (S) qubit and one ancilla (A) qubit. The Rabi rotation induced by dark matter is modeled through an RY(θ) and a Phase gate of angle α. The ancilla measurement outcome is stored in the classical bit C_A and determines the protocol's success or failure status.

rive

$$|\Psi_3^s\rangle = \frac{\sin\left(\frac{\beta}{2}\right)\cos\left(\frac{\theta}{2}\right)|1_A 1_S\rangle + \sin\left(\frac{\theta}{2}\right)e^{i\alpha}|1_A 0_S\rangle}{\sqrt{\sin\left(\frac{\beta}{2}\right)^2\cos\left(\frac{\theta}{2}\right)^2 + \sin\left(\frac{\theta}{2}\right)^2}}. \tag{4.12}$$

The probability of finding the sensing qubit in $|0\rangle$ is therefore

$$\tilde{P} = \frac{\sin\left(\frac{\theta}{2}\right)^2}{\sin\left(\frac{\beta}{2}\right)^2\cos\left(\frac{\theta}{2}\right)^2 + \sin\left(\frac{\theta}{2}\right)^2}. \tag{4.13}$$

Since $P_e = \sin(\theta/2)^2$, we obtain the following:

$$\tilde{P} = \frac{P_e}{\sin\left(\frac{\beta}{2}\right)^2(1-P_e) + P_e}, \tag{4.14}$$

which, for small initial probabilities P_e, approximates $P_e \sin(\beta/2)^{-2}$. Recalling Eq. 4.3, in the ideal case, the condition in Eq. 4.6 is always satisfied with a speedup factor of $\sin(\beta/2)^{-2}$.
In the failure condition of the protocol, i.e. finding the ancilla in state $|0_A\rangle$ after measuring $|\Psi_3\rangle$, the state collapses into

$$\left|\Psi_3^F\right\rangle = |0_A 1_S\rangle\,, \tag{4.15}$$

which carries no information about the interaction with dark matter. The success probability of $|\Psi_3\rangle$ grows linearly in P_e:

$$\begin{aligned} P_{\text{success}} &= \sin\left(\frac{\beta}{2}\right)^2\cos\left(\frac{\theta}{2}\right)^2 + \sin\left(\frac{\theta}{2}\right)^2 \\ &= \sin\left(\frac{\beta}{2}\right)^2 + \cos\left(\frac{\beta}{2}\right)^2 P_e. \end{aligned} \tag{4.16}$$

For small initial probabilities P_e, as we would expect for DM-driven interactions (see Sec. 3.2), P_{success} is minimum. However, conveniently, the offset term $\sin\left(\frac{\beta}{2}\right)^2$ is never

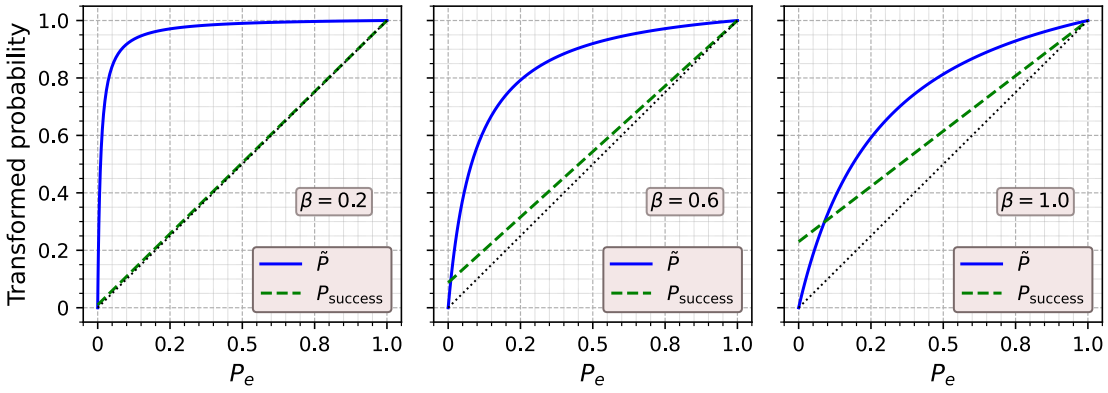

FIGURE 4.3: Probability $\tilde{P}$ of measuring the sensing qubit in $|0\rangle$ when the enhancement protocol succeeds (blue curve), and the protocol success probability P_{success} (green curve), for different values of the controlled-rotation parameter β.

zero for $\beta \neq 0$, meaning that the protocol can always run with a nonzero probability of success. The enhanced and success probability as a function of P_e are shown in Fig. 4.3.
Eq. 4.6 implies that an advantage is obtained when, for small P_e,

$$\frac{d\tilde{P}(P_e)}{dP_e} > 1. \tag{4.17}$$

In the protocol described in this Subsection, the condition in Eq. 4.17 holds for $\beta < \pi/2$, and, as β tends to zero, the variation of $\tilde{P}$ for small changes in P_e increases. On the other hand, lowering β also reduces P_{success}, making β a delicate parameter in balancing the sensitivity gain and the protocol success rate.
Another observation from Eq. 4.16 is that P_{success} depends on P_e, meaning that also the measurement of the ancilla qubit is sensitive to dark matter signal. Instead of completely rejecting failed attempts during post-selection, we can include this additional information in the analysis to further improve the estimate of P_e, by leveraging the ratio of successes and failures of the protocol itself. However, due to $dP_{\text{success}}/dP_e < 1$, the benefit of this added information to the overall sensitivity is expected to be modest.

After measuring the ancilla qubit, in the success condition, hence being in state $|\Psi_3^s\rangle$, we can apply an X rotation to the ancilla and the sensing qubits to end up in a state that has the same form of $|\Psi_2\rangle$, except for the different amplitudes associated to $|0_A 0_S\rangle$ and $|0_A 1_S\rangle$. It is natural to ask whether further advantage can be obtained by repeating the post-selection transformation multiple times. A straightforward calculation shows that, after m iterations, $\tilde{P}$ and P_{success} are given by

$$\tilde{P} = \frac{P_e}{\sin\left(\frac{\beta}{2}\right)^{2m}(1-P_e) + P_e}, \tag{4.18}$$

$$P_{\text{success}} = \prod_{k=1}^{m} \left[\frac{\sin\left(\frac{\beta}{2}\right)^{2k}(1-P_e) + P_e}{\sin\left(\frac{\beta}{2}\right)^{2(k-1)}(1-P_e) + P_e} \right]. \tag{4.19}$$

The advantage in the increased slope of $\tilde{P}$ is counterbalanced by the rapidly decreasing value P_{success}, as it is composed of all the individual success probabilities of a single

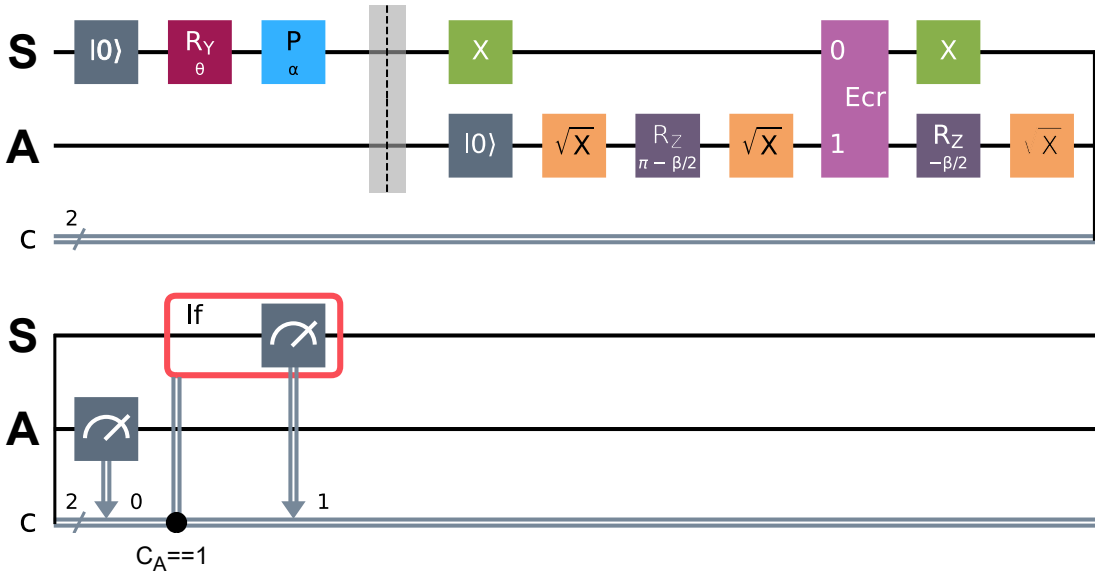

FIGURE 4.4: Quantum circuit equivalent to the one shown in Fig. 4.2, transpiled using the universal native gates set {X, SX, I, RZ, ECR}, featuring only one two-qubit gate.

iteration. In general, no benefit would be obtained by repeating the protocol more than once, even under an ideal noise-free condition.

We observe that the quantum circuit implementing the transformation contains only a few gates. To better underline the NISQ nature of this protocol, we recast the whole set of operations into an equivalent form using an example native gate set from existing quantum devices: {X, SX, I, RZ, ECR}. The circuit is shown in Fig. 4.4, and contains only one two-qubit gate. Due to the simplicity of this quantum circuit, the enhancement operation is compatible with modern quantum superconducting hardware capabilities, and the protocol here introduced can be considered fully NISQ-compatible. We note that another popular native gate set, i.e. {X, SX, I, RZ, CZ} can be used to rewrite the quantum circuit in terms of only one two-qubit CZ gate.

4.1.2 One sensing and two ancilla quantum circuit

Different gate and mid-circuit measurements useful for the detection experiment may be accessible by further increasing the available Hilbert space by leveraging two ancilla qubits. The measurement schemes reported in this Subsection were found by experimenting with different gate combinations. Despite not yielding a decisive sensitivity increase with respect to the two-qubit scheme proposed in Subsec. 4.1.1, they might be preferable to mitigate possible device limitations. Two protocols are presented below.

Concatenated enhancement protocol

A sensing qubit coupled to two ancillas can undergo the operation described in Fig. 4.5. The main idea is to distribute the enhancement operation across the two ancillas in a way that retrieves meaningful information when either only the second mid-circuit measurement or both return a success. Before the first mid-circuit

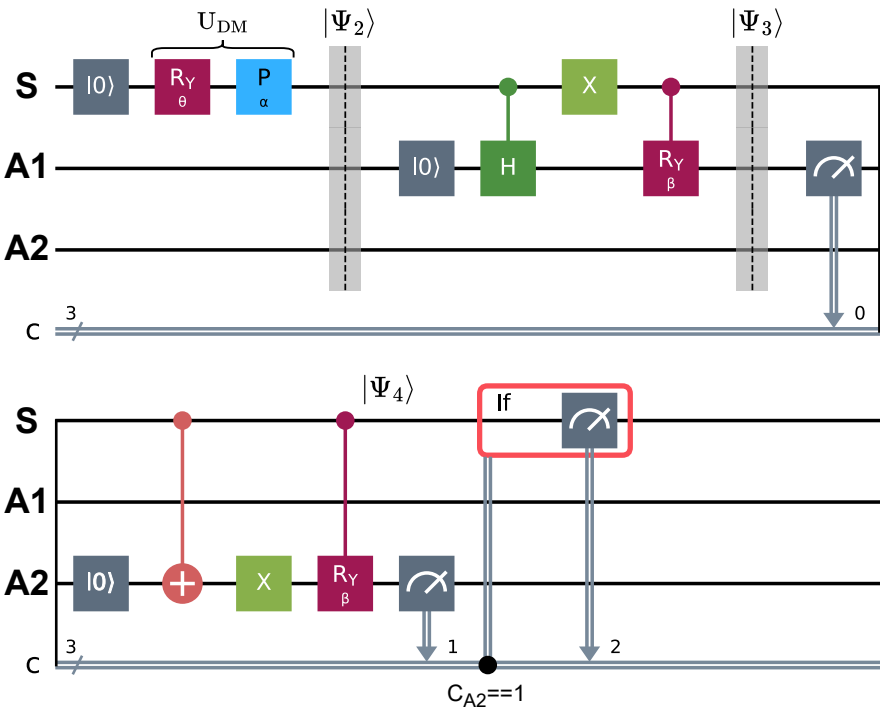

FIGURE 4.5: Quantum circuit describing an enhanced direct detection protocol using one sensing (S) and two ancilla (A1, A2) qubits. Two mid-circuit measurements create four success/failure combinations.

measurement, the quantum state is

$$\begin{aligned}|\Psi_3\rangle = &\cos\left(\frac{\beta}{2}\right)\cos\left(\frac{\theta}{2}\right)|0_{A2}0_{A1}1_S\rangle + \sin\left(\frac{\beta}{2}\right)\cos\left(\frac{\theta}{2}\right)|0_{A2}1_{A1}1_S\rangle \\ &+ \frac{1}{\sqrt{2}}\sin\left(\frac{\theta}{2}\right)e^{i\alpha}|0_{A2}0_{A1}0_S\rangle + \frac{1}{\sqrt{2}}\sin\left(\frac{\theta}{2}\right)e^{i\alpha}|0_{A2}1_{A1}0_S\rangle\,.\end{aligned} \tag{4.20}$$

After measuring the first ancilla qubit (A1), imposing the success condition leads to

$$\left|\Psi_3^S\right\rangle = \frac{\sin\left(\frac{\beta}{2}\right)\cos\left(\frac{\theta}{2}\right)|0_{A2}1_{A1}1_S\rangle + \frac{1}{\sqrt{2}}\sin\left(\frac{\theta}{2}\right)e^{i\alpha}|0_{A2}1_{A1}0_S\rangle}{\sqrt{\sin\left(\frac{\beta}{2}\right)^2\cos\left(\frac{\theta}{2}\right)^2 + \frac{1}{2}\sin\left(\frac{\theta}{2}\right)^2}}. \tag{4.21}$$

Instead, imposing the failure condition, we obtain

$$\left|\Psi_3^F\right\rangle = \frac{\cos\left(\frac{\beta}{2}\right)\cos\left(\frac{\theta}{2}\right)|0_{A2}0_{A1}1_S\rangle + \frac{1}{\sqrt{2}}\sin\left(\frac{\theta}{2}\right)e^{i\alpha}|0_{A2}0_{A1}0_S\rangle}{\sqrt{\cos\left(\frac{\beta}{2}\right)^2\cos\left(\frac{\theta}{2}\right)^2 + \frac{1}{2}\sin\left(\frac{\theta}{2}\right)^2}}. \tag{4.22}$$

Compared to the failure in the two-qubit scheme (Eq. 4.15), Eq. 4.22 retains information about U_{DM}. The states $\left|\Psi_3^S\right\rangle$ and $\left|\Psi_3^F\right\rangle$ evolve following the rest of the quantum circuit. The A1 success and failure conditions are described below.

- **A1 success:** right before measuring A2, the state is

$$|\Psi_4\rangle = \frac{\sin\left(\frac{\beta}{2}\right)\cos\left(\frac{\beta}{2}\right)\cos\left(\frac{\theta}{2}\right)|0_{A2}1_{A1}1_S\rangle}{\sqrt{\sin\left(\frac{\beta}{2}\right)^2\cos\left(\frac{\beta}{2}\right)^2\cos\left(\frac{\theta}{2}\right)^2+\sin\left(\frac{\beta}{2}\right)^4\cos\left(\frac{\theta}{2}\right)^2+\frac{1}{2}\sin\left(\frac{\theta}{2}\right)^2}} + \frac{\sin\left(\frac{\beta}{2}\right)^2\cos\left(\frac{\theta}{2}\right)|1_{A2}1_{A1}1_S\rangle+\frac{1}{\sqrt{2}}\sin\left(\frac{\theta}{2}\right)e^{i\alpha}|1_{A2}1_{A1}0_S\rangle}{\sqrt{\sin\left(\frac{\beta}{2}\right)^2\cos\left(\frac{\beta}{2}\right)^2\cos\left(\frac{\theta}{2}\right)^2+\sin\left(\frac{\beta}{2}\right)^4\cos\left(\frac{\theta}{2}\right)^2+\frac{1}{2}\sin\left(\frac{\theta}{2}\right)^2}}. \tag{4.23}$$

If A2 collapses in $|1_{A2}\rangle$ (A2 success), the final enhanced probability becomes

$$\tilde{P} = \frac{\frac{1}{2}P_e}{\sin\left(\frac{\beta}{2}\right)^4(1-P_e)+\frac{1}{2}P_e}, \tag{4.24}$$

characterized by a derivative of approximately $\sin(\beta/2)^{-4}/2$ for P_e close to zero. The success probability is

$$P_{\text{success}} = \frac{\sin\left(\frac{\beta}{2}\right)^4(1-P_e)+\frac{1}{2}P_e}{\sin\left(\frac{\beta}{2}\right)^2\cos\left(\frac{\beta}{2}\right)^2(1-P_e)+\sin\left(\frac{\beta}{2}\right)^4(1-P_e)+\frac{1}{2}P_e}, \tag{4.25}$$

which, for small β (to maximize the slope of $\tilde{P}$), scales like $\sin(\beta/2)^2$. If A2 collapses in $|0_{A2}\rangle$ (A2 fail), the resulting state carries no information about P_e.

- **A1 fail:** analogously, before measuring A2, the state is

$$|\Psi_4\rangle = \frac{\cos\left(\frac{\beta}{2}\right)^2\cos\left(\frac{\theta}{2}\right)|1_{A2}0_{A1}1_S\rangle}{\sqrt{\cos\left(\frac{\beta}{2}\right)^4\cos\left(\frac{\theta}{2}\right)^2+\cos\left(\frac{\beta}{2}\right)^2\sin\left(\frac{\beta}{2}\right)^2\cos\left(\frac{\theta}{2}\right)^2+\frac{1}{2}\sin\left(\frac{\theta}{2}\right)^2}} - \frac{\cos\left(\frac{\beta}{2}\right)\sin\left(\frac{\beta}{2}\right)\cos\left(\frac{\theta}{2}\right)|0_{A2}0_{A1}1_S\rangle+\frac{1}{\sqrt{2}}\sin\left(\frac{\theta}{2}\right)e^{i\alpha}|1_{A2}0_{A1}0_S\rangle}{\sqrt{\cos\left(\frac{\beta}{2}\right)^4\cos\left(\frac{\theta}{2}\right)^2+\cos\left(\frac{\beta}{2}\right)^2\sin\left(\frac{\beta}{2}\right)^2\cos\left(\frac{\theta}{2}\right)^2+\frac{1}{2}\sin\left(\frac{\theta}{2}\right)^2}}. \tag{4.26}$$

In the success condition of qubit A2, the final enhanced probability is

$$\tilde{P} = \frac{\frac{1}{2}P_e}{\cos\left(\frac{\beta}{2}\right)^4(1-P_e)+\frac{1}{2}P_e}. \tag{4.27}$$

In this case, the derivative in $P_e \approx 0$ becomes $\cos(\beta/2)^{-4}/2$, and the success probability is

$$\frac{\cos\left(\frac{\beta}{2}\right)^4(1-P_e)+\frac{1}{2}P_e}{\cos\left(\frac{\beta}{2}\right)^4(1-P_e)+\cos\left(\frac{\beta}{2}\right)^2\sin\left(\frac{\beta}{2}\right)^2(1-P_e)+\frac{1}{2}P_e}, \tag{4.28}$$

which scales like $\cos(\beta/2)$. If A2 collapses in $|0_{A2}\rangle$ (A2 fail), similarly to the previous case, the resulting state carries no information about P_e.

TABLE 4.1: Trade-off between sensitivity to P_e and the conditional success/failure outcomes mid-circuit.

Ancilla 1	Ancilla 2	$\frac{d\tilde{P}}{dP_e}$	Occurrence
Success	Success	Very high	Very unlikely
Fail	Success	Moderate	Moderate
Success	Fail	0	Moderate
Fail	Fail	0	Likely

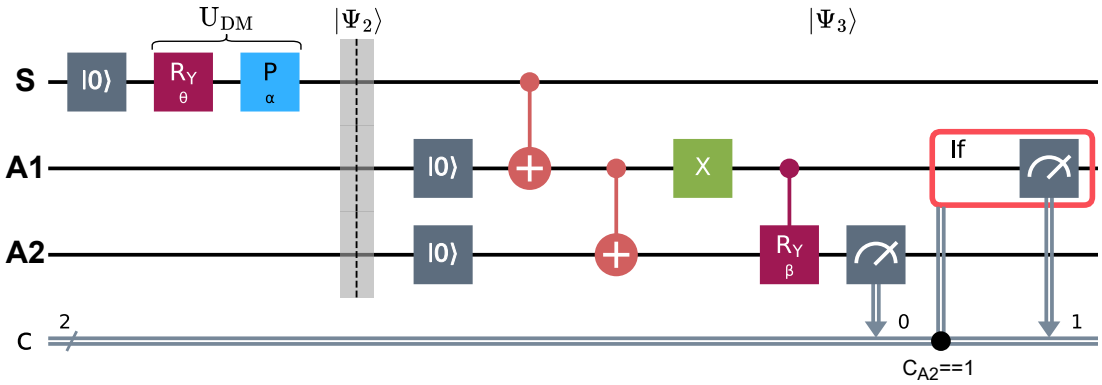

FIGURE 4.6: Enhanced direct detection protocol using one sensing (S) and two ancilla (A1, A2) qubits. Information from U_{DM} is retrieved without measuring the sensing qubit.

Overall, concatenating the enhancement protocol by performing two mid-circuit measurements on A1 and A2 leads to four possible configurations. Since, generally, β should be small to achieve an advantage (see Fig. 4.3), the tradeoffs between success probability and sensitivity to P_e can be roughly summarized as in Table 4.1.

Numerical simulations carried out in the ideal (noise-free) regime indicated that this multipartite scheme offers no clear performance benefit over the two-qubit implementation. However, as the parameter β is varied, the protocol sensitivity to different types of noise changes significantly. This three-qubit protocol offers tunability between the four possible success-fail combinations and may be optimized to mitigate noise effects, potentially achieving enhanced performance with respect to the two-qubit case in realistic, noisy environments.

Ancilla transfer protocol

Figure 4.6 illustrates an alternative sensing protocol that is equivalent to the two-qubit scheme described in Subsec. 4.1.1, but which does not require measuring the sensing qubit. In this design, the excitation probability P_e is coherently transferred from the sensing qubit to the first ancilla. Consequently, when engineering the qubit–readout resonator couplings, one can prioritize high-fidelity readout on the ancilla while allowing the sensing qubit to be weakly coupled, suppressing Purcell-induced relaxation and possibly allowing for increasing the Rabi oscillation time τ of the experiment. A weak coupling between the sensing qubit and a readout resonator may still be required to calibrate the qubit frequency at each flux bias point. From state $|\Psi_2\rangle$ in

Fig. 4.6:

$$|\Psi_2\rangle = \cos\left(\frac{\theta}{2}\right)|0_{A2}0_{A1}0_S\rangle + \sin\left(\frac{\theta}{2}\right)e^{i\alpha}|0_{A2}0_{A1}1_S\rangle\,. \tag{4.29}$$

After applying the entangling gate sequence, before measuring A2, the quantum state becomes

$$\begin{aligned}|\Psi_3\rangle = &\cos\left(\frac{\beta}{2}\right)\cos\left(\frac{\theta}{2}\right)|0_{A2}1_{A1}0_S\rangle \\ &+ \sin\left(\frac{\beta}{2}\right)\cos\left(\frac{\theta}{2}\right)|1_{A2}1_{A1}0_S\rangle + \sin\left(\frac{\theta}{2}\right)e^{i\alpha}|1_{A2}0_{A1}1_S\rangle\,.\end{aligned} \tag{4.30}$$

After measuring A2 and identifying the outcome $|1_{A2}\rangle$ as success, the quantum state partially collapses into a form equivalent to $|\Psi_3^S\rangle$ in Eq. 4.12, except that $\tilde{P}$ can now be inferred by measuring A1.

4.1.3 Two sensing and one ancilla quantum circuit

From a scalability standpoint, the direct dark matter search experiment could benefit from deploying multiple identical two-qubit devices operating in parallel, each implementing the enhancement scheme described in Subsec. 4.1.1, thus enabling an increased data acquisition rate. Further enhancement is achievable by coupling a single ancilla to multiple sensing qubits, utilizing the fact that the free Rabi evolution time $\tau \sim 100$ µs is expected to be much longer than the duration of the enhancement protocol ~ 1 µs. By coupling two sensing qubits (S1 and S2) to the same ancilla (A), we can let S1 and S2 evolve under U_{DM} at the same time, then apply a two-qubit enhancement between S1 and A, then a second enhancement between S2 and A. The quantum circuit is depicted in Fig. 4.7.

Applying an X gate is required if the first mid-circuit measurement succeeds, i.e. the ancilla qubit collapses in $|1_A\rangle$, as shown in the first conditional block of the quantum circuit. Identifying a speedup factor per qubit $\mathcal{G}$ of the two-qubit enhanced scheme (compared to the base experiment consisting of uncoupled qubits), the speedup factor when coupling multiple sensing qubits to the same ancilla grows following

$$\mathcal{G}' = 2\mathcal{G}\frac{n-1}{n}, \tag{4.31}$$

where n is the total number of physical qubits in use.

4.2 Impact of noise in the enhancement protocol

The objective of this Section is to develop a numerical simulation framework to quantitatively assess the performance gain associated with the transformations introduced in Sec. 4.1, under realistic noise conditions in an NISQ-era device. This analysis is essential to understand the cumulative impact of typical error sources, such as relaxation, dephasing, imperfect state preparation, and readout infidelity, on the overall sensitivity of the detection protocol. For instance, the presence of thermal population impacts the enhancement in a nontrivial way. Because the derivative $d\tilde{P}_e/dP_e$ decreases with increasing P_e, the contribution of thermal population in the absence of a signal is amplified more (in relative terms) than the additional excitation caused by the signal itself. As a result, a certain amount of thermal population can degrade the performance of the enhancement protocol in use, especially in high-temperature and

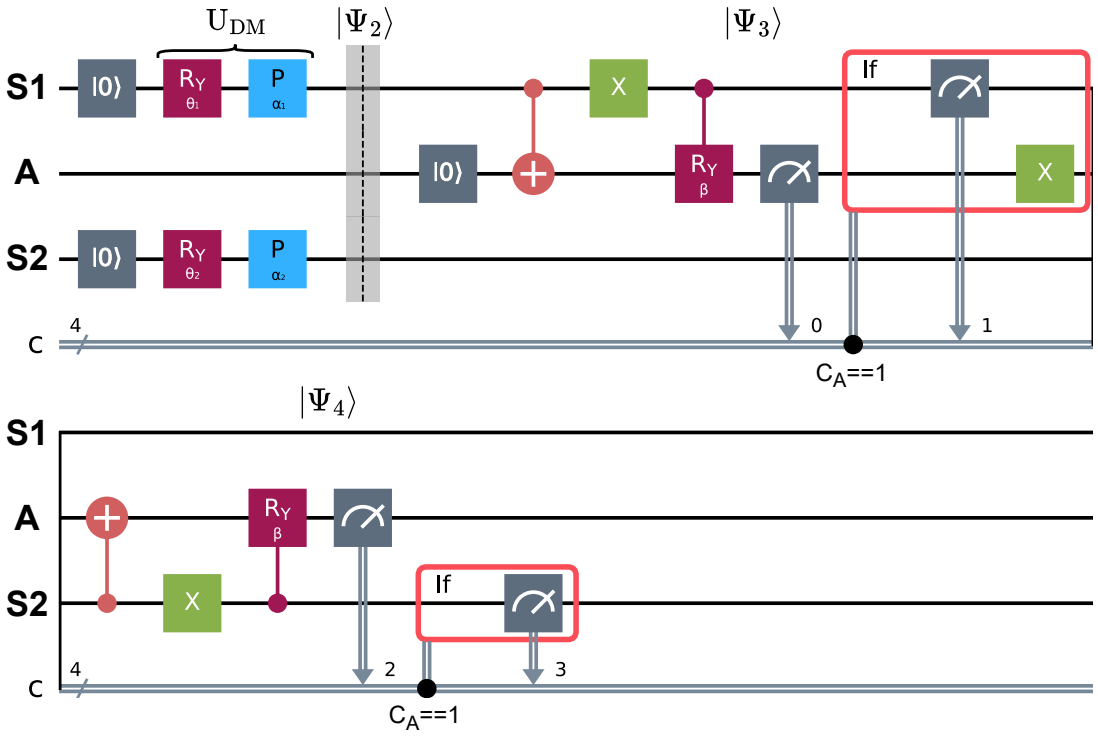

FIGURE 4.7: Two sensing qubits (S1, S2) coupled to the same ancilla (A), evolving individually under U_{DM} and undergoing the same enhancement protocol.

low-frequency regimes. Another example of a possible detrimental error is an imperfect mid-circuit readout, misidentifying the success and failure protocol conditions.

4.2.1 Noise model

The application of noise channels to quantum gates was carried out by resorting to the Kraus representation introduced in Subsec. 1.2.3, automatically implemented leveraging the Qiskit Software Development Kit [205] (v. 1.2.4). Within this framework, to execute the quantum circuit on a qubit state that is allowed to decohere for a time τ (comparable with the qubit's T_1 and T_2), the Rabi evolution has to be modeled as a noisy gate sequence.
In the Lindblad master equation formalism, we can separate the unitary Rabi-driving terms (U) and the dissipative processes (D), so that a single sensing qubit density matrix time-derivative reads:

$$\dot{\rho} = \mathcal{L}_U[\rho] + \mathcal{L}_D[\rho] = -\frac{i}{\hbar}[\mathcal{H}_{\text{drive}}, \rho] + \sum_{i=1}^{2}\left(2L_i\rho L_j^\dagger - \frac{1}{2}\{L_i^\dagger L_i, \rho\}\right), \tag{4.32}$$

where $\mathcal{H}_{\text{drive}} \propto \sigma_y$, and L_1 and L_2 are defined as in Eqs. 1.27 and 1.28, respectively. The non-commuting Lindbladian superoperators $\mathcal{L}_U$ and $\mathcal{L}_D$ encode the unitary and dissipative terms of the density matrix time-evolution. Formally, the solution over a duration τ is

$$\rho(\tau) = \rho(0)e^{(\mathcal{L}_U+\mathcal{L}_D)\tau}. \tag{4.33}$$

Since $[\mathcal{L}_U, \mathcal{L}_D] \neq 0$, the Rabi-driven evolution of ρ expressed in terms of noisy gate operations must be carried out through a Suzuki-Trotter decomposition [206]

$$e^{(\mathcal{L}_U+\mathcal{L}_D)\tau} \approx \left[e^{\mathcal{L}_U \frac{\tau}{n}} e^{\mathcal{L}_D \frac{\tau}{n}}\right]^n, \tag{4.34}$$

corresponding to applying n Trotter steps, i.e. alternating Rabi drive and decoherence operations, each acting on small time steps τ/n. Higher values of n imply a higher accuracy of the approximation. Therefore, to simulate a noisy, slow Rabi drive on a qubit, the quantum circuit shown in Fig. 4.8b was implemented, consisting of n repetition of RY(θ/n) rotations, each with an associated finite energy relaxation probability $p_1 = 1 - e^{-\tau/(nT_1)}$ and dephasing probability $p_2 = e^{-\tau/(nT_2)}$. Within the `NoiseModel` class in Qiskit, the composition of different noise channels is handled through the Choi-Jamiolkowski matrix isomorphism [207, 208]. Concretely, any single-qubit CPTP map Λ can be represented by its Choi matrix

$$J_\Lambda = \frac{1}{2}(\Lambda \otimes \mathrm{I}) \left[(|00\rangle + |11\rangle) \otimes (\langle 00| + \langle 11|)\right], \tag{4.35}$$

which in the computational basis $\{|00\rangle, |01\rangle, |10\rangle, |11\rangle\}$ takes the form

$$J_\Lambda = \frac{1}{2}\begin{pmatrix} 1-p_{\mathrm{th}}p_1 & 0 & 0 & p_2 \\ 0 & p_{\mathrm{th}}p_1 & 0 & 0 \\ 0 & 0 & (1-p_{\mathrm{th}})p_1 & 0 \\ p_2 & 0 & 0 & 1-(1-p_{\mathrm{th}})p_1 \end{pmatrix}, \tag{4.36}$$

where p_{th} is the excited state population at thermal equilibrium. The noisy RY gate is then obtained by applying the action of an ideal RY on the Pauli basis, i.e. a matrix $M(\theta/n)$ defined by the components:

$$\mathrm{RY}\left(\frac{\theta}{n}\right) A_m \mathrm{RY}^\dagger\left(\frac{\theta}{n}\right) = \sum_{i=0}^{3} M_{im}\left(\frac{\theta}{n}\right) A_i, \tag{4.37}$$

with $A = \{\mathrm{I}, \sigma_x, \sigma_y, \sigma_z\}$.
The composition becomes

$$\chi_{\Lambda\text{-RY}} = M(\theta/n) J_\Lambda M(\theta/n)^T. \tag{4.38}$$

Finally, by diagonalizing $\chi_{\Lambda\text{-RY}}$, obtaining the eigenvalues λ_i and eigenvectors ξ_i, the effective Kraus operators can be derived through:

$$K_i = \sqrt{\lambda_i}\Phi(\xi_i), \tag{4.39}$$

where Φ is an operation that rearranges the four-component vector ξ_i into a 2×2 matrix. The consistency between solving the Lindblad master equation and applying Trotterized noisy gate sequences is shown in Fig. 4.8, which exhibits good agreement when setting a trotter step number $n = 50$.

To our gate-based noise-modeling framework, we embedded decoherence channels into every operation of a specific universal gate set, chosen to be {X, SX, I, RZ, ECR}. This set was selected because it enables implementation of the detection-enhancement circuit with a single two-qubit gate (see Fig. 4.4). We assigned to each gate a duration consistent with state-of-the-art superconducting quantum processors, during which qubit relaxation and dephasing occur with probabilities determined

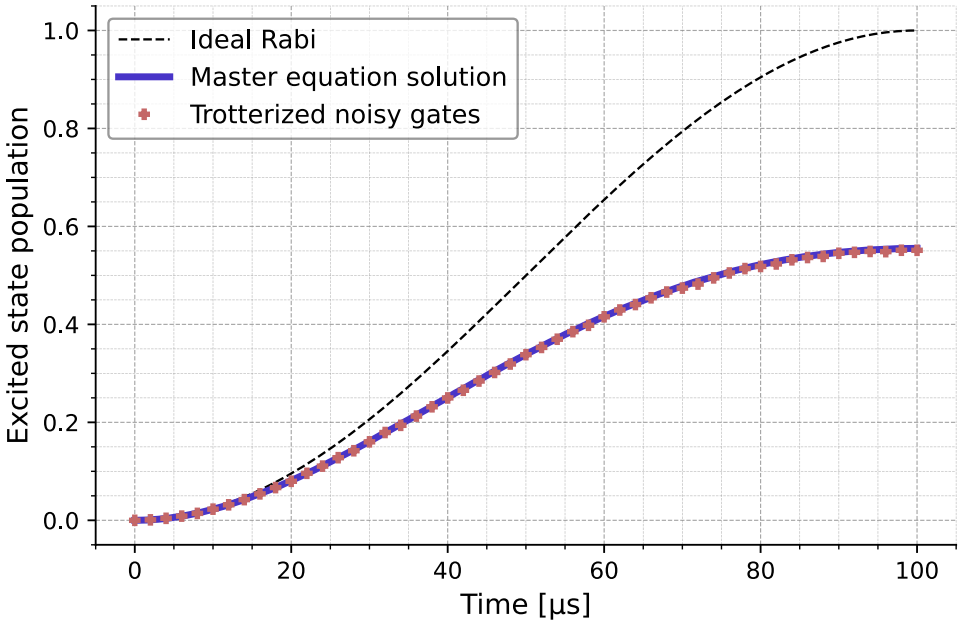

(A) Trotterized evolution compared to the numerical solution.

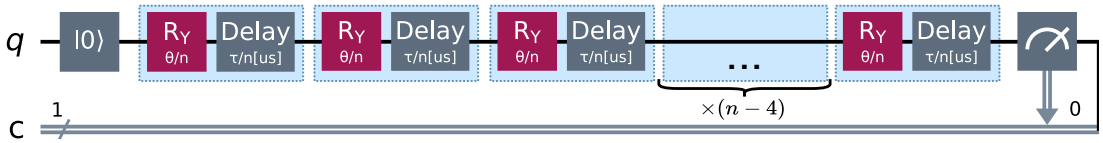

(B) Gate-based noisy Rabi drive.

FIGURE 4.8: Accuracy of the gate-based noise modeling of the resonant slow Rabi oscillation in the presence of relaxation and dephasing. (A) Noisy Rabi evolution for a qubit starting in $|0\rangle$ with $T_1 = 100$ µs and $T_2 = 100$ µs, assuming zero thermal population in $|1\rangle$ at equilibrium and ideal state readout. (B) Quantum circuit illustrating the n-step Trotter-decomposed gate sequence, where RY represents an ideal rotation about the $\hat{y}$ axis, and the Delay operation represents the action of the loss mechanisms. The circuit is sampled with 10^5 shots.

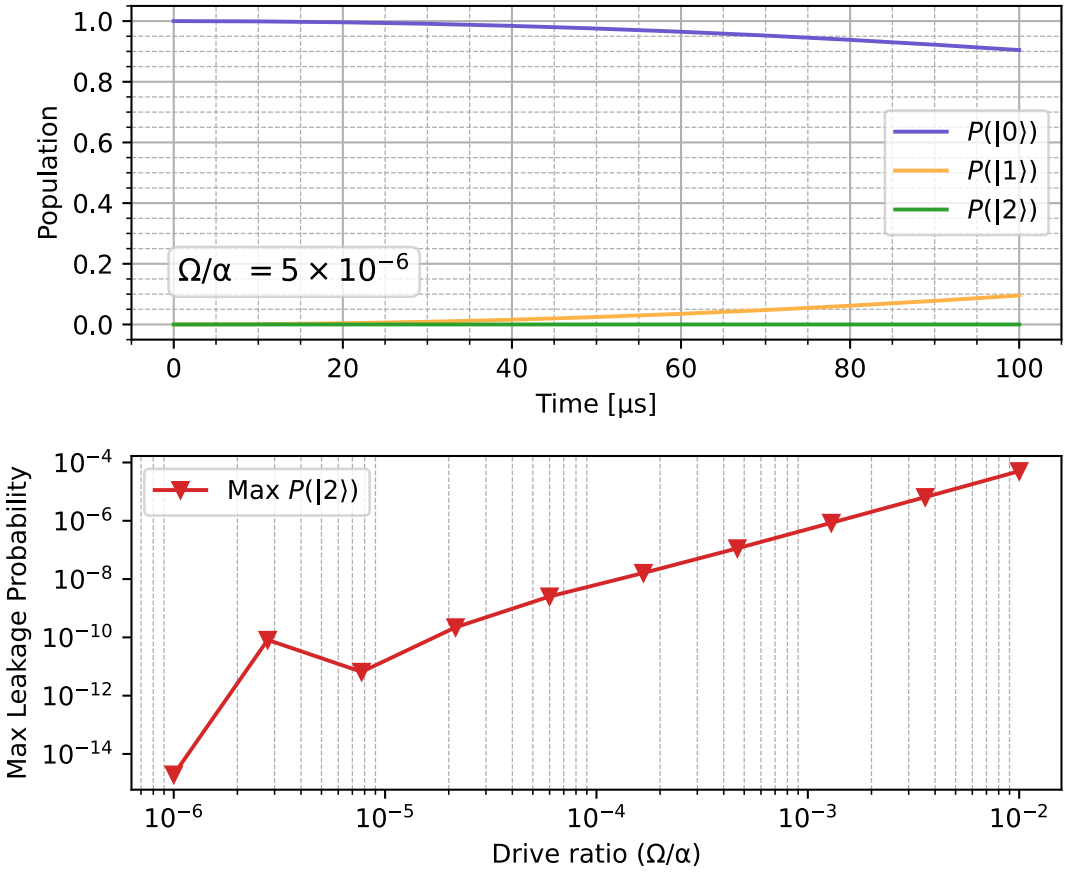

FIGURE 4.9: Three-level transmon time evolution in the presence of a weak drive ($\Omega/\alpha \ll 1$) resonant with ω_q. No dissipation, dephasing, or readout errors have been considered. The case $\Omega/\alpha \ll 5 \times 10^{-6}$ is shown explicitly for an evolution of $\tau = 100$ μs (top), along with the maximum state $|2\rangle$ probability for different Ω/α ratios (bottom).

by T_1 and T_2. In addition, state preparation errors were incorporated by adding a symmetric probability of initializing the qubit in the incorrect computational basis state. Similarly, readout errors were included with a symmetric probability of measuring $|1\rangle$ if the qubit collapsed in $|0\rangle$, and vice versa. Finally, residual thermal excitation of the qubits was included via the Bose-Einstein occupation formula (see Eq. 3.41), determined by the qubit's effective temperature.
The leakage into the non-computational state $|2\rangle$ was evaluated numerically by considering the Hamiltonian:

$$\hat{\mathcal{H}} = \hbar\omega_q \hat{a}^\dagger \hat{a} - \hbar\frac{\alpha}{2}\hat{a}^\dagger\hat{a}^\dagger\hat{a}\hat{a} + \hbar\Omega\left(\hat{a}^\dagger + \hat{a}\right), \tag{4.40}$$

where the creation and annihilation operators were truncated to a 3×3 matrix. A steady weak drive ($\Omega \ll \alpha$) at frequency $\omega_q/2\pi$ has negligible spectral overlap with the $|1\rangle \leftrightarrow |2\rangle$ transition at $\omega_{12} = \omega_q - \alpha$. As the numerical solutions shown in Fig. 4.9 confirm, leakage into state $|2\rangle$ during the dark matter-driven evolution can be safely ignored, being the probability of collapsing into $|2\rangle$ smaller than 10^{-10}.

The complete noise model can be used to predict the outcome of sampling from arbitrary quantum circuits, including the effective gate-based slow Rabi depicted in Fig. 4.8b and the two-qubit enhancement protocol. Fig. 4.10 displays the combined

TABLE 4.2: Parameter settings for the enhanced and base experiment noise model.

	Sensing qubit	**Ancilla qubit**
T_1	100 µs	100 µs
T_2	100 µs	100 µs
T_ϕ	200 µs	200 µs
RZ duration	25 ns	25 ns
SX duration	25 ns	25 ns
X duration	50 ns	50 ns
ECR duration	600 ns	600 ns
Reset duration	1 µs	1 µs
Readout duration	1 µs	1 µs
Effective temperature	35 mK	35 mK
Qubit frequency ($\omega_q/(2\pi)$)	5.0 GHz	5.1 GHz
Rabi evolution time (τ)	100 µs	-
Trotter steps (n)	50	-

effects of noise on the reconstructed probability distribution, $\tilde{P}(P_e)$, along with the experimentally observed success probability $P_{\text{success}}(P_e)$, and the Rabi oscillation observable in a base sampling experiment $P_{\text{base}}(P_e)$, without enhancement. Here, P_e is treated as the ideal probability in the absence of noise and experimental error, $P_e = \sin(\theta/2)^2$. As expected, for a dark matter interaction time $\tau = T_1 = 100$ µs, the presence of noise leads to a noticeable degradation of the curves, although their principal features remain well discernible. Multiple noise scenarios are illustrated, for different values of β, readout error rate r, and state preparation error probability P_{prep} (r and P_{prep} are assumed to be the same for the sensing and ancilla qubits). Table 4.2 collects the other noise parameters relevant to the comparisons, which are common to all the configurations tested.

A key feature reported in Fig. 4.10 is the slope of the blue curve in $P_e = 0$, which is related to the expected sensitivity of the protocol to small displacement P_e induced by dark matter. Together with a strong dependence on β, the probabilities of preparation and readout error also heavily affect $d\tilde{P}/dP_e$, underlining the importance of minimizing these two error types. Intuitively, the slope of $\tilde{P}$ is inversely related to the enhancement success probability P_{success}. This relationship arises because higher error rates increase the probability of registering spurious successes during the enhancement protocol. These false positives directly contribute to the computation of the blue curve, artificially inflating the apparent success rate. However, this phenomenon yields a partial compensatory effect, as the enhancement decreases, more data will be available to analyze.

4.2.2 Test on IBM quantum hardware

To validate the noise model introduced in Subsec. 4.2.1, we implemented the two-qubit enhancement protocol on two of IBM's 127-qubit Eagle r3 superconducting backends, namely `ibm_sherbrooke` and `ibm_brisbane`. These quantum processing units (QPUs) both share the same native gate set as in our simulations: {X, SX, I, RZ, ECR}. Using the IBM cloud interface, we selected the qubit pairs according to the coupling map of each device and the qubit calibration data available at the time of the experiment. The specific qubits chosen for running the experiment exhibited a convenient tradeoff between having low ECR gate error, long coherence times, and

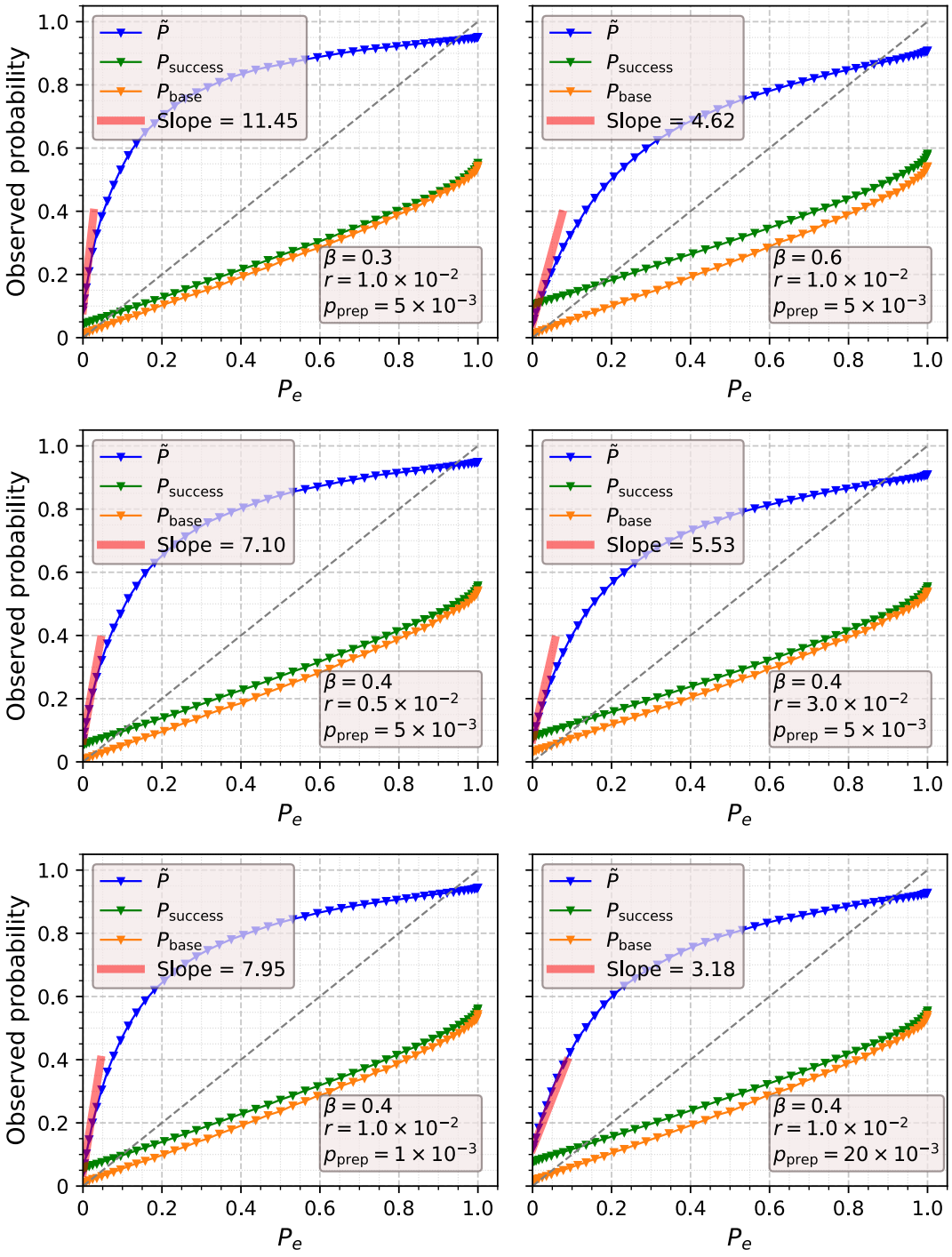

FIGURE 4.10: Observable probability transformations of the enhanced protocol, its success rate, and the base Rabi oscillation in the presence of noise, as a function of the original sensing qubit excitation probability in the absence of noise. Different error configurations are shown, varying the β-parameter of the enhancement circuit, the readout error probability r, and the preparation error probability P_{prep}.

TABLE 4.3: Qubit characterization for testing the enhancement protocol on quantum hardware.

	ibm_sherbrooke		**ibm_brisbane**	
Role	sensing	ancilla	sensing	ancilla
Qubit id	40	39	118	119
T_1 [µs]	251	361	151	159
T_2^* [µs]	52	–	34	–
T_2 [µs]	327	281	126	69
$\omega_q/2\pi$ [GHz]	4.701	4.574	4.733	4.803
$P(\|0\rangle \,\|\, \|1\rangle) \times 10^3$	7.8	28.3	15.6	30.3
$P(\|1\rangle \,\|\, \|0\rangle) \times 10^3$	2.9	18.6	3.4	17.6
Gate error $\times 10^4$	1.4	1.6	2.6	4.9
ECR error $\times 10^3$	3.9		6.8	
ECR duration [ns]	590		660	

high preparation-readout fidelity, compared to the other qubits in the QPUs. Table 4.3 summarizes the relevant parameters at the time of measurement. Both QPUs employ readout pulses with a duration of approximately 1.3 µs.

In the table, we report the state preparation and measurement errors in terms of $P(|1\rangle \,|\, |0\rangle)$ and $P(|0\rangle \,|\, |1\rangle)$, corresponding to the probability of registering $|1\rangle$ when preparing $|0\rangle$, and vice versa. Dephasing is commonly characterized by the Ramsey time (T_2^*) and the Hahn-echo time (T_2), the latter being usually higher, thanks to the implementation of echo sequences to cancel out spurious phase shift mechanisms. Since our protocol exposes the sensing qubits to their environment for the duration τ of the dark matter interaction (without mitigation sequences), the Ramsey time is the metric limiting the evolution time τ.

IBM's platform does not report T_2^* directly, hence we performed gate-based Ramsey measurements to assess the T_2^* parameters of the sensing qubits (See Appendix A). Based on those results, we fixed the interaction time at $\tau = 10$ µs. Lacking pulse-level control of the QPUs, the Trotterized Rabi technique discussed in Subsec. 4.2.1 was implemented on quantum hardware as well as on simulations. Since the only variational gate in the basis set is RZ, the Trotterized slow-Rabi simulation transpiles into a sequence of RZ-SX-RZ-SX for each RY. However, since IBM's RZ gates are virtual (see Subsec. 2.2.1), this decomposition only marginally increases the complexity of the quantum circuit executed on the hardware. To limit the effect of single-qubit gate errors, the Trotter step number was set to $n = 5$. This step reduction does not undermine the conclusion of this feasibility study, aimed solely at demonstrating the protocol's viability on real qubits with coherence times comparable to τ.

Fig. 4.11 compares the quantum hardware results and simulations, plotting the transformed probability $\tilde{P}$, the protocol success probability P_{success}, and the base Rabi experiment P_{base}, for a β-parameter set to 0.4. For each qubit, the noise model takes into account a symmetric error rate r equal to the mean value of $P(|1\rangle \,|\, |0\rangle)$ and $P(|0\rangle \,|\, |1\rangle)$, and a simmetric preparation error rate P_{prep} corresponding to $P(|1\rangle \,|\, |0\rangle)$, since a major systematic in the experiment is associated with measuring the ancilla qubit in $|1\rangle$ when it collapsed in $|0\rangle$, returning a false protocol success condition. The opposite case leads to a loss of events due to a false fail condition, but it is less impactful in a regime where $P_{\text{success}} < 10\%$.

The width of the error belts in the graphs shown in Fig. 4.11 for the quantum hardware calculation accounts for the statistical error (two standard deviations), with

a shot number of 10^4. The simulation results were evaluated with 10^5 shots. Overall, the simulation results return a slightly more pessimistic prediction of the observed probabilities than the hardware results (P_{success} is higher close to $P_e = 0$, indicating that more false successes were registered), which we attribute to a conservative choice of r and P_{prep}. The increase in false successes reflects on the slope of $\tilde{P}$, which also appears less steep than the one obtained on quantum hardware.
Precise noise modeling of complex architectures such as Eagle r3 is generally a challenging task, and it is outside the scope of this thesis. For instance, coherence times, qubit frequencies, error rates, and gate fidelities are subject to variations over time. The comparison carried out in this Section, however, demonstrates the feasibility of testing the enhancement protocols directly on quantum computers, even without pulse-level access. In principle, the dark matter detection experiment itself (both the base and the enhanced versions) could be carried out on existing QPUs.
In the case of non-tunable transmon architectures, instead of searching for resonant peaks, the excitation probability of a sensing qubit can be sampled over time in search of a Rabi oscillation. This simple method is limited by not having full detector control (in the case of remote access to the quantum device) and a harder interpretation of the experiment's systematic uncertainties.

4.3 Detection experiment simulation

This Section focuses on quantifying the performance gain of the enhancement protocol introduced in Sec. 4.1 in terms of setting an exclusion limit on the kinetic mixing strength ϵ between the dark photon and the ordinary Standard Model photon. The detection experiment simulation makes use of the noise model developed and tested in Subsec. 4.2.1.

4.3.1 Simulation workflow

The noisy simulation is articulated as follows:

1. Define flux-tunable transmon qubit objects (sensing and ancilla).
2. Define a mixing strength ϵ and a dark photon mass m_X, retrieving the Rabi strength Ω from Eq. 3.28 after a duration τ.
3. Simulate numerically the noise-free evolution of the sensing qubit under a Rabi with strength Ω, accounting for qubit-dark matter detuning.
4. Map the noise-free excitation probability P_e to the observed noisy ones $\tilde{P}$, P_{success}, P_{base}.
5. Sample the excitation counts from the observed probabilities sweeping on the flux bias.

Transmon qubit modeling

The sensing qubit is modeled as a `TunableTransmon` object in the scQubits Python library [209] (v. 4.1.0), i.e. a Hamiltonian expressed in the charge basis of the form

$$\hat{\mathcal{H}} = \hbar E_C (\hat{n} - n_g)^2 - \frac{\hbar}{2} E_J^{\text{eff}}(\phi_{\text{ext}}) \sum_n \left(|n\rangle \langle n+1| + |n+1\rangle \langle n| \right), \tag{4.41}$$

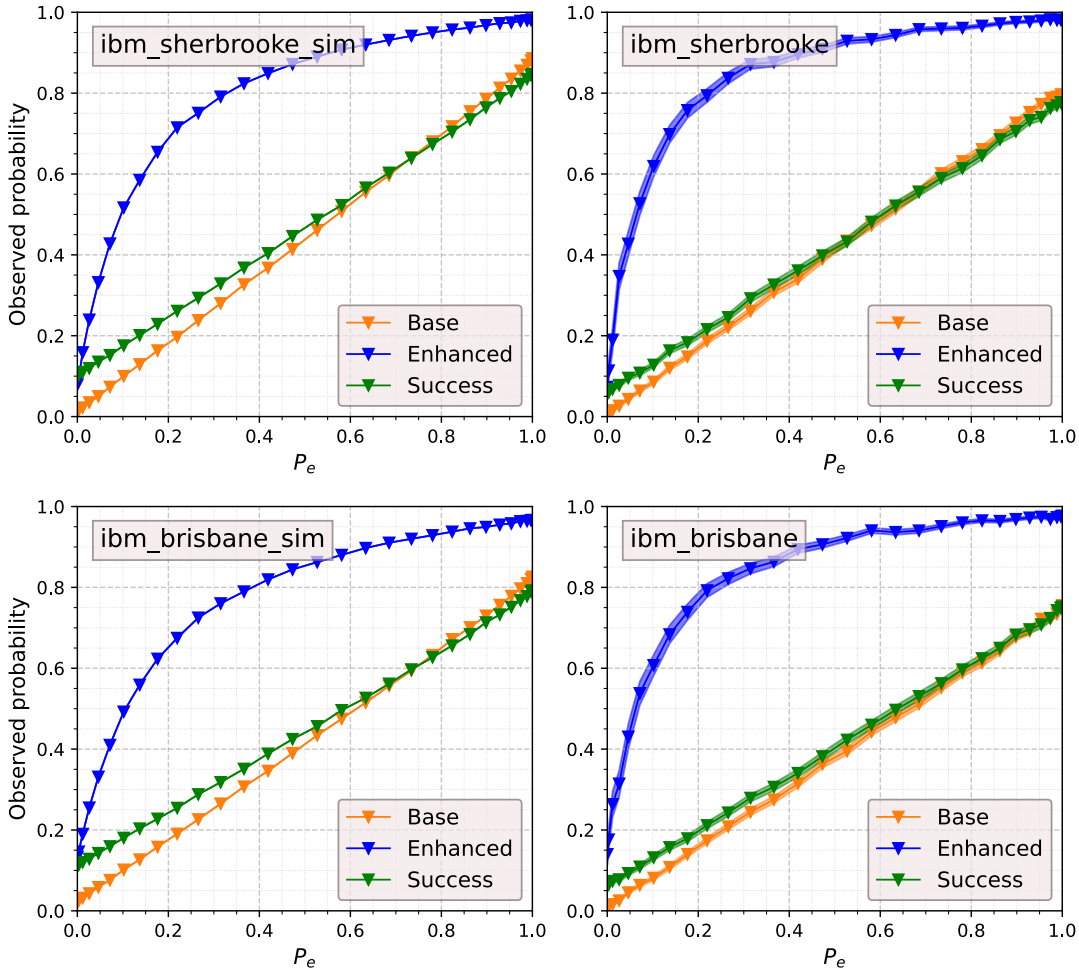

FIGURE 4.11: Observable probability transformations of the enhanced protocol, its success rate, and the base Rabi oscillation calculated with `ibm_sherbrooke` and `ibm_brisbane` (right column) compared with the corresponding noise simulation (left column).

with $\hat{n}\,|n\rangle = n\,|n\rangle$ and

$$E_J^{\text{eff}}(\phi_{\text{ext}}) = E_J\sqrt{\cos^2(\pi\phi_{\text{ext}}) + d^2\sin^2(\pi\phi_{\text{ext}})}, \tag{4.42}$$

where ϕ_{ext} is expressed in units of the flux quantum Φ_0. Modifications to the Hamiltonian due to the coupling to a readout structure and the ancilla(s) qubit(s) are not considered for this study, as they are assumed to be dispersive and alter only marginally E_C, E_J, and $|n\rangle$. Within the simulation, the sensing qubit is uniquely determined by its zero-bias frequency $\omega_q/2\pi$, the $E_J(\phi = 0)/E_C$ ratio, and the SQUID parameter d.
To consider decoherence and the antenna-like interaction with dark matter, the qubit is also equipped with a finite quality factor Q, a dephasing time T_ϕ, and a dipole length fixed at $l = 250$ µm. An important consideration is that T_ϕ is subject to variations depending on the flux bias working point, because the derivative of ω_q with respect to ϕ_{ext} depends on the SQUID asymmetry.
Neglecting anharmonic corrections:

$$\frac{d\omega_q}{d\phi_{\text{ext}}} = \frac{1}{\hbar}\frac{d}{d\phi_{\text{ext}}}\left(\sqrt{8E_C E_J^{\text{eff}}}\right) \propto \frac{(d^2-1)}{2}\frac{\sin(2\pi\phi_{\text{ext}})}{\sqrt{\cos(\pi\phi_{\text{ext}}) + d^2\sin(\pi\phi_{\text{ext}})}}. \tag{4.43}$$

We can model:

$$\frac{1}{T_\phi} = \mathrm{A} + \mathrm{B}\left|\frac{d\omega_q}{d\phi_{\text{ext}}}\right|, \tag{4.44}$$

where A and B are determined by the noise power spectrum that the qubit is subject to ($B \sim 10^{-5}$ [rad]/s). Therefore, we expect T_ϕ to be less dependent on ϕ_{ext} as d increases (i.e. the SQUID is more asymmetrical). However, values of d close to one limit the transmon's frequency tunability range. The tradeoff between achieving low $d\omega_q/d\phi_{\text{ext}}$ and large frequency span $\Delta = (\omega_q^{\max} - \omega_q^{\min})/2\pi$ is shown in Fig. 4.12. To ensure that the qubit maintains a high dephasing time at any flux bias point, d was set to determine a tunability range of roughly 300 MHz for $\omega_q \sim 5$ GHz, based on the experimental results achieved in [117, 210, 211]. The relaxation time T_1 is evaluated as $T_1 = Q/\omega_q$, varying with the flux bias.

Detuned Rabi oscillation

The Rabi strength Ω relates to the ideal dark matter-driven excitation probability $P_e(\tau)$, in the resonant condition ($\omega_q/2\pi = m_X$), as:

$$\Omega = \frac{2}{\tau}\arcsin\left(\sqrt{P_e(\tau)}\right), \tag{4.45}$$

where $P_e(\tau)$ is calculated using Eq. 3.28. To account for a non-zero qubit-dark matter detuning $\delta = |\omega_q - 2\pi m_X|$, we recur to Eq. 2.57, which works under the RWA and well represents the time evolution obtained by numerically solving the qubit drive Hamiltonian (see Fig. 2.7). The detuned noise-free excitation probability $P_e^\delta(\tau)$ becomes

$$\begin{aligned} P_e^\delta(\tau) = &\frac{\frac{4}{\tau^2}\arcsin\left(\sqrt{P_e^{(\delta=0)}(\tau)}\right)^2}{\frac{4}{\tau^2}\arcsin\left(\sqrt{P_e^{(\delta=0)}(\tau)}\right)^2 + \delta^2} \\ &\times \sin\left[\left(\frac{4}{\tau^2}\arcsin\left(\sqrt{P_e^{\delta=0}(\tau)}\right)^2 + \delta^2\right)\frac{\tau}{2}\right]. \end{aligned} \tag{4.46}$$

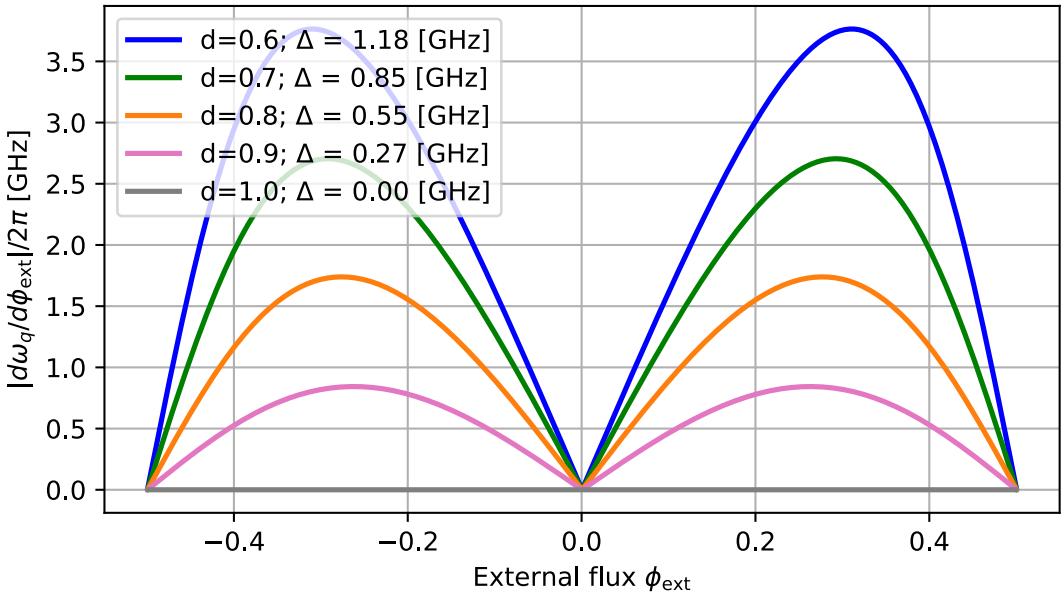

FIGURE 4.12: Dynamic range variability of a flux-tunable transmon qubit, as a function of the bias flux quanta concatenated in the SQUID loop ϕ_{ext}. The qubit is set to have $\omega_q^{max}/2\pi = 5$ GHz, with different amounts of junction asymmetry.

Noisy probability mapping

The noise model introduced in Subsec. 4.2.1 depends on the T_1 times and the frequencies of the qubits involved, which vary during the frequency sweep. This information is important to update in the model as it affects the thermal equilibrium population. For this reason, the noise model is extended to encompass a range of frequencies, implementing a transformation g of the ideal excitation probability P_e:

$$g : (P_e, \omega_q) \to g(P_e, \omega_q) = \begin{pmatrix} \tilde{P} \\ P_{\text{success}} \\ P_{\text{base}} \end{pmatrix}, \tag{4.47}$$

where P_{base} is obtained by sampling the circuit in Fig. 4.8b, while $\tilde{P}$ and P_{success} are retrieved from sampling the circuit in Fig. 4.8b (i.e. the sensing qubit time evolution) concatenated with the one in Fig. 4.4, setting a specific qubit frequency $\omega_q/2\pi$ and the ancilla at $\omega_q/2\pi + 100$ MHz, $T_1 = Q/\omega_q$ for the sensing qubit and

$$T_1 = \frac{Q}{(\omega_q + 2\pi \cdot 100\,\text{MHz})} \tag{4.48}$$

for the ancilla. For each qubit frequency $\omega_q/2\pi$, we sample the noise model on a dense grid of ideal excitation probabilities P_e, and compute the three performance curves $\tilde{P}$, P_{success}, and P_{base}, as exemplified in Fig. 4.10. We then fit each curve with a smooth interpolant, extracting an array of interpolation parameters

$$\mathbf{k}_i^{\omega_q}, \quad i = 1, 2, 3, \tag{4.49}$$

with i representing $\tilde{P}$, P_{success}, and P_{base}, respectively. Repeating this procedure over an entire frequency grid $\boldsymbol{\omega} = \{\omega_q\}$ produces, for each i, a function f_i such that

$$f_i : \omega_q \;\mapsto\; \mathbf{k}_i^{\omega_q}. \tag{4.50}$$

The interpolants used in each fit are inspired by the expected trend of the noisy probabilities, with the addition of degrees of freedom to adapt the curves to the noise model predictions:

$$\tilde{P} = \frac{a_1 P_e}{(b_1 + P_e)} + c_1 P_e + d_1; \qquad \mathbf{k}_1 = (a_1,\, b_1,\, c_1,\, d_1), \tag{4.51}$$

$$P_{\text{success}} = e^{-a_2 \arcsin\left(\sqrt{P_e}\right)} \sin\left[b_2 \arcsin\left(\sqrt{P_e}\right)\right]^2 + c_2; \qquad \mathbf{k}_2 = (a_2,\, b_2,\, c_2), \tag{4.52}$$

$$P_{\text{base}} = e^{-a_3 \arcsin\left(\sqrt{P_e}\right)} \sin\left[b_3 \arcsin\left(\sqrt{P_e}\right)\right]^2 + c_3; \qquad \mathbf{k}_3 = (a_3,\, b_3,\, c_3). \tag{4.53}$$

We expect $\mathbf{k}_i^{\omega_q}$ to vary smoothly with ω_q. For this reason, the process is repeated in a dense frequency grid $\omega_q/2\pi$, and mixed degree polynomial interpolations are performed on each parameter set, so that for any target frequency ω' we recover the corresponding parameters $\mathbf{k}_i^{\omega'}$. In practice, once the noise model is evaluated on a ω_q-P_e grid to obtain the set of parameters $\{\mathbf{k}_1^{\omega_q}, \mathbf{k}_2^{\omega_q}, \mathbf{k}_3^{\omega_q}\}_{\omega_q \in \omega_q\text{-grid}}$, we can retrieve any $\{\tilde{P}, P_{\text{success}}, P_{\text{base}}\}$ at an arbitrary pair (ω', P_e) within the extreme points of the grid.
We proceeded in two steps:

1. ω_q **interpolation:** Interpolate $\omega_q \mapsto \mathbf{k}_i^{\omega_q}$ at ω' to obtain $\mathbf{k}_i^{\omega'}$.
2. P_e **interpolation:** Plug P_e into each of the three P–vs–P_e interpolants described by $\mathbf{k}_i^{\omega'}$.

This scheme thus implements a continuous mapping

$$(\omega_q, P_e) \;\longmapsto\; \left(\tilde{P},\, P_{\text{success}},\, P_{\text{base}}\right) \tag{4.54}$$

across the entire ω_q-P_e plane.

Probability sampling

By setting the dark photon mass m_X and the kinetic mixing strength ϵ, we can calculate the noise-free excitation probability P_e^{δ}, where δ is the qubit-dark matter detuning. For each probe frequency, we determine the corresponding external flux concatenated in the transmon's SQUID to retrieve the qubit Hamiltonian in Eq. 4.41, then retrieve the noise model-inferred probabilities, extended through the mapping described earlier in this Subsection. An example outcome is depicted in Fig. 4.13, where each probed frequency was sampled $n_{\text{shots}} = 10^6$ times, with the noise model parameters summarized in Table 4.4.
The large frequency sweep between 2.8 GHz and 6.2 GHz may not be feasible to achieve with a single sensing qubit, as it would require a low junction asymmetry parameter d, increasing Γ_ϕ far from the flux bias sweet spots. Still, the simulation can be thought of as using multiple devices with the same qubit quality factors and higher asymmetry, operating at different frequencies that cover the whole interval altogether. From the histogram, an exponential decrease in thermal population emerges as the qubit frequency rises, lying on a flat background attributed to readout error. The net effect of the enhancement scheme is to lower background counts while roughly keeping the same number of counts under the signal peak at $m_X = 4.5$ GHz. Whether

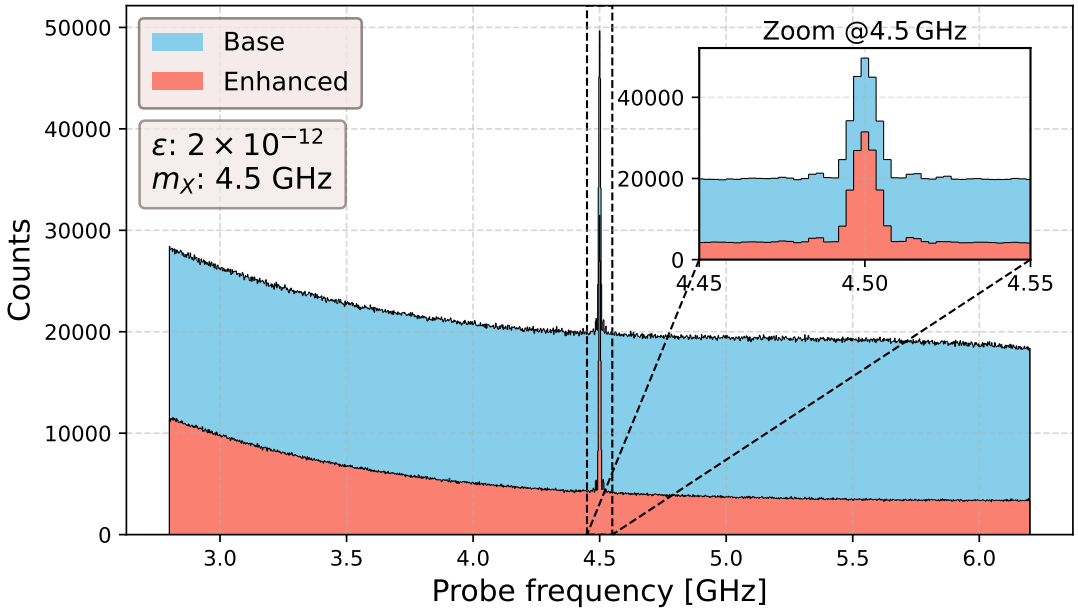

FIGURE 4.13: Monte Carlo simulation of a dark photon search experiment between 2.8 GHz and 6.2 GHz, assuming a kinetic mixing strength of 2×10^{-12} and dark photon mass $m_X = 4.5$ GHz, under realistic NISQ noise. The noise model parameters are collected in Table 4.4. The base experiment consists of a Rabi sampling of a single sensing qubit, while the enhanced experiment comprises a sensing qubit coupled to an ancilla, executing the protocol shown in Fig. 4.2, with $\beta = 0.4$.

the enhanced histogram leads to a higher sensitivity to ϵ or not depends on the trade-off between enhancing the signal-to-dark count ratio and having less data to analyze, conditioned by $P_{\text{success}} \lesssim 0.1$. Subsec. 4.3.2 describes the statistical framework used to evaluate the sensitivity to ϵ.

We note that, by construction, the ability to distinguish the signal peak on top of the dark counts improves with $\sqrt{n_{\text{shots}}}$, as it is only subject to fixed amounts of dark count and signal rates. The factor $\sqrt{n_{\text{shots}}}$ arises from the binomial distribution that characterizes counting experiments. The statistical error is considered the dominant source of uncertainty, and we assume that the broadband dark count landscape is well approximated by the exponential plus constant shape true at $n_{\text{shots}} = 10^6$. Increasing the number of measurements further may require more complex modeling, taking into account the frequency dependence on gate and readout fidelities. On the other hand, for small ϵ, the signature peak narrows, and we expect the background count underneath the peak to be smooth within a small frequency interval. In Subsec. 4.3.3, we discuss the achievable exclusion limits on the mixing strength parameter ϵ for a feasible data-taking timespan. Evaluating systematic uncertainties, such as detector aging, temporal drifts, or fluctuations in T_1, T_2, ω_q, and r, which may not average to zero within the experiment's timescale, is beyond the scope of this thesis, as they would be strongly dependent on the specific detector, requiring data-driven estimation.

4.3.2 Simulation data analysis

Leveraging the simulation described earlier in this Section, we can vary m_X and lower ϵ until the statistical fluctuations of background counts cover the signal events. To quantitatively assess an exclusion limit on ϵ, we use the Neyman-Pearson lemma [212] to perform a hypothesis test between H_0 (no signal) and H_1 (signal with strength ϵ).

TABLE 4.4: Noise model and experiment settings for the enhanced and base experiment, referring to Fig. 4.13.

	Sensing qubit	**Ancilla qubit**
Q	3.14×10^6	3.14×10^6
T_1	100 µs @ 5 GHz	100 µs @ 5 GHz
T_2	100 µs @ 5 GHz	100 µs @ 5 GHz
T_ϕ	200 µs	200 µs
E_J/E_C	90 @ 5 GHz	-
C_Σ	100	-
Readout error (r)	0.02	0.02
Preparation error (P_{prep})	0.002	0.002
RZ duration	0 ns (virtual)	0 ns (virtual)
SX duration	25 ns	25 ns
X duration	50 ns	50 ns
ECR duration	600 ns	600 ns
Reset duration	1 µs	1 µs
Readout duration	1.3 µs	1.3 µs
Effective temperature	35 mK	35 mK
Qubit frequency ($\omega_q/(2\pi)$)	[2.8, 6.2] GHz	[2.9, 6.3] GHz
Rabi evolution time (τ)	100 µs	-
Trotter steps (n)	50	-

We define the likelihood ratio test variable as

$$\Lambda = \frac{\mathcal{L}(\boldsymbol{\theta}_0)}{\mathcal{L}(\boldsymbol{\theta}_1)}, \tag{4.55}$$

where $\mathcal{L}(\boldsymbol{\theta}_0)$ and $\mathcal{L}(\boldsymbol{\theta}_1)$ are the likelihood functions of the arrays $\boldsymbol{\theta_0}$ and $\boldsymbol{\theta_1}$, which model the probability density functions for H_0 and H_1, respectively. In a binned likelihood framework, where each bin is disjoint and associated with an underlying probability density function $\lambda(x;\, \boldsymbol{\theta})$, the expected count prediction in the i-th bin is

$$\mu_i(\boldsymbol{\theta}) = \int_{i\text{-th bin}} \lambda(x;\, \boldsymbol{\theta}) dx. \tag{4.56}$$

In our study, x represents the x-axis in the histogram generated via the Monte Carlo method, i.e. the probed frequency. Assuming independent Poisson fluctuations in each bin, the binned log-likelihood is

$$\ln(\mathcal{L}(\boldsymbol{\theta})) = \sum_{i=1}^{N} \left[n_i \ln(\mu_i(\boldsymbol{\theta})) - \mu_i(\boldsymbol{\theta}) \right], \tag{4.57}$$

where $i = (1,\, 2,\, \ldots,\, N)$ represents the bin index, n_i the counts in each bin, and N is the total number of bins. The Poisson fluctuations assumption is a valid approximation of the intrinsically Binomial statistics of each bin count. Since P_{base} and $\tilde{P}$ are small, the Binomial probability distribution converges to a Poissonian.
For Wilk's theorem [213], if H_0 is true, the variable

$$q = -2\ln(\Lambda) = -2\left[\ln \mathcal{L}(\boldsymbol{\theta}_0) - \ln \mathcal{L}(\boldsymbol{\theta}_1)\right] \tag{4.58}$$

follows asymptotically (i.e. for a large n_i in each bin) a χ^2_{dof} distribution. The number of degrees of freedom corresponds to dof $= \dim(\boldsymbol{\Theta}_1) - \dim(\boldsymbol{\Theta}_0)$, where $\boldsymbol{\Theta}_0$ and $\boldsymbol{\Theta}_1$ are the parameter spaces containing the solutions $\boldsymbol{\theta}_0$ and $\boldsymbol{\theta}_1$, respectively, requiring $\boldsymbol{\Theta}_0 \subset \boldsymbol{\Theta}_1$. For a chosen significance level α, H_0 is rejected in favor of H_1 if the test statistics variable q resulting from the experiment is

$$q > \chi^2_{\text{dof},\,1-\alpha}, \tag{4.59}$$

where $\chi^2_{\text{dof},\,1-\alpha}$ is the $(1-\alpha)$-quantile of the χ^2_{dof} distribution, i.e. the value such that:

$$\alpha = \int_{\chi^2_{\text{dof},\,1-\alpha}}^{+\infty} f_{\text{dof}}(z)dz. \tag{4.60}$$

Here, $f_{\text{dof}}(z)$ is the χ^2_{dof} probability density function. The condition in equation Eq. 4.59 is equivalent to obtaining t with probability $1-\alpha$ when the null hypothesis H_0 is true. In our analysis, we set the significance level to $\alpha = 0.05$, which translates into an exclusion limit on ϵ at a 95% confidence level, as the values reported in Figs. 1.1 and 1.2 are.
Practically, we carry out the ϵ exclusion limit estimation as follows:

1. Produce several counts vs probed frequency histograms on a range of mixing strengths ϵ, for the base and enhancement detection experiments.

2. Fit each histogram using the maximum likelihood estimation method under H_0 with a fifth-order polynomial background

$$\lambda(x;\,\boldsymbol{\theta}_0|H_0) = a + bx + cx^2 + dx^3 + ex^4 + fx^5; \quad \boldsymbol{\theta}_0 = (a,\,b,\,c,\,d,\,e,\,f)\,, \tag{4.61}$$

and under H_1 with a fifth-order polynomial plus a signal term:

$$\begin{aligned}\lambda(x;\,\boldsymbol{\theta}_1|H_1) =& A\frac{\sin\left[\Omega(x-m_X)\right]}{\left[\Omega(x-m_X)\right]^2} + a + bx + cx^2 + dx^3 + ex^4 + fx^5;\\ &\boldsymbol{\theta}_1 = (A,\,\Omega,\,m_X,\,a,\,b,\,c,\,d,\,e,\,f)\,,\end{aligned} \tag{4.62}$$

where $\boldsymbol{\theta}_0$ and $\boldsymbol{\theta}_1$ are constrained by the normalization condition $\int_{x\in X}\lambda dx = 1$.

3. Retrieve the test statistics as a function of the mixing strength $t(\epsilon)$ and determine the threshold value for ϵ such that $q = \chi^2_{\text{doi},\,0.95}$, designating it as the exclusion limit on ϵ at 95% C.L.

4. Repeat steps 1-3 for different values of m_X and noise configurations, comparing the exclusion limits obtained with the base and enhanced experiments.

Fig. 4.14 shows an explicit example of how the null hypothesis H_0 and the alternative hypothesis H_1 are fitted to our data. The three histograms obtained by sampling from $\tilde{P}$, P_{success}, and P_{base} with 10^6 shots per bin. Then each histogram is fitted independently with the models $\lambda(x;\,\boldsymbol{\theta}_0|H_0)$ and $\lambda(x;\,\boldsymbol{\theta}_1|H_1)$. In the figure legend, we report the corresponding P_{value} associated with the reduced chi-squared statistic, defined as

$$P_{\text{value}} = \int_{\chi^2_{\text{dof}}}^{+\infty} f_{\text{dof}}(z)dz, \tag{4.63}$$

which provides a good approximation to the outcome of the likelihood-ratio test. In particular, from Fig. 4.14, it emerges how the enhanced experiment analysis enables easier discrimination than the base one.

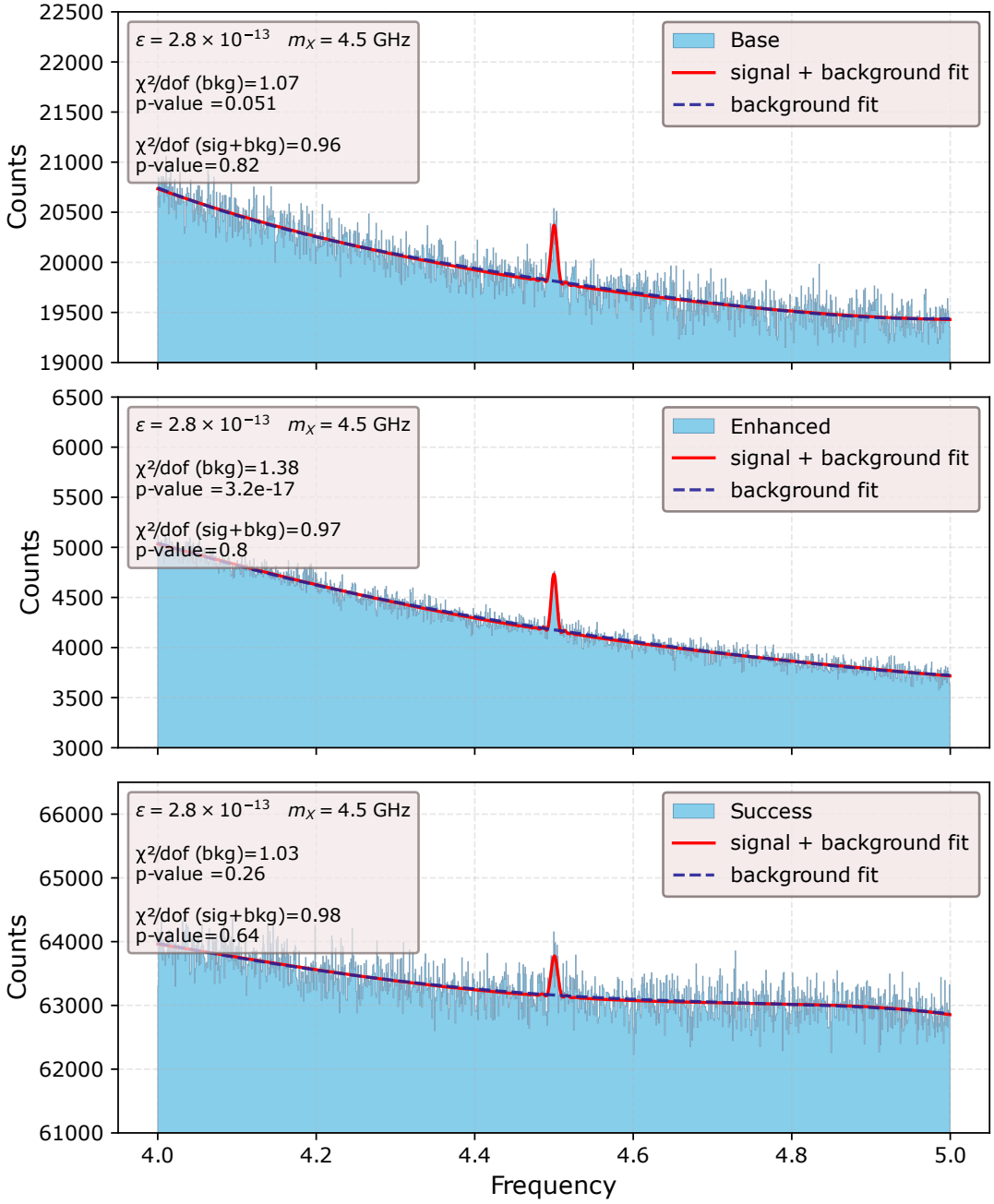

FIGURE 4.14: Simulated base and enhancement dark matter search, assuming $\epsilon = 2.8 \times 10^{-13}$ and $m_X = 4.5$ GHz, showing the fit under the background only hypothesis H_0 (dashed blue line) and background plus signal hypothesis H_1 (red continuous line). The χ^2 statistic underlines the difference in the sensitivity to the mixing strength ϵ. Each point in frequency is separated by ≈ 0.8 MHz.

Extracting failed attempts information

From Eq. 4.16 and Fig. 4.14, we observe that the success probability of the enhancement protocol P_{success} is itself dependent on P_e. From the ratio of success attempts over the total, we can retrieve additional information that potentially benefits the analysis. To achieve this, we retrieve the histogram of the success attempt counts for each bin, which has the same shape as the base and enhanced experiments, i.e. a peak in correspondence with m_X. Fitting the histogram under H_0 and H_1 as for the sensing qubit measurement data, we obtain the likelihoods $\mathcal{L}^{\text{s}}(\boldsymbol{\theta}_0^{\text{s}})$ and $\mathcal{L}^{\text{s}}(\boldsymbol{\theta}_1^{\text{s}})$. Assuming independence between the normal, enhanced likelihoods $\mathcal{L}(\boldsymbol{\theta}_0)$, $\mathcal{L}(\boldsymbol{\theta}_1)$, we modify the likelihoods as

$$\begin{aligned} \mathcal{L}(\boldsymbol{\theta}_0) &\to \mathcal{L}(\boldsymbol{\theta}_0) \cdot \mathcal{L}^{\text{s}}(\boldsymbol{\theta}_0), \\ \mathcal{L}(\boldsymbol{\theta}_1) &\to \mathcal{L}(\boldsymbol{\theta}_1) \cdot \mathcal{L}^{\text{s}}(\boldsymbol{\theta}_1), \end{aligned} \tag{4.64}$$

so that the statistical test becomes

$$q \to q = -2\left[\ln \mathcal{L}(\boldsymbol{\theta}_0) + \ln \mathcal{L}^{\text{s}}(\boldsymbol{\theta}_0) - \ln \mathcal{L}(\boldsymbol{\theta}_1) - \ln \mathcal{L}^{\text{s}}(\boldsymbol{\theta}_1)\right], \tag{4.65}$$

leveraging failed enhancement attempts that would otherwise be lost.
By varying ϵ, we compute the P_{value} associated with the likelihood ratio test, determining the exclusion limit on ϵ at 95% C.L. Fig. 4.15 displays the P_{value} as a function of ϵ for different values of m_X, with the corresponding exclusion limits on the kinetic mixing strengths $\epsilon_{95\%\,\text{C.L.}}$ obtained with three methods: base experiment, enhanced experiment, and enhanced experiment combined with the additional information retrieved from the ancilla qubit measurement. To take into account the added complexity of the enhanced experiment, i.e. requiring two qubits where only one acts as a sensor, we opted to double the number of shots per probed frequency for the base experiment (2×10^6), corresponding to running two base experiments with identical setup. In this way, the comparison is fair in the sense that we compare two-qubit vs two-qubit scenarios.
As seen in Fig. 4.15, the enhanced protocol consistently outperforms the base one, with its advantage increasing with m_X. This is attributable to the reduced thermal population at higher qubit frequencies, as the thermal excitation probability is effectively amplified by the enhancement protocol as well. Including the ancilla information in the enhanced experiment partially compensates for this effect, leading to a more significant improvement where the enhanced scheme alone suffers the most from the presence of thermal population.
Due to the several parameters affecting the amount of noise and errors in the simulation, we expect the sensitivity to ϵ of the experiment –as well as the speedup gain $\mathcal{G}$ from the enhanced protocols– to depend nontrivially on parameters such as r, P_{prep}, T, the qubit coherence times, and the enhancement parameter β. In order to investigate how the different error mechanisms affect speedup and obtain more general considerations about the benefit of the enhancement scheme, we select distinct noise scenarios and retrieve $\epsilon_{95\%\,\text{C.L.}}$ from each.

High state preparation fidelity

In this scenario, we assume higher state preparation fidelity and a more conservative readout rate assumption. More precisely, the noise parameters are reported in Tab. 4.5. Fig. 4.16 shows the speedup factor $\mathcal{G}$ of the enhanced protocol (with and without the success rate information) with respect to the base experiment. In the mass interval between 2.5 GHz and 6 GHz, the speedup factor is strictly above one, indicating that

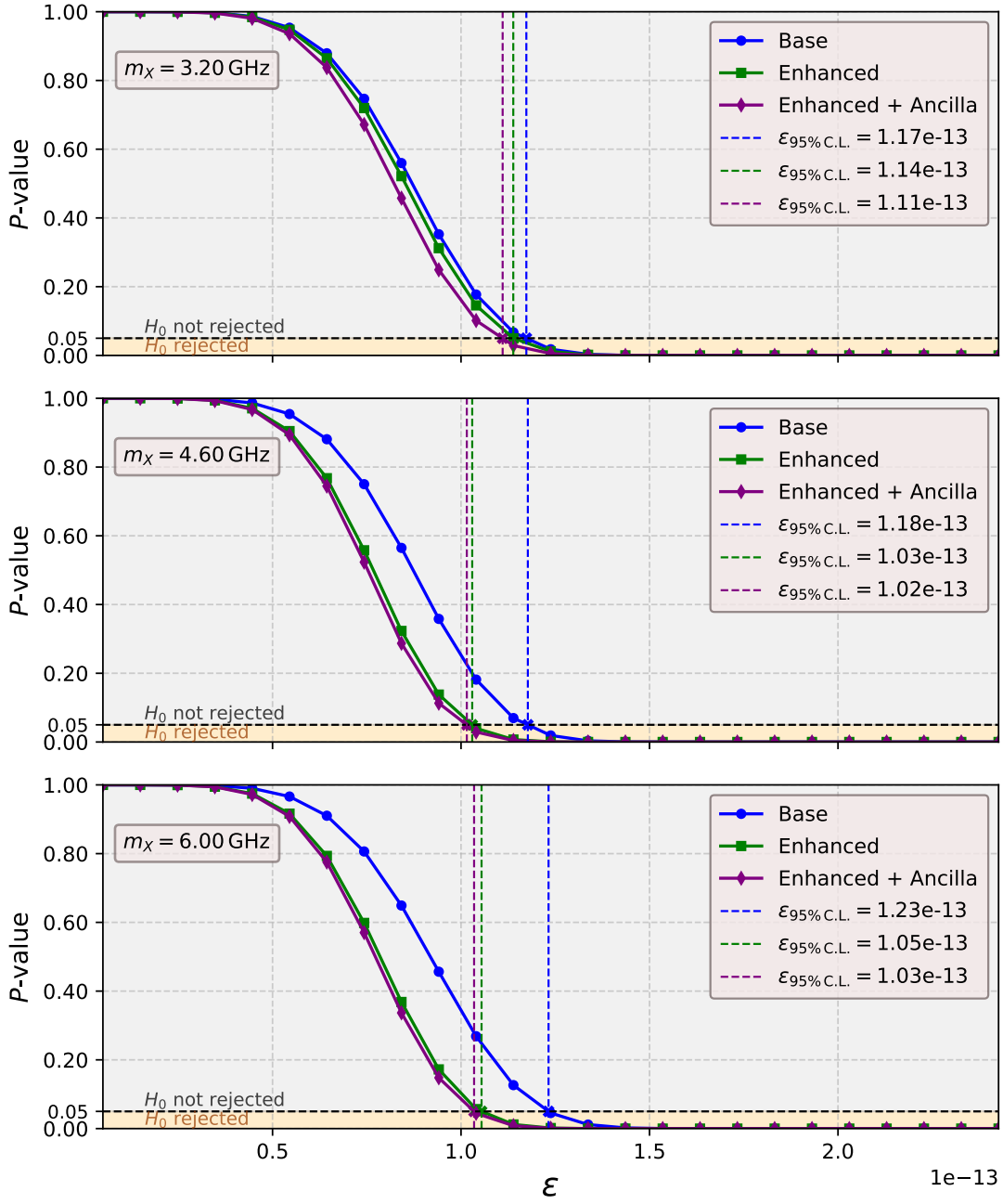

FIGURE 4.15: P_{value} of the log-likelihood ratio test statistic under the null hypothesis H_0 (no signal) and the signal hypothesis H_1 (signal with strength ϵ). The base experiment ran with 2×10^6 shots per probed frequency, while the enhanced experiment ran with 1×10^6 shots. Three dark photon mass scenarios are reported at $m_X = 3.2$ GHz, $m_X = 4.6$ GHz, and $m_X = 6.0$ GHz, exhibiting the larger benefit of the enhancement protocol at larger masses.

TABLE 4.5: Noise model and experiment settings for a low P_{prep}-high r scenario.

	Sensing qubit	**Ancilla qubit**
Q	3.14×10^6	3.14×10^6
T_1	100 µs @ 5 GHz	100 µs @ 5 GHz
T_2	100 µs @ 5 GHz	100 µs @ 5 GHz
T_ϕ	200 µs	200 µs
Readout error (r)	0.05	0.05
Preparation error (P_{prep})	0.001	0.001
Effective temperature	35 mK	35 mK
Rabi evolution time (τ)	100 µs	-

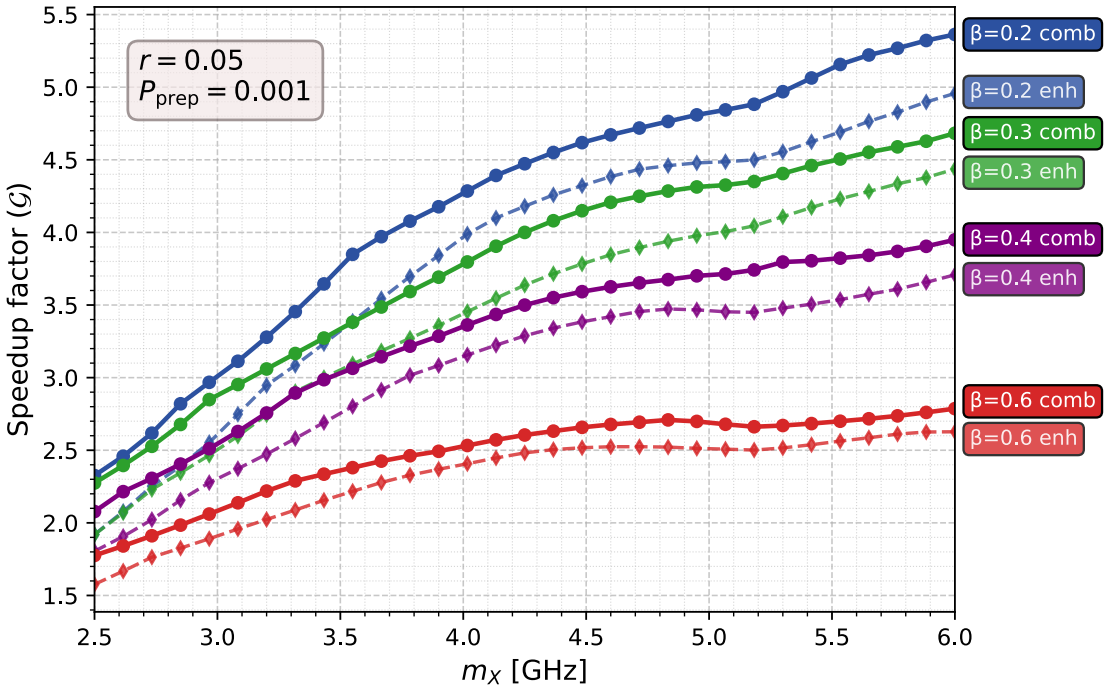

FIGURE 4.16: Speedup factor of the enhanced dark photon search experiment using the noise parameters summarized in Table 4.5, with respect to a base experiment, for different candidate masses m_X and values for the enhancement parameter β. The bare protocol using only the sensing qubit (*enh*) is compared with the same experiment including the information on the ancilla measurement (*comb*), i.e. the probability to succeed the circuit condition.

TABLE 4.6: Noise model and experiment settings for a high P_{prep}-low r scenario.

	Sensing qubit	**Ancilla qubit**
Q	3.14×10^6	3.14×10^6
T_1	100 µs @ 5 GHz	100 µs @ 5 GHz
T_2	100 µs @ 5 GHz	100 µs @ 5 GHz
T_ϕ	200 µs	200 µs
Readout error (r)	0.005	0.005
Preparation error (P_{prep})	0.01	0.01
Effective temperature	35 mK	35 mK
Rabi evolution time (τ)	100 µs	-

the enhancement protocol is always more convenient to carry out with respect to its equivalent (i.e. two base experiments).
The rise of $\mathcal{G}$ in Fig. 4.16 results from the thermal background population decreasing with higher qubit frequency, while the dark-matter signal magnitude is less affected. Since $d\tilde{P}/dP_e$ decreases rapidly with P_e, the before-enhancement thermal population (in the absence of signal) produces proportionally larger changes in $\tilde{P}$ than when thermal and signal contributions coexist.

High readout fidelity

In contrast to the high state preparation fidelity case, here we assume high readout fidelity and lower the state preparation fidelity. The noise model parameters associated with this scenario are reported in Tab. 4.6. Fig. 4.17 shows the speedup factors $\mathcal{G}$ corresponding to the parameters in Table 4.17. Notably, we obtain $\mathcal{G} < 1$ for most mass-β configurations, meaning that carrying out a base experiment using two non-communicating sensing qubits would be advantageous. This scenario highlights the need to achieve state-of-the-art qubit initialization fidelity for the enhancement protocol to be useful.

Optimal noise scenario

Here we test an optimistic –yet within reach of NISQ devices– case characterized by high readout and state preparation fidelity, as well as doubled quality factors and dephasing times of all the qubits involved (see Tab. 4.7). Note that the evolution time is kept at $\tau = 100$ µs since we expect the coherence time of dark matter to be $\tau_{\text{DM}} \sim 100$ µs and it is not a controllable parameter in experiments. Fig. 4.18 shows the speedup factors under these noise settings. For most enhancement parameters β, $\mathcal{G}$ remains above one for roughly the entire mass range under consideration. On the other hand, the speedup $\mathcal{G}$ is significantly smaller than the low-readout, high-state preparation scenario. This result, together with those obtained in the previous scenarios, suggests that the enhancement protocol efficiently reduces the impact of dark counts arising from readout errors, while initial-state preparation errors remain a challenge. The minimal requirement of using two coupled qubits for the enhancement protocol implementation, where only one directly picks up the dark matter signal, effectively reduces $\mathcal{G}$ by a factor of two in a two-qubit versus two-qubit comparison with the base experiment. By coupling multiple sensing qubits to an ancilla, following the scheme presented in Subsec. 4.1.3, the half-factor tends to cancel out. Since $\mathcal{G}$ surpasses 0.5 in all tested scenarios, we conclude that state preparation errors, despite

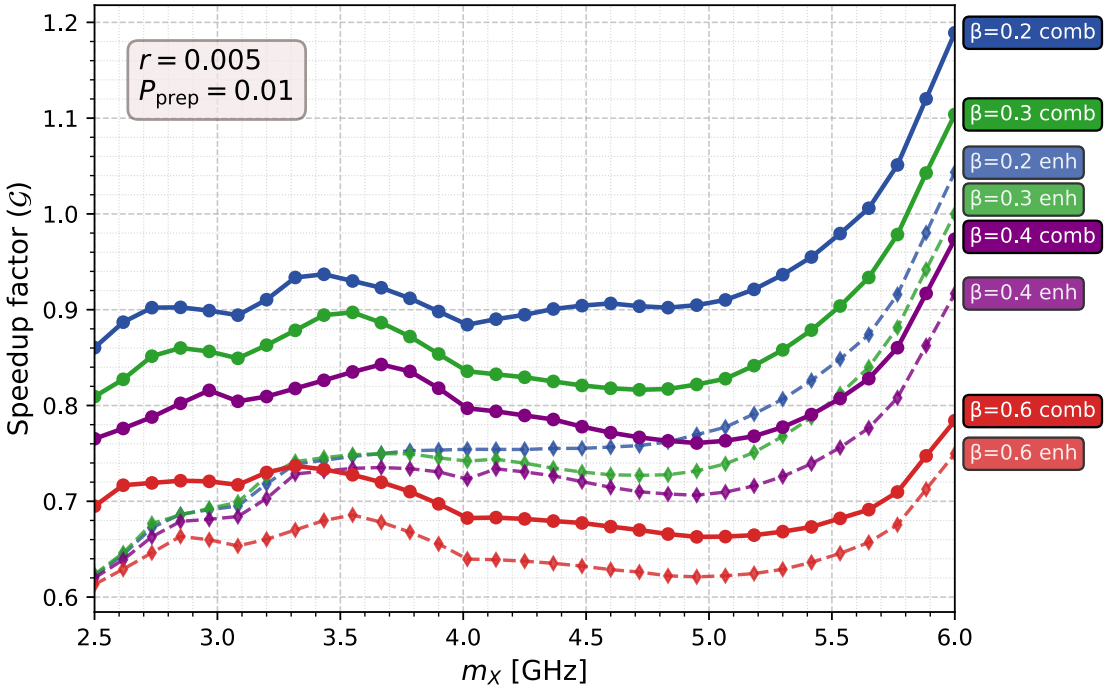

FIGURE 4.17: Speedup factor of the enhanced dark photon search experiment using the noise parameters summarized in Table 4.6, with respect to a base experiment, for different candidate masses m_X and values for the enhancement parameter β. The bare protocol using only the sensing qubit (enh) is compared with the same experiment including the information on the ancilla measurement (comb), i.e. the probability to succeed the circuit condition.

TABLE 4.7: Noise model and experiment settings in the optimal scenario.

	Sensing qubit	**Ancilla qubit**
Q	6.28×10^6	6.28×10^6
T_1	200 µs @ 5 GHz	200 µs @ 5 GHz
T_2	200 µs @ 5 GHz	200 µs @ 5 GHz
T_ϕ	400 µs	400 µs
Readout error (r)	0.005	0.005
Preparation error (P_{prep})	0.001	0.001
Effective temperature	35 mK	20 mK
Rabi evolution time (τ)	100 µs	-

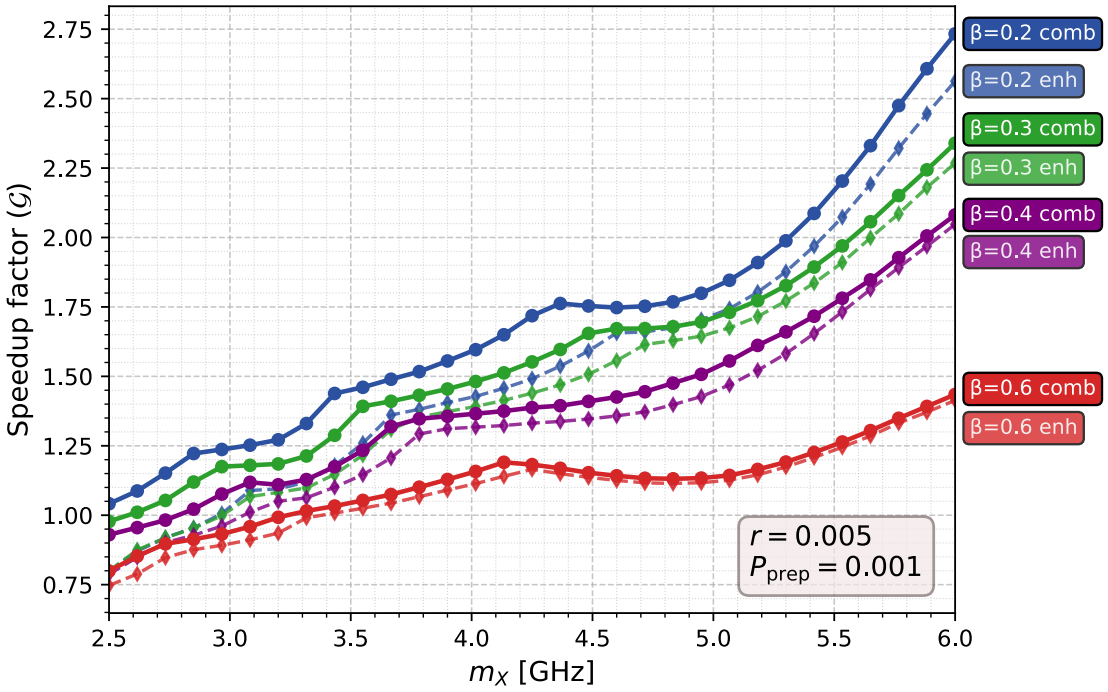

FIGURE 4.18: Speedup factor of the enhanced dark photon search experiment using the noise parameters summarized in Table 4.7, with respect to a base experiment, for different candidate masses m_X and values for the enhancement parameter β. The bare protocol using only the sensing qubit (enh) is compared with the same experiment including the information on the ancilla measurement (comb), i.e. the probability to succeed the circuit condition.

being more damaging in enhanced experiments than in base ones, still allow a margin for beneficial speedup for most noise configurations.

4.3.3 Exclusion limit projection

In Sec. 4.3.2, we focused on assessing the improvement in the sensitivity to dark matter of the enhanced experiment relative to the base experiment. Here, we attempt to estimate the exclusion limits achievable in an experiment within typical timespans of rare event search experiments.
In the absence of temporal drifts, and under the assumption that P_{prep}, r, Q, T, and gate fidelities remaining constant over the narrow frequency span of the dark matter signal peak, the exclusion limit on ϵ scales as $n_{\text{shots}}^{-1/4}$, due to the estimation of P_e being affected by the binomial statistics, and $P_e \propto \epsilon^2$. To estimate the executable number of shots for each probed frequency, given a fixed data-taking duration, we consider:

- DM-induced interaction with the sensing qubit, set to $\tau = 100$ µs.
- Active qubit reset operations, which can reasonably take less than 10 µs.
- Ancilla and sensing qubits readout, which is also expected to be shorter than 10 µs.
- Sum of the gate durations of the enhancing circuit. Considering the limited amount of gates involved, we attribute a total of around 1 µs to the gates execution.

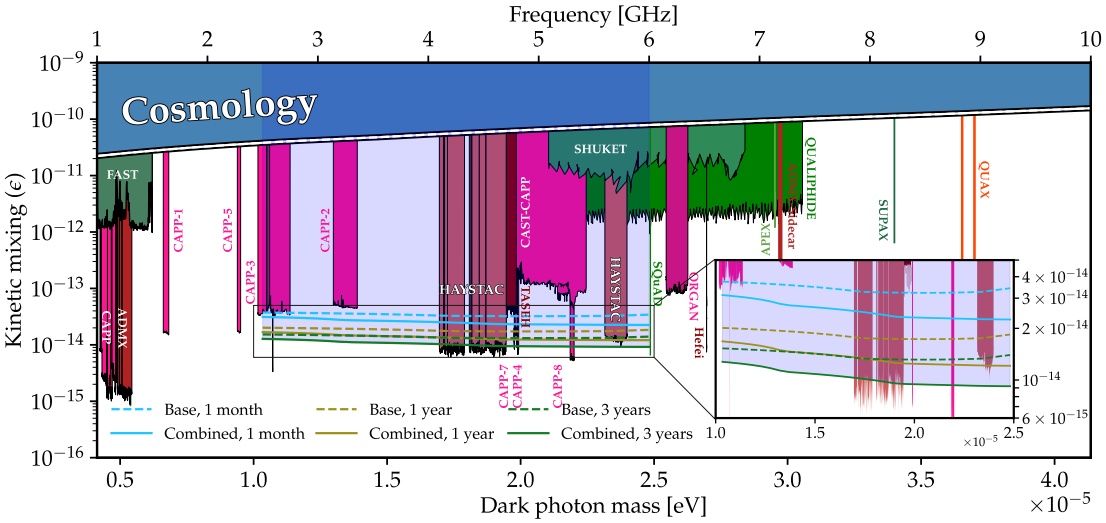

FIGURE 4.19: Mass-dependent exclusion limits at 95% C.L. on the kinetic mixing strength ϵ between the dark photon field and the Standard Model photon in the 1 - 10 GHz range. The inset shows the projected exclusion limits achievable in direct transmon detection search experiments. Labels *base* and *combined* indicate the original experiment proposal and the enhanced version introduced in this thesis.

- Classical overhead: the time necessary to store the measurement outcomes on classical hardware, which can be reduced to $\lesssim 1$ µs.

We set a conservative shot time of 130 µs and the frequency span of the tunable sensing qubits to 300 MHz. Considering 3000 flux bias points to probe frequency intervals of 100 kHz, we estimate around 80×10^6 shots per probed frequency in one year of data taking. In order to probe the 2.5 - 6.0 GHz interval with sensing qubits with a 300 MHz tuning range, 12 distinct sensing qubits with roughly disjoint frequency spans are required. With a total of 120 physical qubits, 10 copies of each sensing qubits can be employed in parallel, either stored on different chips, or within a single, larger one. Assuming the enhanced scheme to occur in a regime where many sensing qubits are coupled to the same ancilla, the speedup factor reported in Fig. 4.18 increases by a factor approaching two, according to Eq. 4.31. In this regime, most of the 120 qubits are designed as sensing, so that the multiplicities of the base and enhanced experiments are approximately the same, i.e. with the same number of physical qubits allows running the same amount of base and enhanced experiments. Running the experiment simulation and the statistical analysis in an optimal noise-error scenario, using the parameters reported in Table 4.7, we retrieve the mass-dependent kinetic mixing exclusion limit $\epsilon_{95\%\,\text{C.L.}}$, assuming one month, one year, and three years of data taking. The results, compared to the exclusion limits set by other experiments in the 1 - 10 GHz range, are shown in Fig. 4.19. The limits for the data collection for one year were simulated directly, while those for one month and three years were extrapolated according to the $n_{\text{shots}}^{-1/4}$ scaling.

With respect to other haloscope-based experiments, the direct detection performed with transmon qubits covers a much larger spectrum, including currently unexplored intervals centered around 3.0 GHz and 3.7 GHz. Over three years of data taking, exclusion limits $\sim 1 \times 10^{-14}$ can be achieved across the full spectrum under consideration. This exclusion limit is competitive with existing haloscope experiments such as CAPP, HAYSTACK, and TASEH, but extended to a broader range of frequencies. In agreement with the speedup factors shown in Fig. 4.18, the combined experiment

(i.e. using the enhanced protocol combined with the ancilla excitation probability information) has the same sensitivity to ϵ as the base experiment using 2-5 times more data.

This chapter concludes the part of the thesis devoted to exploring the sensitivity of transmon qubits to weak resonant fields, with particular emphasis on their potential for detecting light-coupled dark matter candidates such as the dark photon. In addition, we have investigated a protocol in which the weak signal accumulated by a sensing qubit is mapped onto a more accessible observable, thereby enabling a more efficient sampling strategy and an effective speedup of the experiment. Finally, through numerical simulations, we quantitatively benchmarked the performance of this enhanced scheme against a baseline approach, highlighting the achievable gains in sensitivity and efficiency. The next chapter describes the development of a sensing device allowing us to carry out an enhanced search experiment, towards fabrication and characterization in a cryogenic environment.

Chapter 5

Design and characterization of transmon qubit devices

This chapter focuses on the design, simulation, and characterization of transmon qubit devices towards developing a detection experiment able to implement the gate-based signal enhancement scheme discussed in Chapter 4. The proposed devices leverage a coplanar architecture, where transmon qubits are capacitively coupled to coplanar waveguide resonators. When needed, qubits in the same device are coupled through a CPW resonator to enable an entangling cross-resonance interaction.

5.1 Qubit design and simulation

The coherence time of transmon qubits is strongly influenced by the shunt-capacitance pad geometry: the pad shape determines the electric-field concentration within lossy oxide interfaces and inside the substrate, which in turn affects dielectric bulk and surface-loss contributions to decoherence [154]. In addition, the pad geometry determines the dipole length l and the shunt capacitance C_s, modifying the qubit's coupling to external electromagnetic fields, including dark-matter–driven fields (see Eqs. 3.28 and 3.39).
Upon studies demonstrating state-of-the-art coherence times [149–151], we adopted a floating double-pad geometry consisting of two large symmetric pads connected by a Josephson element (a single junction or a SQUID). The design was carried out using the KQCircuits Python library (v. 4.9.4) [214], developing a custom transmon qubit layout named *clockmon*. The clockmon qubit supports up to six T-shaped couplers with tunable length, width, and distance from the pads. An optional circular notch pattern provides additional control over C_s without altering the overall pad extension. Two metal leads with a customizable relative angle connect each pad to a junction (or SQUID) terminal, enabling electrical contact for a variety of junction designs. Fig. 5.1 shows some of the available clockmon design options.
The following subsections describe the simulation methods used to extract parameters related to the qubit's frequency, anharmonicity, and dielectric loss estimations, for the specific geometry adopted.

5.1.1 Capacitance matrix extraction

To estimate the effective shunt capacitance and coupling to the readout resonator of a floating qubit, finite element simulations of the specific qubit-coupler geometry were required. These were carried out using the Ansys Q3D extractor (release 2022 R1) [215], a quasi-static solver that enables reconstructing the Maxwell capacitance matrix of each node in the equivalent circuit. Fig. 5.2 illustrates the circuit diagram of

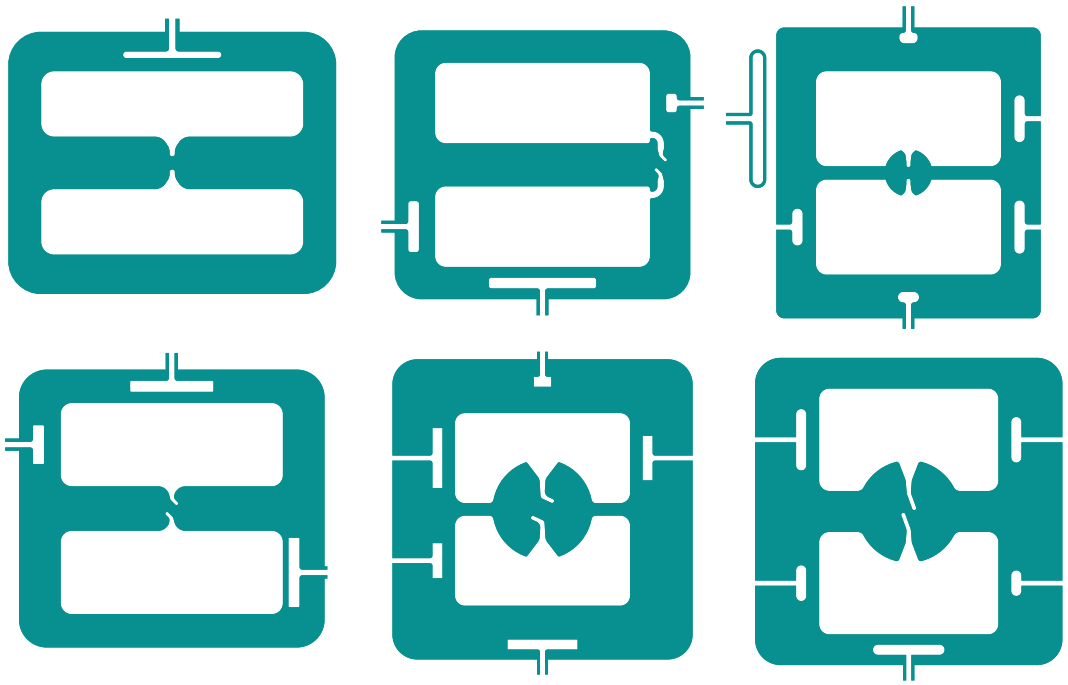

FIGURE 5.1: Examples of geometrical configurations allowed within the KQCircuits-compatible clockmon qubit.

the qubit pads and their couplings to ground and the readout resonator.
Using the node flux representation, and following the steps reported in [216], the capacitance values of the floating qubit networks can be reduced to those of an effective grounded transmon, with C_g corresponding to that in Eq. 2.61. The formulas linking the two representations are

$$C_s = \frac{(C_{33} + C_{13})(C_{22} + C_{12})}{C_{33} + C_{22} + C_{13} + C_{12}} + C_{23}, \tag{5.1}$$

$$C_g = \frac{C_{12}C_{33} - C_{13}C_{22}}{C_{22} + C_{12} + C_{33} + C_{13}}. \tag{5.2}$$

The right-hand terms in Eqs. 5.1 and 5.2 were estimated using Ansys Q3D through a quasi-static three-dimensional finite element simulation. The simulated layout consisted of the transmon qubit and the readout resonator T-shaped coupler, made floating. The other readout resonator components (such as the CPW or other couplers to structures far from the qubit, contributing to C_r and L_r) are not relevant in the calculation of C_s and C_q as they are either too far from the qubit pads or do not host voltage anti-nodes of the readout mode.
At this simulation stage, a straight 200 µm waveguide extension was added to the coupler pad. This procedure adds a small correction to C_{22} and C_{33}, subtracting from the ground plane the area near the qubit that will be occupied by the readout resonator in the full design. The total effective qubit capacitance C_Σ is calculated by adding to C_s a stray junction capacitance $C_J = 0.1$ fF. The qubit design was dimensioned to reach $C_\Sigma \approx 90$ - 100 fF, ensuring an anharmonicity α in the 190 - 240 MHz range (depending on the qubit frequency), while maintaining the transmon regime $E_J/E_C \gtrsim 50$ for frequencies $\omega_q/2\pi$ of a few-GHz.

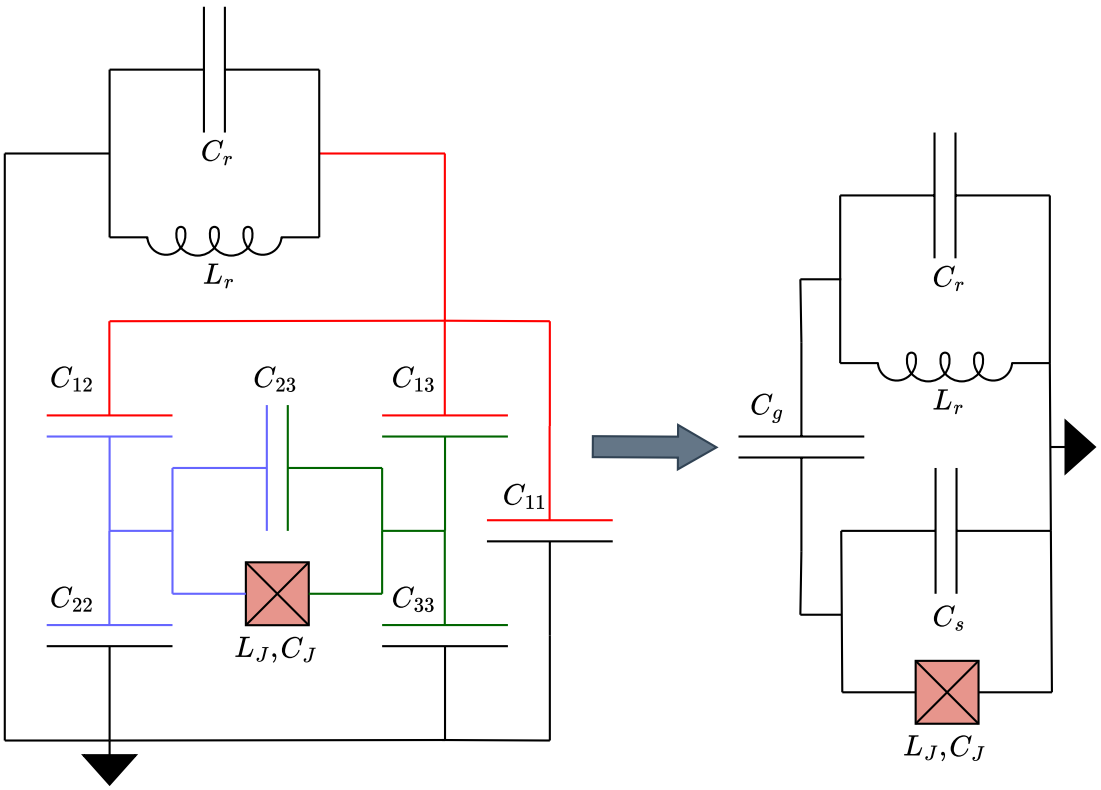

FIGURE 5.2: Circuit diagram of a floating transmon coupled to a readout resonator, with nodes 1, 2, 3 indicating the resonator coupler, its closest pad, and its farthest pad, respectively (left). Equivalent circuit diagram of a grounded transmon coupled to a readout resonator with a capacitance C_g (right).

TABLE 5.1: Thicknesses and loss tangent values considered for the transmon dielectric loss simulations.

Region	**MA**	**SA**	**MS**	**Substrate**	**Air**	**Metal**
Thickness [nm]	4.8	2.4	0.3	550	1200	200
Loss tangent	9.9×10^{-3}	1.7×10^{-3}	3.5×10^{-4}	1.3×10^{-7}	0	0

5.1.2 Dielectric losses

As discussed in Subsec. 2.3.1, dielectric losses in transmon qubits are one of the leading causes of decoherence in transmon qubits with state-of-the-art coherence times. The geometry dependence of dielectric losses can be captured using finite-element solvers by computing the electric field distribution for the qubit mode and calculating the fraction of energy stored inside the dielectric substrate of the chip and the oxide interfaces between materials. The energy participation ratios (EPRs) extracted can be combined with the loss tangent attributed to each lossy element to retrieve the dielectric-limited quality factor Q_{dielec}, according to Eq. 2.82.

A crucial problem in leveraging finite-element 3D solvers for this task is the fact that the electric field diverges at metal edges, i.e. close to oxide interfaces, where high precision in estimating the electric field is desirable. Achieving sufficient precision through mesh refinement is highly memory-intensive, limiting the feasibility of full 3D simulations on modern desktop computing resources. To address this, a hybrid 3D–2D strategy can be adopted. In this approach, the 3D solver is used to evaluate EPRs in noncritical regions, while in critical metal edge regions it only provides the total stored energy. A complementary 2D solver then models the cross-section field distribution of the metal edges, extracting normalized EPR contributions from vacuum, dielectric substrate, and interfaces. By combining the normalized results from the 2D simulations with the total energy information obtained from the 3D model, the effective EPRs of the metal edge regions can be reconstructed. This method is accurate under the approximation that the metal edge region EPRs are constant along the metal perimeters, which is reasonable to assume where gaps between metals remain roughly constant.

Fig. 5.3 illustrates the 3D and 2D steps of the dielectric loss simulation of the double pad transmon. In the 3D step (Fig. 5.3a), the double pad is simulated using the Ansys HFSS [217] Eigenmode (release 2022 R1), replacing the junction element with a lumped linear inductance L_J and parasitic capacitance C_J. The 2D step extracts a cross-section in the layout as indicated in Fig. 5.3b and simulates a DC field within a restricted area, with finer meshing where high field concentrations are expected.

This dielectric loss estimation approach requires setting specific oxide layer thicknesses within MA, MS, and SA, which may vary across different fabrication techniques. Moreover, the oxide layers are assumed to have uniform thicknesses, which may not be guaranteed in the fabrication process. Leveraging the measurement reported in [158], we consider the median thickness of the three surfaces reported in Table 5.1.

Fig. 5.4 illustrates how the hybrid 3D-2D approach captures a different surface EPR distribution than relying on the 3D simulation alone. The much coarser meshing resulting from the 3D eigenmode simulation suggests that this approach tends to underestimate the surface EPR, especially in the thinnest ones (MS and MA). Combining the EPR in the 3D-only and 3D-2D approaches with the loss tangent reported in Table 5.1, we obtain $Q_{\text{dielec}} = 4.3 \times 10^6$ and $Q_{\text{dielec}} = 2.3 \times 10^6$, respectively.

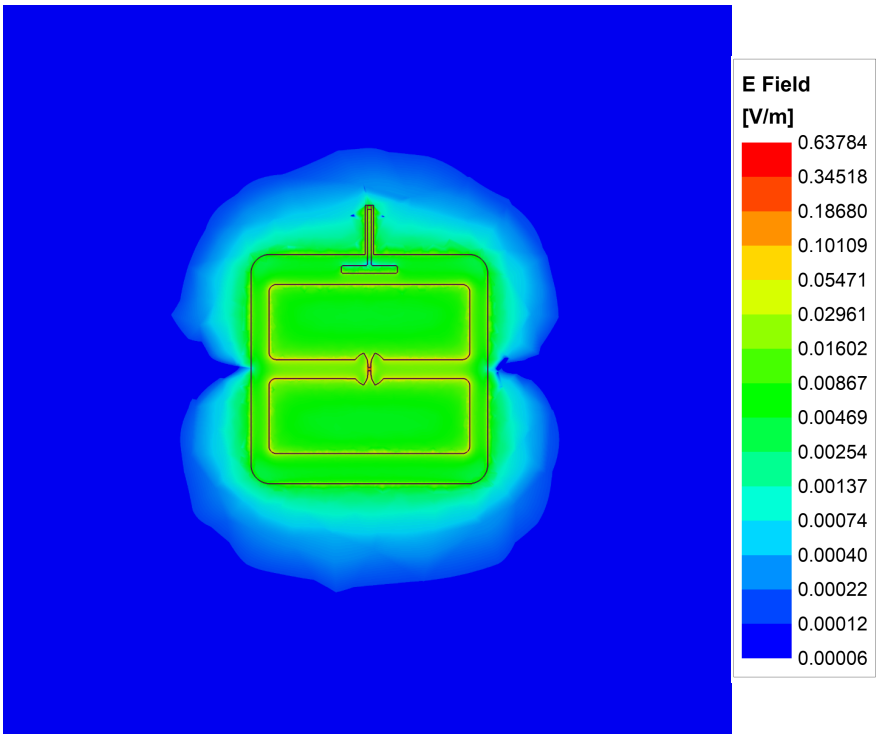

(A) 3D Ansys HFSS Eigenmode field solution.

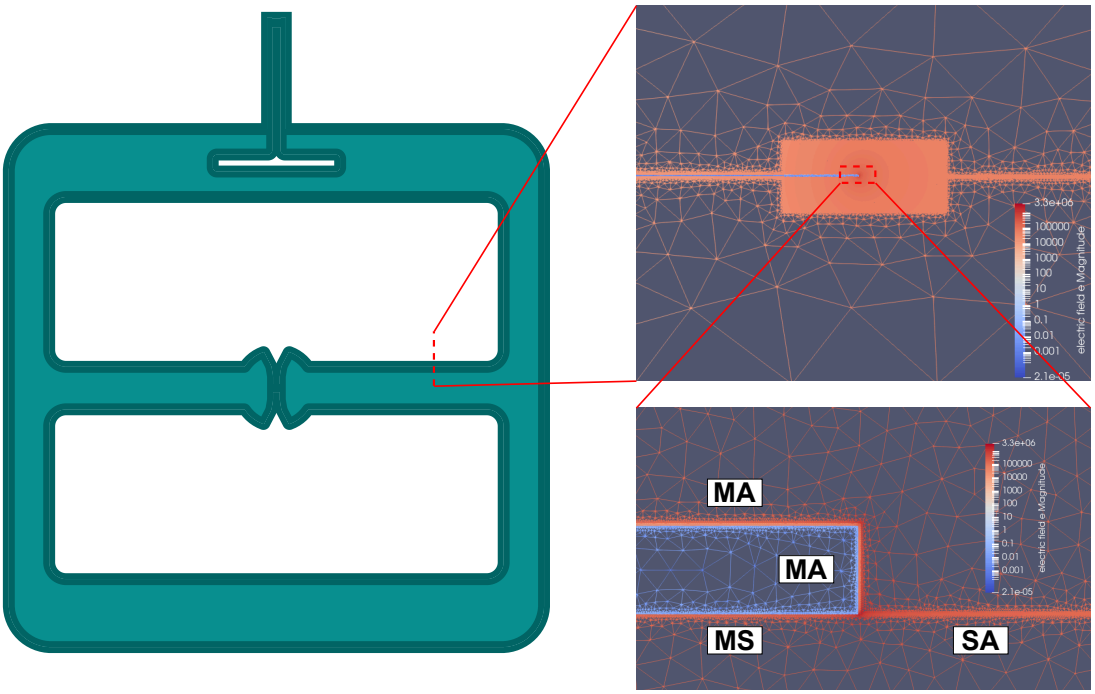

(B) 2D cross-section DC simulation.

FIGURE 5.3: EPR finite-element simulation for a transmon qubit. (A) 3D step, rendering the full geometry (including substrate and air volumes with thicknesses reported in Table 5.1, not shown in the projection). The electric field intensity at the qubit's eigenmode is displayed on a logarithmic scale. (B) 2D step, simulating the electric field in a metal-edge cross-section, with fine meshing on the critical regions.

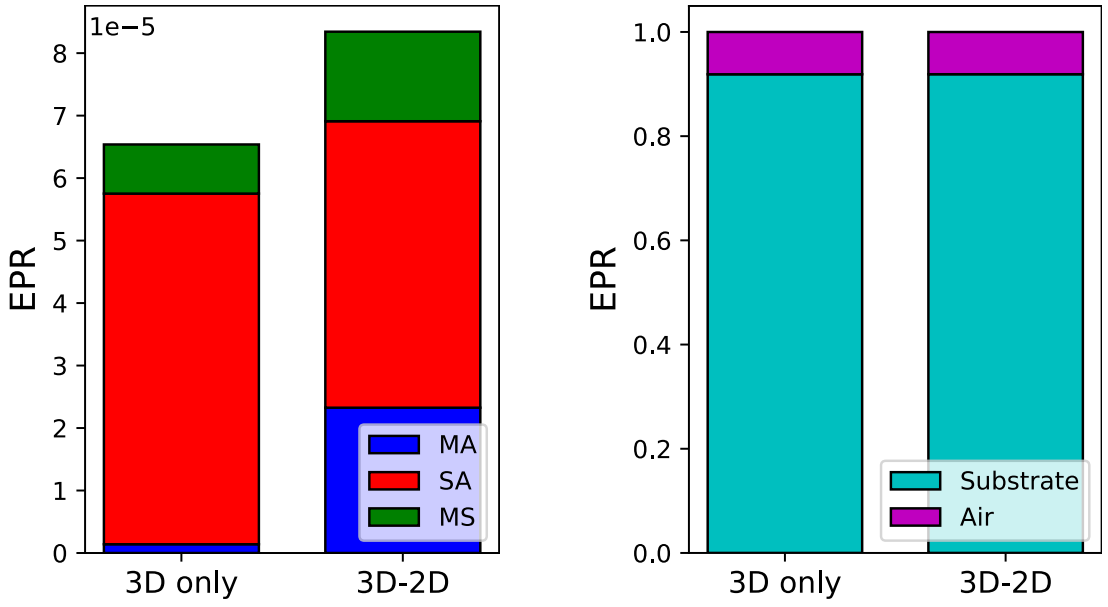

(A) Surface EPR.

(B) Bulk EPR.

FIGURE 5.4: Energy participation ratios across (A) oxide interfaces and (B) bulk, simulated for the same design before and after applying the correction estimated through cross-section simulation near metal edges.

5.1.3 Couplings to driveline and fluxline

The photon-sensing experiment discussed in Chaps. 3 and 4 requires flux tunability of the transmons to probe a range of dark photon candidate masses. This motivates the study of different flux-line geometries and a quantitative assessment of their coupling to the qubit, identifying a balance between inductive and capacitive contributions. Strong inductive coupling is desirable for the fluxline, as it ensures that a large magnetic flux is threaded through the SQUID loop per unit current, while stray capacitive coupling should be minimized to suppress qubit decay through the flux line. A similar trade-off applies to the driveline, which must couple (capacitively) strongly enough to enable fast single-qubit gates, yet weakly enough to limit qubit relaxation through the line. The extraction of the effective couplings was carried out using Ansys HFSS.

Fluxline modeling

The fluxline is a grounded DC line that allows us to exert an external flux through the SQUID loop. The current path near the SQUID determines the amount of flux quanta induced, given a current intensity. Two fluxline geometries are frequently documented in the literature [145, 218–220], which we will refer to as *L*-shaped and *straight*-shaped.

In order to address the most convenient fluxline geometry, we created a SQUID loop region placeholder, consisting of a 30×30 µm^2 region between the qubit leads. We then generated a 1 mA DC current flowing through the fluxline port, simulating the current intensity and direction nearby the placeholder and the magnetic field strength $\mathbf{H}$ in the SQUID area. The magnetic flux threading the loop was calculated, in units of flux quantum Φ_0, as

$$\phi_{\text{ext}} = \frac{1}{\Phi_0}\int_S \mathbf{B}\cdot d\mathbf{S} = \frac{\mu_0}{\Phi_0}\int_S \mathbf{H}\cdot d\mathbf{S}, \tag{5.3}$$

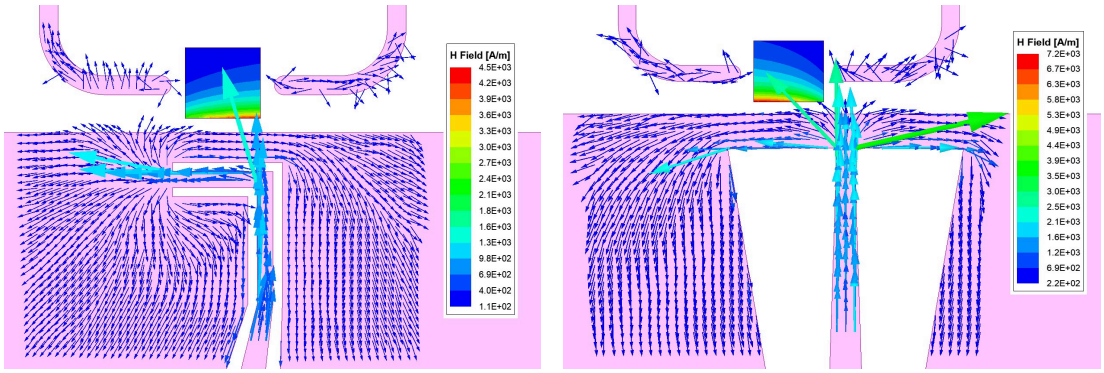

(A) L-shape. (B) Straight shape.

FIGURE 5.5: 3D Ansys HFSS current solutions for (A) an L-shaped fluxline and (B) a straight fluxline. The SQUID loop is substituted by a placeholder square area, and the magnetic field intensities $|\mathbf{H}| = \mu_0|\mathbf{B}|$ inside those areas are reported.

TABLE 5.2: Effective coupling strengths between qubit and flux line and derived qubit emission rate contributions at $\omega_q/2\pi = 5$ GHz.

	L-shape	**Straight shape**
ϕ_{ext} @ 1 mA	0.14	0.27
C_{f} [aF]	14.5	93.1
$\Gamma_{\text{Purcell, ind}}$ [ms^{-1}]	0.17	0.65
$\Gamma_{\text{Purcell, cap}}$ [ms^{-1}]	0.10	4.35

where S is the SQUID loop area. The L-shaped and the straight-shaped fluxlines were compared, keeping the same distance of 8.3 µm from the ground plane edge. The current distributions and magnetic field magnitudes in the placeholder are shown in Fig. 5.5. Table 5.2 collects the inductive and capacitive couplings to the qubits, as well as the individual decay rate contributions $\Gamma_{\text{Purcell, cap}}$ and $\Gamma_{\text{Purcell, ind}}$, calculated using Eqs. 2.84 and 2.85.
The two geometries exhibit markedly different coupling strengths. The L-shaped fluxline induces only about half as many flux quanta per mA as the straight fluxline. However, its effective capacitance to the qubit is significantly smaller, leading to a stronger suppression of spontaneous emission. These differences can be understood by noting that the L-shaped fluxline couples capacitively to the two pads of the qubit more symmetrically than the straight-shaped one, thereby reducing the effective coupling. The straight fluxline, in fact, is displaced from the junction leads midpoints, which enhances its coupling to one pad relative to the other. To justify the different inductive coupling strengths, we show in Fig. 5.5 that the L-shaped geometry generates a secondary current flow opposite to the primary one. Although weaker, this counterflow runs closer to the SQUID and partially shields it from the magnetic field generated by the primary current flow. Such compensation does not occur in the straight geometry, where the current splits evenly and only one branch contributes significantly to threading flux through the loop.

Driveline modeling

Unlike fluxlines, drivelines are not connected to the ground plane. Their couplings to the qubits affect gate durations at a given pulse amplitude. Assuming a signal with

RMS voltage V_0 on the driveline, the coupling strength to the qubit is

$$\Omega = V_0 \frac{C_d}{C_\Sigma + C_d} \sqrt{\frac{\hbar}{2Z_0}}, \tag{5.4}$$

and the duration of a π-pulse is

$$t_\pi = \frac{\pi}{\Omega} = \frac{C_\Sigma + C_d}{V_0 C_d} \sqrt{\frac{2Z_0}{\hbar}}. \tag{5.5}$$

Assuming a characteristic line impedance of 50 Ω, $V_0 = 125$ µV (corresponding to an on-chip power of -65 dBm) and $C_d = 90$ aF, the π-pulse duration for a qubit with $\omega_q/2\pi = 5$ GHz will correspond to $t_\pi \approx 16$ ns. We consider the capacitance value of $C_d = 90$ aF as the desirable coupling for a driveline, as it corresponds to an emission rate of approximately 250 µs, compatible with the target T_1 in our sensing experiment. In our device layout, driveline tapering was designed in an attempt to reach the qubit's proximity while keeping the bulk of the line far enough to decrease spurious coupling.

5.2 Qubit readout structure

The standard dispersive readout, introduced in Sec. 2.2.2, requires matching target parameters, e.g. dispersive shift χ, readout resonator linewidth k, and readout resonator frequency $\omega_r/2\pi$. Except for the Josephson element, which we always treat as a lumped nonlinear inductor with known critical current, all the other parameters are strictly related to design features such as pad shapes, coupler sizes, impedance engineering, and waveguide lengths. This section describes the technique implemented to tie target Hamiltonian parameters to a corresponding geometry.

5.2.1 Dispersive coupling engineering

Under the assumption of purely capacitive couplings between the readout resonator and its qubit, the coupling strength g in the dispersive limit can be calculated using Eq. 2.61. To extract the dispersive shift χ, we leveraged the QuCAT toolbox (v. 1.0.3) [221], a quantum circuit analyzer that retrieves the Hamiltonian of the quantum circuit as

$$\hat{\mathcal{H}} = \sum_m \hbar\omega_m \hat{a}_m^\dagger \hat{a}_m + \sum_j \sum_{n\geq 2} E_j \frac{(-1)^{n+1}}{(2n)!} \hat{\varphi}_j^{2n}, \tag{5.6}$$

with

$$\hat{\varphi}_j = \sum_m \varphi_{\mathrm{zpf},m,j} (\hat{a}_m + \hat{a}_m^\dagger) = \sum_m \frac{2\pi}{\Phi_0} \sqrt{\frac{\hbar}{2\omega_m C_m}} (\hat{a}_m + \hat{a}_m^\dagger). \tag{5.7}$$

Here, m is the mode index, j indicates the Josephson junction with inductive energy E_j, and n is the Taylor expansion order of the cosine potential of each junction. The terms $\varphi_{\mathrm{zpf},m,j}$ are the zero-point phase fluctuations in mode m and junction j, where each mode is associated with frequency $\omega_m/2\pi$ and capacitance C_m. Given an arbitrary circuit, the modes are identified by leveraging black-box quantization, i.e. linearizing the Josephson elements, and modeling an equivalent circuit consisting of a series of RLC resonators, based on the admittance matrix poles, through Foster decomposition [222]. Once the modes are obtained, the Hamiltonian in Eq. 5.6 is derived, perturbatively adding the junction nonlinearities. This approach is valid only for low-dissipative weakly anharmonic circuits (which is the case of transmon qubits). Diagonalizing the

Hamiltonian at first-order perturbation theory, we obtain

$$\begin{aligned}\hat{\mathcal{H}} = &\sum_m \left[\left(\hbar\omega_m - A_m - \sum_{n\neq m} \frac{\chi_{mn}}{2} \right) \hat{a}_m^\dagger \hat{a}_m \right] \\ &- \sum_m \left[\frac{A_m}{2} \hat{a}_m^\dagger \hat{a}_m^\dagger \hat{a}_m \hat{a}_m + \sum_{n\neq m} \chi_{mn} \hat{a}_m^\dagger \hat{a}_m \hat{a}_n^\dagger \hat{a}_n \right],\end{aligned} \tag{5.8}$$

where A_m is the anharmonicity (self-Kerr) of mode m, and χ_{nm} is the cross-Kerr term for modes m and n, respectively, linked to the state-dependent mode frequency shifts. In order to determine the values of L_J and the coupling capacitance C_g for a single qubit coupled to a readout resonator, so that the system matches a target qubit frequency $\omega_q^t/2\pi$ and dispersive shift χ^t, taking into account the dependence of C_Σ on C_g, we fixed the resonator frequency and numerically minimized:

$$f : \begin{pmatrix} L_J \\ C_g \end{pmatrix} \rightarrow \begin{pmatrix} |\omega_q - \omega_q^t| \\ |\chi - \chi^t| \end{pmatrix}, \tag{5.9}$$

where ω_q was the qubit mode in the effective Hamiltonian (see Eq. 5.8), and χ the cross-Kerr. Both quantities were extracted simultaneously from the QuCAT analysis of the lumped circuit diagram. Once C_g was determined, the corresponding coupler size in the design was obtained from an empirical relationship derived from multiple capacitive simulations. In particular, the coupler's length (see Fig. 5.6) was chosen as the sweep variable, leaving other parameters fixed, and a capacitive Ansys Q3D simulation was carried out for each point in the sweep, extracting the corresponding C_Σ and C_g as described in Subsec. 5.1.1.

5.2.2 Readout resonator linewidth

The linewidth of the readout resonator k determines the Purcell decay rate of the qubit (see Eq. 2.83), as well as the readout pulse duration. In particular, the pulse duration must be enough to let the resonator reach a steady state with a stable average photon occupation number $\bar{n}$, which occurs within a timescale of the order of $1/k$. In designing the readout resonator, the trade-off between having a low Purcell decay rate and short readout pulses should be optimized.
The input impedance for a lossless transmission line is [96]

$$Z_{\text{in}}(\omega) = Z_0 \frac{Z_L + iZ_0 \tan\left(\frac{\pi}{2}\frac{\omega}{\omega_r}\right)}{Z_0 + iZ_L \tan\left(\frac{\pi}{2}\frac{\omega}{\omega_r}\right)}, \tag{5.10}$$

where Z_0 is the line characteristic impedance, and Z_L is the load impedance at the far end of the CPW. Considering a $\lambda/4$ readout resonator capacitively coupled to a feedline, and shorted to ground at the far end, $Z_L = 0$. Near resonance ($\omega \approx \omega_r$), Eq. 5.10 simplifies to

$$Z_{\text{in}}(\omega) \rightarrow Z_{\lambda/4} = -iZ_0 \frac{2}{\pi} \frac{\omega_r}{\omega - \omega_r}. \tag{5.11}$$

The current-voltage relations at the feedline terminals can be related using the transfer matrix formalism (ABCD)

$$\begin{pmatrix} V_1 \\ I_1 \end{pmatrix} = \begin{pmatrix} A & B \\ C & D \end{pmatrix} \begin{pmatrix} V_2 \\ I_2 \end{pmatrix}, \tag{5.12}$$

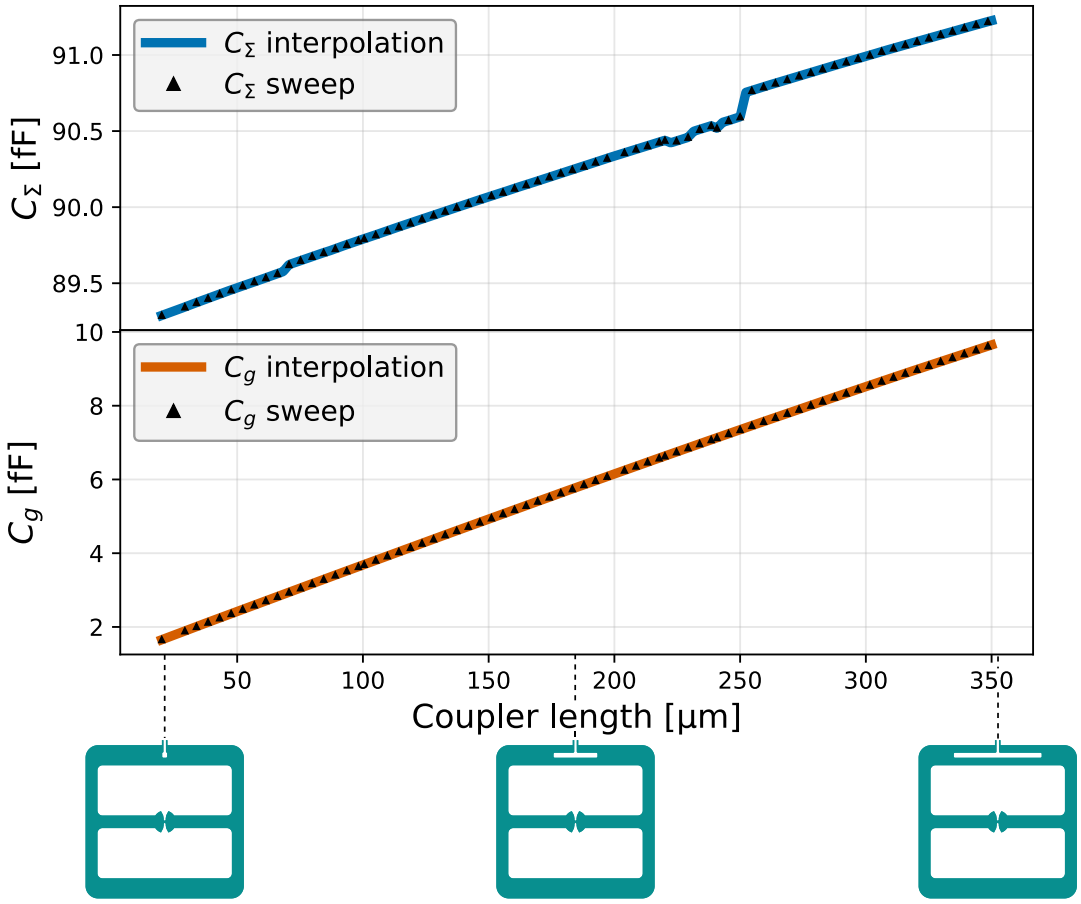

FIGURE 5.6: Qubit effective shunt capacitance C_Σ and coupling to the readout resonator C_g as a function of the coupler length, extracted by sweeping the capacitance matrix extraction in the coupler length variable.

where V_1 and I_1 refer to the feedline input, while V_2 and I_2 refer to the feedline output. By modeling the resonator and its feedline capacitance C_k as a parallel impedance

$$Z(\omega) = \frac{1}{i\omega C_k} + Z_{\lambda/4}, \tag{5.13}$$

the transfer matrix elements become $A = D = 1$, $C = 1/Z(\omega)$, $B = 0$. The forward transmission coefficient $S_{21}(\omega)$ can be written in terms of ABCD elements as [223]

$$S_{21}(\omega) = \frac{2}{A + B/Z_0 + CZ_0 + D}. \tag{5.14}$$

Therefore,

$$S_{21}(\omega) = \frac{2}{2 + Z_0/Z(\omega)}. \tag{5.15}$$

The coupling quality factor Q_c, assuming that internal losses are negligible ($Q_i \gg Q_c$, with Q_i the internal quality factor), is equal to

$$Q_c = \frac{\omega_r \frac{dB}{dw}|_{\omega_0}}{G(\omega)}, \tag{5.16}$$

where $G(\omega)$ is the external conductance related to the power leaving the resonator into the feedline, defined as

$$G(\omega) = \mathrm{Re}\left\{\frac{1}{Z_0 + -\frac{i}{\omega C_k}}\right\}, \tag{5.17}$$

and $B(\omega)$ is the reactive susceptance, related to the energy stored in the resonator:

$$B(\omega) = \mathrm{Im}\left\{\frac{1}{Z_{\lambda/4}}\right\} = \frac{\pi}{2Z_0}\frac{\omega - \omega_r}{\omega_r}. \tag{5.18}$$

Substituting Eq. 5.17 and Eq. 5.18 into Eq. 5.16, in the limit of a weak coupling ($\omega C_k Z_0 \ll 1$), we obtain the quality factor expression

$$Q_c = \frac{\pi}{2\omega_r^2 Z_0^2 C_k^2}. \tag{5.19}$$

From the quality factor Q definition, $Q_c = \omega_r/k$, therefore:

$$k = \frac{2}{\pi}\omega_r^3 Z_0^2 C_k^2. \tag{5.20}$$

For a $\lambda/2$ resonator, with impedance

$$Z_{\lambda/2} = -iZ_0\frac{1}{\pi}\frac{\omega_r}{\omega - \omega_r}, \tag{5.21}$$

quality factor and linewidth become

$$Q_c = \frac{\pi}{\omega_r^2 Z_0^2 C_k^2} \qquad k = \frac{1}{\pi}\omega_r^3 Z_0^2 C_k^2. \tag{5.22}$$

Similarly to the approach in Subsec. 5.2.1, we identify a mapping between the coupling capacitance C_k, extracted using the Ansys Q3D capacitance analysis, and one

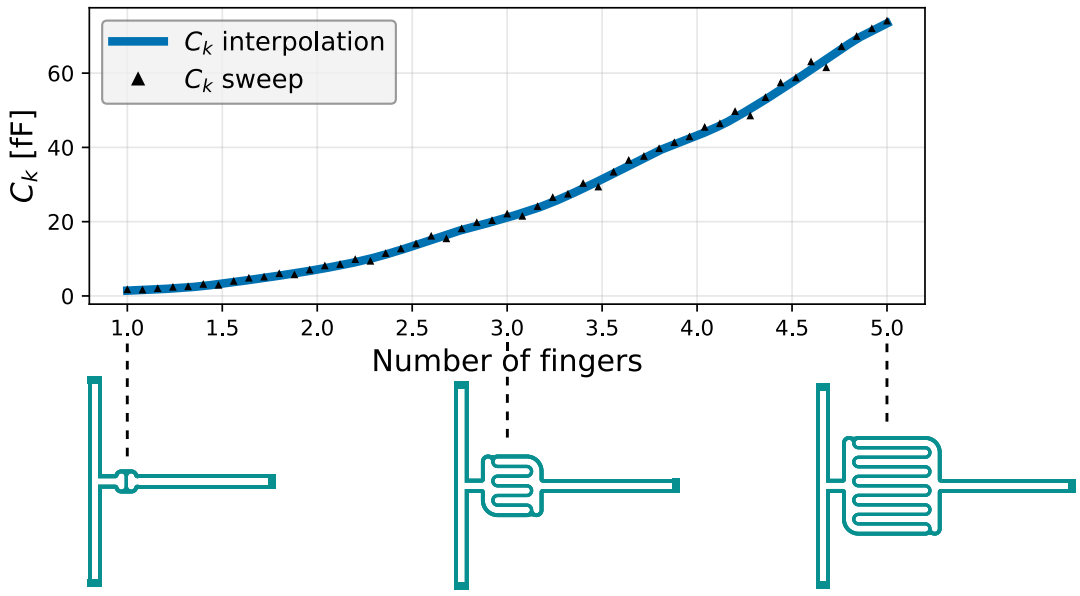

FIGURE 5.7: Readout resonator coupling capacitance C_k to the feedline, as a function of the number of fingers in the interdigitated conductor variable.

geometrical parameter. The coupler is a rounded interdigitated element that smoothly increases as a function of the finger number (the latter extended to be continuous, see Fig. 5.7). Waveguide segments have been added to the Ansys Q3D simulations, to better capture the transmission line-ground plane placement on a realistic layout. Subsequently, the effect of those waveguides was subtracted to retrieve C_k. By leveraging this mapping, once the target C_k was chosen, the design parameter was automatically determined in the layout.

5.2.3 Purcell filter

A standard approach to radically improve the readout pulse duration without affecting the qubit's T_1 is to filter out the feedline impedance seen by the qubit far from the resonator frequency ω_r. This can be achieved by adding a Purcell filter, i.e. a bandpass resonator between feedline and readout resonator, with $\omega_p \approx \omega_r$ [95]. We engineered a feedline-embedded wideband resonator, matching the architecture demonstrated in [224]. In this implementation, the Purcell filter is a waveguide with one capacitively coupled end to the feedline input port, and the other end split into two branches. One branch connects the readout output port, while the other branch is shorted to ground. Circuit analysis shows the qubit's Purcell decay quality factor contribution to be

$$Q_{\text{Purcell}} = Q_F \frac{C_\Sigma}{C_F} \left(\frac{|Z_g||Z_k|}{Z_0^2} \right)^2 \left(\frac{2\delta + \delta^2}{1+\delta} \right), \tag{5.23}$$

with $\delta = (\omega_q - \omega_r)/\omega_r$, Q_F being the Purcell filter quality factor, C_F the equivalent LC capacitance of the Purcell filter mode, Z_g and Z_k the impedances of the qubit-readout resonator and readout resonator-Purcell filter capacitors, respectively.
Considering standard design values $Q_F = 10$, $C_\Sigma = 90$ fF, $C_F = 285$ fF (corresponding to $\omega_p/2\pi = 7$ GHz and $Z_0 = 50\ \Omega$), $\omega_q/2\pi = 5$ GHz, $Z_g = 1/(i\omega_q C_g)$, $Z_k = 1/(i\omega_q C_k)$, with $C_g = C_k = 5$ fF, $Q_{\text{Purcell}} \approx 180 \times 10^6$. Without Purcell filter, considering the same coupling strengths C_k and C_g and frequencies, the quality

factor can be derived using Eq. 2.83, knowing that $Q_{\text{Purcell}} = \omega_q/\Gamma_{\text{Purcell, res}}$, finding $Q_{\text{Purcell}} \approx 4 \times 10^6$. Qualitatively, the use of a Purcell filter enables either stronger coupling between the qubit and the readout structure, thereby speeding up the readout, or further suppressing Purcell decay while maintaining the same readout pulse duration.

5.3 Two-qubit gate engineering

Among commonly leveraged entangling interactions introduced in Subsec. 2.2.3, the cross-resonant one was chosen. This choice is motivated by the possibility of engineering purely microwave-driven cross-resonance interactions, without adding constraints to the flux tunability of sensing and ancilla qubits in the detection protocol. Moreover, the qubit-qubit coupling can be mediated by a bus resonator (CPW) with fixed frequency, avoiding technological overhead brought by tunable coupler schemes. Notably, the echoed cross-resonance is the two-qubit gate natively implemented in some of the quantum devices available on the IBM cloud-based platform at the time of writing.

5.3.1 Tuning the qubit-qubit coupling

The target Hamiltonian values χ_1^t, χ_2^t, ω_{q1}^t, ω_{q2}^t, g_1^t, g_2^t were determined following a procedure analogous to the one described in Subsec. 5.2.1, minimizing the function

$$f : \begin{pmatrix} L_{J1} \\ L_{J2} \\ C_{g1} \\ C_{g2} \\ C_{c1} \\ C_{c2} \end{pmatrix} \rightarrow \begin{pmatrix} |\omega_{q1} - \omega_{q1}^t| \\ |\omega_{q2} - \omega_{q2}^t| \\ |\chi_1 - \chi_1^t| \\ |\chi_2 - \chi_2^t| \\ |g_{c1} - g_{c1}^t| \\ |g_{c2} - g_{c2}^t| \end{pmatrix} \tag{5.24}$$

computed with QuCAT for the circuit diagram shown in Fig. 5.8. Here, labels 1 and 2 indicate the two qubits (q_1 and q_2), and g_{c1}, g_{c2} the coupling strength between each qubit to the bus coupler, considering a purely capacitive coupling governed by Eq. 2.61 (opportunely corrected when applied to $\lambda/2$ resonators). In Eq. 5.24, C_{c1} and C_{c2} are the coupling capacitances of qubits q_1 and q_2 to the coupler bus. In the minimization, $\omega_{r1}/2\pi$, $\omega_{r2}/2\pi$ and the coupler frequency $\omega_c/2\pi$ were fixed and modeled by their effective LC capacitances $\{C_{r1}, C_{r2}, C_c\}$ and inductances $\{L_{r1}, L_{r2}, L_c\}$, assuming a characteristic impedance of $Z_0 = 50\ \Omega$.

5.3.2 Cross-resonance dynamic simulation

The cross-resonance Hamiltonian in Eq. 2.76 contains spurious terms that should be minimized at the pulse level, through echo sequences and cancellation tones, as well as at the design level. The terms composing the Hamiltonian are proportional to Pauli strings that can be computed perturbatively [225]. One term that is particularly relevant is the always-on component of the ZZ coupling, which does not depend on the drive strength Ω and acts continuously on the two qubits:

$$\omega_{ZZ,\,\text{static}} = \frac{J^2}{2(\alpha_1 + \Delta)^2} \frac{2(\alpha_1 + \Delta)(\alpha_1 + \alpha_2)}{\Delta - \alpha_2}, \tag{5.25}$$

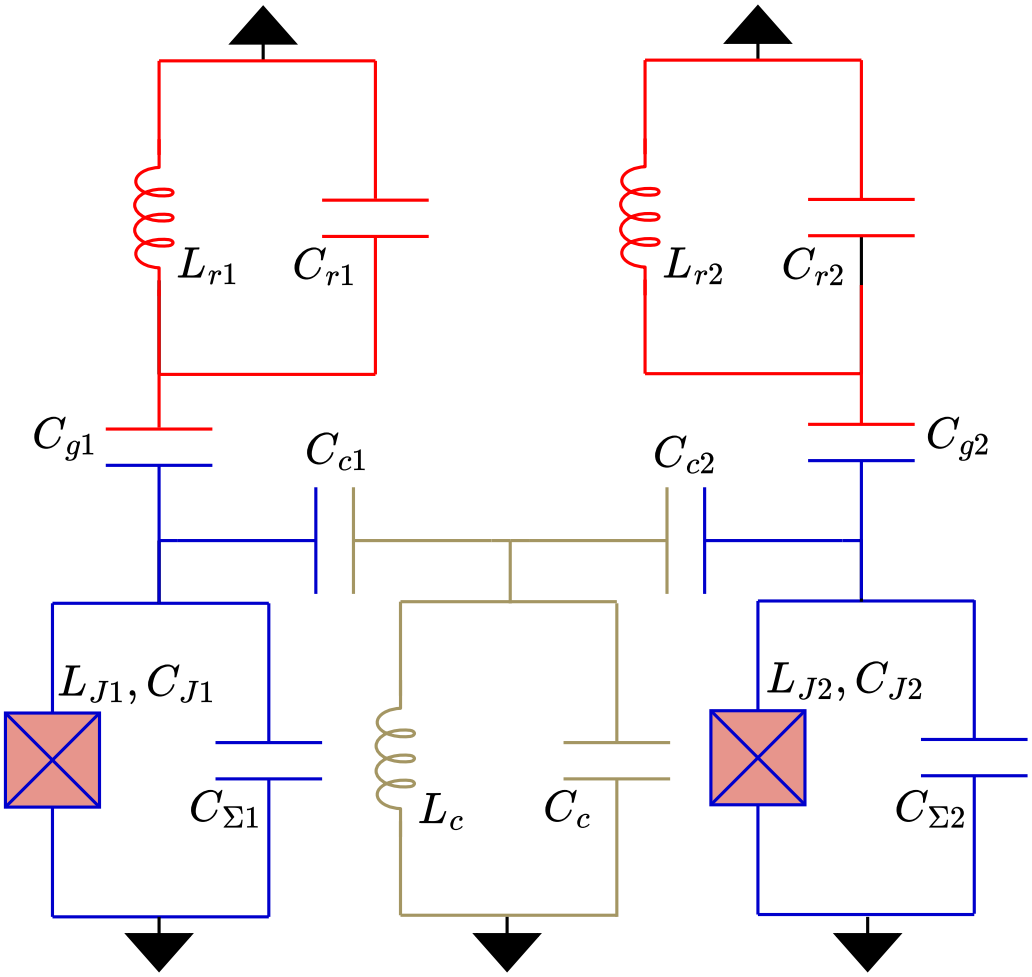

FIGURE 5.8: Circuit diagram of two qubits (blue) coupled capacitively via bus resonator (moss green), and coupled to their respective readout resonators (red).

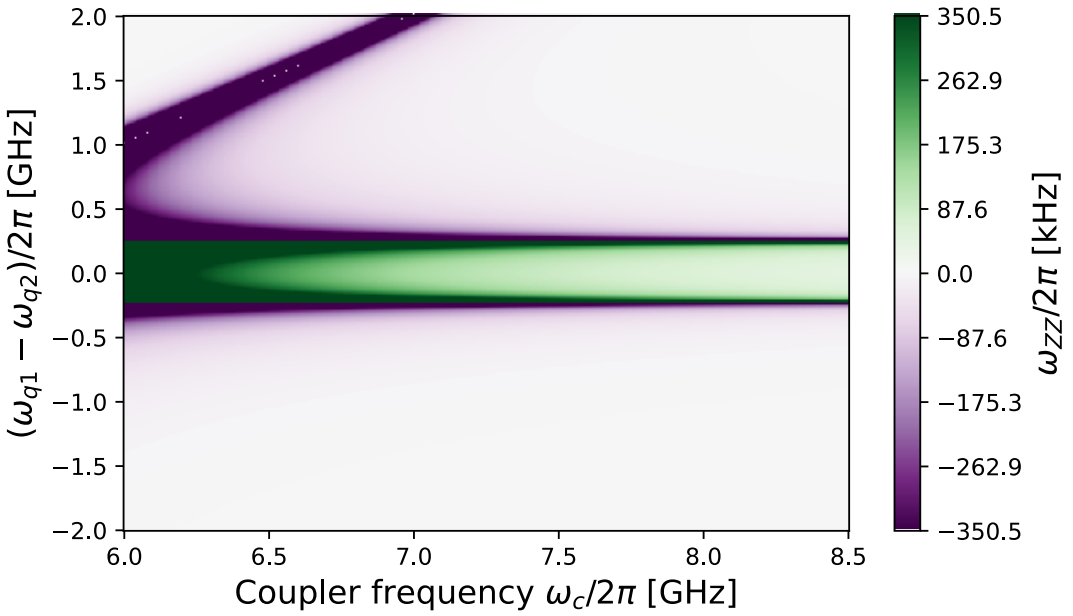

FIGURE 5.9: Static ZZ interaction strength coefficient for two qubits coupled through a bus resonator, as a function of the coupler frequency and the qubit-qubit-detuning, considering $g_{c1}/2\pi = g_{c2}/2\pi = 90$ MHz.

where α_1 and α_2 are the anharmonicities of q_1 and q_2, $\Delta = \omega_1 - \omega_2$. The effective coupling strength J, in the case mediated by a bus resonator, reads:

$$J = \frac{g_{c1}g_{c2}(\omega_1 + \omega_2 - 2\omega_c)}{2(\omega_1 - \omega_r)(\omega_2 - \omega_r)}. \tag{5.26}$$

The poles at $\Delta = \{\pm\alpha_1, \pm\alpha_2\}$ in Eq. 5.25 were avoided by identifying $\Delta/2\pi = 100$ MHz as a suitable operating point, which can be kept constant over the sensing qubit frequency sweep required by the search experiment, by also tuning the ancilla. Fig. 5.9 shows $\omega_{ZZ,\,\text{static}}$ as a function of the coupler frequency and the qubit-qubit detuning.

In addition to limiting the cross-resonance gate fidelity, because the static ZZ interaction is present continuously during the sensing qubit evolution time, frequency shifts conditioned on the ancilla state may appear, deviating from the expected time evolution of the two qubits when ideally uncoupled. We consider spurious effects of this kind to be negligible, although a precise evaluation of the impact of static ZZ would be required on real hardware. The dynamically-driven contributions to the cross-resonance are reported in Appendix B. Fig. 5.10 reports the magnitude of the most relevant single and two-qubit rotations affecting the cross-resonance dynamics. The term Ω_{IZ} was neglected as it was roughly one order of magnitude smaller than Ω_{ZZ} for the chosen values of ω_1, ω_2, ω_c, and J. Also the term ω_{IY} was not included as it is physically equivalent to ω_{IX}.

To obtain an approximate cross-resonance pulse duration and evaluate the impact of the spurious term on the time evolution of q_1 and q_2, we considered the following Hamiltonian in the frame rotating at ω_2:

$$\hat{\mathcal{H}}_{\text{CR}} = \hbar\frac{\Delta}{2}\left(\sigma_{z1} \otimes \text{I}\right) + \hbar J\left(\sigma_{+1}\sigma_{-2} + \sigma_{-1}\sigma_{+2}\right) + \hbar\Omega\left(\sigma_{x1} \otimes \text{I}\right) + \hbar m\Omega\left(\text{I} \otimes \sigma_{x2}\right). \tag{5.27}$$

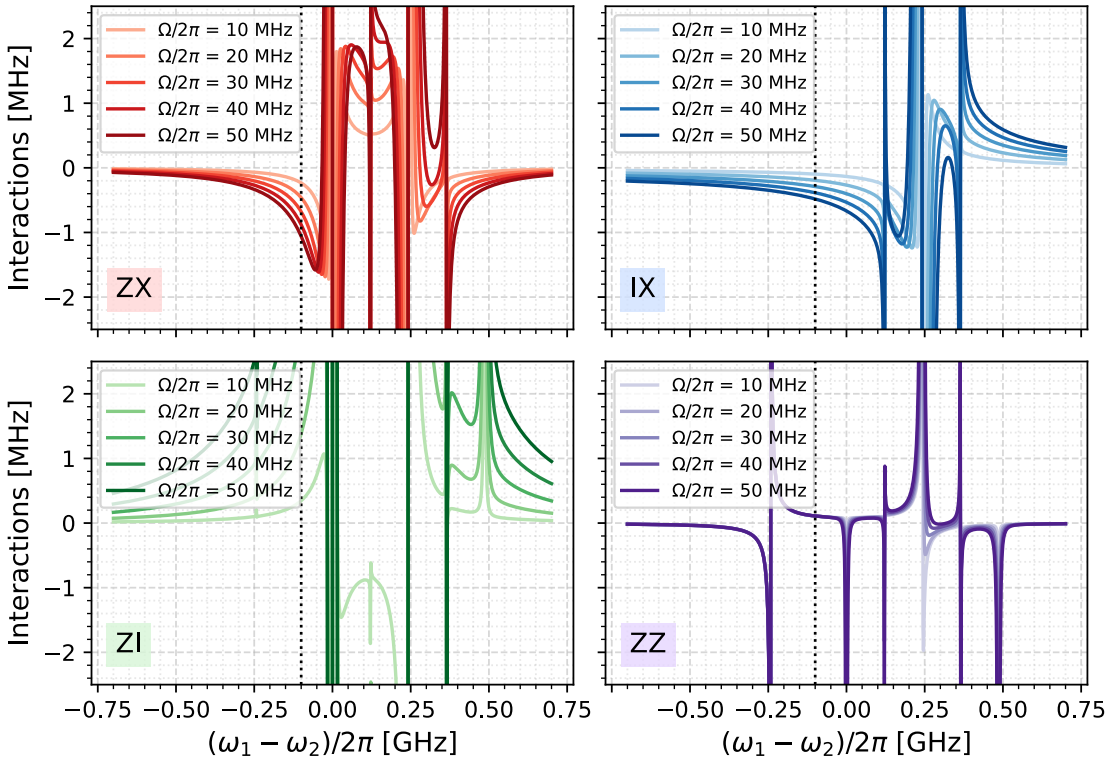

FIGURE 5.10: Pauli coefficients for a cross-resonance Hamiltonian up to the third order in $\Delta = \Omega/(\omega_1 - \omega_2)$, considering a coupling strength $J/2\pi = 3.2$ MHz at $\Delta/2\pi = 100$ MHz, a coupler frequency $\omega_c/2\pi = 7$ GHz, and $\omega_{q1}/2\pi = 4.5$ GHz.

Here, we keep the convention in which labels 1 and 2 denote q_1 and q_2, respectively. The dimensionless parameter m quantifies residual qubit-driveline crosstalk: when a drive at frequency $\omega_2/2\pi$ is applied to the control line of q_1, a fraction m of the drive amplitude couples directly to q_2, producing an unintended resonant excitation. We set $m = 0.01$, corresponding to a spurious drive coupling to q_2 that is two orders of magnitude weaker than the intended coupling to q_1 (in terms of voltage ratio). In terms of power ratio, this translates to a 40 dB difference, which is a realistic assumption for real devices [226].

Fig. 5.11 illustrates the time evolution under Eq. 5.27 of the Pauli operator expectation values of the two qubits over time, for the initial states $|\Psi_0\rangle = |0_{q1}0_{q2}\rangle$ and $|\Psi_0\rangle = |1_{q1}0_{q2}\rangle$. In particular, $\langle Y_2\rangle = \langle\sigma_{y2}\rangle$ represents the desired q_1-state dependent cross-resonance behavior that we intend to maximize. As expected, the presence of a spurious resonant drive for q_2 alters the qubit dynamics significantly. Complex oscillating behavior is observed for $\langle X_1\rangle = \langle\sigma_{x1}\rangle$ and $\langle Y_1\rangle = \langle\sigma_{y1}\rangle$, which persists even after turning off crosstalk ($m = 0$).

To simulate the standard echoed cross-resonance (CR) sequence, we partitioned the total evolution time T into two equal intervals. During the first interval, the system evolves under $\hat{\mathcal{H}}_{\text{CR}}$ (Eq. 5.27). At the beginning of the second interval, we applied a π-rotation around $\hat{x}$ on q_1, then a π-phase inversion of the microwave drive, while the detuning and exchange terms remain unchanged. The Hamiltonian acting in the second half, therefore, becomes:

$$\hat{\mathcal{H}}'_{\text{CR}} = \hbar\frac{\Delta}{2}\left(\sigma_{z1}\otimes \text{I}\right) + \hbar J\left(\sigma_{+1}\sigma_{-2} + \sigma_{-1}\sigma_{+2}\right) - \hbar\Omega\left(\sigma_{x1}\otimes \text{I}\right) - \hbar m\Omega\left(\text{I}\otimes\sigma_{x2}\right). \quad (5.28)$$

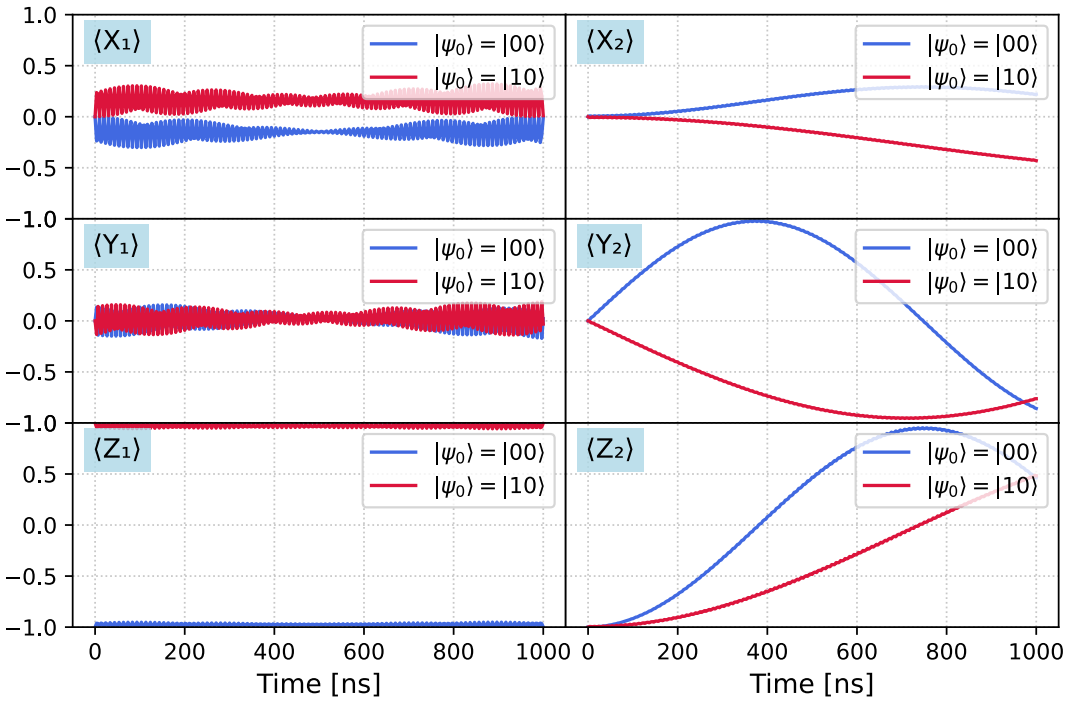

FIGURE 5.11: Expectation values of the Pauli operators for two detuned ($\Delta/2\pi = 100$ MHz) coupled qubits ($J/2\pi = 3.2$ MHz) under a non-echoed cross-resonance drive with amplitude $\Omega/2\pi = 8$ MHz.

As a result, the Pauli operator expectation values evolve as shown in Fig. 5.12. With respect to the non-echoed evolution, the fast oscillations in $\langle X_1 \rangle$ and $\langle Y_1 \rangle$ are suppressed, leaving oscillations produced by the Δ and J proportional terms in $\hat{\mathcal{H}}_{\text{CR}}$ and $\hat{\mathcal{H}}'_{\text{CR}}$. Crucially, the $\langle Y_1 \rangle$ evolution now exhibits a cleaner initial state-dependence, which is maximum at around 500 ns for the coupling strengths and detunings considered. Further optimization –beyond the scope of this thesis– could be carried out to increase the two-qubit gate fidelity. For instance, pulse-shaping (such as DRAG and related multi-quadrature envelopes to suppress leakage and phase errors), active cancellation tones, and rotary pulses (accounting for unitary errors and crosstalk originating from other nearby qubits, if present) could be implemented, and then tuned on real hardware using closed-loop calibration and benchmarking.

5.4 Design and measurement of superconducting devices

Following the quantum circuit design and simulation strategies discussed in Secs. 5.1, 5.2, and 5.3, we produced several device layouts of increasing complexity, up to a dark matter detector prototype compatible with the enhancement protocols discussed in Chapter 4.

At the time of writing, some of these devices have been fabricated and characterized, while the fabrication of others is scheduled. This part of the thesis work aimed to refine our design, simulation, and fabrication pipeline to reliably produce a detection device with well-characterized specifications.

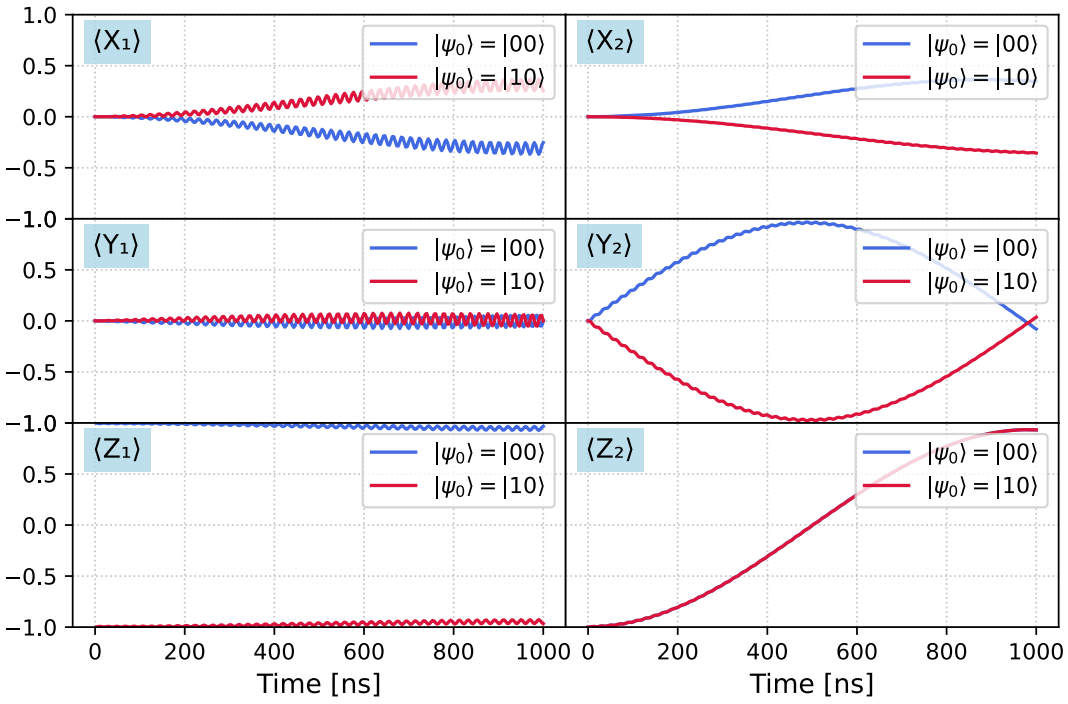

FIGURE 5.12: Expectation values of the Pauli operators for two detuned ($\Delta/2\pi = 100$ MHz) coupled qubits ($J/2\pi = 3.2$ MHz) under an echoed cross-resonance drive with amplitude $\Omega/2\pi = 8$ MHz. For each time t evaluated in these plots, the first half evolved through $\hat{\mathcal{H}}_{\text{CR}}$, and the second half through $\hat{\mathcal{H}}'_{\text{CR}}$ (see Eqs. 5.27 and 5.28).

5.4.1 Uncoupled qubits with standard readout

The simplest design we considered, in order to verify the Jaynes-Cummings interactions between qubit and readout resonator, consists of four uncoupled qubits. Each qubit is coupled to a $\lambda/4$ readout resonator, in turn coupled to a feedline. The latter is a simple transmission waveguide that connects two launchpads (left and right in Fig. 5.13), which can be used interchangeably as the input and output of the feedline. The device is designed on a 7.5×7.5 mm^2 frame, with four launchpads at the midpoints of each side. The top and bottom launchpads connect two bifurcated drivelines reaching the four qubits.

The four qubit pads share the same geometry, hence having approximately the same effective capacitance $C_\Sigma = 90$ fF. A small variability in C_Σ (less than 1%) is expected, since the different readout coupler lengths weakly affect it (see Eq. 5.1). The $\lambda/4$ resonators are capacitively coupled both to the qubits and to the feedline, splitting close to the feedline into two branches. One branch connects the interdigitated feedline coupler, while the other terminates at ground at the far end of the CPW. Similar readout geometries were implemented in [227]. The waveguide trace and gap widths were chosen to be $w = 10$ µm and $s = 6$ µm, giving a characteristic impedance of $Z_0 = 50$ Ω, assuming a substrate dielectric constant of $\epsilon_r = 11.4$. Drivelines were tapered close to the qubit to $w = 3.3$ µm and $s = 2$ µm, with a simulated effective capacitance to the transmons of ≈ 120 aF, and an estimated driveline decay-limited time of $T_{1,\text{drive}} \sim 120$ - 160 µs.

The readout resonator CPW lengths were determined by fixing the expected unloaded

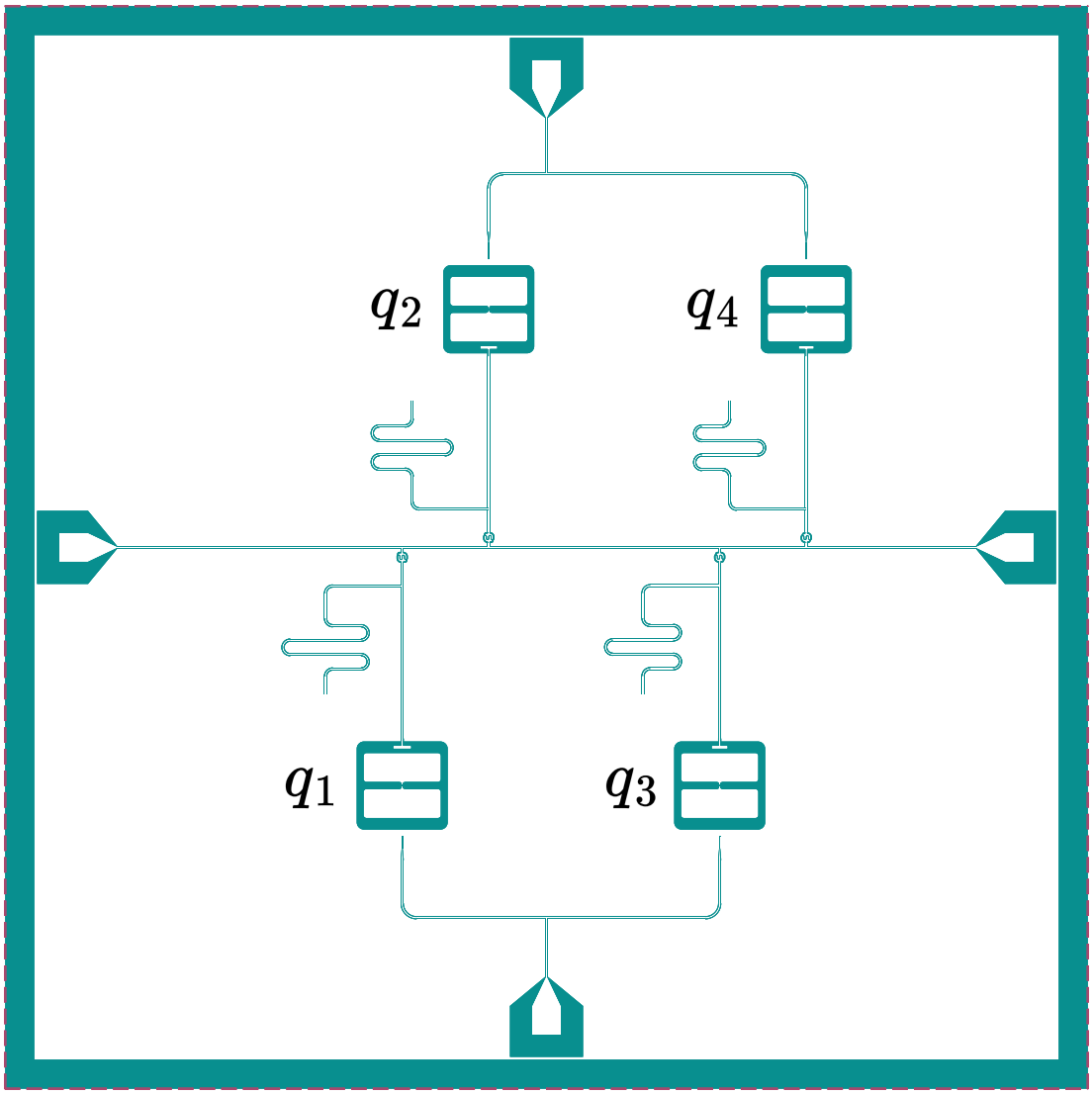

FIGURE 5.13: Coplanar quantum circuit layout consisting of four uncoupled qubits with standard dispersive coupling readout architectures and dedicated drivelines.

TABLE 5.3: Target design parameters for the four-uncoupled qubits device (Fig. 5.13). The frequencies $\omega_q/2\pi$ and $\omega_r/2\pi$ are bare.

	q1	**q2**	**q3**	**q4**
$\omega_q/2\pi$ [GHz]	4.5	4.7	4.9	5.1
$\alpha/2\pi$ [MHz]	-239	-238	-237	-236
$\omega_r/2\pi$ [GHz]	7.0	7.2	7.4	7.6
$k/2\pi$ [MHz]	1.4	1.4	1.4	1.4
$\chi/2\pi$ [kHz]	350	350	350	350
$g/2\pi$ [MHz]	77.2	77.6	78.1	78.4
L_J [nH]	12.5	11.5	10.7	9.9
$T_{1,\text{Purcell}}$ [µs]	~ 239	~ 236	~ 233	~ 231
$T_{1,\text{Drive}}$ [µs]	~ 158	~ 146	~ 134	~ 123

frequency $\tilde{\omega}_r/2\pi$, then correcting it for the coupling load (the feedline):

$$\omega_r \approx \tilde{\omega}_r + \frac{2}{\pi} Z_0 C_k \tilde{\omega}_r^2. \tag{5.29}$$

The resonator length L thereby reads:

$$L = \pi \frac{v}{\tilde{\omega}_r}. \tag{5.30}$$

The target parameters for this device are summarized in Table 5.3.

Experimental characterization

The device shown in Fig. 5.13 was fabricated in the nanofabrication facilities of the United States National Institute of Standards and Technology (NIST).
On a silicon substrate with a thickness of 300 µm, a Nb film was sputtered (with nominal thickness 110 nm) and capped in vacuum with a thin PdAu layer ($\approx$ 10 nm). Patterning was performed by reactive-ion etching in an SF_6-based plasma. Profilometer measurements of the step at the metal–silicon boundary indicate a total metal-substrate step of $\approx$ 150 nm. Subtracting the metal thickness gives an estimated silicon trench depth of $\approx$ 30 nm on average across the wafer. The ground plane was also patterned with a grid of 25×25 µm^2, squares spaced by 75 µm, to mitigate dissipative magnetic vortices by acting as flux pins. We note that this structure is more complicated than the one examined in Subsec. 5.1.2 for the cross-section simulation. Further improvements in the qubit EPR simulations would include, for instance, the PdAu layer. In this fabrication round, the use of PdAu is expected to reduce metal-air surface losses, as discussed in [228].
In addition to fabrication, characterization in a cryogenic environment was also carried out at NIST, by the Superconductive Electronics Group. A diagram of the measurement setup is illustrated in Fig. 5.14. The scattering parameter $S_{21}(\omega)$ was measured, identifying the four readout resonances, shown in Fig. 5.15. The complex transmission coefficient $S_{21}(\omega)$ for a single resonance was modeled as a Lorentzian curve

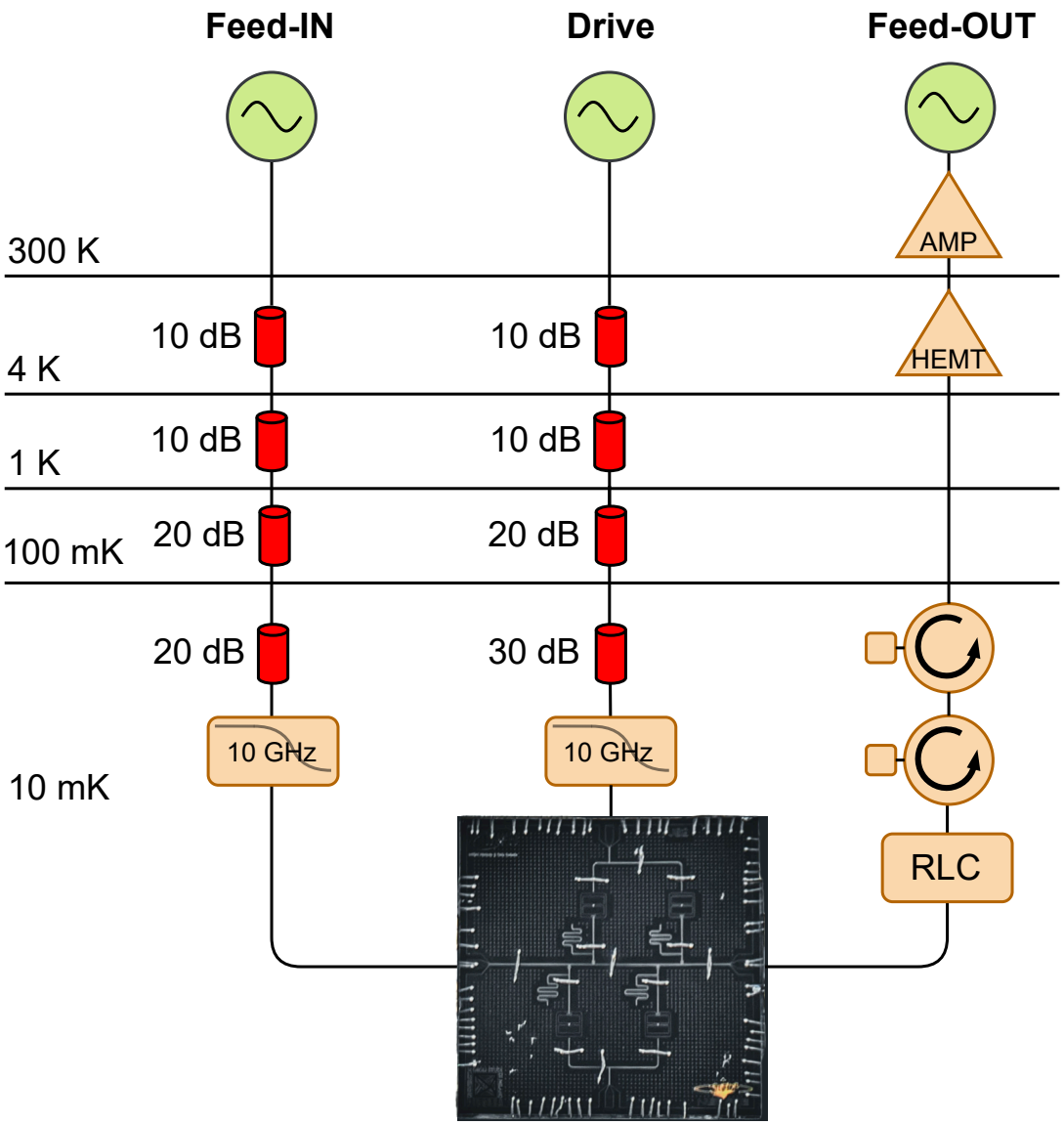

FIGURE 5.14: Cryogenic measurement chain used to characterize the four-uncoupled qubits device. The feedline input carries a total of 60 dB attenuation distributed across the cryostat stages and a low-pass filter that suppresses signals above 10 GHz. The drive line, which targets qubits q_2 and q_4, has 70 dB of distributed attenuation and another low-pass filter at 10 GHz. The feedline output connects a bandpass (RLC) filter and two circulators, each providing approximately 20 dBm of isolation (attenuation toward the chip). The first amplifier is a high-electron-mobility transistor (HEMT) located at 4 K, followed by a room-temperature amplifier stage.

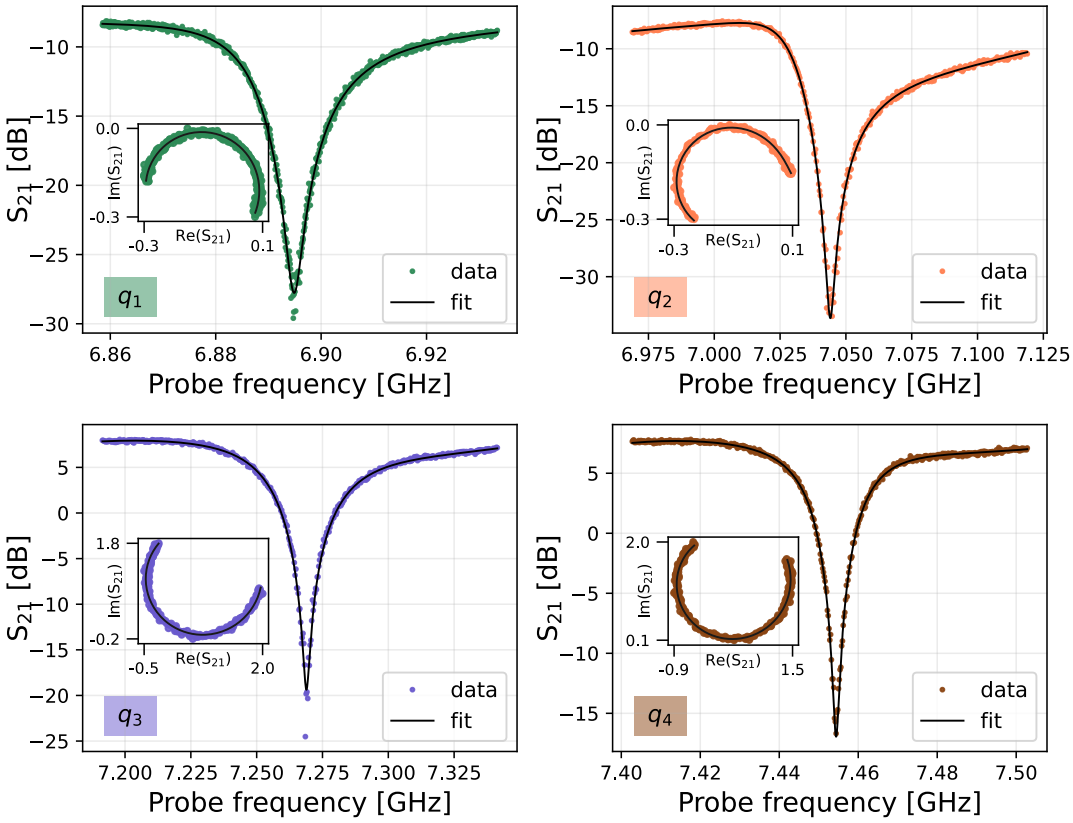

FIGURE 5.15: Readout resonances for the four uncoupled qubits device, with standard feedline. Magnitude and circular fits were performed to extract the resonance parameters.

rotated in the complex plane:

$$S_{21}(\omega) = Ae^{i\phi}\left(1 - \frac{Q_l/Q_c e^{i\varphi}}{1 + 2iQ_l\frac{\omega-\omega_r}{\omega_r}}\right) + c_0 + c_1(\omega_r - \omega) + c_2(\omega_r - \omega)^2 + c_3(\omega_r - \omega)^3. \tag{5.31}$$

In Eq. 5.31, A and ϕ parametrize a scale factor and a rotation, while φ accounts for possible feedline mismatches. To increase the flexibility of the model to capture other frequency-dependent background contributions, a complex-valued cubic polynomial was added. An immediate experimental observation is that the measured resonator linewidths are anomalously large, $k \sim$ 20 - 40 MHz, corresponding to $Q_c \sim$ 150 - 300. This result is in strong disagreement with both the expected coupling of approximately 5×10^3, derived from the procedure described in Subsec. 5.2.2. Also, preliminary finite-element simulations of the readout structure (Ansys HFSS), which were carried out prior to device manufacturing, returned modal quality factors of approximately 5×10^3. Possible explanations include underestimated inductive contributions to the feedline coupling, radiative or packaging losses, unintended parasitic coupling to nearby structures, additional dissipative channels introduced by the sample mount or wire bonds, or inaccuracies in the simulated boundary conditions and material loss parameters. In particular, we emphasize the lack of specific wire bond connections in the measured device, which, based on later studies (see Appendix D), could have led to substantial improvements in the resonators' quality factors.

The central resonant frequencies are also lower than expected by around 100 - 150 MHz, potentially suggesting a higher coupling to the load than expected. Other contributions not taken into account for the waveguide length corrections are the added capacitance and inductance to ground from the couplers. Moreover, a substrate dielectric coefficient that differs from the predictions may also introduce systematic frequency displacements. For instance, a real value of $\epsilon_r = 11.7$ instead of the assumed $\epsilon_r = 11.4$ would reduce the resonant frequencies by $\sim 1\%$, corresponding to ~ 70 MHz.

Qubit spectroscopy was carried out using the continuous-wave two-tone method. A fixed-frequency readout tone was sent at the resonator frequency $\omega_r/2\pi$, while a second, weaker drive tone swept through the frequency range expected for the transmon transitions. The resulting change in the qubit's energy levels population produces a measurable shift in the resonator. This shift is detected as a change in the transmission parameter S_{21}, observable as an amplitude and/or phase response, thus identifying the transmon transition frequencies. Fig. 5.16 shows the two-tone spectroscopy for q_1, revealing the most significant transmon transitions $\omega_q = \omega_{01}, \omega_{12}, \omega_{02}$. The latter arises from a two-photon excitation process occurring at $\omega_{02}/2$.

Standard time domain protocols were used to quantify relaxation and dephasing. For the T_1 measurement, the qubit, initialized in the ground state $|0\rangle$, was driven to the excited state $|1\rangle$ with a calibrated π-pulse. After a variable delay τ, the qubit state was read out dispersively via the resonator. The excited-state population was reconstructed from the transmission S_{21} (in-quadrature) fitting the curve

$$\text{In-quadrature signal} = Ae^{-\tau/T_1} + B, \tag{5.32}$$

where A and B account for readout error and residual excitation. Dephasing was measured with a Ramsey interferometry sequence. A $\pi/2$-pulse was applied to the qubit, placing its state on the Bloch sphere equator. After a free evolution time τ. a second $\pi/2$-pulse mapped the accumulated phase onto the population, which is

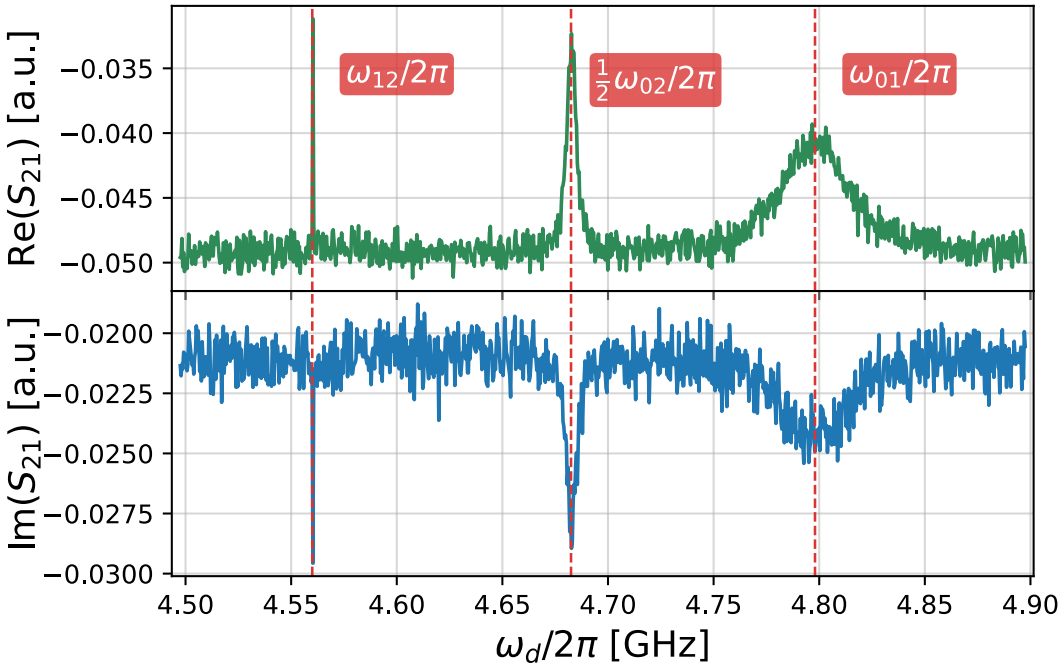

FIGURE 5.16: Two-tone spectroscopy for q_1 in the four uncoupled qubit device, highlighting the transitions $|0\rangle \leftrightarrow |1\rangle$, $|0\rangle \leftrightarrow |2\rangle$, and $|1\rangle \leftrightarrow |2\rangle$.

immediately measured. The drive frequency $\omega_d/2\pi$ was set slightly detuned from the qubit frequency $\omega_q/2\pi$, so that the measured signal exhibited a sinusoidal modulation at the Ramsey frequency $\Delta = \omega_q - \omega_d$ and phase ϕ, rather than a very slowly varying envelope caused by potential mismatch between ω_q and the drive tone. The resulting trace was fitted with a damped oscillation of the form

$$\text{In-phase signal} = A\cos(\Delta\tau + \phi)e^{-\tau/T_2^*} + B. \tag{5.33}$$

Each measurement was repeated several times for each delay τ, and the outcome was averaged. The results for q_1 are shown in Fig. 5.17.

The complete set of measured parameters is collected in Table 5.4. We note that the Purcell limit $T_{1,\text{Purcell}}$ retrieved using Eq. 2.83 is constantly lower than the T_1 observed experimentally, indicating that it is a conservative estimate. Another approach, based on retrieving the admittance seen by the qubit and using Eq. 2.87, was carried out using the scikit-rf Python package (v. 1.3.0) [229], creating the lumped circuit shown in Fig. 5.2 with the addition of the readout resonator coupling to the feedline, and substituting the qubit with a port terminated at 50 Ω. Using the qubit's admittance extracted with scikit-rf evaluated at $\omega_q/2\pi$, we obtain another set of $T_{1,\text{Purcell}}$ limits, which are reported in Table 5.5.

With respect to the predictions in Table 5.4, only the one for q_1 is in good agreement with the measured T_1. Both estimation methods (Eq. 2.83 and Eq. 2.87) consistently yield conservative estimates. Hence, these expressions provide a reliable lower bound for T_1 in device simulations and are therefore appropriate for safe design analysis.

The qubit associated with the highest-frequency resonator (q_4) was not observed. Its absence may be due to errors in the junction deposition, or subsequent damage during chip preparation and installation in the sample holder. Another possibility is that, since $k \gg \chi$, the qubit signal was covered by noise, thus making characterization impractical.

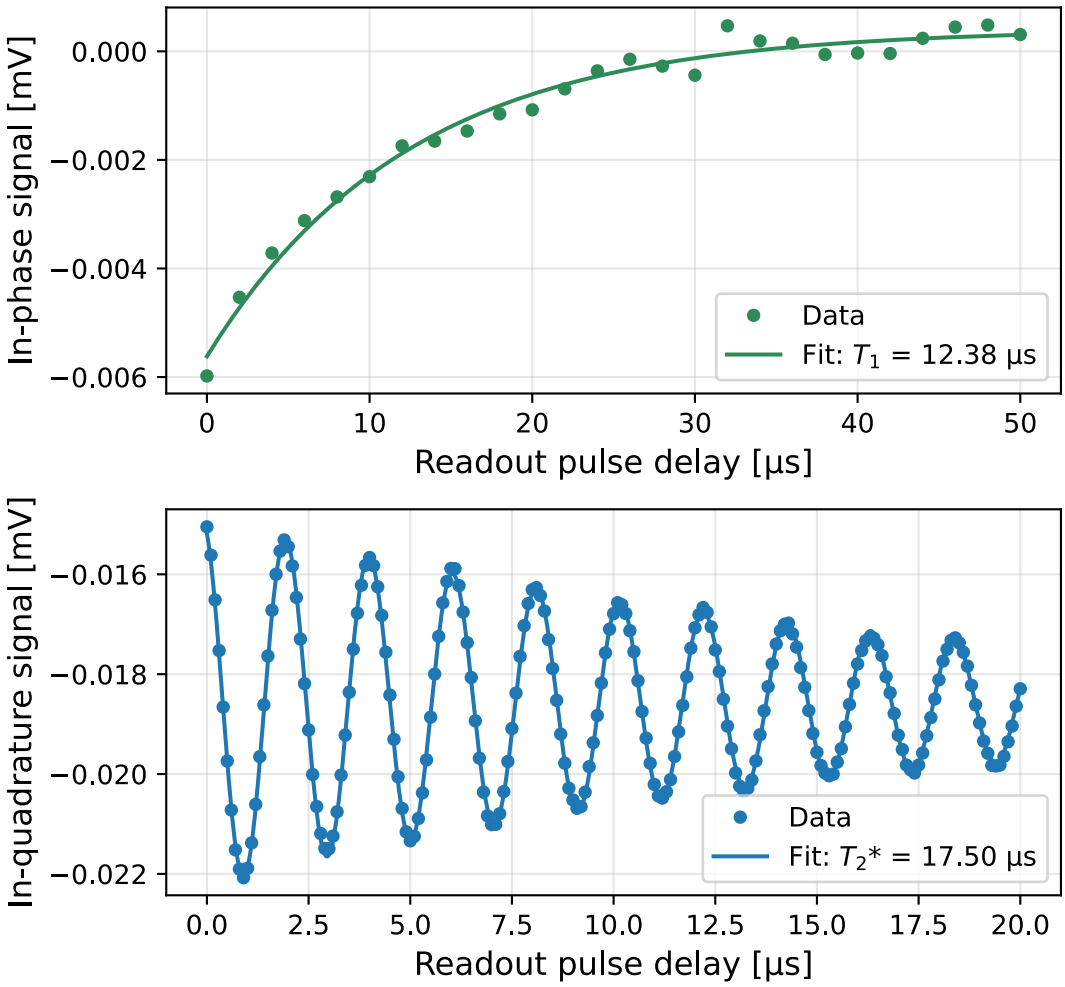

FIGURE 5.17: Standard time domain measurements on q_1 for the four-uncoupled qubits device. T_1 (top) and T_2^*, detuning the $\pi/2$-pulse by $\Delta/2\pi = 0.487$ MHz from $\omega_q/2\pi$ (bottom).

TABLE 5.4: Experimental characterization of the four-uncoupled qubits device (Fig. 5.13). The frequencies $\tilde{\omega}_q/2\pi$ and $\tilde{\omega}_r/2\pi$ are dressed. We assume $\alpha \approx \tilde{alpha}$, where $\tilde{\alpha}$ is dressed.

	$\mathbf{q_1}$	$\mathbf{q_2}$	$\mathbf{q_3}$	$\mathbf{q_4}$
$\tilde{\omega}_q/2\pi$ [GHz]	4.797	5.242	5.281	–
$\alpha/2\pi$ [MHz]	≈ -240	≈ -250	≈ -240	–
$\tilde{\omega}_r/2\pi$ [GHz]	6.89	7.032	7.27	7.45
$k/2\pi$ [MHz]	24.2	38.2	46.7	22.0
Q_c	308	220	165	359
$\chi/2\pi$ [kHz]	315	375	325	–
$g/2\pi$ [MHz]	62.1	58.4	60.1	–
L_J [nH]	11.0	9.4	9.2	–
$T_{1,\text{Purcell}}$ [μs]	~ 7.5	~ 3.9	~ 3.7	–
T_1 [μs]	12.4	5.4	5.2	–
T_2^* [μs]	17.5	9.6	8.7	–

TABLE 5.5: Four-uncoupled qubits device Purcell filter estimation through circuit admittance (Fig. 5.13).

	q1	**q2**	**q3**	**q4**
$T_{1,\text{Purcell}}$ [μs]	~ 15.6	~ 2.3	~ 2.9	–

5.4.2 Uncoupled qubits with Purcell filter readout

The device described in this Subsection differed from the one in Subsec. 5.4.1 in the readout architecture. Here, the four readout resonators are coupled to a Purcell filter embedded in the feedline. The filter couples strongly to one readout port (input) through an interdigitated coupler, and is directly connected to the second readout port (output). Near the readout port, the waveguide splits, and one branch connects the filter to ground, fixing the resonant modes. Fig. 5.18a illustrates the device design. The mode we targeted for Purcell decay protection is the second-lowest of the Purcell filter, i.e. the $3/4\lambda$, aiming at a frequency in between the ones of the readout resonators.
The positioning of the readout resonator couplers to the feedline-embedded Purcell filter determines whether the coupling is far or close to the voltage anti-nodes. To maximize the capacitive contribution to the coupling, we placed the resonators close to the second anti-node as shown in Fig. 5.18b. Being a single Purcell filter designed to work for all four qubits, the mode resonance was set to be broadband $\sim$ 1 GHz, corresponding to a quality factor $Q_F \sim 10$. We tuned Q_F by varying the dimension of the interdigitated coupler (matching 50 fF) and the length of the grounded branch of the CPW, starting from the splitting point near the output port (the shorter, the higher Q_F).
As for the uncoupled qubit device with a simple readout architecture described in Subsec. 5.4.1, the device was fabricated and measured at NIST by the same research groups. The cryogenic setup is analogous to the one shown in Fig. 5.14.

Experimental characterization

The transmission spectra shown in Fig. 5.19 refer to two fabricated variants of this device. The top and bottom panels consist of Purcell filters with lengths of 12.42 mm and 12.02 mm, respectively. The variant at 12.02 mm was measured in an attempt to characterize the Purcell filter mode of interest, and the four readout resonators were shorted to ground through wire bonding before characterization. For this reason, the bottom panel in Fig. 5.19 does not show the four readout resonances, although it exhibits two unidentified spurious resonances around 5 GHz. The transmission spectra were fitted using a Lorentzian model, which yielded a central frequency $\omega_p/2\pi = 6.56$ GHz, $Q_F = 16.8$ for the variant at 12.42 mm and $\omega_p/2\pi = 6.90$ GHz, $Q_F = 9.8$ for the variant at 12.02 mm. Table 5.6 summarizes the design targets for the device and the respective measured values.
The Purcell filter center frequency was targeted to be in the middle of the readout resonators' span, approximately at 7.3 GHz. The waveguide geometry was optimized using the scikit-rf package, extracting $S_{21}(\omega)$. However, the measured value deviated considerably (700 MHz), affecting the Purcell decay protection. The readout resonator frequencies fell outside the broadband filter, which resulted in being between the qubits and the readout resonators frequencies. We attribute this to the cause of

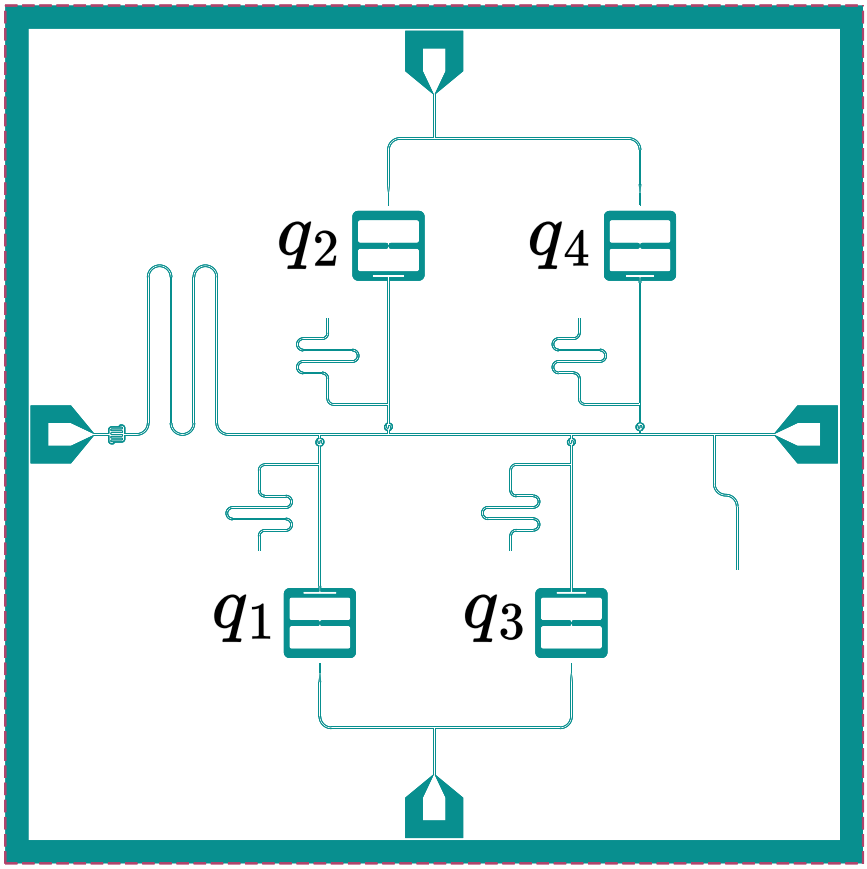

(A) Four-uncoupled qubit layout with feedline-embedded Purcell filter.

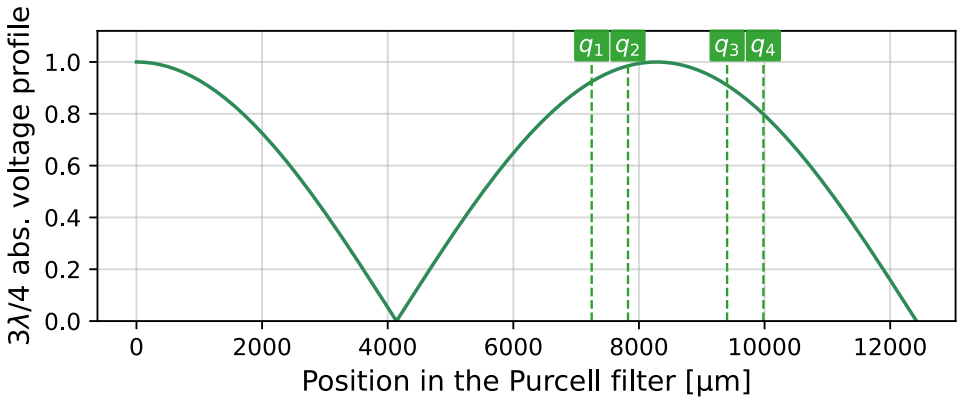

(B) Purcell voltage profile and readout resonator positioning.

FIGURE 5.18: Four-uncoupled qubit device with Purcell-filtered readout. (A) Coplanar quantum circuit layout consisting of four uncoupled qubits with dispersive coupling to an embedded Purcell filter and dedicated drivelines. (B) Normalized absolute voltage profile of the $3/4\lambda$ Purcell filter mode as a function of the position in the filter waveguide, starting from the Purcell coupler to the ground termination, and the distance coordinate of the four readout resonators. The variant with a Purcell filter of length 12.42 mm is shown.

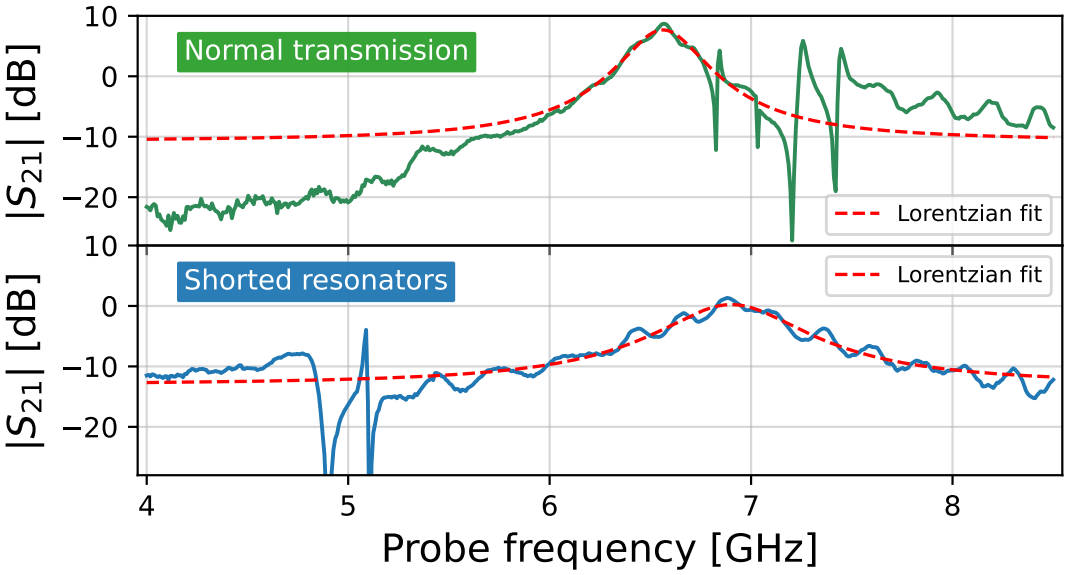

FIGURE 5.19: Transmission coefficient S_{21} as a function of the probe power, for a Purcell filter of lengths 12.42 mm (top) and 12.02 mm (bottom). The variant at 12.02 mm was measured with the readout resonators shorted to ground through wire bonding. A Lorentzian fit is displayed for both panels in a dashed red line.

TABLE 5.6: Target and measured parameters of the four-uncoupled device with Purcell filter readout. The labels t and m indicate target and measure, respectively.

	$\mathbf{q}_1^t$	$\mathbf{q}_2^t$	$\mathbf{q}_3^t$	$\mathbf{q}_4^t$	$\mathbf{q}_1^m$	$\mathbf{q}_2^m$	$\mathbf{q}_3^m$	$\mathbf{q}_4^m$
$\omega_q/2\pi$ [GHz]	4.5	4.7	4.9	5.1	–	–	–	–
$\tilde{\omega}_q/2\pi$ [GHz]	–	–	–	–	5.132	5.336	–	5.780
$\alpha/2\pi$ [MHz]	−242	−241	−239	−238	–	–	–	–
$\omega_r/2\pi$ [GHz]	7.0	7.2	7.4	7.6	–	–	–	–
$\tilde{\omega}_r/2\pi$ [GHz]	–	–	–	–	6.837	7.032	7.251	7.440
Q_c	$\approx 10^3$	$\approx 10^3$	$\approx 10^3$	$\approx 10^3$	1130	11487	240	340
$\chi/2\pi$ [MHz]	1.30	1.30	1.30	1.30	1.55	1.75	–	1.45
$g/2\pi$ [MHz]	149	150	150	152	113.3	120.4	–	107.7
T_1 [µs]					8.2	4.0	–	5.3
T_2^* [µs]					5.6	5.3	–	9.8

the low T_1 reported in Table 5.6. Qubit q_3 was not found during the two-tone spectroscopy, and higher excitation levels have not been observed for the others. For this reason, the anharmonicities were not extracted.

5.4.3 Coupled qubits

The subsequent device in terms of complexity comprises two transmon qubits coupled via a fixed-frequency bus resonator. The primary objective of this design was to demonstrate a cross-resonance interaction between the qubits and to identify potential improvements in future iterations concerning device modeling and engineering. The readout architecture consists of a continuous transmission line with readout resonators coupled capacitively to it. At this preliminary stage, we opted not to include a Purcell filter for readout improvement. The coupling strengths of the readout $\lambda/4$ resonators to the feedline and qubits were modeled following the same approach described in the previous subsections. The qubit pads feature a circular notch pattern, and as in the devices described earlier in this Section, they were designed to yield a total capacitance of $C_\Sigma = 90$ fF. The full quantum circuit layout is designed on a 5×5 mm^2 chip area. As with the uncoupled qubit devices discussed in Subsecs. 5.4.1 and 5.4.2, fabrication was carried out at the NIST Superconductive Electronics Group nanofabrication facilities, employing the same layer structure and thicknesses. The layout is shown in Fig. 5.20

Device characterization was performed in the cryogenic laboratory of the University of Milano–Bicocca, using the measurement setup illustrated in Fig. 5.21. Four RF lines (feedline input-output and drivelines) were generated by a single Zynq UltraScale+ RFSoC ZCU216 board, with a DAC sampling rate of 9.85 GSPS and an ADC sampling rate of 5 GSPS. Room temperature amplification was added to the feedline input and the driveline to q_2, and a 5 GHz low-pass filter was also added to the q_1 driveline (once verified that the qubit's frequency was below the filter threshold). RF signals generation was handled through the Qibolab software [230] (v. 0.1.10), which provided complete control over RF signal generation and the realization of calibration experiments.

Experimental characterization

The scattering parameters S_{21} of the two readout resonator modes were acquired, and Fig. 5.22 shows the two resonance profiles. Similarly to the uncoupled qubit device (see Subsec. 5.4.1), the readout resonator quality factors fall below expectations, yielding large resonance linewidths (around ~ 30 MHz against our target of 1 MHz). An explanation for such a discrepancy may be related to wire bond positioning, as discussed in Appendix. D. For this device, as for the uncoupled qubit one, the resonators' linewidths are much larger than the dispersive shift ($k \gg \chi$), slowing down measurements (as more time-averaging is needed to overcome noise), and undermining readout fidelity.

Qubit spectroscopies have been carried out using the two-tone spectroscopy technique, by sending a 1 µs probe pulse of varying frequency, and subsequently reading out the resonator's frequency displacement. Fig. 5.23 illustrates the spectroscopy at different probe pulse amplitudes, power-Rabi oscillations in correspondence with the transmon modes. The transition $|1\rangle \leftrightarrow |2\rangle$ was not observed for q_1 or q_1 on this power scale, but it was recovered in a later stage (see Appendix C). Phase information for q_1 and magnitude information for q_2 were reported, respectively.

In addition to spectroscopy, time-domain measurements were conducted. The π-

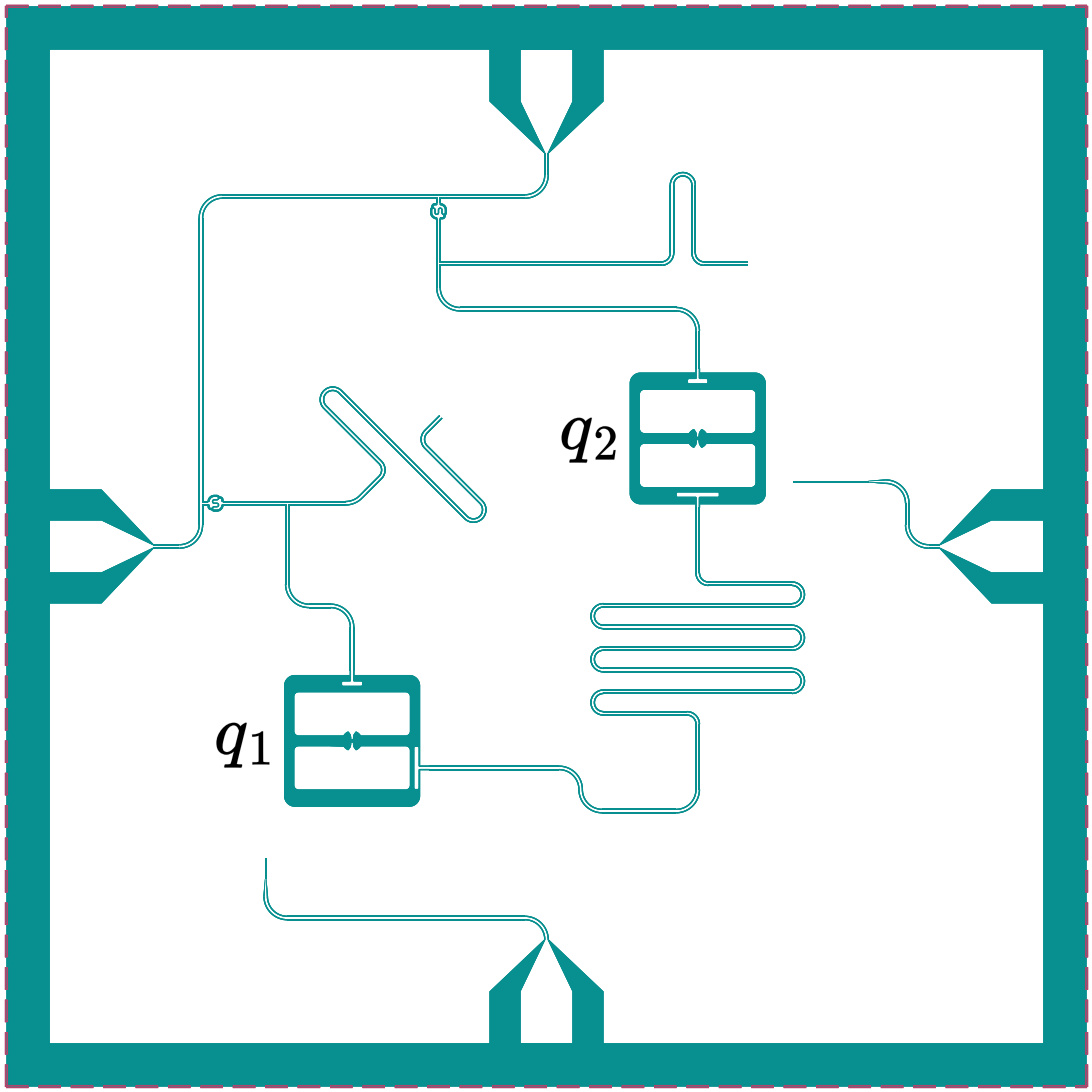

FIGURE 5.20: Coplanar quantum circuit layout consisting of two bus resonator-coupled qubits, with standard dispersive coupling readout architectures and dedicated drivelines.

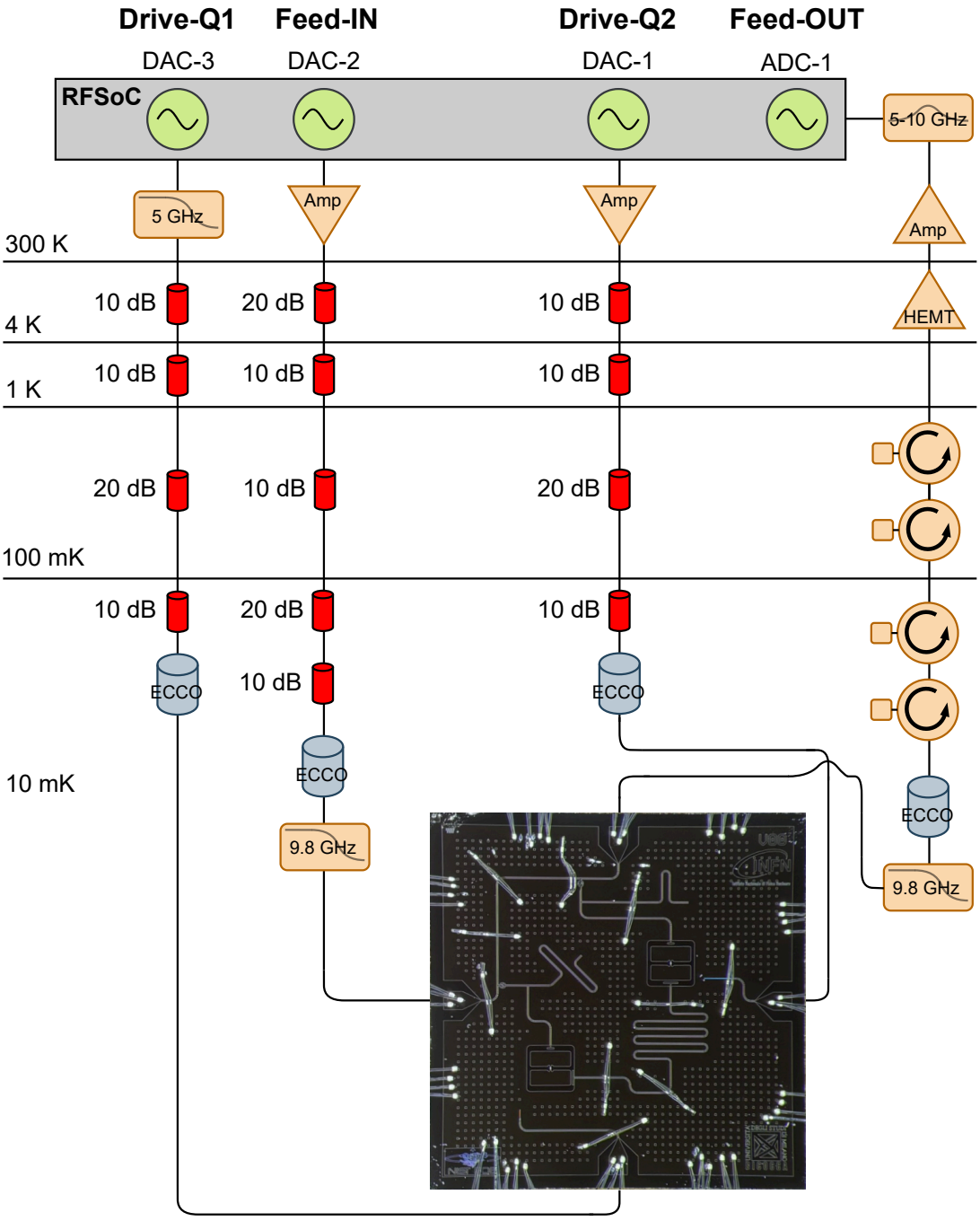

FIGURE 5.21: Cryogenic measurement chain used to characterize the two coupled qubit device. The feedline input carries a total of 70 dB attenuation distributed across the cryostat. At the mixing chamber stage, an Eccosorb infrared filter was added, followed by a low-pass filter that suppresses signals above 9.8 GHz. The two drive-lines have 50 dB of distributed attenuation and Eccosorb infrared filters at the mixing chamber. The feedline output line passes through a low-pass filter and four circulators, each providing approximately 20 dBm of isolation (attenuation toward the chip). The first amplifier is a high-electron-mobility transistor (HEMT) located at 4 K, followed by a room-temperature amplifier stage and a 5-10 GHz bandpass filter.

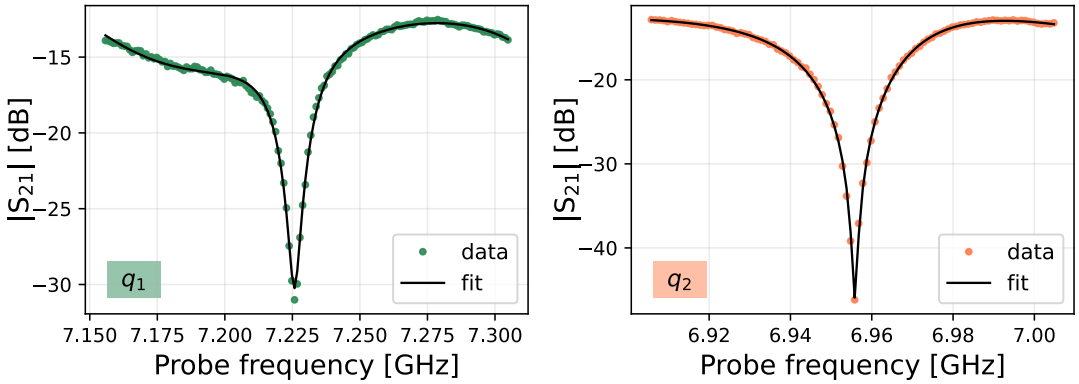

FIGURE 5.22: Readout resonators transmission coefficients S_{21} for the two coupled qubits device.

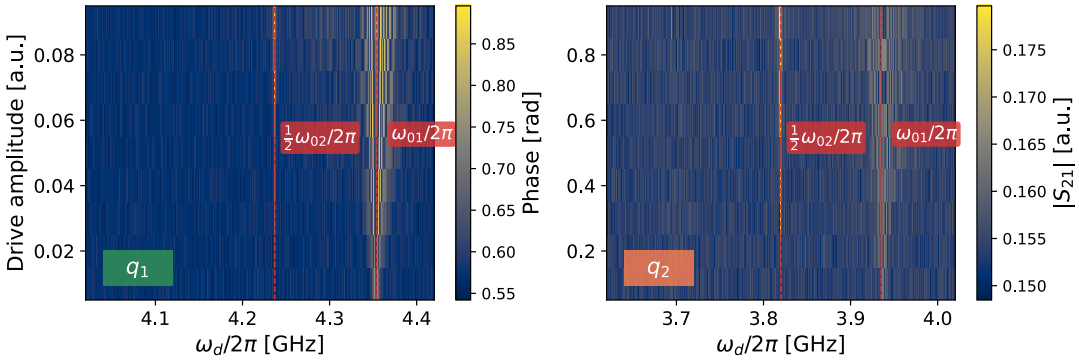

FIGURE 5.23: Two-tone spectroscopy for q_1 (in phase) and q_2 (in magnitude) in the coupled qubits device, highlighting transitions $|0\rangle \leftrightarrow |1\rangle$ and $|0\rangle \leftrightarrow |2\rangle$.

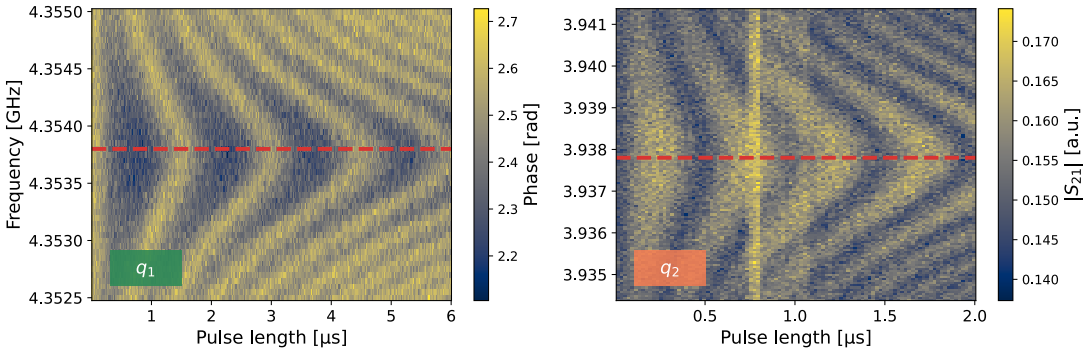

FIGURE 5.24: Rabi oscillations over time as a function of the drive tone frequency (chevron plot) for the coupled qubits device.

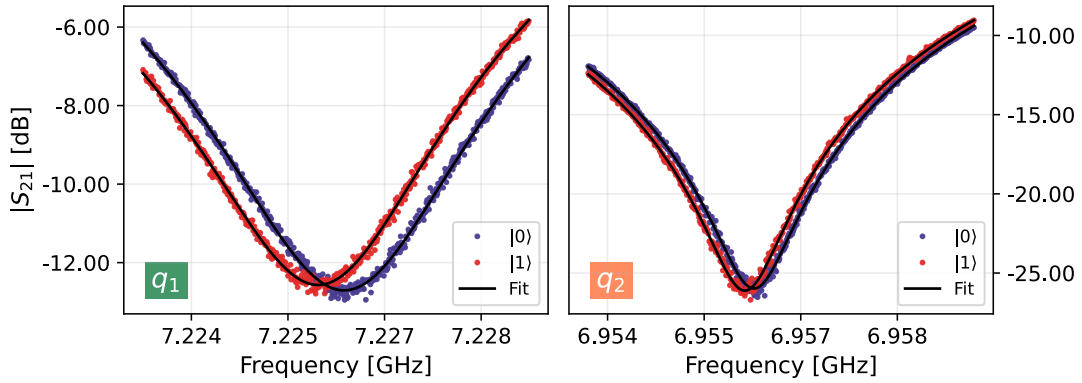

FIGURE 5.25: Readout resonator transmission coefficients S_{21} for the coupled qubits device, when preparing the qubits in state $|0\rangle$ and $|1\rangle$, to extract the dispersive shifts χs of q_1 and q_2.

pulse calibration for each qubit was obtained through Rabi experiments, in which the qubit was driven close to its resonance frequency with pulses of varying duration, and the excitation probability was subsequently measured. The Rabi experiment was repeated, varying the drive frequency, and the results (exhibiting a chevron pattern) are shown in Fig. 5.24. Similarly to the two-tone spectroscopy case, phase information is displayed for q_1 and magnitude information is displayed for q_2.

Once the π-pulse powers were calibrated, opting for a Gaussian envelope and a duration of 60 ns, we measured the dispersive shifts where readout resonator spectroscopies were compared when first preparing the qubits in state $|0\rangle$ and $|1\rangle$, as depicted in Fig. 5.25. We note that for q_1 we attempted to map the output signal to the probability that the qubit was in state $|1\rangle$, although its precision was heavily affected by the large overlap of the state distributions in the IQ plane (see Fig. 2.9b). A similar mapping strategy was not successful for q_2, due to the even lower readout fidelity, as reported in Appendix C. For this reason, in Fig. 5.25 we adopted the excited state probability on the y-axis for q_1, while leaving the signal magnitude for q_2. We also note that the state assignment calibration for the measurement of the T_2-echo was different from the one adopted for T_1 and T_2^*.

For q_2, we observe that $T_2 \geq 2T_1$, which should not occur by construction (see Eq. 1.29). However, this discrepancy is well explainable by considering time variations of the qubit coherence times. In particular, T_1 of q_2 was observed to be above 30 μs, which justified $T_2 \approx 55$ μs. The Purcell limit using Eq. 2.83 with the measured

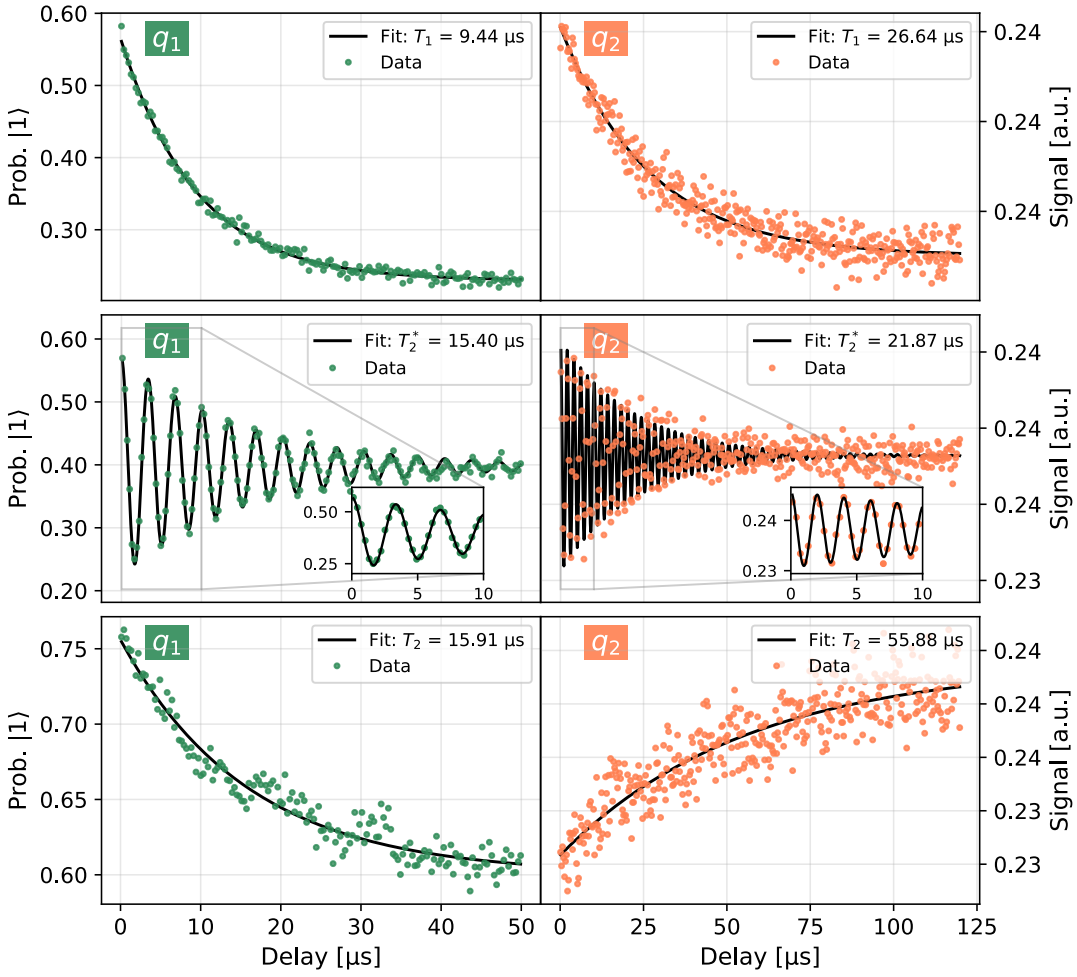

FIGURE 5.26: Coherence time measurements (T_1, T_2^*, T_2) for the coupled qubits device. The Ramsey experiment was carried out with a detuning of approximately 300 kHz for q_1 and 500 kHz for q_2.

TABLE 5.7: Target and measured parameters of the two coupled qubits device. The labels t and m indicate target and measure, respectively.

	$\mathbf{q_1^t}$	$\mathbf{q_2^t}$	$\mathbf{q_1^m}$	$\mathbf{q_2^m}$
$\omega_q/2\pi$ [GHz]	5.0	4.5	–	–
$\tilde{\omega}_q/2\pi$ [GHz]	–	–	4.354	3.938
$\alpha/2\pi$ [MHz]	-245	-245	≈ -239	≈ -238
$\omega_r/2\pi$ [GHz]	7.4	7.2	–	–
$\tilde{\omega}_r/2\pi$ [GHz]	–	–	7.226	6.958
Q_c	6.0×10^3	5.9×10^3	370	142
$\chi/2\pi$ [MHz]	0.25	0.25	0.21	0.07
$g/2\pi$ [MHz]	66.6	62.9	66.8	46.9
T_1 [µs]			9.4	26.6
T_2^* [µs]			15.4	21.9
T_2 [µs]			15.9	55.9

values for χ and Q_c are $T_{1,\text{Purcell}} = 15$ µs for q_1 and $T_{1,\text{Purcell}} = 24$ µs for q_2. Consistent with the uncoupled qubits device, Purcell-limited T_1 calculations resulted in conservative estimates, as the measured value of T_1 for q_2 was longer than $T_{1,\text{Purcell}}$.
Although the individual qubits were successfully characterized, we were unable to detect any clear evidence of qubit–qubit interaction. In particular, we attempted to measure the time evolution of one qubit (target) while driving the other (control) at the target's transition frequency. However, no reproducible behavior analogous to that shown in Fig. 5.11 was observed. Specifically, no slow oscillations on the order of 1 µs were detected in any of the measured Pauli expectation values. Furthermore, the qubit dynamics showed no dependence on the initial state.
We attribute this absence of interaction signatures to one or more possible causes: a significantly reduced effective coupling strength J with respect to the target ($J/2\pi \approx 2$ MHz), a short circuit in the bus coupler possibly caused by fabrication residues or by bent-broken wire bonds contacting the bus coupler central conductor, or an excessive noise level in the measurements due to the low-Q readout resonators. Further investigation will be carried out, including the implementation of a quantum-limited parametric amplifier at the first amplification stage to improve the signal-to-noise ratio.
Table 5.7 collects the target and measured parameters for the coupled-qubits device.

5.4.4 Dark matter detector prototype design

The last device discussed in this Chapter is a prototype of the enhanced direct detection protocol, consisting of three transmon qubits coupled in a chain topology. The central qubit, serving as the ancilla for the signal enhancement circuit, is coupled to two sensing qubits through CPW bus resonators. With respect to the previous devices, the $\lambda/4$ readout resonators were replaced with $\lambda/2$ ones, and qubit readout is not multiplexed on a single transmission line. Rather, to each qubit are associated two launchpads, corresponding to the input and output, coupled through dedicated $\lambda/4$ Purcell filters. Moreover, the qubit single junctions have been replaced by SQUIDs, and the junction leads have been translated closer to the ground plane to enable inductive coupling with straight-shaped fluxlines. The device is designed on a 1×1 cm^2 area and is depicted in Fig. 5.27.

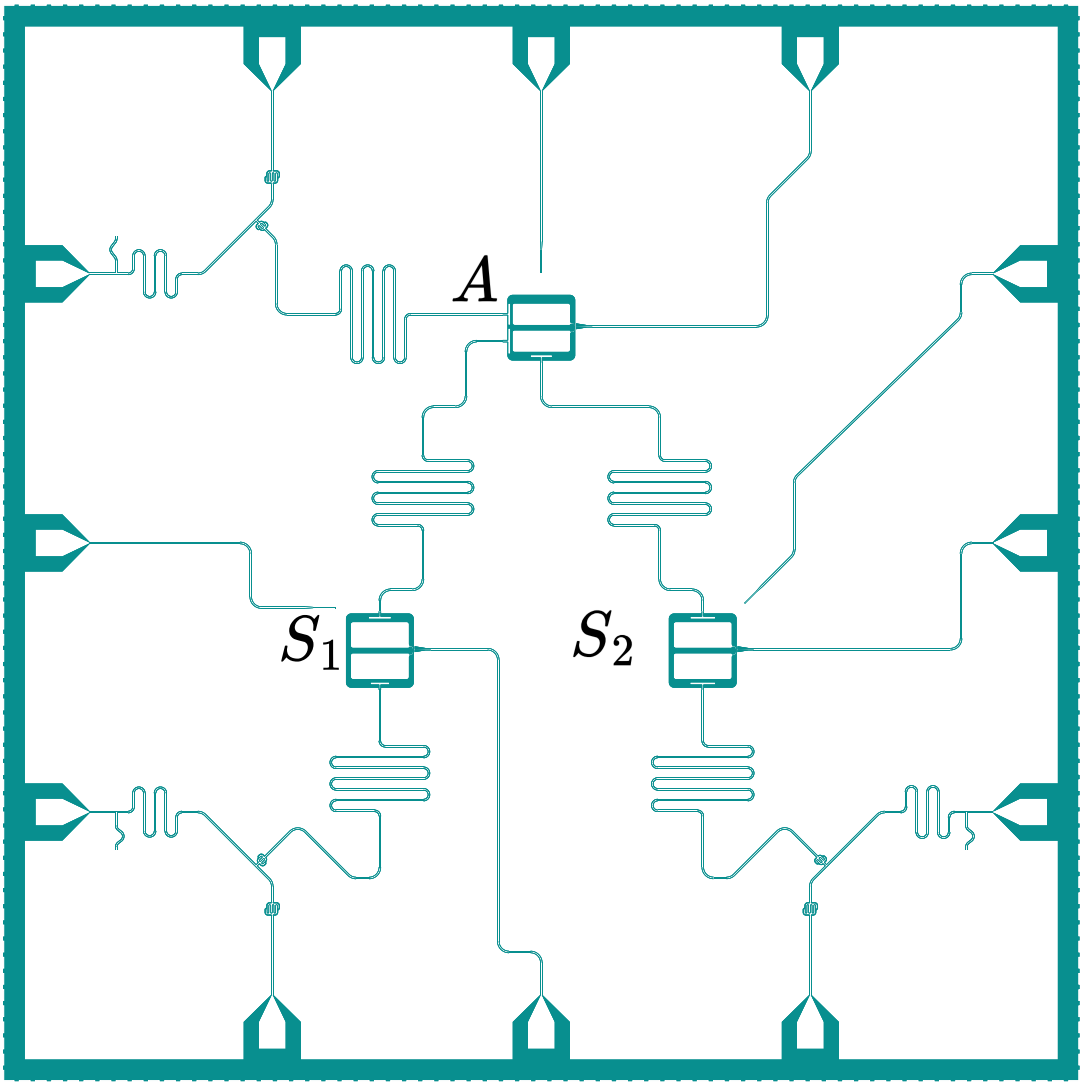

FIGURE 5.27: Coplanar quantum circuit layout of the detection device prototype, consisting of two sensing qubits (S_1, S_2), and one ancilla A. All qubits are frequency-tunable and equipped with drivelines. Readout is not multiplexed and $\lambda/4$ feedline-embedded Purcell filters are used for each qubit.

The optimization of the couplers' geometrical parameters was performed following a procedure analogous to that described in Subsec. 5.3.1. The goal was to simultaneously tune the relevant circuit elements

$$f : \begin{pmatrix} L_{JS1} \\ L_{JS2} \\ L_{JA} \\ C_{gS1} \\ C_{gS2} \\ C_{gA} \\ C_{cS1\text{-}A} \\ C_{cS2\text{-}A} \\ C_{cA\text{-}S1} \\ C_{cA\text{-}S2} \end{pmatrix} \rightarrow \begin{pmatrix} |\omega_{S1} - \omega_{S1}^{t}| \\ |\omega_{S2} - \omega_{S2}^{t}| \\ |\omega_{A} - \omega_{A}^{t}| \\ |\chi_{S1} - \chi_{S1}^{t}| \\ |\chi_{S2} - \chi_{S2}^{t}| \\ |\chi_{A} - \chi_{A}^{t}| \\ |g_{cS1\text{-}A} - g_{cS1\text{-}A}^{t}| \\ |g_{cS2\text{-}A} - g_{cS1\text{-}A}^{t}| \\ |g_{cA\text{-}S1} - g_{cS1\text{-}A}^{t}| \\ |g_{cA\text{-}S2} - g_{cS1\text{-}A}^{t}| \end{pmatrix}, \tag{5.34}$$

TABLE 5.8: Target parameters for the dark matter detection device prototype.

	$\mathbf{S_1}$	$\mathbf{S_2}$	$\mathbf{A}$
$\omega_q/2\pi$ [GHz]	5.10	4.60	5.20
$\alpha/2\pi$ [MHz]	-213	-215	-236
$\omega_r/2\pi$ [GHz]	6.95	6.80	7.10
$\omega_c/2\pi$ [GHz]	6.60	6.40	
C_k [fF]	12.8	13.3	12.4
Q_p	13.3	13.8	15.3
$\chi/2\pi$ [MHz]	0.9	0.9	0.9
$g/2\pi$ [MHz]	68.5	80.7	66.2
$T_{1\,\text{Purcell}}$ [µs]	~ 680	~ 1745	~ 805
$T_{1\,\text{Drive}}$ [µs]	~ 2315	~ 2954	~ 1656
C_d [aF]	3.0	2.9	3.3
$T_{1\,\text{Flux}}$ [µs]	~ 329	~ 407	~ 317
C_f [aF]	7.8	7.8	7.8
ϕ_ext @ 1 mA	0.235	0.235	0.235

where $S1$, $S2$ A denote the first and second sensing qubits and the ancilla, respectively. The labels $S1$-A and A-$S1$ correspond to the coupler capacitances connected to the bus resonator on the sensing-qubit and ancilla sides, respectively (and analogously for $S2$-A and $S2$-A). The challenging aspect of this procedure is that the system Hamiltonian comprises eight fundamental modes (three qubits and five CPW resonators), and excitations beyond the first levels must be accounted for the qubit. During the numerical minimization of the function in Eq. 5.34, the Hamiltonian is rebuilt several times, making the optimization computationally expensive. To reduce the number of calls to the QuCAT's Hamiltonian constructor, we replaced the optimization algorithm from the standard method, i.e. a variant of the Broyden–Fletcher–Goldfarb–Shanno (BFGS) algorithm [231] with the Constrained Optimization BY Linear Approximation COBYLA algorithm [232], and considered only four excitation levels (including ground state) for the qubits and two for the linear resonators.
Table 5.8 collects the target parameters of the device. The sensing qubits effective capacitance was chosen to be $C_\Sigma \approx 100$ fF, since the DM-induced signal is proportional to C_Σ (see Eq. 3.28), while the ancilla target capacitance remained at $C_\Sigma \approx 90$ fF. Furthermore, increasing the size of the pads longitudinally to match a higher C_Σ also increases the dipole length l, which is approximately equal to the distance between the midpoints of the pads.

Chapter 6

Conclusions and outlook

This thesis develops and evaluates a practical approach to using superconducting transmon qubits as sensitive microwave probes for dark-sector fields. The primary candidates of interest are ultralight, weakly-coupled bosons, namely axions, axion-like particles, and dark photons. Searching for these candidates is a common goal of superconducting microwave cavity and haloscope experiments, and the use of qubits is expected to either integrate them to improve their sensitivity or be implemented directly as standalone detectors.

The core detection concept considered in this thesis relies on direct transmon qubit excitation caused by a dark-sector field. When a transmon qubit is tuned into resonance with a monochromatic, coherent microwave field produced by dark-matter conversion, it undergoes Rabi-like dynamics at a rate determined by the strength of dark-sector coupling to the ordinary photon. This coherent evolution provides the detector signal. The experimental protocol begins by preparing the qubit in its ground state, then allowing dark matter interaction (by letting the qubit evolve freely) for a duration compatible with the qubit's coherence time ($\sim$ 100 µs). At the end of this interval, the qubit is measured. By repeating the procedure, it is possible to infer the probability of finding the qubit in its excited state. By sweeping the qubit frequency across a target range, an excess excitation probability at a specific frequency would indicate a resonant field potentially attributable to dark matter.

The central contribution of this thesis is an effective signal amplification method that transforms the qubit's excitation probability (right after interacting with dark matter) into an observable with enhanced sensitivity to weak signals buried in background noise and dark counts. This transformation is implemented through quantum gates that coherently manipulate the qubit state. To enable a nontrivial mapping, the computational Hilbert space is extended by coupling the sensing qubit to an ancilla. The resulting quantum circuit incorporates a mid-circuit measurement of the ancilla followed by post-selection. Successful post-selection dramatically increases the detector sensitivity, producing a rapid variation in the final sensing qubit excitation probability as a function of its state before applying the circuit. Conversely, failed post-selection yields a final quantum state that is independent of the sensing qubit's dark matter interaction history. The protocol, therefore, requires trading off the success probability of post-selection and the advantage achievable when the post-selection succeeds.

This signal enhancement circuit possesses significant practical advantages. It requires only a single two-qubit gate without imposing strict architectural constraints, making it well-suited for modern superconducting quantum computing platforms. Furthermore, unlike existing enhancement schemes in the literature that require preparing multi-qubit entangled states before dark matter interaction and maintaining their coherence throughout long evolution times, this protocol applies enhancement only after the sensing qubit has interacted with dark matter—a considerably less demanding experimental requirement. Nevertheless, the experiment remains subject to noise and

experimental errors, which are comprehensively addressed in this thesis.
We developed simulations based on Kraus-channel descriptions that account for decoherence (i.e. finite T_1 and T_2 during dark matter interaction, readout, and gate implementation), readout errors on both the sensing qubit and ancilla, temperature-induced thermal population, and initial state preparation error. From the results of these simulations, we identified three parameters that heavily affect the overall detection performance: a rotation angle used in the enhancement circuit (which is the only degree of freedom in the transformation), state-preparation fidelity, and readout error. The enhancement protocol shows a good degree of tolerance to a moderate level of state-preparation error and excellent mitigation of readout error effects, yielding significant advantages over a baseline sensing-and-sampling strategy without enhancement.
To quantify the practical benefit, we introduced a speedup metric $\mathcal{G}$, defined as the factor by which the enhanced experiment reduces the required integration time to reach the same exclusion limit of the signal strength as a baseline non-enhanced experiment. The comparison is carried out in a statistical-noise-limited assumption, and considering the same number of qubits. At this stage, the analysis focused on dark photons, as extending the search to axions and axion-like particles would require applying few-tesla magnetic fields directly to the chip, which is not yet feasible without severely degrading qubit coherence.
Considering a two-qubit detector, comprising one sensing qubit and one ancilla in the enhanced configuration, versus two parallel sensing qubits in the base experiment, we evaluated three representative error scenarios. Under low readout performance (5% assignment error) and low state preparation error (0.1%), we obtained $\mathcal{G} \sim 2 - 5$ between 2.5 GHz and 6.0 GHz. With high readout performance (0.5% assignment error) and high state preparation error (1%), the speedup degraded to $\mathcal{G} \sim 0.85 - 1.20$, making the protocol overall disadvantageous. In an optimistic scenario (yet within reach of existing devices), featuring readout and state preparation error probabilities of 0.5% and 0.1% respectively, we achieved $\mathcal{G} \sim 1.05$ - 2.75.
Scaling to multiple sensing qubits coupled to a single ancilla enables the sequential application of enhancement circuits after all sensing qubits have undergone dark matter interaction simultaneously. This architecture increases $\mathcal{G}$ up to a factor of two, yielding $\mathcal{G} \sim 4$ - 10, $\mathcal{G} \sim 1.7$ - 2.4, $\mathcal{G} \sim 2.1$ - 5.5 for the three scenarios mentioned above.
Sensitivity projections for the dark photon kinetic mixing parameter ϵ were calculated in the optimistic noise scenario, assuming statistical error dominance. For a reference deployment of 120 physical qubits in a many-sensors-to-one-ancilla architecture with three years of integration time, the projected exclusion limit on ϵ at the 95% confidence level reaches approximately 1×10^{-14} between 2.5 GHz and 6.0 GHz, corresponding to the mass range 10 eV - 25 eV, far surpassing cosmological constraints and exceeding current limits from haloscope experiments.
A substantial portion of this thesis addresses the realization of a quantum device serving as an enhanced dark matter photon detection prototype. We describe the design and simulation methods for achieving suitable Hamiltonian parameters (qubit and readout resonator frequencies, Kerr nonlinearities) and high coherence (charge noise resilience, minimal surface-oxide participation in decoherence, Purcell decay suppression). These methods were validated through the fabrication and characterization of test devices with increasing architectural complexity. The first device consists of four uncoupled fixed-frequency qubits read out dispersively through a continuous transmission line, while the second one is a variant incorporating a Purcell filter with $\lambda/4$ boundary conditions embedded in the transmission line. The last, third device features two qubits coupled through a bus resonator.
These quantum devices were fabricated by the Superconductive Electronics Group of

the US National Institute of Standards and Technology (NIST) and characterized at both NIST and the University of Milan–Bicocca. Measured parameters (including resonance frequencies, dispersive shifts, anharmonicities, qubit–readout couplings, and coherence times) agree with design expectations and modeling. The notable exception was the readout resonators' loaded quality factors, which were consistently lower than predicted. This discrepancy increased Purcell-induced relaxation to the extent that the T_1 relaxation time of all the qubits measured was Purcell-limited.
The coupled-qubits device demonstrated satisfactory individual qubit performance. However, observations of coherent inter-qubit interaction were inconclusive, potentially due to measurement challenges arising from large-linewidth readout resonators or damaged wire bonding connecting the bus to ground.
Extending the enhancement scheme proposed in this thesis to axions and axion-like particles is straightforward, as the enhancement circuit itself is independent of the specific dark-sector interaction. However, for this direct detection approach, axion search requires a static magnetic field applied directly to the sensor. Superconducting qubits and their packaging have not yet been widely demonstrated to maintain high coherence in such field environments. Consequently, pursuing axion searches requires dedicated research and development on magnetic-field-resilient qubit designs, materials, or alternative packaging approaches that preserve coherence while enabling the necessary magnetic environment.

Next steps in this study include refining device design and simulation to achieve higher readout performance and coherence, establishing reproducibility across fabrication runs, and engineering high-fidelity two-qubit gates with optimized drive and readout pulses. The goal is to realize a state-of-the-art, or near-state-of-the-art, three-qubit quantum device demonstrator of the enhancement.
We also identify two complementary research directions that could further advance dark matter direct detection using gate-based approaches. First, exploring alternative circuit architectures may reveal improved trade-offs between post-selection success probability and signal enhancement by exploiting different sensing-ancilla coupling configurations. Implementing automatic gate-sequence optimization using non-differentiable algorithms such as genetic searches could yield substantial performance gains. Second, leveraging alternatives to transmons, particularly fluxonium qubits, could extend sensitivity to lower frequency regimes (down to a few MHz) while maintaining high coherence, at the cost of increased fabrication complexity and dealing with less mature two-qubit gate techniques. Additionally, operating transmons or fluxoniums in qutrit or qudit regimes may expand the detectable frequency range beyond 10 GHz.

Overall, this thesis demonstrates that near-term superconducting quantum processors can serve as programmable, quantum-enhanced microwave detectors for dark-sector searches. The combination of a hardware-efficient enhancement circuit, realistic noise modeling, and prototype device characterization provides a concrete roadmap from conceptual design to experimentally competitive sensitivity. It also identifies the critical engineering milestones needed to translate statistical sensitivity into robust exclusion limits. By addressing the experimental challenges highlighted in this thesis, programmable superconducting sensors can become a complementary and competitive tool in the global effort to detect dark matter in the microwave regime.

Code Availability

The simulation and design data collected or generated, and the codes developed for this thesis, are openly available on GitHub:

- QubitDM - Qubits for Dark Matter Search [233].
- QDAST - Quantum Design And Simulation Tool [234].

Appendix A

Gate-based Ramsey measurement

In the absence of pulse-level control for remote quantum devices, the T_2^* (Ramsey) can be measured directly at the gate level, assuming the latter are well calibrated when the measurement is taken. The quantum circuit corresponding to this operation is shown in Fig. A.1.
We note that, since the pulse frequency cannot be detuned from its predefined value, the detuned Ramsey experiment (e.g. the one shown in the bottom panel of Fig. 5.17) cannot be carried out. A small displacement of the drive pulse frequency from the qubit's frequency could still create slow modulations of the exponential profile, reducing the measurement's reliability. However, no such modulation was clearly observed on the QPUs when executing the quantum circuits. The quantum circuit was sampled

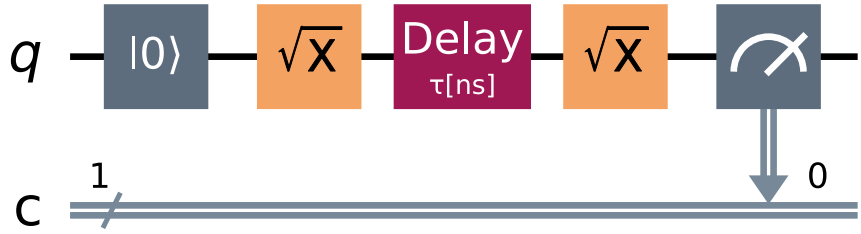

FIGURE A.1: Quantum circuit describing a T_2^* (Ramsey) measurement of a qubit.

several times to estimate the qubit's excitation probability after a delay τ. The experiment was repeated for multiple delays, and T_2^* was extracted by fitting the excitation probability at different delays with the function

$$\text{Excitation probability} = A\cos(\Delta\tau + \phi)e^{-\tau/T_2^*} + B, \tag{A.1}$$

where A and B account for readout error and residual excitation, Δ and ϕ account for the frequency and phase of residual Ramsey modulation.

Appendix B

Perturbative cross-resonance Pauli coefficients

Following the results of [225] on the perturbative calculation of the cross-resonance Hamiltonian, we report the Pauli coefficients calculated up to the third order in Ω/Δ.

$$\omega_{\mathrm{IX}} = -\frac{J\Omega}{\Delta+\alpha_1} + \frac{\Delta\,\alpha_1\,J\Omega^3}{(\Delta+\alpha_1)^3(2\Delta+\alpha_1)(2\Delta+3\alpha_1)}. \tag{B.1}$$

$$\omega_{\mathrm{IY}} = 0. \tag{B.2}$$

$$\begin{aligned}\omega_{\mathrm{IZ}} = \frac{J^2\Omega^2}{2}\Bigg[&\frac{\alpha_1^3-2\alpha_1\Delta^2-2\Delta^3}{\alpha_1\Delta^2(\alpha_1+\Delta)^2(\Delta-\alpha_2)} + \frac{\alpha_1^2+\Delta^2}{\Delta^2\alpha_2(\alpha_1+\Delta)^2}\\ &+\frac{6\alpha_1^5+4\alpha_1^4\Delta-6\alpha_1^3\Delta^2+7\alpha_1^2\Delta^3+12\alpha_1\Delta^4+4\Delta^5}{\Delta^2(\alpha_1+\Delta)^2(2\alpha_1+\Delta)^2(\alpha_1+2\Delta)(3\alpha_1+2\Delta)}\\ &+\frac{2}{\alpha_1(\alpha_1+\Delta)(\alpha_1+\Delta-\alpha_2)} + \frac{2}{(\alpha_1+\Delta)(\alpha_1+\Delta-\alpha_2)^2} + \frac{1}{\Delta(\Delta-\alpha_2)^2}\Bigg].\end{aligned} \tag{B.3}$$

$$\begin{aligned}\omega_{\mathrm{ZI}} = -\frac{\alpha_1\Omega^2}{2\Delta(\alpha_1+\Delta)} + \frac{J^2\Omega^2}{2(\alpha_1+\Delta)^3}\Bigg[&\frac{2(\alpha_1^2+\alpha_1\Delta+\Delta^2)(\alpha_1+\Delta)}{\alpha_1\Delta(\alpha_2-\Delta)}\\ &+\frac{1}{2}\alpha_1\left(\frac{4\alpha_1^2}{\Delta^3}+\frac{11\alpha_1}{\Delta^2}+\frac{3\alpha_1}{(2\alpha_1+\Delta)^2}\right) - \frac{2}{\alpha_1+2\Delta} - \frac{6}{3\alpha_1+2\Delta} + \frac{12}{\Delta}\\ &+\frac{2(\alpha_1+\Delta)^2}{\alpha_1(\alpha_1+\Delta-\alpha_2)} + \frac{2(\alpha_1+\Delta)^2}{(\alpha_1+\Delta-\alpha_2)^2} - \frac{2\alpha_1(\alpha_1+\Delta)}{\Delta\alpha_2}\Bigg].\end{aligned} \tag{B.4}$$

$$\omega_{\mathrm{ZX}} = -\frac{J\Omega}{\Delta}\left(\frac{\alpha_1}{\alpha_1+\Delta}\right) + \frac{J\Omega^3\alpha_1^2(3\alpha_1^3+11\alpha_1^2\Delta+15\alpha_1\Delta^2+9\Delta^3)}{2\Delta^3(\alpha_1+\Delta)^3(\alpha_1+2\Delta)(3\alpha_1+2\Delta)}. \tag{B.5}$$

$$\omega_{\mathrm{ZY}} = 0. \tag{B.6}$$

$$\omega_{ZZ} = \frac{J^2}{2(\alpha_1+\Delta)^2}\Bigg\{\Omega^2\Big[\frac{\alpha_1^3-2\alpha_1\Delta^2-2\Delta^3}{\alpha_1\Delta^2(\alpha_2-\Delta)}+\frac{2(3\alpha_1+\Delta)(\alpha_1^2+\alpha_1\Delta+\Delta^2)}{\Delta^2(2\alpha_1+\Delta)^2} \\ -\frac{8\Delta}{3\alpha_1^2+8\alpha_1\Delta+4\Delta^2}+\frac{2\alpha_1}{\Delta\alpha_2}-\frac{2(\alpha_1+\Delta)}{(\alpha_1+\Delta-\alpha_2)^2}-\frac{2(\alpha_1+\Delta)}{\alpha_1(\alpha_1+\Delta-\alpha_2)}\Big] \\ +\frac{2(\alpha_1+\Delta)(\alpha_1+\alpha_2)}{\Delta-\alpha_2}\Bigg\}. \tag{B.7}$$

Appendix C

Additional measurements for the coupled qubit device

C.1 Anharmonicity extraction

Transitions ω_{12} in the two-tone spectroscopy illustrated in Fig. 5.16 were not visible. Fig. C.1 shows a spectroscopy carried out at higher drive power, making the ω_{12} signal visible.

The measurement yielded, when computing the anharmonicity as $\alpha = \omega_{01} - \omega_{12}$,

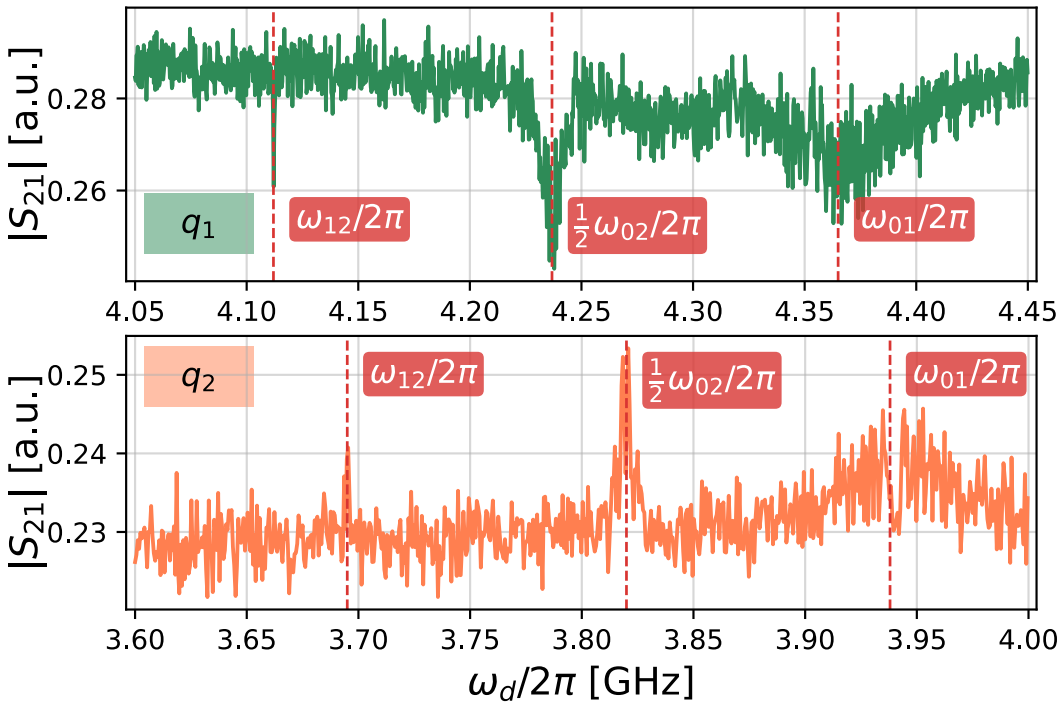

FIGURE C.1: Two-tone spectroscopy for q_1 and q_2 in the coupled qubits device, highlighting the transitions $|0\rangle \leftrightarrow |1\rangle$, $|0\rangle \leftrightarrow |2\rangle$, and $|1\rangle \leftrightarrow |2\rangle$.

$\alpha/2\pi \approx -253$ MHz for q_1 and $\alpha/2\pi \approx= -243$ MHz for q_2. When computing $\alpha = 2\omega_{01} - \omega_{02}$, we obtained $\alpha/2\pi \approx= -256$ MHz for q_1 and $\alpha/2\pi \approx= -236$ MHz for q_2. The bifurcation visible in correspondence with the ω_{01} resonance is compatible with the power-Rabi shape observed in Fig. 5.23.

C.2 State assignment fidelity

To assess the qubit readout performance, state assignment experiments were carried out for both qubits in the device. For q_1, we centered the readout pulse at $\omega_r/2\pi = 7.225382$ GHz with a duration of 5 µs, while for q_2 the frequency was set to $\omega_r/2\pi = 6.9585$ GHz and the duration to 8 µs. The assignment accuracy, i.e. the

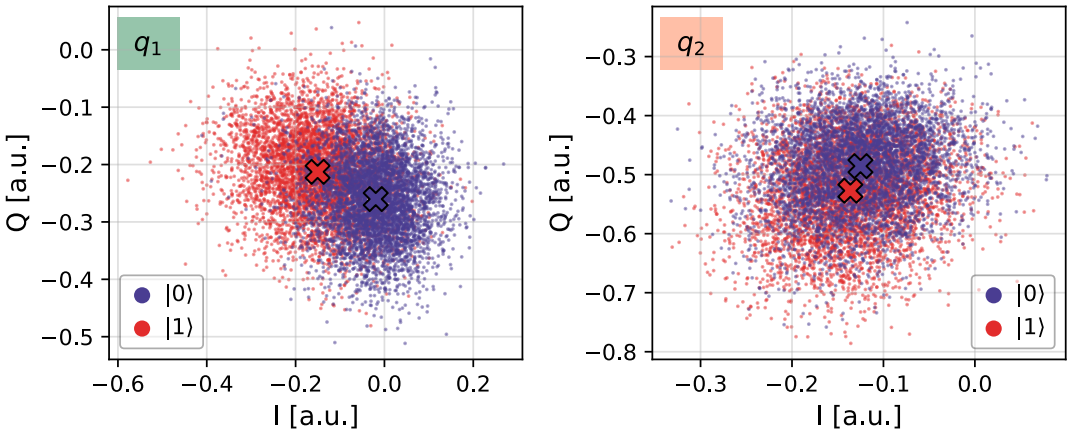

FIGURE C.2: IQ-plane representation of multiple single-shot readout experiments for q_1 (left) and q_2 (right) when prepared in states $|0\rangle$ (blue) and $|1\rangle$ red. The distribution centroids are marked with an "X".

fraction of measurements that were attributed to the correct state in which the qubit collapsed, resulted of 79.7% and 61.3% for q_1 and q_2, respectively.

Appendix D

Impact of wire bonds on CPW quality factors

In an attempt to investigate the cause of the large discrepancy between expected and measured readout resonator quality factors, described throughout Chapter 5, we characterized the impact of wire bond positioning by numerically simulating the CPW eigenmode and its total quality factor Q using Ansys HFSS. Particularly, we observed a substantial quality factor drop in the absence of a wire bond connecting the ground plane placed close to the interdigitated coupler to the feedline. Fig. D.1 shows the CPW eigenmodes corresponding to the readout resonator of qubit Q1 in the coupled qubits device, and the resulting $|S_{21}|$ spectrum with and without the coupler wire bond.

By adding the wire bond in correspondence with the coupler, the simulated quality factor increases from $Q \approx 500$ to $Q \approx 4200$, gaining a factor of ≈ 8. Such an increase may be justified by allowing for a much shorter return path through the wire bond, mitigating the effects of abrupt impedance changes introduced by splits or the coupler shape, and stabilizing the ground plane potentials across the CPW resonator sides, avoiding parasitic slotline modes [235]. Additionally, we observe a ≈ 250 MHz shift in the eigenmode frequency. In the wire bonded coupler case, the frequency appears much closer to the target value of 7.4 GHz (see Table 5.7). We conclude that robust, low-impedance connections between the ground planes near the interdigitated coupler are crucial to recover the ideal CPW resonator behavior. This will be validated experimentally in future cryogenic cooldowns and device characterizations.

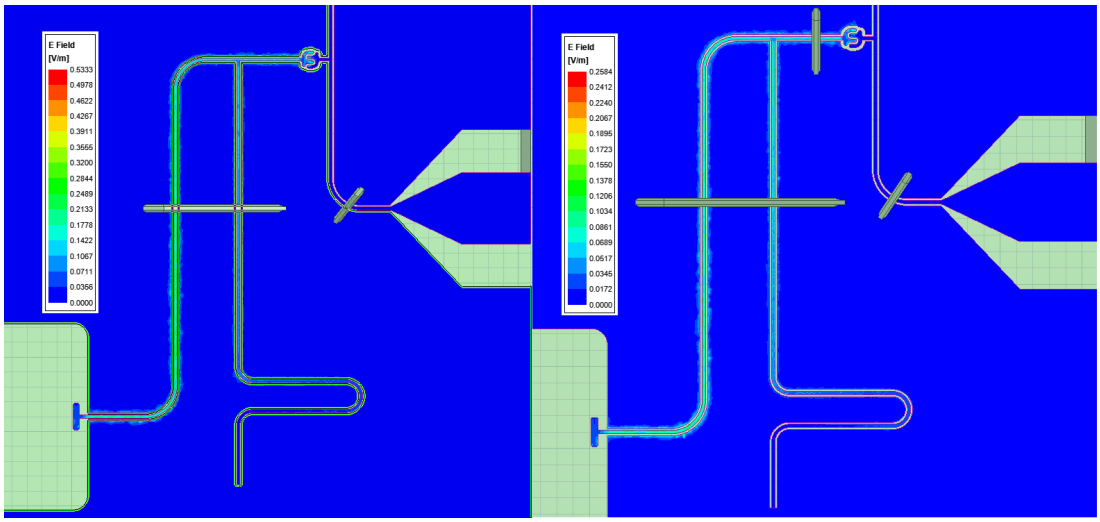

(A) Ansys HFSS Eigenmode field solutions.

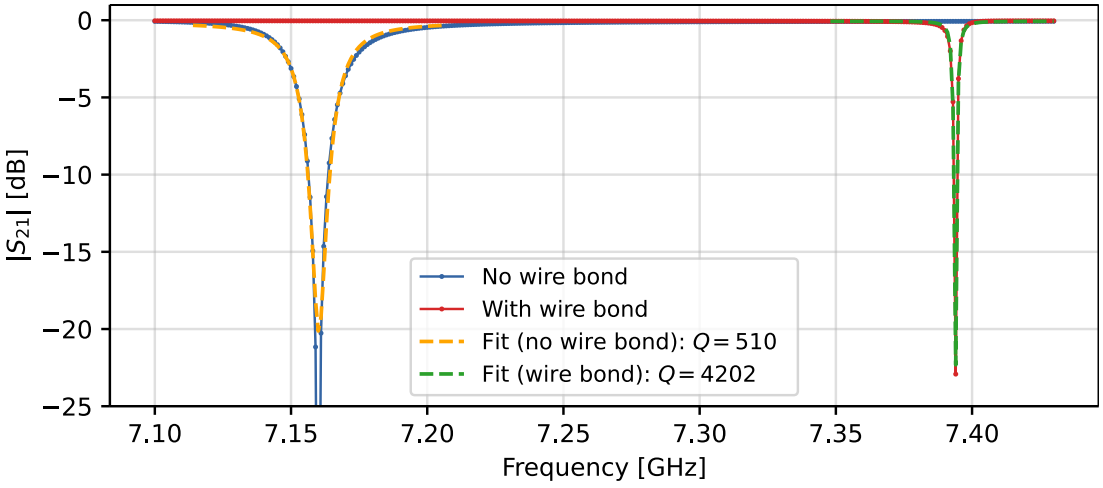

(B) Ansys HFSS modal $|S_{21}|$ solutions.

FIGURE D.1: Ansys HFSS finite-element simulation for the readout resonator of qubit Q1 in the coupled chip device. (A) CPW eigenmodes, without (left) and with (right) wire bond close to the interdigitated coupling to the feedline. (B) Modal simulation of the feedline S_{21} magnitude in the two wire bonding configurations. Resonance fitting quantifies the difference in quality factors.

Bibliography

[1] G. Q. AI and Collaborators. "Quantum error correction below the surface code threshold". In: *Nature* 638.8052 (2025), pp. 920–926. ISSN: 0028-0836, 1476-4687. DOI: 10.1038/s41586-024-08449-y.

[2] V. Giovannetti, S. Lloyd, and L. Maccone. "Quantum Metrology". In: *Phys. Rev. Lett.* 96 (1 2006), p. 010401. DOI: 10.1103/PhysRevLett.96.010401.

[3] R. P. Feynman. "Simulating physics with computers". In: *International Journal of Theoretical Physics* 21.6–7 (1982), pp. 467–488. ISSN: 1572-9575. DOI: 10.1007/bf02650179.

[4] S. Lloyd. "Universal Quantum Simulators". In: *Science* 273.5278 (1996), pp. 1073–1078. ISSN: 1095-9203. DOI: 10.1126/science.273.5278.1073.

[5] A. J. Daley et al. "Practical quantum advantage in quantum simulation". In: *Nature* 607.7920 (2022), pp. 667–676. ISSN: 1476-4687. DOI: 10.1038/s41586-022-04940-6.

[6] B. Fauseweh. "Quantum many-body simulations on digital quantum computers: State-of-the-art and future challenges". In: *Nature Communications* 15.1 (2024). ISSN: 2041-1723. DOI: 10.1038/s41467-024-46402-9.

[7] C. L. Degen, F. Reinhard, and P. Cappellaro. "Quantum sensing". In: *Rev. Mod. Phys.* 89 (3 2017), p. 035002. DOI: 10.1103/RevModPhys.89.035002.

[8] C. H. Bennett and G. Brassard. "Quantum cryptography: Public key distribution and coin tossing". In: *Theoretical Computer Science* 560 (2014), pp. 7–11. ISSN: 0304-3975. DOI: 10.1016/j.tcs.2014.05.025.

[9] D. P. Nadlinger et al. "Experimental quantum key distribution certified by Bell's theorem". In: *Nature* 607.7920 (2022), pp. 682–686. ISSN: 1476-4687. DOI: 10.1038/s41586-022-04941-5.

[10] J. Biamonte et al. "Quantum machine learning". In: *Nature* 549.7671 (2017), pp. 195–202. ISSN: 1476-4687. DOI: 10.1038/nature23474.

[11] H.-Y. Huang et al. "Quantum advantage in learning from experiments". In: *Science* 376.6598 (2022), pp. 1182–1186. ISSN: 1095-9203. DOI: 10.1126/science.abn7293.

[12] M. Cerezo et al. "Challenges and opportunities in quantum machine learning". In: *Nature Computational Science* 2.9 (2022), pp. 567–576. ISSN: 2662-8457. DOI: 10.1038/s43588-022-00311-3.

[13] C. D. Bruzewicz et al. "Trapped-ion quantum computing: Progress and challenges". In: *Applied Physics Reviews* 6.2 (2019). ISSN: 1931-9401. DOI: 10.1063/1.5088164.

[14] K. Wintersperger et al. "Neutral atom quantum computing hardware: performance and end-user perspective". In: *EPJ Quantum Technology* 10.1 (2023). ISSN: 2196-0763. DOI: 10.1140/epjqt/s40507-023-00190-1.

[15] W. Luo et al. "Recent progress in quantum photonic chips for quantum communication and internet". In: *Light: Science and Applications* 12.1 (2023). ISSN: 2047-7538. DOI: 10.1038/s41377-023-01173-8.

[16] J. P. Zwolak and J. M. Taylor. "Colloquium : Advances in automation of quantum dot devices control". In: *Reviews of Modern Physics* 95.1 (2023). ISSN: 1539-0756. DOI: 10.1103/revmodphys.95.011006.

[17] S. Pezzagna and J. Meijer. "Quantum computer based on color centers in diamond". In: *Applied Physics Reviews* 8.1 (2021). ISSN: 1931-9401. DOI: 10.1063/5.0007444.

[18] D. I. Schuster et al. "Resolving photon number states in a superconducting circuit". In: *Nature* 445.7127 (2007), pp. 515–518. ISSN: 1476-4687. DOI: 10.1038/nature05461.

[19] A. D. O'Connell et al. "Quantum ground state and single-phonon control of a mechanical resonator". In: *Nature* 464.7289 (2010), pp. 697–703. ISSN: 1476-4687. DOI: 10.1038/nature08967.

[20] A. V. Dixit et al. "Searching for Dark Matter with a Superconducting Qubit". In: *Phys. Rev. Lett.* 126 (14 2021), p. 141302. DOI: 10.1103/PhysRevLett.126.141302.

[21] S. Chen et al. "Detecting Hidden Photon Dark Matter Using the Direct Excitation of Transmon Qubits". In: *Phys. Rev. Lett.* 131 (21 2023), p. 211001. DOI: 10.1103/PhysRevLett.131.211001.

[22] C. Braggio et al. "Quantum-Enhanced Sensing of Axion Dark Matter with a Transmon-Based Single Microwave Photon Counter". In: *Physical Review X* 15.2 (2025). ISSN: 2160-3308. DOI: 10.1103/physrevx.15.021031.

[23] W. Chao et al. "Probing Light Bosonic Dark Matter with Transmon Qubits". 2025. arXiv: 2412.20850 [hep-ph].

[24] J. Reina-Valero et al. "High-frequency gravitational waves detection with the BabyIAXO haloscopes". In: *Phys. Rev. D* 111 (4 2025), p. 043024. DOI: 10.1103/PhysRevD.111.043024.

[25] R. Linehan et al. "Listening For New Physics With Quantum Acoustics". 2024. arXiv: 2410.17308 [hep-ph].

[26] M. Goryachev and M. E. Tobar. "Gravitational wave detection with high frequency phonon trapping acoustic cavities". In: *Physical Review D* 90.10 (2014). ISSN: 1550-2368. DOI: 10.1103/physrevd.90.102005.

[27] M. Brune et al. "Quantum nondemolition measurement of small photon numbers by Rydberg-atom phase-sensitive detection". In: *Phys. Rev. Lett.* 65 (8 1990), pp. 976–979. DOI: 10.1103/PhysRevLett.65.976.

[28] J. Preskill. "Quantum Computing in the NISQ era and beyond". In: *Quantum* 2 (2018), p. 79. ISSN: 2521-327X. DOI: 10.22331/q-2018-08-06-79.

[29] G. Bertone and D. Hooper. "History of dark matter". In: *Rev. Mod. Phys.* 90 (4 2018), p. 045002. DOI: 10.1103/RevModPhys.90.045002.

[30] M. Cirelli, A. Strumia, and J. Zupan. "Dark Matter". 2024. arXiv: 2406.01705 [hep-ph].

[31] H. M. Lee. "Lectures on physics beyond the Standard Model". In: *Journal of the Korean Physical Society* 78.11 (2021), pp. 985–1017. ISSN: 1976-8524. DOI: 10.1007/s40042-021-00188-x.

[32] V. C. Rubin and J. Ford W. Kent. "Rotation of the Andromeda Nebula from a Spectroscopic Survey of Emission Regions". In: *The Astrophysical Journal* 159 (1970), p. 379. ISSN: 1538-4357. DOI: 10.1086/150317.

[33] W. J. G. de Blok et al. "HIGH-RESOLUTION ROTATION CURVES AND GALAXY MASS MODELS FROM THINGS". In: *The Astronomical Journal* 136.6 (2008), pp. 2648–2719. ISSN: 1538-3881. DOI: 10.1088/0004-6256/136/6/2648.

[34] M. Bartelmann. "Gravitational lensing". In: *Classical and Quantum Gravity* 27.23 (2010), p. 233001. ISSN: 1361-6382. DOI: 10.1088/0264-9381/27/23/233001.

[35] M. Markevitch et al. "Direct Constraints on the Dark Matter Self-Interaction Cross Section from the Merging Galaxy Cluster 1E 0657-56". In: *The Astrophysical Journal* 606.2 (2004), pp. 819–824. ISSN: 1538-4357. DOI: 10.1086/383178.

[36] H. Hildebrandt et al. "KiDS-450: cosmological parameter constraints from tomographic weak gravitational lensing". In: *Monthly Notices of the Royal Astronomical Society* 465.2 (2016), pp. 1454–1498. ISSN: 1365-2966. DOI: 10.1093/mnras/stw2805.

[37] D. Clowe et al. "A Direct Empirical Proof of the Existence of Dark Matter". In: *The Astrophysical Journal* 648.2 (2006), pp. L109–L113. ISSN: 1538-4357. DOI: 10.1086/508162.

[38] Y. Akrami et al. "Planck2018 results: VII. Isotropy and statistics of the CMB". In: *Astronomy & Astrophysics* 641 (2020), A7. ISSN: 1432-0746. DOI: 10.1051/0004-6361/201935201.

[39] D. Larson et al. "SEVEN-YEAR WILKINSON MICROWAVE ANISOTROPY PROBE (WMAP) OBSERVATIONS: POWER SPECTRA AND WMAP - DERIVED PARAMETERS". In: *The Astrophysical Journal Supplement Series* 192.2 (2011), p. 16. ISSN: 1538-4365. DOI: 10.1088/0067-0049/192/2/16.

[40] L. Balkenhol et al. "Measurement of the CMB temperature power spectrum and constraints on cosmology from the SPT-3G 2018 TT, TE, and EE dataset". In: *Phys. Rev. D* 108 (2 2023), p. 023510. DOI: 10.1103/PhysRevD.108.023510.

[41] R. E. Angulo and O. Hahn. "Large-scale dark matter simulations". In: *Living Reviews in Computational Astrophysics* 8.1 (2022). ISSN: 2365-0524. DOI: 10.1007/s41115-021-00013-z.

[42] W. J. Percival. "Large Scale Structure Observations". 2013. arXiv: 1312.5490 [astro-ph.CO].

[43] R. H. Cyburt et al. "Big bang nucleosynthesis: Present status". In: *Rev. Mod. Phys.* 88 (1 2016), p. 015004. DOI: 10.1103/RevModPhys.88.015004.

[44] G. Jungman, M. Kamionkowski, and K. Griest. "Supersymmetric dark matter". In: *Physics Reports* 267.5–6 (1996), pp. 195–373. ISSN: 0370-1573. DOI: 10.1016/0370-1573(95)00058-5.

[45] E. Aprile et al. "First Dark Matter Search with Nuclear Recoils from the XENONnT Experiment". In: *Phys. Rev. Lett.* 131 (4 2023), p. 041003. DOI: 10.1103/PhysRevLett.131.041003.

[46] J. Aalbers et al. "First Dark Matter Search Results from the LUX-ZEPLIN (LZ) Experiment". In: *Phys. Rev. Lett.* 131 (4 2023), p. 041002. DOI: 10.1103/PhysRevLett.131.041002.

[47] H. Baer et al. "LHC SUSY and WIMP dark matter searches confront the string theory landscape". In: *Journal of High Energy Physics* 2019.4 (2019). ISSN: 1029-8479. DOI: 10.1007/jhep04(2019)043.

[48] B. Dasgupta and J. Kopp. "Sterile neutrinos". In: *Physics Reports* 928 (2021), pp. 1–63. ISSN: 0370-1573. DOI: 10.1016/j.physrep.2021.06.002.

[49] L. E. Strigari. "Galactic searches for dark matter". In: *Physics Reports* 531.1 (2013), pp. 1–88. ISSN: 0370-1573. DOI: 10.1016/j.physrep.2013.05.004.

[50] P. M. Candela et al. "Up-scattering production of a sterile fermion at DUNE: complementarity with spallation source and direct detection experiments". In: *Journal of High Energy Physics* 2024.10 (2024). ISSN: 1029-8479. DOI: 10.1007/jhep10(2024)032.

[51] A. Abed Abud et al. "DUNE Phase II: scientific opportunities, detector concepts, technological solutions". In: *Journal of Instrumentation* 19.12 (2024), P12005. ISSN: 1748-0221. DOI: 10.1088/1748-0221/19/12/p12005.

[52] A. Escrivà, F. Kühnel, and Y. Tada. "Primordial black holes". In: *Black Holes in the Era of Gravitational-Wave Astronomy*. Elsevier, 2024, pp. 261–377. ISBN: 9780323956369. DOI: 10.1016/b978-0-32-395636-9.00012-8.

[53] B. P. Abbott et al. "Observation of Gravitational Waves from a Binary Black Hole Merger". In: *Phys. Rev. Lett.* 116 (6 2016), p. 061102. DOI: 10.1103/PhysRevLett.116.061102.

[54] R. D. Peccei. "The Strong CP Problem and Axions". In: *Axions*. Springer Berlin Heidelberg, 2008, pp. 3–17. ISBN: 9783540735182. DOI: 10.1007/978-3-540-73518-2_1.

[55] C. Abel et al. "Measurement of the Permanent Electric Dipole Moment of the Neutron". In: *Phys. Rev. Lett.* 124 (8 2020), p. 081803. DOI: 10.1103/PhysRevLett.124.081803.

[56] R. D. Peccei and H. R. Quinn. "Conservation in the Presence of Pseudoparticles". In: *Physical Review Letters* 38.25 (1977), pp. 1440–1443. ISSN: 0031-9007. DOI: 10.1103/physrevlett.38.1440.

[57] J. Greensite. "An Introduction to the Confinement Problem". Springer Berlin Heidelberg, 2011. ISBN: 9783642143823. DOI: 10.1007/978-3-642-14382-3.

[58] B. B. Markus Kuster Georg Raffelt, ed. "Axions : theory, cosmology, and experimental searches / M. Kuster, G. Raffelt, B. Beltran (Rds.)" eng. Berlin [etc.: Springer, 2008. ISBN: 978-35-407-3517-5.

[59] R. Khatiwada et al. "Axion Dark Matter Experiment: Detailed design and operations". In: *Review of Scientific Instruments* 92.12 (2021). ISSN: 1089-7623. DOI: 10.1063/5.0037857.

[60] M. J. Jewell et al. "New results from HAYSTAC's phase II operation with a squeezed state receiver". In: *Phys. Rev. D* 107.7 (2023), p. 072007. DOI: 10.1103/PhysRevD.107.072007. arXiv: 2301.09721 [hep-ex].

[61] S. Ahn et al. "Extensive Search for Axion Dark Matter over 1 GHz with CAPP'S Main Axion Experiment". In: *Phys. Rev. X* 14 (3 2024), p. 031023. DOI: 10.1103/PhysRevX.14.031023.

[62] A. Quiskamp et al. "Exclusion of Axionlike-Particle Cogenesis Dark Matter in a Mass Window above 100 ¯eV". In: *Phys. Rev. Lett.* 132 (3 2024), p. 031601. DOI: 10.1103/PhysRevLett.132.031601.

[63] A. Rettaroli et al. "Search for axion dark matter with the QUAX–LNF tunable haloscope". In: *Phys. Rev. D* 110 (2 2024), p. 022008. DOI: 10.1103/PhysRevD.110.022008.

[64] V. Anastassopoulos et al. "New CAST limit on the axion–photon interaction". In: *Nature Physics* 13.6 (2017), pp. 584–590. ISSN: 1745-2481. DOI: 10.1038/nphys4109.

[65] K. Ehret et al. "New ALPS results on hidden-sector lightweights". In: *Physics Letters B* 689.4–5 (2010), pp. 149–155. ISSN: 0370-2693. DOI: 10.1016/j.physletb.2010.04.066.

[66] D. F. Jackson Kimball et al. "Overview of the Cosmic Axion Spin Precession Experiment (CASPEr)". In: *Microwave Cavities and Detectors for Axion Research*. Springer International Publishing, 2020, pp. 105–121. ISBN: 9783030437619. DOI: 10.1007/978-3-030-43761-9_13.

[67] G. Aad et al. "Search for short- and long-lived axion-like particles in $H \to aa \to 4\gamma$ decays with the ATLAS experiment at the LHC". In: *The European Physical Journal C* 84.7 (2024). ISSN: 1434-6052. DOI: 10.1140/epjc/s10052-024-12979-0.

[68] J. E. Kim. "Weak-Interaction Singlet and Strong CP Invariance". In: *Phys. Rev. Lett.* 43 (2 1979), pp. 103–107. DOI: 10.1103/PhysRevLett.43.103.

[69] M. Dine, W. Fischler, and M. Srednicki. "A simple solution to the strong CP problem with a harmless axion". In: *Physics Letters B* 104.3 (1981), pp. 199–202. ISSN: 0370-2693. DOI: 10.1016/0370-2693(81)90590-6.

[70] C. O'Hare. "cajohare/AxionLimits: AxionLimits". https://cajohare.github.io/AxionLimits/. Version v1.0. 2020. DOI: 10.5281/zenodo.3932430.

[71] M. Fabbrichesi, E. Gabrielli, and G. Lanfranchi. "The Physics of the Dark Photon: A Primer". Springer International Publishing, 2021. ISBN: 9783030625191. DOI: 10.1007/978-3-030-62519-1.

[72] R. Cervantes et al. "ADMX-Orpheus first search for 70 μeV dark photon dark matter: Detailed design, operations, and analysis". In: *Phys. Rev. D* 106 (10 2022), p. 102002. DOI: 10.1103/PhysRevD.106.102002.

[73] H. Abreu et al. "Search for dark photons with the FASER detector at the LHC". In: *Physics Letters B* 848 (2024), p. 138378. ISSN: 0370-2693. DOI: 10.1016/j.physletb.2023.138378.

[74] A. Anastasi et al. "Combined limit on the production of a light gauge boson decaying into $\mu^+\mu^-$ and $\pi^+\pi^-$". In: *Physics Letters B* 784 (2018), pp. 336–341. ISSN: 0370-2693. DOI: 10.1016/j.physletb.2018.08.012.

[75] J. P. Lees et al. "Search for Invisible Decays of a Dark Photon Produced in e^+e^- Collisions at BaBar". In: *Phys. Rev. Lett.* 119 (13 2017), p. 131804. DOI: 10.1103/PhysRevLett.119.131804.

[76] S. Abrahamyan et al. "Search for a New Gauge Boson in Electron-Nucleus Fixed-Target Scattering by the APEX Experiment". In: *Phys. Rev. Lett.* 107 (19 2011), p. 191804. DOI: 10.1103/PhysRevLett.107.191804.

[77] P. H. Adrian et al. "Searching for prompt and long-lived dark photons in electroproduced e^+e^- pairs with the heavy photon search experiment at JLab". In: *Phys. Rev. D* 108 (1 2023), p. 012015. DOI: 10.1103/PhysRevD.108.012015.

[78] Y. M. Andreev et al. "First Results in the Search for Dark Sectors at NA64 with the CERN SPS High Energy Muon Beam". In: *Phys. Rev. Lett.* 132 (21 2024), p. 211803. DOI: 10.1103/PhysRevLett.132.211803.

[79] J. Berger and A. Bhoonah. "Laboratory constraints on ultralight axion-like particles from precision atomic spectroscopy". 2022. DOI: 10.48550/ARXIV.2206.06364.

[80] P. deNiverville. "Searching for Sub-Gev Dark Matter at Fixed Target Neutrino Experiments". In: *Physics Procedia* 61 (2015), pp. 55–60. ISSN: 1875-3892. DOI: 10.1016/j.phpro.2014.12.010.

[81] Y.-D. Tsai et al. "Constraints on fifth forces and ultralight dark matter from OSIRIS-REx target asteroid Bennu". In: *Communications Physics* 7.1 (2024). ISSN: 2399-3650. DOI: 10.1038/s42005-024-01779-3.

[82] M. Hamada. "The minimum number of rotations about two axes for constructing an arbitrarily fixed rotation". In: *Royal Society Open Science* 1.3 (2014), p. 140145. ISSN: 2054-5703. DOI: 10.1098/rsos.140145.

[83] D. P. DiVincenzo. "The Physical Implementation of Quantum Computation". In: *Fortschritte der Physik* 48.9–11 (2000), pp. 771–783. ISSN: 1521-3978. DOI: 10.1002/1521-3978(200009)48:9/11<771::aid-prop771>3.0.co;2-e.

[84] A. Barenco et al. "Elementary gates for quantum computation". In: *Phys. Rev. A* 52 (5 1995), pp. 3457–3467. DOI: 10.1103/PhysRevA.52.3457.

[85] A. Y. Kitaev. "Quantum computations: algorithms and error correction". In: *Russian Mathematical Surveys* 52.6 (1997), pp. 1191–1249. ISSN: 1468-4829. DOI: 10.1070/rm1997v052n06abeh002155.

[86] D. M. Greenberger, M. A. Horne, and A. Zeilinger. "Going Beyond Bell's Theorem". In: *Bell's Theorem, Quantum Theory and Conceptions of the Universe*. Springer Netherlands, 1989, pp. 69–72. ISBN: 9789401708494. DOI: 10.1007/978-94-017-0849-4_10.

[87] J. M. Lorenz et al. "Systematic benchmarking of quantum computers: status and recommendations". 2025. arXiv: 2503.04905 [quant-ph].

[88] R. Moretti et al. "Enhanced feature encoding and classification on distributed quantum hardware". In: *Machine Learning: Science and Technology* 6.1 (2025), p. 015056. ISSN: 2632-2153. DOI: 10.1088/2632-2153/adb4bc.

[89] M. A. Nielsen and I. L. Chuang. "Quantum Computation and Quantum Information: 10th Anniversary Edition". Cambridge University Press, 2012. ISBN: 9780511976667. DOI: 10.1017/cbo9780511976667.

[90] P. Wang et al. "Single ion qubit with estimated coherence time exceeding one hour". In: *Nature Communications* 12.1 (2021). ISSN: 2041-1723. DOI: 10.1038/s41467-020-20330-w.

[91] T. Strohm et al. "Ion-Based Quantum Computing Hardware: Performance and End-User Perspective". 2024. DOI: 10.48550/ARXIV.2405.11450.

[92] Z. Aqua and B. Dayan. "Atom-Mediated Deterministic Generation and Stitching of Photonic Graph States". In: *PRX Quantum* 6.1 (2025). ISSN: 2691-3399. DOI: 10.1103/prxquantum.6.010340.

[93] J. Bardeen, L. N. Cooper, and J. R. Schrieffer. "Theory of Superconductivity". In: *Physical Review* 108.5 (1957), pp. 1175–1204. ISSN: 0031-899X. DOI: 10.1103/physrev.108.1175.

[94] N. K. Katam, J. Kawa, and M. Pedram. "Challenges and the status of superconducting single flux quantum technology". In: *2019 Design, Automation & Test in Europe Conference & Exhibition (DATE)*. 2019, pp. 1781–1787.

[95] P. Krantz et al. "A quantum engineer's guide to superconducting qubits". In: *Applied Physics Reviews* 6.2 (2019). ISSN: 1931-9401. DOI: 10.1063/1.5089550.

[96] D. M. Pozar. "Microwave Engineering". en. 4th ed. Chichester, England: John Wiley & Sons, 2011.

[97] M. Göppl et al. "Coplanar waveguide resonators for circuit quantum electrodynamics". In: *Journal of Applied Physics* 104.11 (2008). ISSN: 1089-7550. DOI: 10.1063/1.3010859.

[98] J. B. Keller. "Diffusion at finite speed and random walks". In: *Proceedings of the National Academy of Sciences* 101.5 (2004), pp. 1120–1122. ISSN: 1091-6490. DOI: 10.1073/pnas.0307052101.

[99] E. V. Zikiy et al. "High-Q trenched aluminum coplanar resonators with an ultrasonic edge microcutting for superconducting quantum devices". In: *Scientific Reports* 13.1 (2023). ISSN: 2045-2322. DOI: 10.1038/s41598-023-42332-6.

[100] M. V. P. Altoé et al. "Localization and Mitigation of Loss in Niobium Superconducting Circuits". In: *PRX Quantum* 3.2 (2022). ISSN: 2691-3399. DOI: 10.1103/prxquantum.3.020312.

[101] R. Meservey and P. M. Tedrow. "Measurements of the Kinetic Inductance of Superconducting Linear Structures". In: *Journal of Applied Physics* 40.5 (1969), pp. 2028–2034. ISSN: 1089-7550. DOI: 10.1063/1.1657905.

[102] P. K. Day et al. "A broadband superconducting detector suitable for use in large arrays". In: *Nature* 425.6960 (2003), pp. 817–821. ISSN: 1476-4687. DOI: 10.1038/nature02037.

[103] M. Malnou et al. "Performance of a Kinetic Inductance Traveling-Wave Parametric Amplifier at 4 Kelvin: Toward an Alternative to Semiconductor Amplifiers". In: *Physical Review Applied* 17.4 (2022). ISSN: 2331-7019. DOI: 10.1103/physrevapplied.17.044009.

[104] B. Josephson. "Possible new effects in superconductive tunnelling". In: *Physics Letters* 1.7 (1962), pp. 251–253. ISSN: 0031-9163. DOI: 10.1016/0031-9163(62)91369-0.

[105] J. H. Hinken. "Superconductor Electronics". Springer Berlin Heidelberg, 1989. ISBN: 9783642747441. DOI: 10.1007/978-3-642-74744-1.

[106] K. A. Madsen, E. J. Bergholtz, and P. W. Brouwer. "Josephson effect in a Weyl SNS junction". In: *Physical Review B* 95.6 (2017). ISSN: 2469-9969. DOI: 10.1103/physrevb.95.064511.

[107] J. Balgley et al. "Crystalline superconductor-semiconductor Josephson junctions for compact superconducting qubits". In: *Physical Review Applied* 24.3 (2025). ISSN: 2331-7019. DOI: 10.1103/3ssz-jjt6.

[108] N. O. Birge and N. Satchell. "Ferromagnetic materials for Josephson π junctions". In: *APL Materials* 12.4 (2024). ISSN: 2166-532X. DOI: 10.1063/5.0195229.

[109] P. W. Anderson and A. H. Dayem. "Radio-Frequency Effects in Superconducting Thin Film Bridges". In: *Physical Review Letters* 13.6 (1964), pp. 195–197. ISSN: 0031-9007. DOI: 10.1103/physrevlett.13.195.

[110] B. D. Josephson. "The discovery of tunnelling supercurrents". In: *Reviews of Modern Physics* 46.2 (1974), pp. 251–254. ISSN: 0034-6861. DOI: 10.1103/revmodphys.46.251.

[111] V. Ambegaokar and A. Baratoff. "Tunneling Between Superconductors". In: *Physical Review Letters* 10.11 (1963), pp. 486–489. ISSN: 0031-9007. DOI: 10.1103/physrevlett.10.486.

[112] G. Oelsner et al. "Application and fabrication aspects of sub-micrometer-sized Josephson junctions". In: *Low Temperature Physics* 43.7 (2017), pp. 779–784. ISSN: 1090-6517. DOI: 10.1063/1.4995625.

[113] N. Muthusubramanian et al. "Wafer-scale uniformity of Dolan-bridge and bridgeless Manhattan-style Josephson junctions for superconducting quantum processors". In: *Quantum Science and Technology* 9.2 (2024), p. 025006. ISSN: 2058-9565. DOI: 10.1088/2058-9565/ad199c.

[114] I. I. Rabi et al. "A New Method of Measuring Nuclear Magnetic Moment". In: *Phys. Rev.* 53 (4 1938), pp. 318–318. DOI: 10.1103/PhysRev.53.318.

[115] D. Burgarth et al. "Taming the Rotating Wave Approximation". In: *Quantum* 8 (2024), p. 1262. ISSN: 2521-327X. DOI: 10.22331/q-2024-02-21-1262.

[116] J. Koch et al. "Charge-insensitive qubit design derived from the Cooper pair box". In: *Physical Review A* 76.4 (2007). ISSN: 1094-1622. DOI: 10.1103/physreva.76.042319.

[117] M. D. Hutchings et al. "Tunable Superconducting Qubits with Flux-Independent Coherence". In: *Physical Review Applied* 8.4 (2017). ISSN: 2331-7019. DOI: 10.1103/physrevapplied.8.044003.

[118] V. Bouchiat et al. "Quantum Coherence with a Single Cooper Pair". In: *Physica Scripta* T76.1 (1998), p. 165. ISSN: 0031-8949. DOI: 10.1238/physica.topical.076a00165.

[119] J. E. Mooij et al. "Josephson Persistent-Current Qubit". In: *Science* 285.5430 (1999), pp. 1036–1039. ISSN: 1095-9203. DOI: 10.1126/science.285.5430.1036.

[120] T. P. Orlando et al. "Superconducting persistent-current qubit". In: *Phys. Rev. B* 60 (22 1999), pp. 15398–15413. DOI: 10.1103/PhysRevB.60.15398.

[121] V. E. Manucharyan et al. "Fluxonium: Single Cooper-Pair Circuit Free of Charge Offsets". In: *Science* 326.5949 (2009), pp. 113–116. ISSN: 1095-9203. DOI: 10.1126/science.1175552.

[122] A. Blais et al. "Quantum-information processing with circuit quantum electrodynamics". In: *Physical Review A* 75.3 (2007). ISSN: 1094-1622. DOI: 10.1103/physreva.75.032329.

[123] F. Motzoi et al. "Simple Pulses for Elimination of Leakage in Weakly Nonlinear Qubits". In: *Phys. Rev. Lett.* 103 (11 2009), p. 110501. DOI: 10.1103/PhysRevLett.103.110501.

[124] C. P. Koch et al. "Quantum optimal control in quantum technologies. Strategic report on current status, visions and goals for research in Europe". In: *EPJ Quantum Technology* 9.1 (2022). ISSN: 2196-0763. DOI: 10.1140/epjqt/s40507-022-00138-x.

[125] E. Knill et al. "Randomized benchmarking of quantum gates". In: *Physical Review A* 77.1 (2008). ISSN: 1094-1622. DOI: 10.1103/physreva.77.012307.

[126] Z. Chen et al. "Measuring and Suppressing Quantum State Leakage in a Superconducting Qubit". In: *Physical Review Letters* 116.2 (2016). ISSN: 1079-7114. DOI: 10.1103/physrevlett.116.020501.

[127] Z. Li et al. "Error per single-qubit gate below 10^{-4} in a superconducting qubit". In: *npj Quantum Information* 9.1 (2023). ISSN: 2056-6387. DOI: 10.1038/s41534-023-00781-x.

[128] E. Hyyppä et al. "Reducing Leakage of Single-Qubit Gates for Superconducting Quantum Processors Using Analytical Control Pulse Envelopes". In: *PRX Quantum* 5.3 (2024). ISSN: 2691-3399. DOI: 10.1103/prxquantum.5.030353.

[129] A. Blais et al. "Cavity quantum electrodynamics for superconducting electrical circuits: An architecture for quantum computation". In: *Phys. Rev. A* 69 (6 2004), p. 062320. DOI: 10.1103/PhysRevA.69.062320.

[130] E. Jaynes and F. Cummings. "Comparison of quantum and semiclassical radiation theories with application to the beam maser". In: *Proceedings of the IEEE* 51.1 (1963), pp. 89–109. ISSN: 0018-9219. DOI: 10.1109/proc.1963.1664.

[131] V. B. Braginsky and F. Y. Khalili. "Quantum nondemolition measurements: the route from toys to tools". In: *Reviews of Modern Physics* 68.1 (1996), pp. 1–11. ISSN: 1539-0756. DOI: 10.1103/revmodphys.68.1.

[132] L. Chen et al. "Transmon qubit readout fidelity at the threshold for quantum error correction without a quantum-limited amplifier". In: *npj Quantum Information* 9.1 (2023). ISSN: 2056-6387. DOI: 10.1038/s41534-023-00689-6.

[133] D. T. McClure et al. "Rapid Driven Reset of a Qubit Readout Resonator". In: *Physical Review Applied* 5.1 (2016). ISSN: 2331-7019. DOI: 10.1103/physrevapplied.5.011001.

[134] P. D. Kurilovich et al. "High-frequency readout free from transmon multi-excitation resonances". 2025. DOI: 10.48550/ARXIV.2501.09161.

[135] F. Swiadek et al. "Enhancing Dispersive Readout of Superconducting Qubits through Dynamic Control of the Dispersive Shift: Experiment and Theory". In: *PRX Quantum* 5.4 (2024). ISSN: 2691-3399. DOI: 10.1103/prxquantum.5.040326.

[136] S. Hazra et al. "Benchmarking the Readout of a Superconducting Qubit for Repeated Measurements". In: *Physical Review Letters* 134.10 (2025). ISSN: 1079-7114. DOI: 10.1103/physrevlett.134.100601.

[137] S. E. Rasmussen and N. T. Zinner. "Simple implementation of high fidelity controlled-*i*swap gates and quantum circuit exponentiation of non-Hermitian gates". In: *Physical Review Research* 2.3 (2020). ISSN: 2643-1564. DOI: 10.1103/physrevresearch.2.033097.

[138] S. P. Fors, J. Fernández-Pendás, and A. F. Kockum. "Comprehensive explanation of ZZ coupling in superconducting qubits". 2024. DOI: 10.48550/ARXIV.2408.15402.

[139] J. R. Rubbmark et al. "Dynamical effects at avoided level crossings: A study of the Landau-Zener effect using Rydberg atoms". In: *Physical Review A* 23.6 (1981), pp. 3107–3117. ISSN: 0556-2791. DOI: 10.1103/physreva.23.3107.

[140] M. Malekakhlagh, E. Magesan, and D. C. McKay. "First-principles analysis of cross-resonance gate operation". In: *Physical Review A* 102.4 (2020). ISSN: 2469-9934. DOI: 10.1103/physreva.102.042605.

[141] A. D. Córcoles et al. "Process verification of two-qubit quantum gates by randomized benchmarking". In: *Physical Review A* 87.3 (2013). ISSN: 1094-1622. DOI: 10.1103/physreva.87.030301.

[142] N. Sundaresan et al. "Reducing Unitary and Spectator Errors in Cross Resonance with Optimized Rotary Echoes". In: *PRX Quantum* 1.2 (2020). ISSN: 2691-3399. DOI: 10.1103/prxquantum.1.020318.

[143] D. Danin and F. Tennie. "Procedure for reducing cross-resonance gate errors using pulse-level control". In: *Quantum Science and Technology* 10.1 (2024), p. 015026. ISSN: 2058-9565. DOI: 10.1088/2058-9565/ad895b.

[144] A. Shukla, M. Sisodia, and A. Pathak. "Complete characterization of the directly implementable quantum gates used in the IBM quantum processors". In: *Physics Letters A* 384.18 (2020), p. 126387. ISSN: 0375-9601. DOI: 10.1016/j.physleta.2020.126387.

[145] Y. Sung et al. "Realization of High-Fidelity CZ and ZZ-Free iSWAP Gates with a Tunable Coupler". In: *Physical Review X* 11.2 (2021). ISSN: 2160-3308. DOI: 10.1103/physrevx.11.021058.

[146] F. Marxer et al. "Long-Distance Transmon Coupler with cz-Gate Fidelity above 99.8%". In: *PRX Quantum* 4.1 (2023). ISSN: 2691-3399. DOI: 10.1103/prxquantum.4.010314.

[147] A. Kandala et al. "Demonstration of a High-Fidelity cnot Gate for Fixed-Frequency Transmons with Engineered ZZ Suppression". In: *Physical Review Letters* 127.13 (2021). ISSN: 1079-7114. DOI: 10.1103/physrevlett.127.130501.

[148] M. AbuGhanem. "IBM quantum computers: evolution, performance, and future directions". In: *The Journal of Supercomputing* 81.5 (2025). ISSN: 1573-0484. DOI: 10.1007/s11227-025-07047-7.

[149] M. Bal et al. "Systematic improvements in transmon qubit coherence enabled by niobium surface encapsulation". In: *npj Quantum Information* 10.1 (2024). ISSN: 2056-6387. DOI: 10.1038/s41534-024-00840-x.

[150] S. Kono et al. "Mechanically induced correlated errors on superconducting qubits with relaxation times exceeding 0.4 ms". In: *Nature Communications* 15.1 (2024). ISSN: 2041-1723. DOI: 10.1038/s41467-024-48230-3.

[151] M. Tuokkola et al. "Methods to achieve near-millisecond energy relaxation and dephasing times for a superconducting transmon qubit". In: *Nature Communications* 16.1 (2025). ISSN: 2041-1723. DOI: 10.1038/s41467-025-61126-0.

[152] J. Baker-Jarvis and S. Kim. "The Interaction of Radio-Frequency Fields with Dielectric Materials at Macroscopic to Mesoscopic Scales". In: *Journal of Research of the National Institute of Standards and Technology* 117 (2012), p. 1. ISSN: 2165-7254. DOI: 10.6028/jres.117.001.

[153] N. S. Smirnov et al. "Wiring surface loss of a superconducting transmon qubit". In: *Scientific Reports* 14.1 (2024). ISSN: 2045-2322. DOI: 10.1038/s41598-024-57248-y.

[154] J. M. Martinis. "Surface loss calculations and design of a superconducting transmon qubit with tapered wiring". In: *npj Quantum Information* 8.1 (2022). ISSN: 2056-6387. DOI: 10.1038/s41534-022-00530-6.

[155] A. Melville et al. "Comparison of dielectric loss in titanium nitride and aluminum superconducting resonators". In: *Applied Physics Letters* 117.12 (2020). ISSN: 1077-3118. DOI: 10.1063/5.0021950.

[156] M. Checchin et al. "Measurement of the Low-Temperature Loss Tangent of High-Resistivity Silicon Using a High-Q Superconducting Resonator". In: *Physical Review Applied* 18.3 (2022). ISSN: 2331-7019. DOI: 10.1103/physrevapplied.18.034013.

[157] C. E. Murray. "Material matters in superconducting qubits". In: *Materials Science and Engineering: R: Reports* 146 (2021), p. 100646. ISSN: 0927-796X. DOI: 10.1016/j.mser.2021.100646.

[158] J. Verjauw et al. "Investigation of Microwave Loss Induced by Oxide Regrowth in High- Q Niobium Resonators". In: *Physical Review Applied* 16.1 (2021). ISSN: 2331-7019. DOI: 10.1103/physrevapplied.16.014018.

[159] M. Müller et al. "Magnetic field robust high quality factor NbTiN superconducting microwave resonators". In: *Materials for Quantum Technology* 2.1 (2022), p. 015002. ISSN: 2633-4356. DOI: 10.1088/2633-4356/ac50f8.

[160] R. Gao et al. "Epitaxial titanium nitride microwave resonators: Structural, chemical, electrical, and microwave properties". In: *Physical Review Materials* 6.3 (2022). ISSN: 2475-9953. DOI: 10.1103/physrevmaterials.6.036202.

[161] D. P. Lozano et al. "Low-loss α-tantalum coplanar waveguide resonators on silicon wafers: fabrication, characterization and surface modification". In: *Materials for Quantum Technology* 4.2 (2024), p. 025801. ISSN: 2633-4356. DOI: 10.1088/2633-4356/ad4b8c.

[162] E. M. Purcell, H. C. Torrey, and R. V. Pound. "Resonance Absorption by Nuclear Magnetic Moments in a Solid". In: *Physical Review* 69.1–2 (1946), pp. 37–38. ISSN: 0031-899X. DOI: 10.1103/physrev.69.37.

[163] A. A. Houck et al. "Controlling the Spontaneous Emission of a Superconducting Transmon Qubit". In: *Physical Review Letters* 101.8 (2008). ISSN: 1079-7114. DOI: 10.1103/physrevlett.101.080502.

[164] E. A. Sete, J. M. Martinis, and A. N. Korotkov. "Quantum theory of a bandpass Purcell filter for qubit readout". In: *Physical Review A* 92.1 (2015). ISSN: 1094-1622. DOI: 10.1103/physreva.92.012325.

[165] J. Heinsoo et al. "Rapid High-fidelity Multiplexed Readout of Superconducting Qubits". In: *Physical Review Applied* 10.3 (2018). ISSN: 2331-7019. DOI: 10.1103/physrevapplied.10.034040.

[166] J. Braumüller et al. "Concentric transmon qubit featuring fast tunability and an anisotropic magnetic dipole moment". In: *Applied Physics Letters* 108.3 (2016). ISSN: 1077-3118. DOI: 10.1063/1.4940230.

[167] G. Catelani et al. "Relaxation and frequency shifts induced by quasiparticles in superconducting qubits". In: *Physical Review B* 84.6 (2011). ISSN: 1550-235X. DOI: 10.1103/physrevb.84.064517.

[168] G. Catelani et al. "Decoherence of superconducting qubits caused by quasiparticle tunneling". In: *Physical Review B* 86.18 (2012). ISSN: 1550-235X. DOI: 10.1103/physrevb.86.184514.

[169] K. Serniak et al. "Hot Nonequilibrium Quasiparticles in Transmon Qubits". In: *Physical Review Letters* 121.15 (2018). ISSN: 1079-7114. DOI: 10.1103/physrevlett.121.157701.

[170] A. Abrikosov. "The magnetic properties of superconducting alloys". In: *Journal of Physics and Chemistry of Solids* 2.3 (1957), pp. 199–208. ISSN: 0022-3697. DOI: 10.1016/0022-3697(57)90083-5.

[171] D. Bafia et al. "Quantifying Trapped Magnetic Vortex Losses in Niobium Resonators at mK Temperatures". 2025. DOI: 10.48550/ARXIV.2503.14616.

[172] R. Barends et al. "Minimizing quasiparticle generation from stray infrared light in superconducting quantum circuits". In: *Applied Physics Letters* 99.11 (2011). ISSN: 1077-3118. DOI: 10.1063/1.3638063.

[173] C. M. Caves. "Quantum limits on noise in linear amplifiers". In: *Physical Review D* 26.8 (1982), pp. 1817–1839. ISSN: 0556-2821. DOI: 10.1103/physrevd.26.1817.

[174] A. Agrawal et al. "Stimulated Emission of Signal Photons from Dark Matter Waves". In: *Physical Review Letters* 132.14 (2024). ISSN: 1079-7114. DOI: 10.1103/physrevlett.132.140801.

[175] J. F. Kam et al. "Characterization of entanglement on superconducting quantum computers of up to 414 qubits". In: *Physical Review Research* 6.3 (2024). ISSN: 2643-1564. DOI: 10.1103/physrevresearch.6.033155.

[176] H. Lee, P. Kok, and J. P. Dowling. "A quantum Rosetta stone for interferometry". In: *Journal of Modern Optics* 49.14–15 (2002), pp. 2325–2338. ISSN: 1362-3044. DOI: 10.1080/0950034021000011536.

[177] J. Krause et al. "Magnetic Field Resilience of Three-Dimensional Transmons with Thin-Film Al/AlOx/Al Josephson Junctions Approaching 1 T". In: *Physical Review Applied* 17.3 (2022). ISSN: 2331-7019. DOI: 10.1103/physrevapplied.17.034032.

[178] Y. Y. Gao et al. "Practical Guide for Building Superconducting Quantum Devices". In: *PRX Quantum* 2.4 (2021). ISSN: 2691-3399. DOI: 10.1103/prxquantum.2.040202.

[179] P. Winkel et al. "Implementation of a Transmon Qubit Using Superconducting Granular Aluminum". In: *Physical Review X* 10.3 (2020). ISSN: 2160-3308. DOI: 10.1103/physrevx.10.031032.

[180] A. Dixit, A. Chou, and D. Schuster. "Detecting Axion Dark Matter with Superconducting Qubits". In: Fermi National Accelerator Lab. (FNAL), Batavia, IL (United States). 2018.

[181] B. Royer et al. "Itinerant Microwave Photon Detector". In: *Physical Review Letters* 120.20 (2018). ISSN: 1079-7114. DOI: 10.1103/physrevlett.120.203602.

[182] J.-C. Besse et al. "Single-Shot Quantum Nondemolition Detection of Individual Itinerant Microwave Photons". In: *Physical Review X* 8.2 (2018). ISSN: 2160-3308. DOI: 10.1103/physrevx.8.021003.

[183] R. Moretti et al. "Transmon Qubit Modeling and Characterization for Dark Matter Search". In: *IEEE Transactions on Quantum Engineering* 7 (2026), pp. 1–8. ISSN: 2689-1808. DOI: 10.1109/tqe.2025.3633176.

[184] S. Chaudhuri et al. "Radio for hidden-photon dark matter detection". In: *Physical Review D* 92.7 (2015). ISSN: 1550-2368. DOI: 10.1103/physrevd.92.075012.

[185] A. Mitridate et al. "Snowmass white paper: Light dark matter direct detection at the interface with condensed matter physics". In: *Physics of the Dark Universe* 40 (2023), p. 101221. ISSN: 2212-6864. DOI: 10.1016/j.dark.2023.101221.

[186] S. Chen et al. "Search for QCD axion dark matter with transmon qubits and quantum circuit". In: *Physical Review D* 110.11 (2024). ISSN: 2470-0029. DOI: 10.1103/physrevd.110.115021.

[187] S. Huang et al. "Microwave Package Design for Superconducting Quantum Processors". In: *PRX Quantum* 2.2 (2021). ISSN: 2691-3399. DOI: 10.1103/prxquantum.2.020306.

[188] P. Sikivie. "Invisible axion search methods". In: *Reviews of Modern Physics* 93.1 (2021). ISSN: 1539-0756. DOI: 10.1103/revmodphys.93.015004.

[189] A. Kringhøj et al. "Magnetic-Field-Compatible Superconducting Transmon Qubit". In: *Physical Review Applied* 15.5 (2021). ISSN: 2331-7019. DOI: 10.1103/physrevapplied.15.054001.

[190] J. G. Kroll et al. "Magnetic field compatible circuit quantum electrodynamics with graphene Josephson junctions". In: *Nature Communications* 9.1 (2018). ISSN: 2041-1723. DOI: 10.1038/s41467-018-07124-x.

[191] D. J. Marsh. "Axion cosmology". In: *Physics Reports* 643 (2016), pp. 1–79. ISSN: 0370-1573. DOI: 10.1016/j.physrep.2016.06.005.

[192] X. Y. Jin et al. "Thermal and Residual Excited-State Population in a 3D Transmon Qubit". In: *Physical Review Letters* 114.24 (2015). ISSN: 1079-7114. DOI: 10.1103/physrevlett.114.240501.

[193] D. S. Lvov et al. "Thermometry based on a superconducting qubit". In: *Physical Review Applied* 23.5 (2025). ISSN: 2331-7019. DOI: 10.1103/physrevapplied.23.054079.

[194] F. Wang et al. "High-coherence fluxonium qubits manufactured with a wafer-scale-uniformity process". In: *Physical Review Applied* 23.4 (2025). ISSN: 2331-7019. DOI: 10.1103/physrevapplied.23.044064.

[195] B.-L. Najera-Santos et al. "High-Sensitivity ac-Charge Detection with a MHz-Frequency Fluxonium Qubit". In: *Physical Review X* 14.1 (2024). ISSN: 2160-3308. DOI: 10.1103/physrevx.14.011007.

[196] D. Ristè et al. "Initialization by Measurement of a Superconducting Quantum Bit Circuit". In: *Physical Review Letters* 109.5 (2012). ISSN: 1079-7114. DOI: 10.1103/physrevlett.109.050507.

[197] P. Magnard et al. "Fast and Unconditional All-Microwave Reset of a Superconducting Qubit". In: *Physical Review Letters* 121.6 (2018). ISSN: 1079-7114. DOI: 10.1103/physrevlett.121.060502.

[198] G. Kim et al. "Fast unconditional reset and leakage reduction of a tunable superconducting qubit via an engineered dissipative bath". In: *Physical Review Applied* 24.1 (2025). ISSN: 2331-7019. DOI: 10.1103/6wc6-78y3.

[199] Y. Zhou et al. "Rapid and unconditional parametric reset protocol for tunable superconducting qubits". In: *Nature Communications* 12.1 (2021). ISSN: 2041-1723. DOI: 10.1038/s41467-021-26205-y.

[200] S. Chen et al. "Quantum Enhancement in Dark Matter Detection with Quantum Computation". In: *Physical Review Letters* 133.2 (2024). ISSN: 1079-7114. DOI: 10.1103/physrevlett.133.021801.

[201] S. F. Huelga et al. "Improvement of Frequency Standards with Quantum Entanglement". In: *Physical Review Letters* 79.20 (1997), pp. 3865–3868. ISSN: 1079-7114. DOI: 10.1103/physrevlett.79.3865.

[202] A. Yeremeyev et al. "Variational preparation of entangled states in a system of transmon qubits". 2025. DOI: 10.48550/ARXIV.2504.01754.

[203] M. S. Moreira et al. "Realization of a quantum neural network using repeat-until-success circuits in a superconducting quantum processor". In: *npj Quantum Information* 9.1 (2023). ISSN: 2056-6387. DOI: 10.1038/s41534-023-00779-5.

[204] A. Pérez-Salinas et al. "Data re-uploading for a universal quantum classifier". In: *Quantum* 4 (2020), p. 226. ISSN: 2521-327X. DOI: 10.22331/q-2020-02-06-226.

[205] A. Javadi-Abhari et al. "Quantum computing with Qiskit". 2024. DOI: 10.48550/ARXIV.2405.08810.

[206] H. F. Trotter. "On the product of semi-groups of operators". In: *Proceedings of the American Mathematical Society* 10.4 (1959), pp. 545–551. ISSN: 1088-6826. DOI: 10.1090/s0002-9939-1959-0108732-6.

[207] A. Jamiołkowski. "Linear transformations which preserve trace and positive semidefiniteness of operators". In: *Reports on Mathematical Physics* 3.4 (1972), pp. 275–278. ISSN: 0034-4877. DOI: 10.1016/0034-4877(72)90011-0.

[208] M.-D. Choi. "Completely positive linear maps on complex matrices". In: *Linear Algebra and its Applications* 10.3 (1975), pp. 285–290. ISSN: 0024-3795. DOI: 10.1016/0024-3795(75)90075-0.

[209] P. Groszkowski and J. Koch. "Scqubits: a Python package for superconducting qubits". In: *Quantum* 5 (2021), p. 583. ISSN: 2521-327X. DOI: 10.22331/q-2021-11-17-583.

[210] A. Vepsäläinen et al. "Improving qubit coherence using closed-loop feedback". In: *Nature Communications* 13.1 (2022). ISSN: 2041-1723. DOI: 10.1038/s41467-022-29287-4.

[211] J. M. Chávez-Garcia et al. "Weakly Flux-Tunable Superconducting Qubit". In: *Physical Review Applied* 18.3 (2022). ISSN: 2331-7019. DOI: 10.1103/physrevapplied.18.034057.

[212] In: *Philosophical Transactions of the Royal Society of London. Series A, Containing Papers of a Mathematical or Physical Character* 231.694–706 (1933), pp. 289–337. ISSN: 2053-9258. DOI: 10.1098/rsta.1933.0009.

[213] S. S. Wilks. "The Large-Sample Distribution of the Likelihood Ratio for Testing Composite Hypotheses". In: *The Annals of Mathematical Statistics* 9.1 (1938), pp. 60–62. ISSN: 0003-4851. DOI: 10.1214/aoms/1177732360.

[214] D. Cucurachi et al. "KQCircuits". 2021. DOI: 10.5281/zenodo.4944796.

[215] ANSYS, Inc. "ANSYS Q3D Extractor, Release 2022 R1". Computer software. ANSYS, Inc. Southpointe, 2600 Ansys Drive, Canonsburg, PA, USA, 2022.

[216] Y. Yanay et al. "Two-dimensional hard-core Bose–Hubbard model with superconducting qubits". In: *npj Quantum Information* 6.1 (2020). ISSN: 2056-6387. DOI: 10.1038/s41534-020-0269-1.

[217] ANSYS, Inc. "ANSYS HFSS, Release 2022 R1". Computer software. ANSYS, Inc. Southpointe, 2600 Ansys Drive, Canonsburg, PA, USA, 2022.

[218] R. Moretti et al. "Design and Simulation of a Transmon Qubit Chip for Axion Detection". In: *IEEE Transactions on Applied Superconductivity* 34.3 (2024), pp. 1–5. ISSN: 2378-7074. DOI: 10.1109/tasc.2024.3350582.

[219] R. Barends et al. "Coherent Josephson Qubit Suitable for Scalable Quantum Integrated Circuits". In: *Physical Review Letters* 111.8 (2013). ISSN: 1079-7114. DOI: 10.1103/physrevlett.111.080502.

[220] L. Ding et al. "High-Fidelity, Frequency-Flexible Two-Qubit Fluxonium Gates with a Transmon Coupler". In: *Physical Review X* 13.3 (2023). ISSN: 2160-3308. DOI: 10.1103/physrevx.13.031035.

[221] M. F. Gely and G. A. Steele. "QuCAT: quantum circuit analyzer tool in Python". In: *New Journal of Physics* 22.1 (2020), p. 013025. ISSN: 1367-2630. DOI: 10.1088/1367-2630/ab60f6.

[222] R. M. Foster. "A Reactance Theorem". In: *Bell System Technical Journal* 3.2 (1924), pp. 259–267. ISSN: 0005-8580. DOI: 10.1002/j.1538-7305.1924.tb01358.x.

[223] Q.-M. Chen et al. "Scattering coefficients of superconducting microwave resonators. I. Transfer matrix approach". In: *Physical Review B* 106.21 (2022). ISSN: 2469-9969. DOI: 10.1103/physrevb.106.214505.

[224] E. Jeffrey et al. "Fast Accurate State Measurement with Superconducting Qubits". In: *Physical Review Letters* 112.19 (2014). ISSN: 1079-7114. DOI: 10.1103/physrevlett.112.190504.

[225] E. Magesan and J. M. Gambetta. "Effective Hamiltonian models of the cross-resonance gate". In: *Physical Review A* 101.5 (2020). ISSN: 2469-9934. DOI: 10.1103/physreva.101.052308.

[226] S. Kosen et al. "Signal Crosstalk in a Flip-Chip Quantum Processor". In: *PRX Quantum* 5.3 (2024). ISSN: 2691-3399. DOI: 10.1103/prxquantum.5.030350.

[227] J. Rönkkö et al. "On-premises superconducting quantum computer for education and research". In: *EPJ Quantum Technology* 11.1 (2024). ISSN: 2196-0763. DOI: 10.1140/epjqt/s40507-024-00243-z.

[228] R. D. Chang et al. "Eliminating Surface Oxides of Superconducting Circuits with Noble Metal Encapsulation". In: *Physical Review Letters* 134.9 (2025). ISSN: 1079-7114. DOI: 10.1103/physrevlett.134.097001.

[229] A. Arsenovic et al. "scikit-rf: An Open Source Python Package for Microwave Network Creation, Analysis, and Calibration [Speaker's Corner]". In: *IEEE Microwave Magazine* 23.1 (2022), pp. 98–105. ISSN: 1557-9581. DOI: 10.1109/mmm.2021.3117139.

[230] S. Efthymiou et al. "Qibolab: an open-source hybrid quantum operating system". In: *Quantum* 8 (2024), p. 1247. ISSN: 2521-327X. DOI: 10.22331/q-2024-02-12-1247.

[231] D. R. S. Saputro and P. Widyaningsih. "Limited memory Broyden-Fletcher-Goldfarb-Shanno (L-BFGS) method for the parameter estimation on geographically weighted ordinal logistic regression model (GWOLR)". In: *AIP Conference Proceedings*. Author(s), 2017. DOI: 10.1063/1.4995124.

[232] M. J. D. Powell. "A Direct Search Optimization Method That Models the Objective and Constraint Functions by Linear Interpolation". In: *Advances in Optimization and Numerical Analysis*. Springer Netherlands, 1994, pp. 51–67. ISBN: 9789401583305. DOI: 10.1007/978-94-015-8330-5_4.

[233] R. Moretti. "QubitDM - Qubits for Dark Matter Search". Version v0.1.0. 2025. DOI: 10.5281/zenodo.17434661.

[234] R. Moretti. "QDAST - Quantum Design and Simulation Tool". Version v0.1.0. 2025. DOI: 10.5281/zenodo.17435134.

[235] Z. Chen et al. "Fabrication and characterization of aluminum airbridges for superconducting microwave circuits". In: *Applied Physics Letters* 104.5 (2014). ISSN: 1077-3118. DOI: 10.1063/1.4863745.